University of Glasgow

Steele, John Douglas (1987) *Development of quantitative microanalysis techniques and their application to selected biological systems.* PhD thesis.

http://theses.gla.ac.uk/5578/

DEVELOPMENT OF QUANTITATIVE MICROANALYSIS TECHNIQUES AND THEIR

APPLICATION TO SELECTED BIOLOGICAL SYSTEMS

by John Douglas Steele

Submitted for the degree of Doctor of Philosophy in the

University of Glasgow.

February 1987

DECLARATION

This thesis has been written solely by me and is an account of my research undertaken in the Department of Physics and Astronomy, The University, Glasgow. The work described is my own, except where otherwise stated.

The following papers have been published, presenting results mentioned in this thesis.

i) "Evaluation of EDX detector parameters". J D Steele, J N Chapman, P F Adam (1984) in "Electron Microscopy 1984" Proc 8th European Congress on Electron Microscopy (Budapest), p373.

ii) "Characterisation of Biological Hydroxyapatite Spectra with a view to evaluating Trace Element Concentrations". J D Steele, J N Chapman and H Y Elder in "MICRO 84", Proc of Royal Micro. Soc., Vol 19 part 4S , p86.

iii) "The Shape of the Bremsstrahlung background in thin film X-ray Spectra". W A P Nicholson, P F Adam, A J Craven and J D Steele (1984) in "Analytical Electron Microscopy" (D B Williams and D C Joy eds.) San Francisco Press p257.

iv) "A Single-Stage Process for Quantifying Electron Energy-loss Spectra". J D Steele, J M Titchmarsh, J N Chapman and J H Paterson (1985) in "Ultramicroscopy" $\underline{17}$ 273.

v) "The Separation of Characteristic Signals from Complex EELS Spectra". J N Chapman, J D Steele, J H Paterson and J M Titchmarsh (1985) in "EMAG 85" Inst. Phys. Conf. Ser. No. 78 p177.

This thesis has not been submitted in any previous application for a degree.

CONTENTS

CHAPTER 8   CONCLUSIONS AND FUTURE WORK

APPENDIX 1

ACKNOWLEDGEMENTS

SUMMARY

The objective of the research that I have undertaken was to develop two quantitative techniques used in analytical electron microscopy; energy dispersive X-ray microanalysis (EDX) and electron energy loss spectroscopy (EELS) and to apply those techniques to a selected biological system. More specifically the aim was to develop a technique for quantifying, at high spatial resolution, trace concentrations of Al in mineralised bone.

The Al was highly localised and therefore it was important to select the microanaltyical technique with the required spatial resolution ($<1\mu m$) compatible with the highest sensitivity. In practice, the choice was relatively simple because the signals from the trace concentrations could not be detected using EELS due to the combined effects of plural inelastic scattering in the sample, and a low signal to background ratio. The former problem resulted from the difficulty in preparing sufficiently thin samples, and the latter is an inherent problem of EEL spectroscopy. Therefore EDX was chosen for the mineralised bone study.

As is always the case, artefacts are introduced into the spectral data by the measurement system itself and it was necessary to first quantify these artefacts before attempting to process the EDX spectra. Standards of accurately known composition are often used to quantify the characteristic signals extracted from EDX spectra. Unfortunately, suitable standards were not available for the elements of interest. Therefore, a standardless quantitation procedure was used. Since the accuracy of the method was dependent upon the accuracy of the

parameterised characteristic cross-sections, some time was spent determining the optimal parameterisation.

Significant problems exist when attempting to extract the Al and Mg signals from the EDX mineralised bone spectra. Essentially these are due to the extensive overlap between the major P peak and the vanishingly small Al (and Mg) signals of interest. In addition it is difficult to model the bremsstrahlung background (for characteristic signal extraction) at the Al and Mg X-ray energies because of the combined effects of absorption in the detector and specimen, and incomplete charge collection in the detector. However, a technique was developed which greatly improves the accuracy of the characteristic signal extraction over existing methods.

A new method of EEL spectral processing was developed in which the characteristic signals are separated from the background counts and quantified in a single process. This "single-stage" technique appears to have some advantages over the standard "extrapolation" method of spectral processing; eg when dealing with adjacent edge signals or small signals on relatively large backgrounds.

A detailed investigation was made into all the problems associated with the application of EELS to the mineralised bone study of interest here; ie the difficulties of EEL mineralised bone specimen preparation and the very low Al signal/background ratio which is predicted, even if suitable mineralised bone samples could have been prepared.

Finally, a brief investigation was made into the physiological implications of the mineralised bone atomic ratios obtained in the EDX study.

CHAPTER 1

INTRODUCTION

In much of the early analytical X-ray work, wavelength dispersive detectors and proportional counters were used (e.g. Dolby, 1963). Unfortunately, the opposing requirements of the electron optics and the detector geometries, together with the difficulties involved in using such detectors, hindered the development of the technique in the electron microscope. Mineralising tissues were the first biological specimens to be examined by microanalysis because they seemed the least likely to be damaged by the electron beam. Also, because of their similarity to naturally occurring minerals, they could be easily prepared by the established techniques of grinding and polishing (e.g. Boyde et al, 1963). Later, Höhling et al (1970, 1972) demonstrated that relatively simple methods of preparing thin sections of mineralising tissues could lead to biologically significant results. The early successes of these and other workers. lead to the (mistaken) belief that bone is an "easy" tissue for microscope analysis.

In the early 70's energy dispersive solid state detectors became available making electron microscopical X-ray analysis easier. However, even when well collimated, the EDX detector accepts X-rays from a much wider solid angle than the crystal spectrometer. The problems found with the new EDX detectors were typically due to the detection of a very significant amount of bulk instrumental radiation which could severely interfere with the accurate analysis of thin samples (e.g. Goldstein et al, 1977). Nicholson et al (1977a) described a number of modifications to a transmission electron microscope (TEM) which greatly reduced the level of detected instrumental radiation. Then followed a

series of physiological studies on the bone mineralising process (Nicholson et al, 1977b), Dempster et al (1978, 1979), rachitic (vitamin D deficient) bone (Dempster al al, 1980a, 1980b) and Al poisoned bone (vitamin D resistant osteomalacia), (Boyce et al, 1981 and 1982). More recently using an EEL imaging technique, Arsenault et al (1983a), (1983b) have imaged the distribution of Ca, P, S and Al in normal and pathological (Al poisoned) mineralising bone.

This thesis is an extension to the aforementioned studies with particular emphasis on the problems associated with the accurate extraction of "vanishingly" small signals, either overlapped by other major characteristic signals, or superimposed on a relatively large number of background counts. Chapters 2 and 3 describe respectively; the electron/specimen interactions giving rise to the EDX and EEL characteristic signals, and the scanning transmission electron microscope (STEM) used for spectral acquisition. In Chapter 4 two EDX studies are described; the first concerning the quantitation of the EDX detector efficiency, and the second consisting of a further investigation into the parameterisation of the characteristic cross-section data of Gray (1981). Chapter 5 describes the development and application of a technique for processing mineralised bone spectra which greatly improves the accuracy of the signal extraction. A new method of EEL spectral processing in which the characteristic counts are separated from the background counts and quantified in a single process is described in Chapter 6. Chapter 7 discusses in detail the problems associated with the application of EELS for the Al/mineralised bone study of interest here; i.e. the difficulties associated with EEL mineralised bone specimen preparation, and the problem of a low Al

signal/background ratio which is predicted, even if suitable mineralised bone samples could be prepared. Finally, the physiological interpretation of the EDX mineralised bone atomic ratios is discussed in Appendix 1.

CHAPTER 2

THEORETICAL CONSIDERATIONS

2.1 INTRODUCTION

In this chapter the theoretical background of EDX and EELS is discussed. This discussion is mainly concerned with a description of the signals resulting from the interaction of a monoenergetic beam of electrons with a thin specimen. By thin it is implied that an incident electron will interact once with the specimen and only lose a small fraction of its energy. However, plural inelastic scattering involving small energy losses is also important since it limits the practical application of EELS. Therefore, Section 2.10 will describe some effects of plural scattering.

Quantitation of EDX and EEL spectra requires the ability to predict the probability that a particular type of inelastic scattering interaction involving the K and L shells of an atom will occur. Atomic theories are often used to describe this interaction, its probability usually being expressed as a cross-section. The most frequently used method of calculating ionisation cross-sections follows the theory of Bethe (1930) which is based on the Born approximation and assumes that the incident electron can be regarded as a sudden and small external pertubation to the atom. The first Born approximation is known to be valid in cases where the incident electron energy is large compared with the ionisation energy of the inner shell (Inokuti 1971) and where the average scattering angle and momentum transfer are small (Inokuti et al 1978). These conditions hold to a reasonable approximation for the case of K-shell excitations of light elements by incident electrons of energy >30 keV (Egerton 1979). Finally, it should be noted that in the

4

following discussion no account is taken of exchange effects that may result owing to the indistinguishability of the incident and atomic electrons. Massey (1931) suggests that exchange effects are only important if the incident electron loses a significant fraction of its energy. Under such circumstances the basic assumptions implicit to the Born approximation would be invalid.

2.2   THE BASIC FORMULA FOR INELASTIC SCATTERING

An electron of mass m_0, velocity v_0 and charge $-e$ collides with a stationary atom in an energy state E_0. The atom undergoes a transition to an excited state n during the electron scattering. The electron loses energy $\Delta E = E_n - E_0$ and is scattered into a small solid angle centred about an angle θ with respect to the incident electron direction. In the momentum representation (see Figure 2.1), one can describe the electron before and after collision by the wave vectors $\underline{k}$ and $\underline{k}_n$ respectively. For fast (but non-relativistic) collisions the cross-section $d\sigma_n$ for the scattering event can be derived from the first Born approximation as (Inokuti 1971)

$$d\sigma_n = \frac{4\pi m_0 e^4}{\hbar^4} \frac{Z_n}{k^2 K^4} \left| \mathcal{E}_n(K) \right|^2 d\left(K^2\right) \qquad 2.1$$

where Z_n is the number of electrons in the nth shell, $\hbar K$ is the transfer of momentum from the incident electron to the atom and $\mathcal{E}_n(K)$ is the inelastic scattering form factor which reflects the internal dynamics of

5
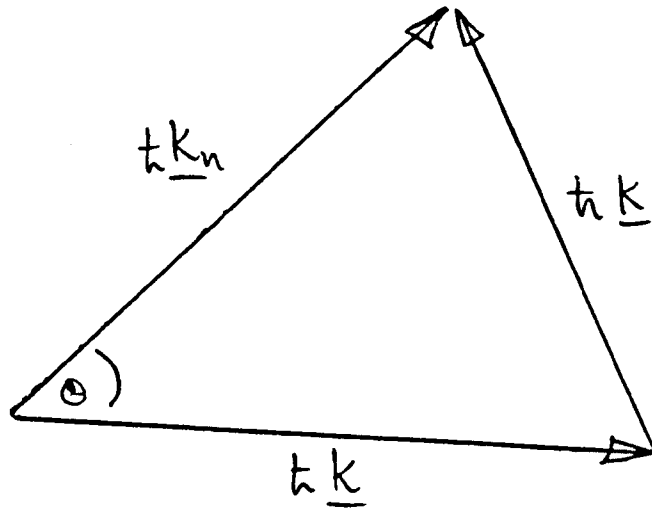
Figure 2.1

the atom. This last term can be written as

$$\mathcal{E}_n(K) = \langle f | \exp(2\pi i K' r) | i \rangle$$

where i> and f> are the initial and final states of the atomic electron.
It is apparent therefore that the atomic electron wavefunctions should
be known for cross-section evaluation. If the parameter Q is defined as

$$Q = \hbar^2 K^2 / 2m_o$$

then Equation 2.1 can be written as

$$d\sigma_n = \left[\frac{\pi e^4 z_n}{(\frac{1}{2} m_o v_o^2) Q} d(\ln Q) \right] \left[|\mathcal{E}_n(K)|^2 \right] \quad 2.2$$

It should be noted that Equation 2.2 explicitly contains v_o rather than
the kinetic energy $T_o = eV_o$ where V_o is the voltage through which the
incident electron has been accelerated. The variable $E_o = \frac{1}{2} m_o v_o^2$ is
related to T_o by the following equation

$$E_o = \frac{1}{2} m_o c^2 \beta_o^2 = \frac{1}{2} m_o c^2 \left[1 - \left(\frac{1}{1 + T_o/m_o c^2} \right)^2 \right]$$

where β_o is the ratio of v_o to the speed of light c.

Equation 2.2 may be considered to be composed of two factors. The

6

first term in brackets is the Rutherford cross-section (Rutherford 1911) for the scattering of an electron by a free and initially stationary electron. This term can be evaluated from the observable quantities k, k_n and θ_n which describe the incident electron alone. The inelastic scattering form factor however, depends only on the properties of the target atom and reflects the conditional probability that the atom will make a transition to a particular excited state n. The first term is relatively simple to evaluate and it is the second term which constitutes the central object of study (e.g. Inokuti 1971).

A quantity often used in atomic physics is the generalised oscillator strength $f_n(K)$ (Bethe 1930) which is related to the inelastic scattering form factor by

$$ f_n(K) = \Delta E \, R^{-1} \left(K a_0 \right)^{-1} \left| \mathcal{E}_n(K) \right|^2 $$

where ΔE is the energy lost by the incident electron, R is the Rydberg energy and a_0 is the Bohr radius. These parameters are defined as

$$ \Delta E = E_n - E_0 $$
$$ R = m_0 e^4 / 2\hbar^2 $$
$$ a_0 = \hbar^2 / m_0 e^2 $$

Equation 2.2 can then be rewritten as (Inokuti 1971)

$$ d\sigma_n = \frac{\pi e^4 Z_n}{\left(\frac{1}{2} m_0 v_0^2 \right) \Delta E} f_n(K) \, d\left[\ln (K a_0)^2 \right] \qquad 2.3 $$

Equations 2.1 to 2.3 define the cross-section for an electron losing energy ΔE and being scattered through an angle θ. However, for EELS quantitation one requires a partial cross-section for electrons losing energy within a given range and being scattered through all angles (θ) up to a maximum scattering angle β. This will be described in Section 2.8.

For EDX quantitation the final state of the individual electrons is unimportant. Instead a total ionisation cross-section for the removal of electrons from an inner shell to an excited state is required. In addition, it is also necessary to know the probability that the vacancy in the atomic inner shell created by this excitation will decay via a radiative transition and emit an X-ray of a particular type (e.g. $K\alpha$ or $K\beta$).

2.3   TOTAL IONISATION CROSS-SECTIONS FOR EDX

To obtain the total ionisation cross-section Equation 2.3 must be integrated over all kinematically possible values of momentum transfer $\hbar K$ i.e.

$$\sigma_n = \frac{\pi e^4 Z_n}{\left(\frac{1}{2} m_o v_o^2\right)} \int_{(Ka_o)^2_{min}}^{(Ka_o)^2_{max}} f_n(K) \frac{d\left[\ln (Ka_o)^2\right]}{\Delta E \, (Ka_o)^2} \qquad 2.4$$

The minimum value of $(Ka_o)^2$ occurs at $\theta = 0$ (i.e. forward scattering) whilst the maximum value of Ka_o occurs at $\theta = \pi$. Values for these limits are discussed by Inokuti (1971).

8

Egerton (1979) has evaluated Equation 2.4 numerically for K and L shell ionisation using a semi-analytic model involving hydrogenic wavefunctions. Rez (1984) has evaluated Equation 2.4 numerically using hydrogenic and Hartree-Slater wavefunctions; however, these latter calculations were not performed over a wide enough range of elements to be of much general use in microanalysis. Currently the most useful approach involves expressing σ_n in terms of an asymptotic expansion in $E_0 = 1/2\, m_0 v_0^2$. This is possible because the basic theoretical framework assumes sufficiently large values of E_0. If it is also assumed that the atomic electrons may be described by hydrogenic wavefunctions then the ionisation cross-section per atom may be expressed as (Bethe 1930)

$$\sigma_n = \frac{\pi e^4 Z_n}{\left(\frac{1}{2} m_0 v_0^2\right) I_n} \; b_n \; \ln\left[\frac{2 m_0 v_0^2}{B_n}\right] \qquad 2.5$$

where I_n is the binding energy of the nth inner shell. The parameter b_n was estimated by Bethe (using hydrogenic wave functions) to be between 0.2 and 0.6 for inner shells and, for a given shell, to be a function of atomic number. The energy B_n was estimated by Bethe to be of the order of I_n. With the values of the constants inserted Equation 2.5 becomes

$$\sigma_n = \frac{\pi e^4 Z_n}{\left(\frac{1}{2} m_0 v_0^2\right) I_n} \; b_n \; \ln\left[\frac{c_n m_0 v_0^2}{2 I_n}\right] \qquad 2.6a$$

where $c_n = 4I_n/B_n$. It should be noted that the use of hydrogenic wavefunctions is a reasonable approximation for the K-shell of most atoms since the predominant interaction with an incident electron takes place close to the centre of the atom, where the outer shells do not appeciably distort the inner-shell wave functions (Egerton 1979). In the following discussion on total ionisation cross-sections only K-shell excitation will be considered (i.e. $Z_n = 2$).

Equation 2.6a is non-relativistic and its validity may be in doubt at the incident electron energies of interest in microanalysis. There is no calculation with relativistic wavefunctions for the incident, outgoing, bound and ejected electrons with a relativistic interaction. However, Inokuti (1966) proposed that the Bethe formula would have an extended range of validity if the following modification of the logarithmic term was adopted

$$\ln\left[\frac{c_K\left(\frac{1}{2}m_0 v_0^2\right)}{I_n}\right] \longrightarrow \ln\left[\frac{c_K\left(\frac{1}{2}m_0 c^2 \beta_0^2\right)}{I_n\left(1-\beta_0^2\right)}\right] - \beta_0^2$$

The "relativistic Bethe" formula for K-shell ionisation can therefore be expressed as

$$\sigma_K = \frac{2\pi e^4}{\left(\frac{1}{2}m_0 c^2 \beta_0^2\right)I_k}\, b_K\left[\ln\left(c_K\left(\frac{1}{2}m_0 c^2 \beta_0^2\right)/I_k\right) - \ln\left(1-\beta_0^2\right) - \beta_0^2\right] \qquad 2.7a$$

This modification is discussed by Inokuti (1971).

2.4 THE FANO PLOT

Equations 2.6a and 2.7a can be rewritten as

$$\frac{\sigma_k \left(\frac{1}{2} m_0 v_0^2\right) I_k}{2\pi e^4} = b_k \ln\left(\frac{1}{2} m_0 v_0^2 / I_k\right) + b_k \ln c_k \qquad 2.6b$$

$$\frac{\sigma_k \left(\frac{1}{2} m_0 v_0^2\right) I_k}{2\pi e^4} = b_k \left[\ln\left(\frac{1}{2} m_0 v_0^2 / I_k\right) - \ln\left(1-\beta_0^2\right) - \beta_0^2\right] + b_k \ln c_k \qquad 2.7b$$

for the non-relativistic and relativistic cases respectively. Both equations are in the form of a straight line with a slope corresponding to b_k and an intercept with the vertical axis at $b_k \ln c_k$. When a set of data on the total ionisation cross-section σ_n is plotted according to either equation it is termed a Fano plot (Fano 1954).

The Fano plot assumes no theoretical values of slope and intercept and therefore can be applied to any set of data on σ_n. The following information can be obtained from such a plot. Firstly, if the graph shows straight line behaviour it suggests (but not necessarily establishes), the applicability of the Bethe theory for the range of σ chosen in the data. Secondly, some values of b_k and c_k may be extracted from the slope and intercept. This will be discussed more fully in Chapter 4.

2.5   CHOICE OF BETHE PARAMETERS

Assuming the Bethe form as described by Equation 2.5 or 2.6 is chosen to describe the total ionisation cross-section, the problem becomes that of choosing the Bethe parameters (b_K and c_K) best suited for the electron kinetic energy and sample atomic number.

As was noted in Section 2.2, the Bethe equation has an explicit dependence on v_o^2. However, the parameter $E_o = 1/2\ m_o v_o^2$ has been set equal to the kinetic energy T_o of the incident electron by many workers (e.g. Powell 1976). Chapman et al (1984) suggest that provided one defines clearly if the electron kinetic energy has been substituted for E_o, either choice seems to provide an adequate guide to the parameterisation of K-shell ionisation cross-sections. If this substitution has been performed Equation 2.6a can be rewritten as

$$\sigma_K = \frac{2\pi e^4}{T_o I_K}\ b_K'\ \ln\left[\frac{c_K' T_o}{I_K}\right] \qquad\qquad 2.6(c)$$

where b_K^1 and c_K^1 are the new Bethe parameters.

The Bethe parameters may be expected to vary (at least to some extent) with the overvoltage U_K (defined here as T_o/I_K) and atomic number Z. Powell (1976) calculated "effective" values of b_K^1 as a function of U_K assuming $c_K^1 = 2.42$ and the relation $B_K = 1.65\ E_K$ recommended by Mott et al (1949). These calculations show b_K^1 increasing from ~0.2 at the lowest values of U_K (≥ 1) and then lending to saturate at 0.55 – 0.65 for large values of U_K (≥ 25). This is due to the generalised oscillator strength being distributed over a range of excitation energies extending up to about $4I_K$ (Powell 1976). In situations where

12

$U_K > 25$ care should also be taken since relativistic effects can become significant.

The Bethe parameters may also be functions of atomic number. As was stated in Section 2.3, the parameter b_K^1 was predicted by Bethe (1930) to vary with Z for a given atomic shell. It should also be noted that c_K depends on the values of the generalised oscillator strength for all excitation energies and kinematically allowed values of momentum transfer, and thus c_K^1 will vary with atomic number (Inokuti 1971, Powell 1976).

However, in an extensive review of experimental results Powell (1976) found the Bethe form (Equation 2.6c) to be generally satisfactory within the range $4 \le U_K \le 25$ and concluded that data from different experiments on the same element led to as wide a variation in the Bethe parameters as was obtained when a range of different elements was studied. He therefore proposed that to a good approximation b_K^1 and c_K^1 could be regarded as constants for a given shell rather than functions of atomic number. Goldstein et al (1977) found that their experimental data could be fitted to an equation involving non-varying Bethe parameters as did Gray et al (1983). It should be noted that in the aforementioned studies, different Bethe parameters were derived by the different workers to best fit their data. Table 2.1 summarises those values.

Other workers(e.g. Schreiber and Wims (1981), Maher et al (1981) and Zaluzec (1984)) have found it advantageous to allow the Bethe parameters to vary with atomic number. Zaluzec (1984) suggested the following parameterisation with Z for the Bethe parameters b_K and C_K in

13

Cross section	b_K	c_K
Bethe-Powell	0.9	0.65
Modified Bethe	0.67	0.89
Goldstein	0.61	0.89

Table 2.1

Element	b_K	c_K
Mg	0.802	0.791
Al	0.790	0.807
P	0.767	0.835
Ca	0.717	0.884

Table 2.2

Element	b'_K	c'_K
Mg	1.053	1.009
Al	1.028	1.005
P	0.985	0.995
Ca	0.890	0.971

Table 2.3

Element	b_K	c_K
Al	0.707	1.113
P	0.913	0.933

Table 2.4

$$b_K = 0.9880 - 0.01883Z + 3.066 \times 10^{-4} Z^2 - 2.154 \times 10^{-5} Z^3 \qquad 2.7$$

$$C_K = 0.2821 + 0.0770Z - 3.807 \times 10^{-3} Z^2 + 8.262 \times 10^{-5} Z^3 - 4.784 \times 10^{-7} Z^4 \qquad 2.8$$

The elements Mg, Al, P and Ca were of most interest in the work to be described. Table 2.2 summarises the values of b_K and c_K calculated for those elements from Equation 2.8. Schreiber and Wims (1981) found that their data could be best described by an expression of the form

$$\sigma_k = \pi e^4 Z_k \frac{b_K' \ln(c_K' U_K)}{I_K^2 U_K^d} \qquad 2.9$$

where $c_K^1 = 1.0$ and b_K^1 and d are functions of atomic number i.e.

$$b_K' = 8.874 - 8.158 \ln Z + 2.9055 (\ln Z)^2 - 0.35778 (\ln Z)^3$$
$$\text{for} \quad Z \leq 30 \quad \text{and} \qquad 2.10$$
$$d = 1.0667 - 0.00476 Z$$

Table 2.3 summarises some values of b_K^1 and d calculated from Equation 2.10. Rez (1984) calculated theoretical Bethe parameters (the values for Al and P are given in Table 2.4) and suggested that in general the Bethe parameterisation was effective for $U_K > 2$. He also noted that the Bethe parameters are similar for a given sub shell and that b_K was always about 1.

In the studies described, the absolute value of cross-section (for

given atomic number and incident electron energy) can differ by as much as a factor of 2. Figure 2.2 shows graphs of the total ionisation cross-section for the four elements of interest here.

However, in the work to be described it is the ratios of the ionisation cross-sections for different elements at the same incident electron energy which are important. The ratios calculated from those studies show a much reduced spread in values. More specifically, the studies based on the Bethe formula agree to within 10% over a wide range of atomic number; however, this can rise to 20% for low and high atomic number elements (Chapman et al 1984). Table 2.5 summarises these ratios for the elements of interest here. Also summarised is the mean and standard deviation in the mean of each of the cross-section ratios from which it can be seen that there are spreads of $\sim$5.4%, 2.4% and 3% in the published cross-section ratios. These spreads are small because the total ionisation cross-sections change relatively slowly over the atomic number range of interest.

2.6   FLUORESCENCE YIELD AND PARTITION FUNCTION

The probability that a vacancy in the K-shell is filled through a radiative transistion is termed the fluorescence yield ω. The values of ω were taken from an extensive review by Langenberg and van Eck (1979) where mean values of the fluorescence yield were obtained for 62 elements with atomic numbers between 3 and 98. The errors quoted for the lowest atomic number elements are less than 2.5% and decrease with increasing atomic number.

The ratio of the $K\alpha$ intensity to the total K shell yield (s) is termed the partition function. The values of s   were taken from

Elemental Ratio	Bethe-Powell	Modified Bethe	Goldstein	Schreiber and Wims	Zaluzec	Average and spread
Mg/Ca	4.36	4.24	4.19	4.02	4.65	4.29±.23
Al/Ca	3.49	3.40	3.37	3.53	3.57	3.47±.08
P/Ca	2.30	2.24	2.24	2.32	2.40	2.30±.07

Table 2.5

Element	Ionisation energy/keV	ω	s
Mg	1.309	0.0270	1.0
Al	1.546	0.0377	1.0
P	2.146	0.0576	1.0
Ca	4.028	0.165	0.887

Table 2.6
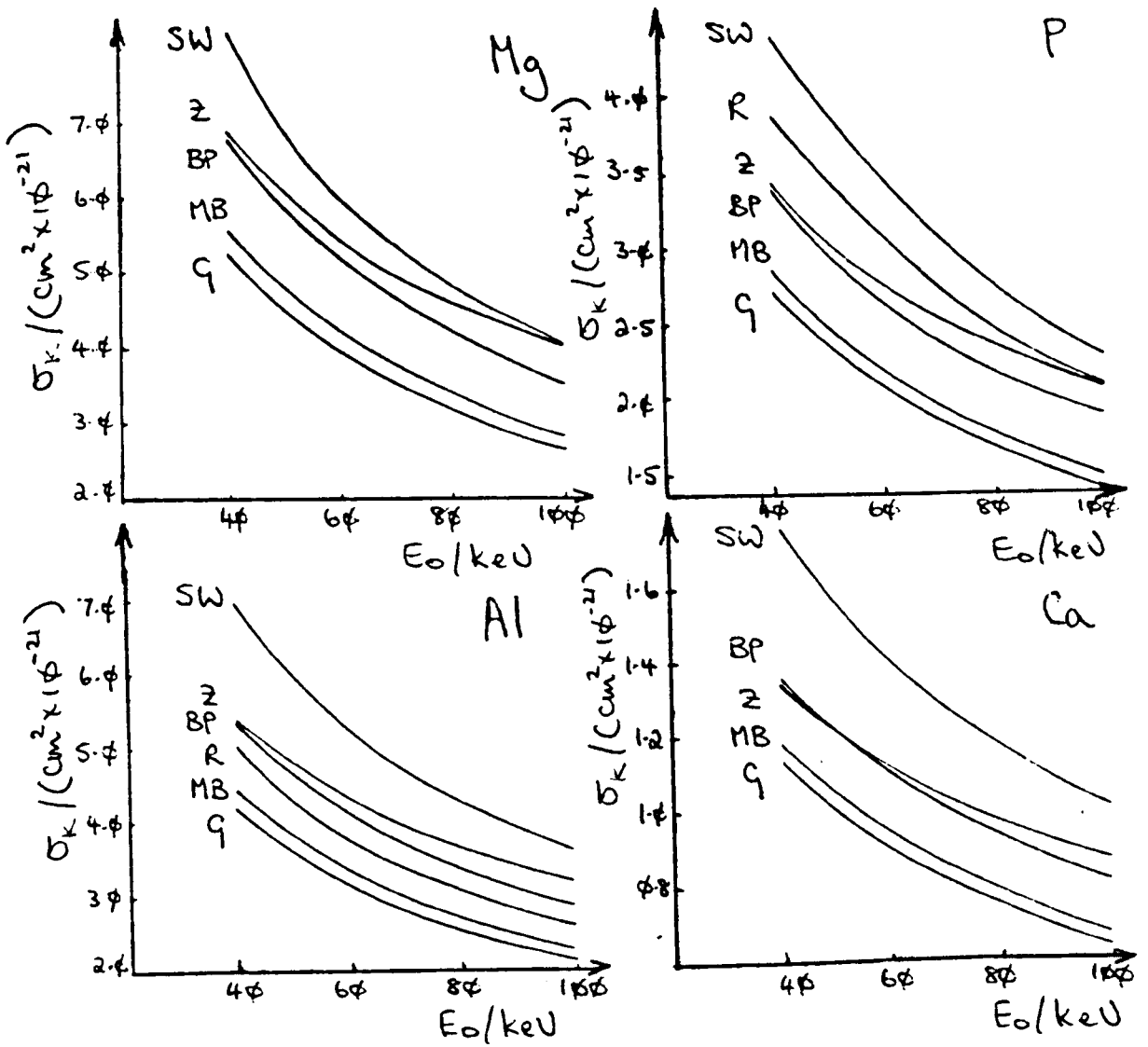
Figure 2.2
BP   Bethe-Powell
G   Green et al
MB   Gray et al
SW   Schreiber et al
Z   Zaluzec
R   Rez

Heinrich et al (1979). Khan et al (1980) have obtained values of s
which show a high degree of consistancy with the former work. Ca was
the only element of interest in this particular study where the $K\alpha$ and
$K\beta$ peaks were resolved due to the finite resolution of the Si(Li) X-ray
detector (see Chapter 3). Table 2.6 provides a summary of the values
of ω and s used.

2.7 X-RAY PRODUCTION

Following the notation in the previous sections the intensity of
the X-rays I_x produced by the electron beam/specimen interaction can be
described as

$$I_x = N_x I_i \left(\sigma_n \omega s \right)$$ 2.11

where I_i is the incident beam current and N_x is the number of atoms per
unit area of type x. Finally it should be noted that characteristic
X-ray production is isotropic (Berengi et at 1978). Bremsstrahlung
production is anisotropic and will be discussed in Section 2.11.

2.8 PARTIAL CROSS-SECTIONS FOR EEL MICROANALYSIS

As was stated earlier, the cross-section of use in EEL quantitation
is that for electrons losing a given amount of energy ΔE and being
scattered into all angles less than β. In EELS, cross-sections which
are differential with respect to energy loss are often used. Equation
2.3 can therefore be written as

16

$$\frac{d\sigma_n}{d(\Delta E)} = \frac{\pi e^4}{(\frac{1}{2}m_o v_o^2)} \frac{df(K, \Delta E)}{d(\Delta E)} \frac{d[\ln(ka_o)^2]}{\Delta E} \qquad 2.12$$

Equation 2.12 now has to be integrated over all values of momentum transfer up to that corresponding to scattering through an angle equal to β.

$$\frac{d\sigma_n(\beta)}{d(\Delta E)} = \frac{\pi e^4}{(\frac{1}{2}m_o v_o^2)} \int_{(ka_o)^2_{min}}^{(ka_o^2)_{max}} \frac{df(K, \Delta E)}{d(\Delta E)} \frac{d[\ln(ka_o)^2]}{\Delta E (ka_o)^2} \qquad 2.13$$

In this case $(ka_o)^2_{min}$ corresponds to $\theta = 0$ and $(ka_o)^2_{max}$ corresponds to that for $\theta = \beta$. Inokuti (1971) provides expressions for the calculation of these limits.

Numerical evaluation of Equation 2.13 has been performed using Hartree-Slater wavefunctions (e.g. Leapman et al 1980, Rez 1984); however, the generalised oscillator strengths for a wide range of elements are not very readily available. The semi-analytic hydrogenic model of Egerton (1979) and (1984) is probably the most widely used source of cross-sections for EEL quantitation.

Since the K-shells of most elements are tightly bound it has been shown (Egerton 1981, Rez et al 1984) that these shells can be accurately described by hydrogenic wavefunctions. Egerton (1979) has compared hydrogenic cross-sections with Auger, X-ray and energy loss measurements and found good agreement. Cross-sections calculated from a relativistic form of the SIGMAK program have been compared with those of

17

the Hartree-Slater model for various light elements. The agreement was generally better than 8% (Egerton 1984). The cross-sections calculated from the relativistic form of the SIGMAK program differ from the non-relativistic calculations by only about 5% for 100 keV incident electrons (Egerton 1984).

The shape of the energy differential cross-section for the L-shell is correctly predicted by the Hartree-Slater model (Rez et al 1984); however, the hydrogenic model requires the use of an empirical factor to match experimentally determined edge shapes. Egerton (1981) found good agreement between the Hartree-Slater cross-sections of Leapman et al (1980) and the hydrogenic SIGMAL cross-sections for P and Ca. These calculations assumed β = 10 mrad and the cross-sections integrated from edge onset over an energy range of 50 eV in the case of P and 70 eV in the case of Ca.

The intensity of electrons which have lost energy ΔE, $I_e(\Delta E)$ can be described as

$$I_e(\Delta E) = N_x I_i \, d\sigma/d(\Delta E)$$

2.14

where N_x is the number of atoms of type x per unit area and I_i is the current in the beam incident on the specimen. The above relationship is fundamental to the "single-stage" EEL signal processing and quantitation technique described in Chapter 6.

2.9   SOLID STATE EFFECTS IN EELS

As stated earlier, the calculations of inner shell cross-sections are based on atomic models and therefore neglect solid state effects. These effects arise from short or long range periodicity of the interatomic spacing and add a "fine structure" to the overall shape of the edge.   It is usual to divide this structure into two categories, energy loss near edge fine structure (ELNES) and extended energy loss fine structure (EXELFS).

ELNES consists of typically one or two well defined peaks which occur within the first 25 eV above an ionisation edge.   Kossel (1920) provided an early explanation as follows.   Excited electrons undergo quantum mechanically allowed transitions to discrete unoccupied states above the Fermi level.   Therefore, ELNES reflects the density of unfilled states near the absorbing atom.   In turn, the density of states is determined through the band structure by long range order in the solid.   However, the true situation appears to be more complicated and details of the theory are still under discussion (e.g. Colliex et al, 1984).   Dissimilar structures are usually observed in the edges corresponding to different elements within the same sample (Egerton, 1983) and there are indications that ELNES may be related to a "local density of states" (Friedel 1954, Colliex et al 1984).

EXELFS consists of a weak oscillatory modulation of the energy loss edge intensity and extends up to a few hundred eV beyond the ionisation edge.   It is analogous to EXAFS modulations present in X-ray absorption spectra (e.g. Stern, 1978) and is an interference effect caused by backscattering of the ejected electron, particularly from the nearest neighbour atoms.   It should be noted that the modulations are due to a limited redistribution of generalised oscillator strength and not by any

19

changes in the final density of states (Csillag, 1984).

In summary therefore, ELNES is not predicted by the atomic models used for quantitation since it results from transitions to bound states which are not included in the continuum cross-sections. EXELFS modulation being an interference effect, only results in a redistribution of the intensity in the ionisation edge.

Finally, it should be noted that the atomic potential and inner shell binding energy of a particular atom may be altered by the bonding of the valence electrons. This can give rise to a "chemical shift" of the energy at which the edge occurs and the effect can have a magnitude of up to ± 5 eV (Ferrier 1981). Chapters 6 and 7 discuss these effects in the context of EEL quantitation.

2.10   VALENCE ELECTRON EXCITATION AND PLURAL SCATTERING

Plural inelastic scattering by valence electrons involving low energy losses (~ 25 eV) is important since such scattering limits the general applicability of EELS. For light and medium atomic number elements the mean free path λ for valence shell excitations is typically between 500 and 1500 eV for 100 keV incident electrons (Egerton, 1983). Therefore, for specimens of thickness $t > \lambda$ plural scattering of the incident electrons is likely. The probability of an electron being scattered n times in passing through a specimen is given by the Poisson formula

$$P_n = \left(t/\lambda \right)^n / n! \, \exp\left(-t/\lambda \right)$$

2.15

For $t<<\lambda$, $P_o>>P_1>>P_2$ and the majority of the incident electrons lose no energy or undergo one scattering event. However, for specimens where $t \geq \lambda$ the probability of two or more scattering events becomes appreciable. As the specimen thickness increases the multiple scattering contributions to the background beneath an inner shell edge cause the background to increase faster than the edge signal. Therefore the signal/background ratio is reduced (Egerton 1981). Also, plural scattering tends to reduce the "visibility" of the edge onset since there is a significant probability of electrons being scattered from an inner shell and subsequently being scattered from a valence electron in separate events. Just above the edge threshold the intensity transferred out of the edge is greater than that transferred into the signal from the pre-edge background. Thus the edge onset is obscured.

In conclusion therefore, practical limitations are set on the maximimum thickness of a specimen suitable for EELS. Chapter 8 will discuss the problems found in preparing suitably thin samples of mineralised bone, and the thicknesses of the samples obtained by different preparation methods.

2.11   BREMSSTRAHLUNG

An electron incident on an atom can lose energy by interacting with the nuclear field. The energy lost by the electron results in the emission of an X-ray photon at an angle η to the incident beam direction. This interaction, which is known as bremsstrahlung radiation, gives rise to a continuous photon spectrum in the range 0eV to the incident electron energy. Bremsstrahlung production decreases monotonically

with increasing η for $60° < \eta < 180°$.

An accurate knowledge of bremsstrahlung cross-sections was important for the EDX spectral processing described in Chapters 4 and 5. Following Gray (1981) and Chapman et al (1983) a modified theory of Bethe and Heitler (e.g. Koch and Motz 1959) was chosen to best describe bremsstrahlung production. The former showed that for incident electron energies >40 keV, X-ray photon energies <30 keV and targets with atomic number <50 there was a very close agreement between a modified Bethe-Heitler (MBH) theory, the exact but incomplete numerical calculations by Pratt and co-workers (e.g. Pratt et al 1977) and experimental observations. More specifically, Chapman et al (1984) state that the accuracy of the MBH equation should be better than 5% for the ranges specified. In an earlier paper by Gray et al (1983) doubt was expressed over the validity of the MBH equation at low photon energies (<3 keV). Adam (1986) has performed a detailed comparison between the predictions of the MBH equation and the calculations by Pratt and co-workers for photon energies down to 0 keV. The agreement between the MBH and numerical calculations was found to be better than 2.5%.

A reduced cross-section for bremsstrahlung production σ_r can be defined as

$$\sigma_r = (T_0 E / Z^2) \, d^2\sigma_B / dE \, d\Lambda \qquad\qquad 2.16$$

where $d^2\sigma_B/dE \, d\Lambda$ is the cross-section for bremsstrahlung production (differential in both photon energy E and emergence solid angle Λ), T_0

is the incident electron kinetic energy and $\bar{z}$ is the atomic number of the element. σ_r is slowly varying with respect to E and therefore Crozier (1985) was able to parameterise σ_r for fixed T_0 and η as

$$\sigma_r(z, E) = A0_z + A1_z E + A2_z E^2$$

2.17

where the coefficents $A0_z$, $A1_z$ and $A2_z$ are found by fitting Equation 2.17 to the MBH equation. Typically the accuracy of this fit is better than 2% for $z > 4$ and $1 < E < 30$ keV (Chapman et al 1984). Values of the coefficients for $T_0 = 100$ keV and $\eta = 100.5°$ for a range of elements are given in Table 2.7. The advantage of this parameterisation is that it significantly reduces the time required to evaluate what would otherwise be a cumbersome expression.

Element	A0	A1	A2
C	0.2162E3	-0.6623E1	0.9340E-1
O	0.2110E3	-0.5952E1	0.7503E-1
Al	0.2022E3	-0.4919E1	0.5006E-1
P	0.1997E3	-0.4630E1	0.4345E-1
Ca	0.1945E3	-0.4069E1	0.3118E-1
Co	0.1890E3	-0.3517E1	0.1984E-1

Table 2.7

CHAPTER 3

INSTRUMENTAL CONSIDERATIONS

3.1   INTRODUCTION

All of the work reported has been performed using an extended VG HB5 scanning transmission electron microscope (STEM) with its associated spectroscopic detectors.   This chapter describes the microscope, its detectors, and the standard operating conditions used to acquire spectra.

3.2   THE MICROSCOPE

Figures 3.1(a) and (b) show a schematic diagram of the VG HB5 STEM. It contains the same basic components as the first STEM described by Crewe, (1971); a field emission gun, probe forming lenses (condenser and objective), scanning coils, an electron spectrometer, and various detectors.   The major modifications (Craven and Buggy 1981b) consist of the addition of a second condenser lens, a "Z - lift stage" and post-specimen lenses.

The basic principle of a STEM is the following.   The demagnified image of a high intensity electron source (the probe) is formed on the specimen and is then scanned across the specimen in a raster pattern. The electrons transmitted through the specimen are detected and used to modulate synchronously scanned display screens.   Alternatively the probe can be held fixed and the various signals resulting from the probe/specimen interaction detected and used for microanalytic studies of chemical composition and structure.

In a STEM an important factor which determines the spatial resolution for quantitation is the probe size.   The smaller the probe,
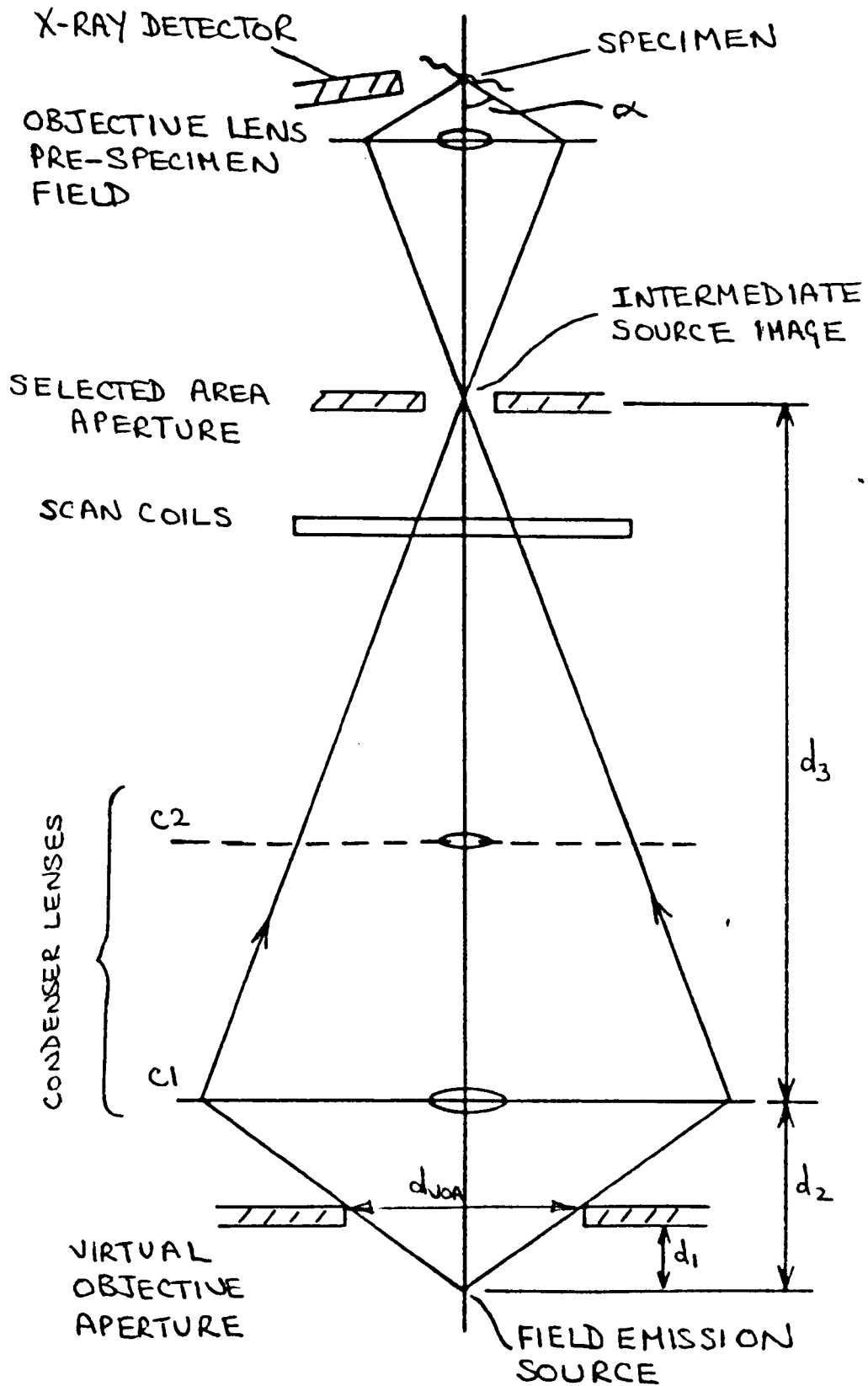
Figure 3.1(a)   Probe forming electron-optics of the VG HB5 STEM.

d_1=96mm d_2=172mm d_3=250mm
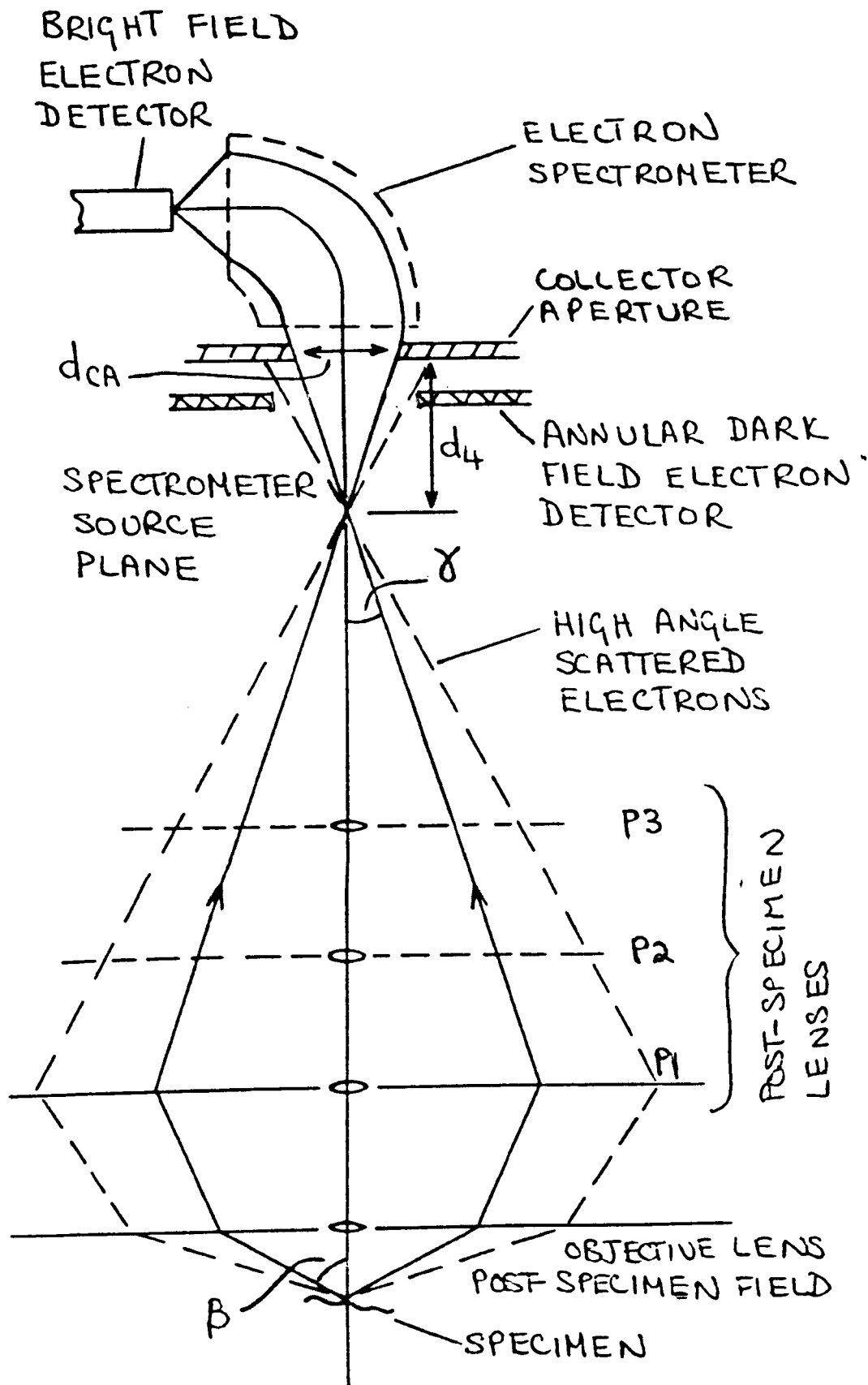
Figure 3.1(b) Post-specimen electron optics of the VG HB5 STEM.

the higher the spatial resolution. When a small probe is used a high brightness source is required and the field emission gun is ideal. Using such a source it is possible to obtain a probe of diameter ~1 nm with a current of ~1 nA. However, resolution on this scale was not required for this particular study. Probe convergence angles sizes and currents that were used will be discussed in Section 3.4.

In the HB5 the specimen is situated between the upper and lower objective lens pole pieces (see Figure 3.2). The probe forming electron optics consists of condenser lens Cl and the objective lens pre-specimen field (see Figure 3.1(a)). Collection of the electrons after passing through the specimen is performed by the objective lens post-specimen field and post-specimen lenses (see Figure 3.1(b)).

Various detectors are available for image formation and microanalysis on the HB5. An electron spectrometer coupled to an electron detector can be used for either bright field imaging or EELS. An annular electron detector collects the high angle scattered electrons for dark field imaging. The major component of the work to be described involved the use of an EDX detector which will be discussed in detail later in this chapter.

3.3   BASIC MICROSCOPE OPERATING CONDITIONS

The standard operating conditions for microanalysis were chosen to provide a satisfactory compromise between several conflicting requirements. Firstly the probe should be of an acceptable convergence angle and size whilst still providing the maximum detectable signal from the specimen. Secondly, artefacts due to stray scattering and lens aberrations should be minimised. To provide a basis for

25

UPPER POLE—
PIECE OF
OBJECTIVE
LENS

CARTRIDGE

100.5°

FIELD OF VIEW
OF EDX DETECTOR

SPECIMEN

Ta COLLIMATOR
OF EDX DETECTOR

LOWER POLE PIECE
OF OBJECTIVE LENS

ELECTRON BEAM
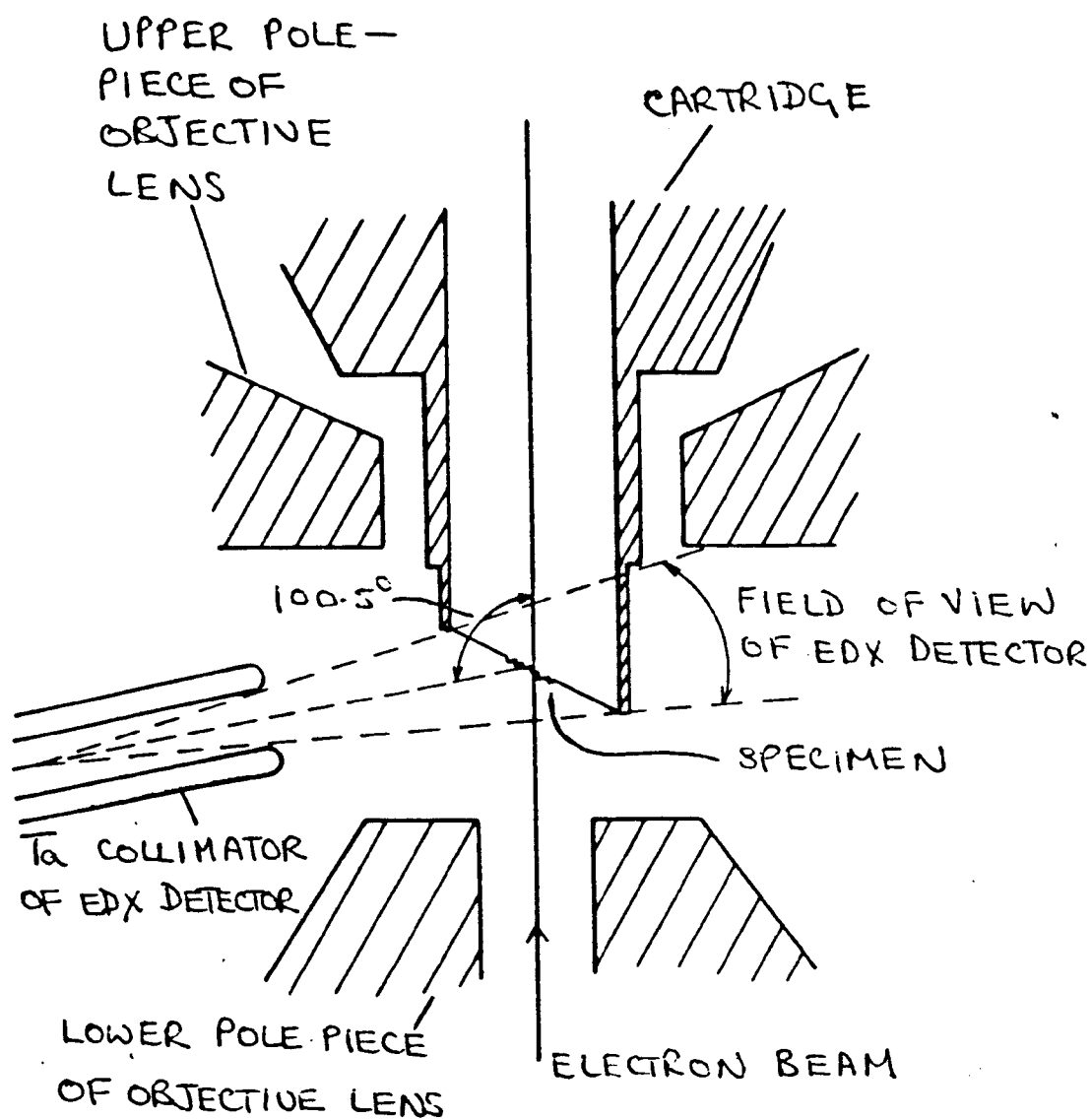
Figure 3.2   Relative locations of specimen, X-ray detector, and objective
lens in the HB5 STEM.

meeting these requirements and to allow known operating conditions to be reproduced, the following procedure was adopted. The excitation of the objective lens was kept constant at a pre-set value (Craven and Buggy 1981b) and, as Figure 3.1(a) shows, the intermediate electron source image was focused on the selected area aperture (SAA) plane. A constant specimen height was desirable since the position of the image plane varies with specimen height. The use of the "Z - lift stage" (Craven and Buggy 1981b) to maintain constant specimen height was considered preferable to altering the excitation of the post-specimen lenses to maintain a known angular compression for the electrons transmitted through the specimen. This stage was particularly useful when different regions of a specimen tilted for X-ray acquisition were examined.

3.4   PROBE CHARACTERISTICS AND THE MINIMISATION OF STRAY SCATTERING

In the work to be described, the probe convergence angle is important since it defines the probe size, and therefore the resolution attainable for microanalysis. In addition it must be taken into account when EELS quantitation is being performed (Craven et al 1981a, Crozier1985). For microanalysis the probe convergence semi-angle α (see Figure 3.1(a)) is defined by the virtual objective aperture (VOA) and the pre-specimen lens excitations. The objective aperture (OA), which is located just below the specimen is not used to define α since a large amount of stray scattering generated by this aperture is detected (Waddell 1982).

The presence of a stray scattering contribution in recorded spectra complicates the spectral processing procedure. The minimisation of the

stray scattering is therefore important. As has already been described, the VOA is used to define the probe convergence angle. Some stray scattering still occurs from the edge of this aperture; however, it can be considerably reduced by inserting the selected area aperture (SAA) into the plane of the intermediate electron source image (see Figure 3.1(a)). This aperture, being larger in diameter than the intermediate electron source image, does not define the probe angle but does result in virtually no instrumental signal being detected; i.e. the SAA acts as a spray aperture.

When the electron probe strikes the specimen, electrons are scattered through a wide variety of angles and some of these electrons can restrike the specimen at a different point , the specimen support (grid), or the cartridge within which the specimen sits. Nicholson (1974) has shown that single-hole mounts rather than fine mesh grids reduce the spurious contribution to X-ray spectra from the material surrounding the specimen. In addition a special cartridge has been designed and built (Craven et al, 1984) which has minimal bulk material in the field of view of the X-ray collimator and the general specimen region. Both single hole mounts and the special cartridge were used when all of the EDX spectra were recorded. In EELS the requirements for the minimisation of a stray scattering contribution to the spectra are somewhat different. A discussion of this will be therefore left to Section 3.6.

Two VOA's were used in the work to be described. The choice of VOA selected for a particular experiment was determined by the criterion stated at the beginning of Section 3.3. From consideration of Figure

27

3.1(a) α can be described as

$$\alpha = \frac{d_{VOA}/2}{d_1 \times (d_3/d_2) \times M_{OI}}$$

where d_{VOA} is the diameter of the VOA of interest, d_1, d_2 and d_3 are the dimensions indicated and M_{OI} is the objective lens pre-specimen demagnification. Assuming M_{OI} =1/30, Table 3.1 shows the approximate values of α for the VOA's of interest. Crozier (1985) calculated the convergence angle for a number of VOA's using a convergent beam electron diffraction pattern from a single crystal. The value of α obtained for the 250μm VOA was 25.5$\pm$0.5 mrad.

Spherical aberration in the objective lens is the most important effect which defines the probe diameter. This can be described as

$$d_s = \frac{1}{2} C_s \alpha^3$$

where C_s is the spherical aberration coefficient for the objective lens pre-specimen field and d_s is the resulting probe diameter. Assuming C_s = 3.5 mm, approximate values of d_s can be calculated (see Table 3.1). The use of a probe of diameter 0.26μm offers low spatial resolution compared to that used in most other studies on the HB5. Justification for the choice of this probe size (and the HB5) for the study of the distribution of trace light element concentrations in mineralised bone will be given in Chapter 5.

Probe currents were measured experimentally by inserting the OA blade into the path of the beam. The currents obtained are summarised in Table 3.1.

VOA/μm	B/mrad	probe size	probe current
500	53.0	0.26μm	2·8nA
250	26.9	340Å	0.6nA

Table 3.1

3.5 POST-SPECIMEN ELECTRON OPTICS AND DETECTORS

The post-specimen lenses (PSL's) are used to match the angular scattering distribution of the electrons transmitted through the specimen to the bright field and annular dark field detectors (Craven and Buggy 1981(b)).

The bright field detector (BF), which can be used for either imaging or EELS, consists of an electron spectrometer and an electron detector (see Figure 3.1(b)). The electron spectrometer disperses the electrons with respect to momentum and focuses them onto a slit of variable width in front of the electron detector. For general imaging purposes the slit is opened as wide as possible. The electron detector consists of a scintillator coupled via a light pipe to a photomultiplier tube, the electrical output of which is used to modulate the BF display screen. Electrons scattered through low angles (generally <27 mrad) are used to provide this signal.

The annular dark field electron detector (ADF), see Figure 3.1(b), can collect those electrons scattered through much higher angles (up to several hundred mrad) excluding those travelling close to the optic axis. The electrical output of the ADF detector is used to modulate the dark field display screen.

3.6 EEL SPECTROSCOPY

Deflection coils in the electron spectrometer allow the EEL spectrum to be scanned across the slit in front of the electron detector. The spectrum, which can be scanned over a maximum energy range of $\sim$2 keV is thus recorded serially. When setting up the microscope for EELS the slit width is adjusted to provide a maximum

energy resolution (of ~1 eV) without loss of signal.

A stray signal can be introduced into the EEL spectrum which arises from two sources (Craven and Buggy, 1984); either stray electrons and X-rays passing through the slit opening or hard X-rays generated by electrons hitting the slit material, being transmitted through this material. In the former case the stray signal is proportional to the slit width and in the latter case it is independent of the slit width. Fortunately, subtraction of this stray scattering contribution to recorded spectra is only required for the extraction of characteristic signals occurring at high energy losses (Craven and Buggy, 1984).`

The electron spectrometer normally has a fixed focus and therefore the source for the spectrometer is required to be in a fixed plane. The PSL´s are used to provide a variation in the maximum angle of collection whilst maintaining a fixed source point. Chromatic aberration results in a defocus of EEL spectra at high energy losses. Craven and Buggy (1981)(b) have calculated PSL excitations, which for a given objective lens excitation and specimen height, minimise chromatic aberration effects.

In EELS a knowledge of the electron collection semi-angle β , see Figure 3.1(b), is fundamental to quantitation. β is defined by the diameter of the collector aperture (CA) and the excitation of the PSL(s). The 500μm CA used in conjunction with PSL P1 alone was used for all the EEL spectra acquistion to be described. From consideration of Figure 3.1(b) β can be described as

$$\beta = M_{ps} \tan^{-1} \left(\frac{d_{CA}/2}{d_4} \right)$$

where d_{CA} is the diameter of the collector aperture, d_4 is the dimension indicated and M_{PS} is the angular compression of the post specimen optics (M_{PS} is defined as the ratio of β to γ (see Figure 3.1(b))). Assuming that the spectrum is focused, d_4 and M_{PS} are ~ 157 mm and ~ 17 respectively (A J Craven, personal communication). A value of approximately 27 mrad is therefore obtained for β if the 500 μm CA is used for acquisition. Crozier (1985) has measured β for a number of CA and PSL combinations using a selected area diffraction pattern from a single crystal of Au. A collection semi-angle of ~ 26 mrad for the aforementioned combination was obtained by this method.

3.7(i)   X-RAY SPECTROSCOPY

X-rays generated by the electron beam/specimen interaction are recorded with a Link Systems Limited EDX detector. The collimator of the detector, which is situated between the upper and lower objective lens pole pieces (see Figure 3.2), accepts X-rays travelling within a cone of solid angle 0.04 sr about a direction 100.5° to the beam direction. At this angle of detection the bremsstrahlung shape changes only slowly with atomic number (e.g. Chapman et al 1983). This is particularly important in the microanalysis of biological material e.g. mineralising bone, where the precise chemical composition is not known.

The X-ray detector (see Figure 3.3) is a lithium-drifted silicon (Si (Li)) crystal of area ~ 30 mm^2, nominal depth 3 mm and situated in its own vacuum chamber and mounted on the end of a metal cold finger so that it can be cooled to reduce electronic noise. The detector has a nominal energy resolution of 159 eV at 5.9 keV.

A thin window of Be (nominal thickness 8 μm) isolates the detector

ACTIVE REGION
OF Si (Li) CRYSTAL

Au CONTACT
LAYER

Ta COLLIMATOR

TO FET
AND H.T.

Be-WINDOW

HT
NEGATIVE

METAL COLLIMATOR
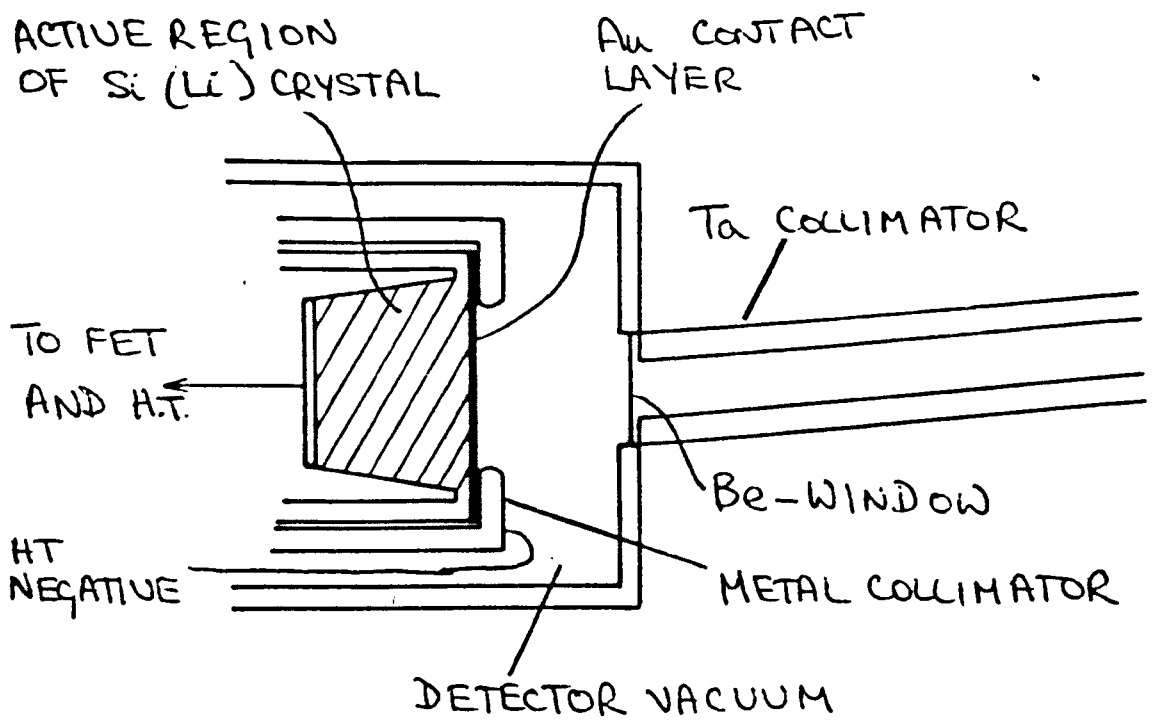
DETECTOR VACUUM

Figure 3.3 Si(Li) detector crystal and X-ray collimation.

vacuum from the microscope. A high voltage bias can be applied across the detector crystal by means of a thin evaporated layer of Au (nominal thickness $\sim 0.01 \mu$m) on the front surface of the crystal. An X-ray emitted by the specimen, and travelling in a direction to enter the collimator will pass through the Be-window, through the Au layer, and be absorbed in the active region of the detector crystal.

Most of the X-rays that enter the crystal ionise a Si atom which in turn emits a photoelectron. The photoelectron de-excites by producing electron-hole pairs within the crystal, the total number of electron-hole pairs produced being proportional to the energy of the photo-electron. The Si ion may emit a photon through de-excitation which will result in more electron-hole pair production. Most of the electron-hole pairs thus created do not recombine because of the electric field applied across the crystal. Instead they give rise to a pulse of current on the electrical contacts of the crystal, the magnitude of the pulse being proportional to the energy of the original incident X-ray. This pulse is detected and processed by the detector nucleonics. Artefacts introduced into the detection system will be discussed in Chapter 5.

3.7(ii) X-RAY NUCLEONICS

The charge liberated by a photon is detected by a specially designed field-effect transistor which forms the first stage of a charge sensitive pre-amplifier. The electrical output of the pre-amplifier is fed to a 2010 pulse processor via an input amplifier. This pulse processor, which was first developed by Kandiah (1966) and is now supplied by Link Systems Limited, essentially converts the input signals

into individual pulses. It includes a pulse pile-up rejector, live time corrector and it discriminates against electronic noise. The processors integration time constant was set to 20 μs to give adequate resolution. The output pulses from the pulse processor are digitised by an analogue to digital converter linked to a computer. The computer acts as a multichannel analyser during acquisition and displays the spectrum as it is being recorded. Once acquisition is finished the spectrum is stored on floppy disk for future processing. The reader is referred to Statham (1981) for a detailed review of X-ray spectroscopy using Si(Li) detectors.

3.8   EDX AND EEL ACQUISTION SYSTEMS AND SOFTWARE

In the work to be described the X-ray spectra were acquired using Link Systems Limited 290 and 860 series computers and software. The EEL spectra were acquired with a system developed by Toltec Computer Limited with hardware interfaces being developed and built in the Department of Natural Philosophy (Craven et al, 1980). Once acquired, spectra are stored on disk for future processing.

Gray (1981) gives a detailed summary of the 290 Link acquisition software which has virtually identical facilities to the 860 system. Crozier (1985) gives a summary of the EEL acquisition software. Artefacts due to the effect of deadtime, dark current, and non-linearity in the electron detector output etc are introduced into the EEL spectra during acquisition (Craven and Buggy 1984). These artefacts were removed from all spectra using the programs written by A J Craven. Programs written by myself for EDX and EEL quantitation will be described in later chapters.

CHAPTER 4

SOME FACTORS AFFECTING EDX MICROANALYSIS

4.1 INTRODUCTION

This chapter describes an investigation into the efficiency of the Si(Li) EDX detector attached to the HB5 STEM and discusses a number of artefacts introduced into X-ray spectra by the detector. Also, the cross-section data obtained by Gray (1981) is investigated to determine whether closer agreement between experimental and predicted cross-sections could be obtained through use of different forms of the Bethe equation. These different forms have been discussed in Section 2.5.

A description of characteristic X-ray and bremsstrahlung production is fundamental to both the investigations described in this chapter. The number of characteristic $K\alpha$ X-rays of element x detected at the characteristic photon energy E_x is related to the K-shell ionisation cross-section σ_{Kx} by

$$P_x = \frac{ti}{e} \, \epsilon(E_x) \, N_x \, \frac{\sigma_{Kx} \, \omega_x \, s_x}{q} \, \frac{d\Omega}{4\pi} \qquad 4.1$$

where t = spectrum acquisition time

  i = incident beam current

  e = charge on electron

  $\epsilon(E_x)$ = detector efficiency at photon energy E_x

  N_x = number of atoms of element x

  ω_x = fluorescence yield

  s_x = partition function

q = area irradiated by the beam

$d\Omega$ = solid angle subtended by the X-ray detector

Similarly, the number of bremsstrahlung X-rays from a sample of element x detected in an energy window dE, centred at E is related to the cross-section for bremsstrahlung production σ_B by

$$B_x(E) = \frac{t\,i}{e}\, \epsilon(E)\, N_x\, \frac{d^2\sigma_B}{dE\,d\Omega}\, \frac{dE\,d\Omega}{q} \qquad\qquad 4\text{-}2$$

4.2 EVALUATION OF THE EDX DETECTOR EFFICIENCY

The efficiency of a Si(Li) detector is frequently determined by use of a radioactive source. This involves comparing accurately known peak intensities with those measured by the Si(Li) detector. Gray (1981) provides a detailed summary of those methods. Alternatively the shape of the bremsstrahlung can be modelled theoretically taking into account detector and specimen absorption (e.g. Gray, 1981). The latter approach facilitates the extraction of characteristic peak intensities which are used in the quantitation of elemental concentrations. This is the approach which will be considered in the following sections. The X-ray spectra that are discussed here were all acquired using the detector attached to the HB5.

4.2.1 The Mid-energy Region

In the mid-energy range (4-14 keV) the efficiency $\epsilon(E)$ of the Si(Li) X-ray detector is essentially unity and the bremsstrahlung shape should be that predicted by the modified Bethe-Heitler equation. From

Equations 2.17 and 4.2, the number of bremsstrahlung counts in an experimental spectrum $B_x(E)$ can be described as

$$B_x(E) = k \sum f_x z_x^2 \left(\frac{AO_x}{E} + A1_x + A2_x E \right) \qquad 4.3$$

where f_x is the atomic fraction of element x and k is a constant depending on the acquisition conditions. The above equation assumes an idealised situation of X-ray production in a thin foil. In practice there are other spurious contributions to an X-ray spectrum due to stray scattering of electrons and X-rays. The presence of peaks characteristic of the local specimen environment may indicate such a contribution. However, the absence of such peaks does not indicate the absence of any stray contribution. If C or O is present then no characteristic peak would be observed using the EDX detector on the HB5. A further source of stray counts can be electrons scattered directly into the X-ray detector (Nicholson et al 1984). Precautions taken to minimise a stray scattering contribution have been described in Section 3.4.

4.2.2(a)   <u>Low Energy Detector Efficiency</u>

X-ray absorption and count redistribution affect the shape of spectra in the low energy ($<$3 keV) region. Therefore, the information on the detector efficiency was obtained from the examination of the simplest possible spectra. The spectra chosen had no major characteristic peaks in the low energy region. To this end, samples of formvar and evaporated cobalt on formvar were used. These samples were

prepared sufficiently thin that X-ray self-absorption effects were minimised. The formvar thickness is believed to be about 500Å (Elder, personal communication). The cobalt film thickness was measured on a Varian Limited Å-scope interferometer and found to be 350 ±100 Å.

The effect of specimen self-absorption is to attenuate the X-ray intensity generated within the specimen. The relation between the attenuated X-ray intensity $I_x(E)$ and the total intensity generated $B_x(E)$ in a specimen of thickness t can be described as (e.g. Goldstein et al,1977)

$$I_x(E) = B_x(E) \frac{1 - \exp\left(-\frac{\mu}{\rho}(E)\rho t \csc \alpha\right)}{\frac{\mu}{\rho}(E)\rho t \csc \alpha} \qquad 4.4$$

where α is the angle between the emergent X-ray and the specimen surface, $\frac{\mu}{\rho}(E)$ is the mass absorption coefficient, and ρ is the density of the material. Normally the specimen was tilted at about 20° to the incident beam direction; therefore, α is about 30° (see Adam, 1986). The mass absorption coefficient can be written as

$$\frac{\mu}{\rho}(E) = \sum_i c_i k_i E^{n_i} \qquad 4.5$$

where C_i is the mass fraction of element i. Thinh et al (1979) define values of k_i and n_i for given energy ranges. Other tabulations of mass absorption coefficient have been made by Springer et al (1976) and Henke et al (1974). The discrepancy between the mass absorption coefficients

37

suggested by those authors can be significant and will be discussed in Section 4.2.3. Figure 4.1 shows the ratio I_x/B_x calculated at the characteristic X-ray energies of Na and Al, plotted against specimen thickness for both formvar and cobalt. For a formvar specimen of thickness 1000Å, fewer than 4% of the X-rays generated are absorbed at the characteristic energy of Na. Since the self-absorption correction for formvar spectra is almost negligible, these will be discussed first.

4.2.2(b) Spectral Processing

Figure 4.2 shows a spectrum recorded from the formvar sample. The Cu peak is due to the presence of a stray scattering contribution from the Cu single hole mount. The usual method of correcting the thin foil spectrum for this contribution consists of scaling the characteristic peak of a spectrum previously recorded from the bulk Cu to the peak in the formvar spectrum. Subtraction of the bulk spectrum should then ensure that to a reasonable approximation, the remaining spectrum has no stray scattering contribution (Nicholson et al 1980).

Factors complicate the above procedure because the bulk contribution to the thin foil spectrum is generated by electrons, many of which will have lost energy in collision processes, striking solid surfaces at a wide variety of angles. In contrast to this, the previously recorded bulk spectra are each obtained using monoenergetic electrons incident on a surface at a well defined angle. Thus the intensity and shape of the scaled bulk bremsstrahlung will only be to a first approximation the same as the stray scattering contribution to a thin foil spectrum. In an effort to minimise the discrepancy a number of Cu spectra were acquired from different regions of the single hole

38
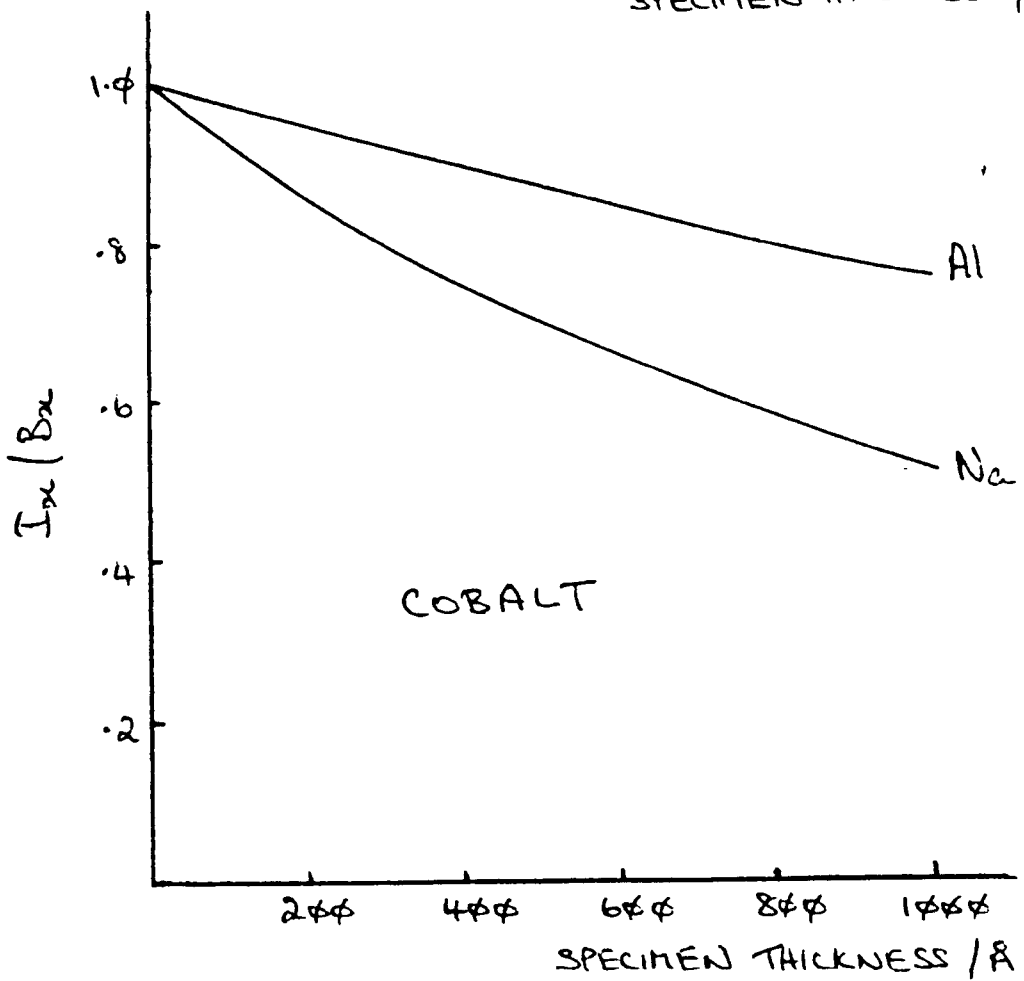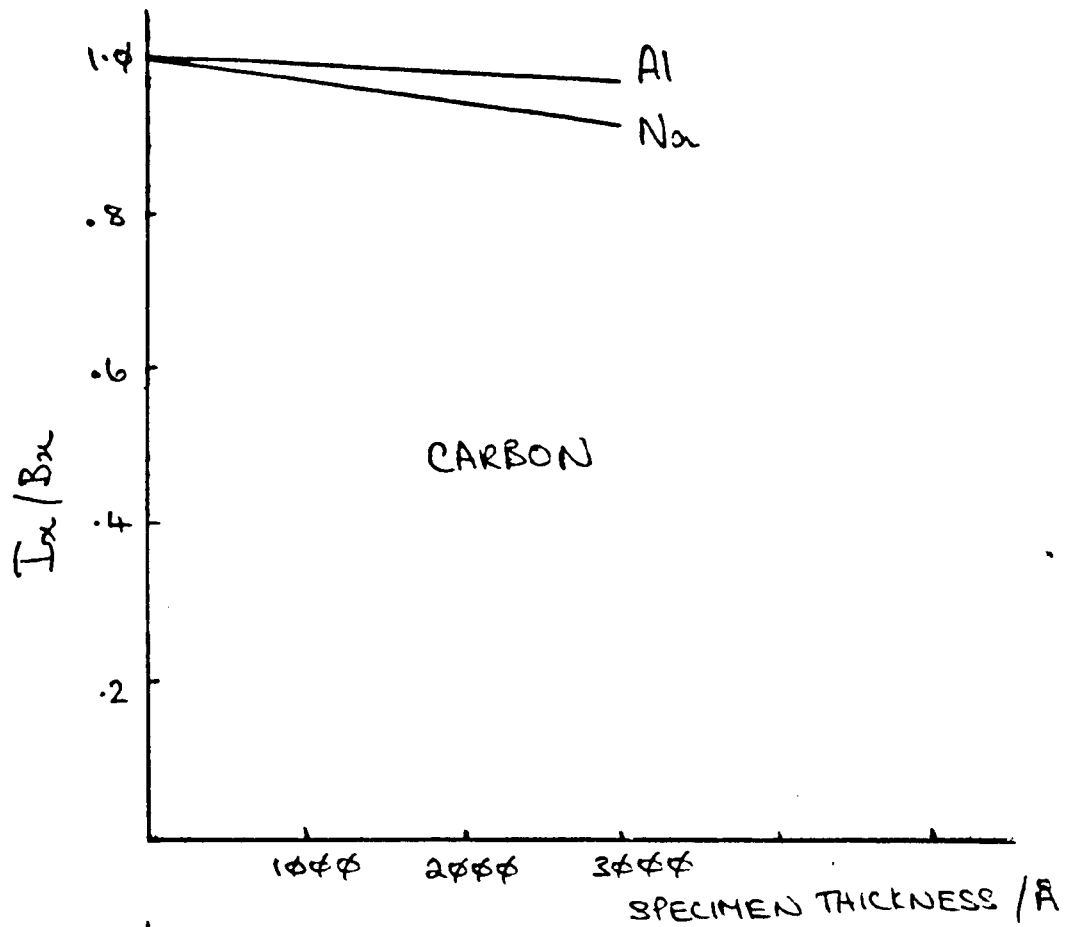
Figure 4.1

mount and summed together. Figure 4.2 shows this spectrum scaled as described and Figure 4.3 shows the formvar spectrum after subtraction. A scaled theoretical bremsstrahlung shape predicted by the MBH equation is also shown in Figure 4.3. This curve has been calculated using Equation 4.3. The scaling region used is as indicated in Figure 4.3. This region was chosen since it is close to the low energy region and $\epsilon(E)$ is approximately unity.

Below 3 keV the MBH curve deviates markedly from the recorded spectrum, see Figure 4.4. Absorption in the Be-window and Au contact layer (see Section 3.7) is assumed to be the main cause of this discrepancy. In addition, a so called Si dead layer may exist between the Au layer and the active crystal volume. This would provide a third region within which X-rays could be absorbed. Thus, the low energy efficiency $\epsilon_L(E)$ of the X-ray detector can be described as (Zaluzec 1979)

$$\frac{I_c(E)}{B_x^I(E)} = \epsilon_L(E) = \exp\left(-\sum_j \frac{\mu}{\rho}(E)_j \, \rho_j \, t_j\right) \qquad 4.6$$

where $I_c(E)$ is the number of counts in the spectrum, $B_x^1(E)$ is the number of counts predicted by the scaled MBH equation (corrected as necessary for specimen self-absorption) and j represents the Be, Au and Si absorbing layers.

Following the approach taken by Gray (1981) t_{Au} was kept constant at 0.01μm and t_{Be} regarded as a variable to be optimised. Absorption in the Au layer has the least effect on detector efficiency and any error in the choice of t_{Au} is compensated for by the optimised t_{Be} value. Gray (1981) found that $t_{si}=0$ provided the best fit for a
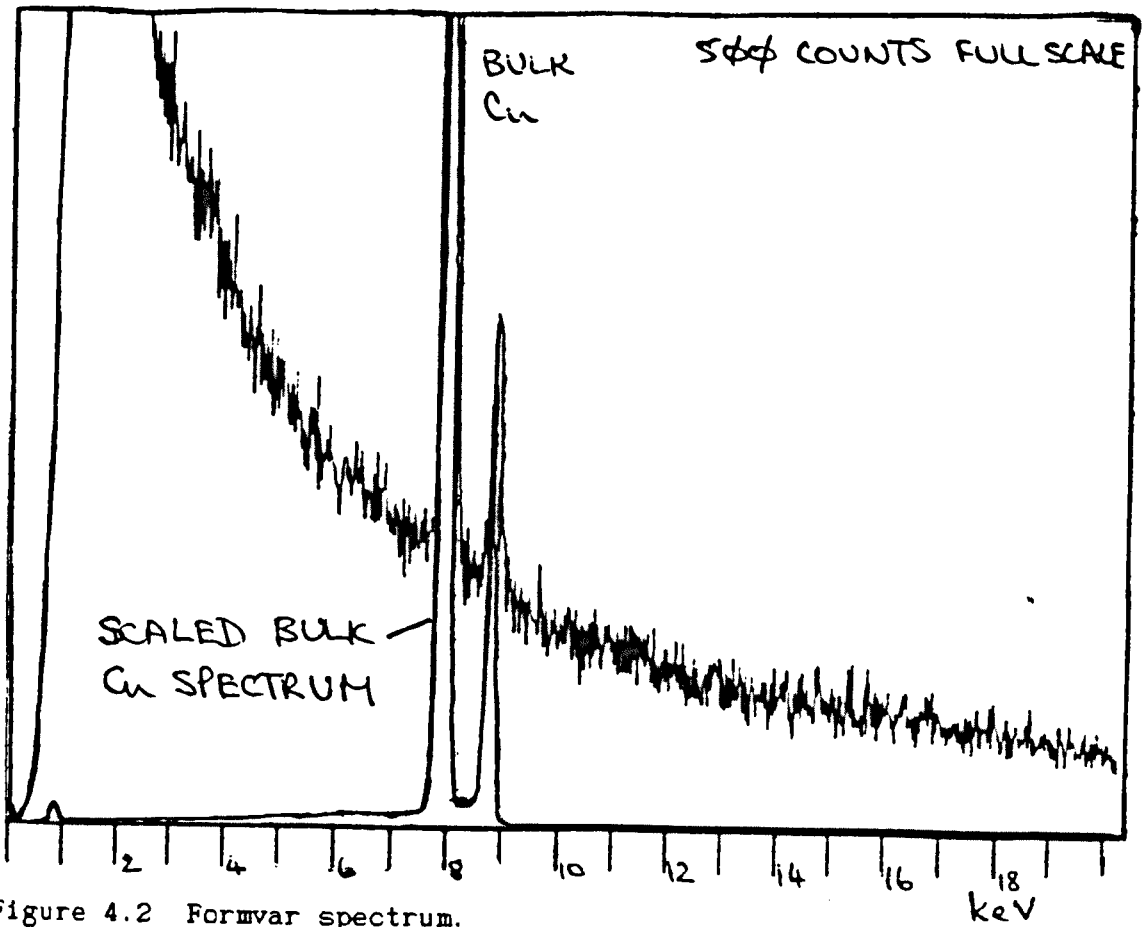
Figure 4.2   Formvar spectrum.
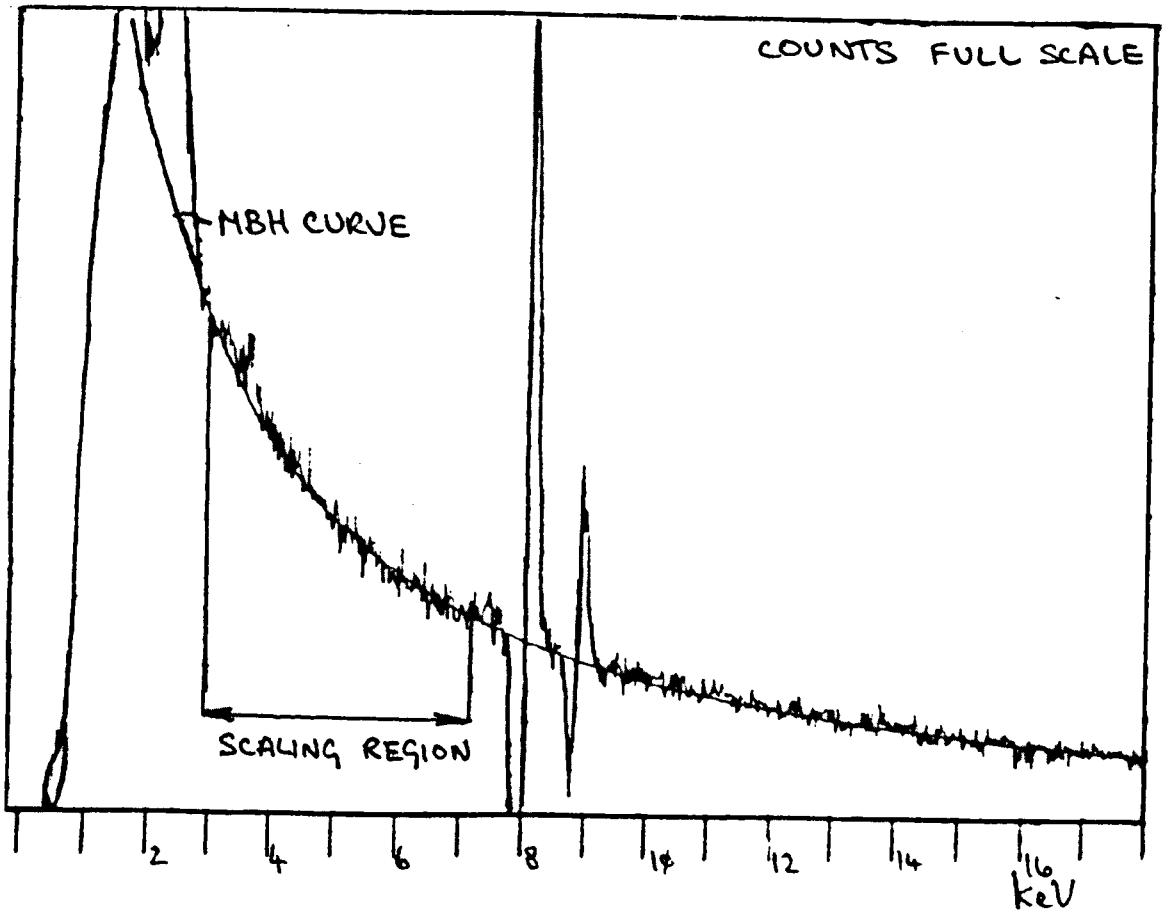
Figure 4.3   Formvar spectrum with bulk Cu contribution
subtracted.
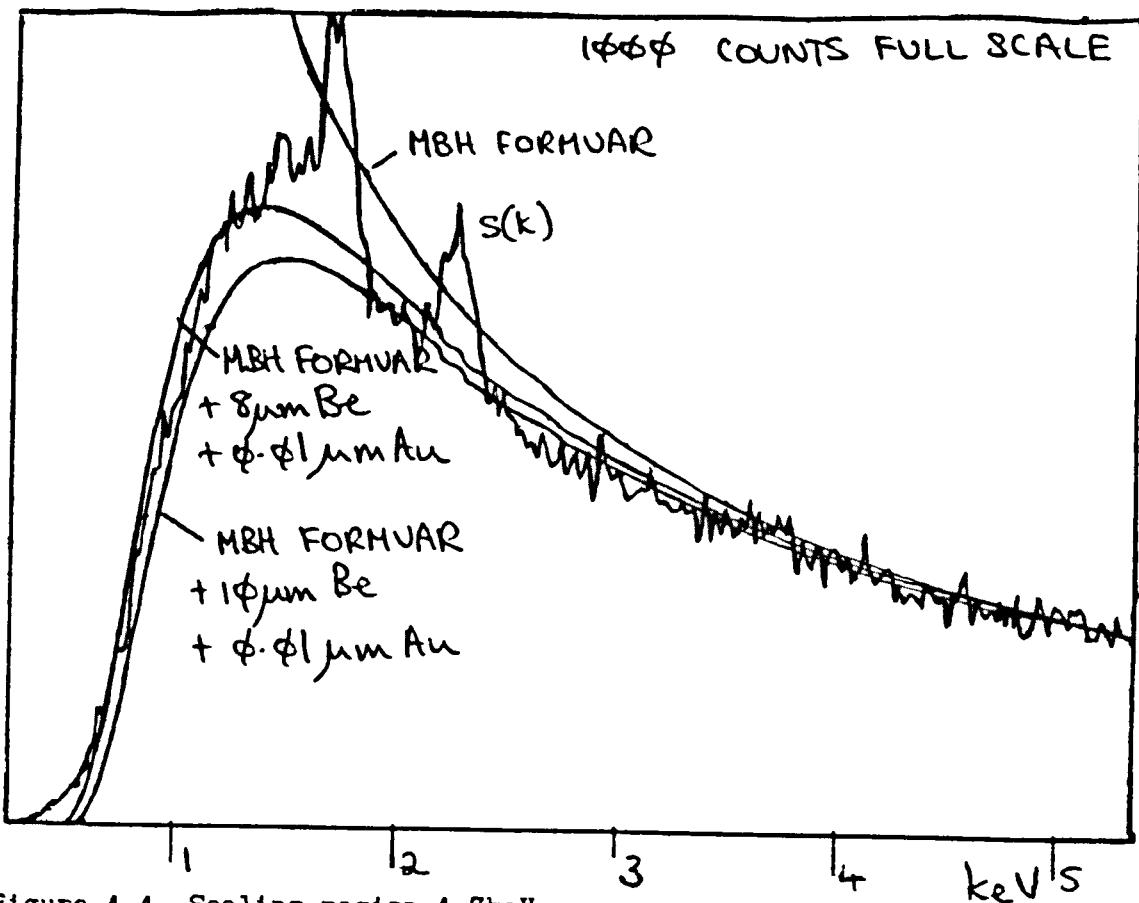
Figure 4.4   Scaling region 4-7keV.
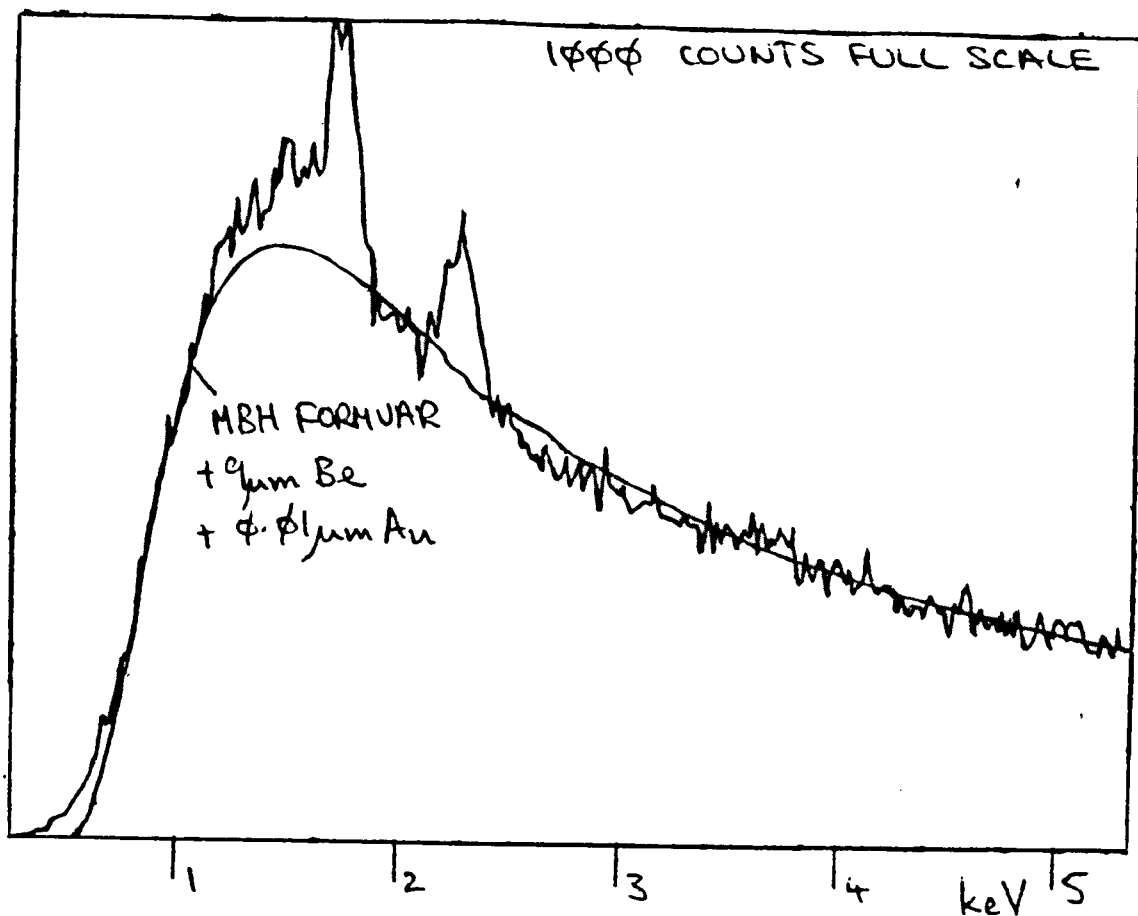
Figure 4.5   Optimum fit.

similar detector when t_{Be} was varied. Craven et al (1984) suggest that it is unlikely that the Si-dead layer is totally insensitive, rather it is a region within which the charge collection efficiency is low. Inefficient charge collection is discussed in Section 4.2.5. $t_{Si}=0$ was chosen, and therefore t_{Be} was the only parameter in Equation 4.6 which was allowed to vary.

Figures 4.4 and 4.5 show the curves calculated for several Be window thicknesses (assuming $t_{Au}=0.01 \mu m$), and it can be seen that $t_{Be}=9.0 \mu m$ gives an optimum fit. The energy region around the Si absorption edge (at ~ 1.84 keV) in the spectrum is not described adequately by Equation 4.6 and therefore this region had to be excluded when determining the optimum value of t_{Be}. (The region is discussed in Section 4.2.5). A chi-square test could have been used to determine the value of t_{Be}; however, the presence of a limited number of channels in the low energy region made this test seem unrealistic. A simple visual check on the goodness of fit was therefore adopted instead. As a test of reproducibility other formvar spectra were examined. A very small spread in optimum t_{Be} values was obtained, and therefore the Be window thickness was estimated as $t_{Be}=9.0 \pm 1.0 \mu m$. Another formvar spectrum is shown in Figure 4.6. Figure 4.7 shows a spectrum acquired from the Co specimen. Curve A, which has been calculated without taking into account specimen self-absorption, does not fit the low energy region. The other two curves (B and C) have been calculated assuming t cosec α = 500 Å and 700 Å. Assuming α = 30°, this corresponds to specimen thicknesses of 333Å and 466Å respectively. As stated earlier, the specimen thickness was measured as 350 $\pm$ 100Å. Thus, when allowance is made for specimen self-absorption, a Be window
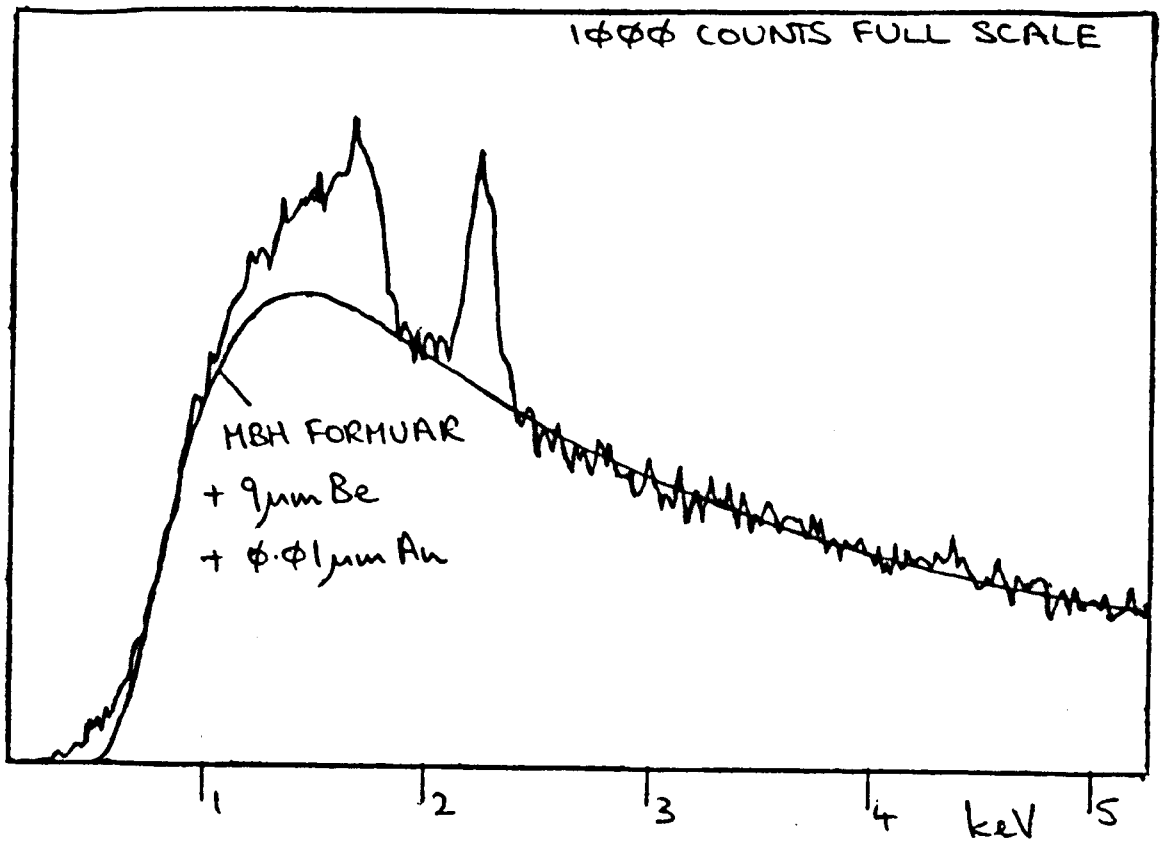
Figure 4.6
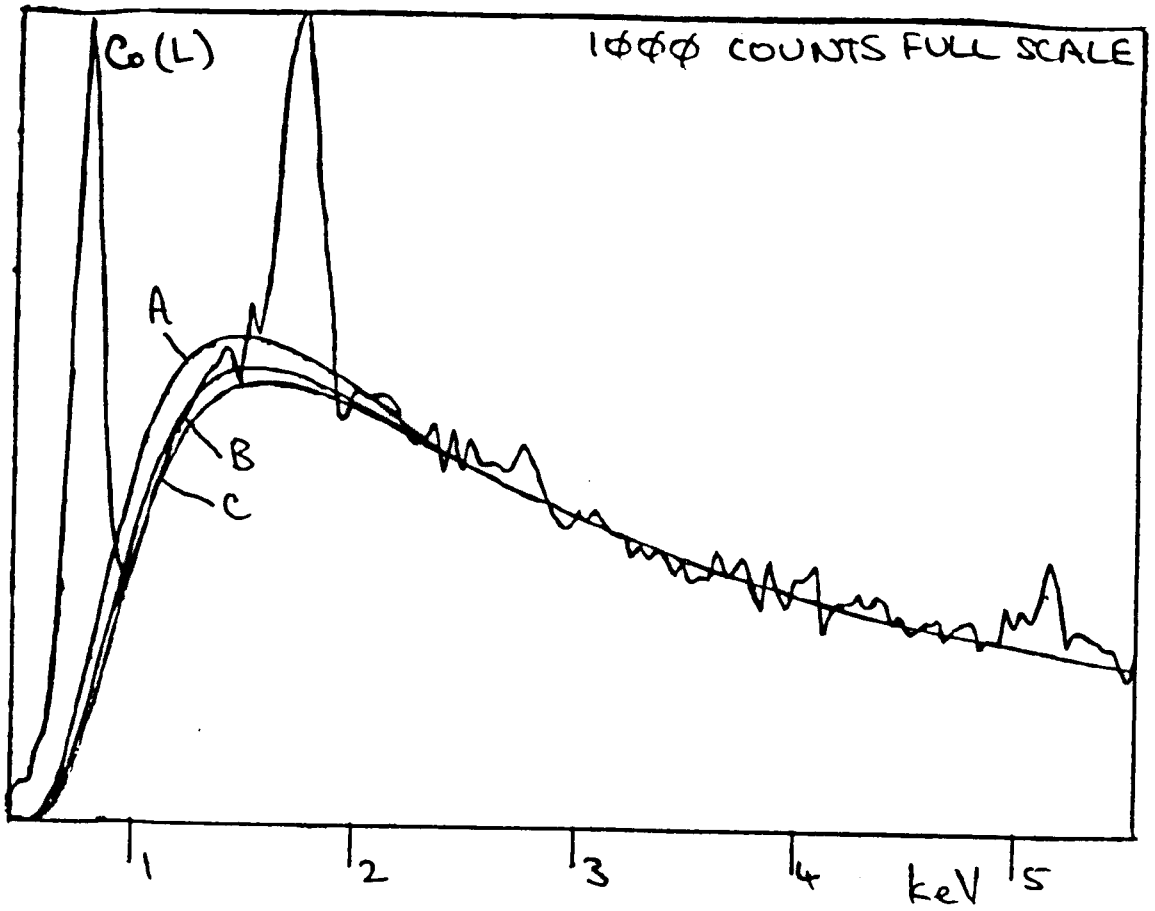
Figure 4.7   Cobalt spectrum.

Curve A:- MBH Co + 9μm Be + 0.01μm Au
Curve B:- MBH Co + 9μm Be + 0.01μm Au + 335Å Co
Curve C:- MBH Co + 9μm Be + 0.01μm Au + 470Å Co

thickness of 9.0 μm is again indicated. Recently, J Paterson has acquired spectra from Ag, Sn and Mo thin foils (self-absorption corrections negligible) and, as expected, t_{Be} = 9 μm provided the optimum fit. Figure 4.8 shows the low energy efficiency of the HB5 EDX detector as a function of X-ray energy.

4.2.3 Uncertainty in the Mass Absorption Coefficients

Table 4.1 summarises mass-absorption coefficients for Be within the energy range which is of interest when determining the detector efficiency. Three sets of coefficients have been taken from Springer et al (1976), Thinh et al (1979) and Henke et al (1974). Clearly there is a discrepancy between the values of mass absorption coefficients for different energies. This is especially significant since the coefficient appears in an exponential term within Equation 4.6

Section 4.2.2 showed that a Be window thickness of 9.0 μm reproducibly fitted experimental spectra when the mass absorption coefficients of Thinh et al (1979) were used. If the absorption coefficients of Springer et al (1976) or Henke et al (1974) had been used instead slightly different optimum values of t_{Be} would have been derived. An estimate of those different t_{Be} values can be obtained from

$$t_{Be}^{j} = \frac{\mu/\rho(E)_{Be}^{T} \times 9.0}{\mu/\rho(E)_{Be}^{j}} \qquad 4.7$$

where $\mu/\rho(E)^{T}_{Be}$ is the mass absorption coefficient from Thinh et al (1979). $\mu/\rho(E)^{j}_{Be}$ is the mass absorption coefficient taken from Springer et al (1976) or Henke et al (1974). The values of t^{j}_{Be} are summarised in Table 4.1. If the coefficients of Springer et al (1976)
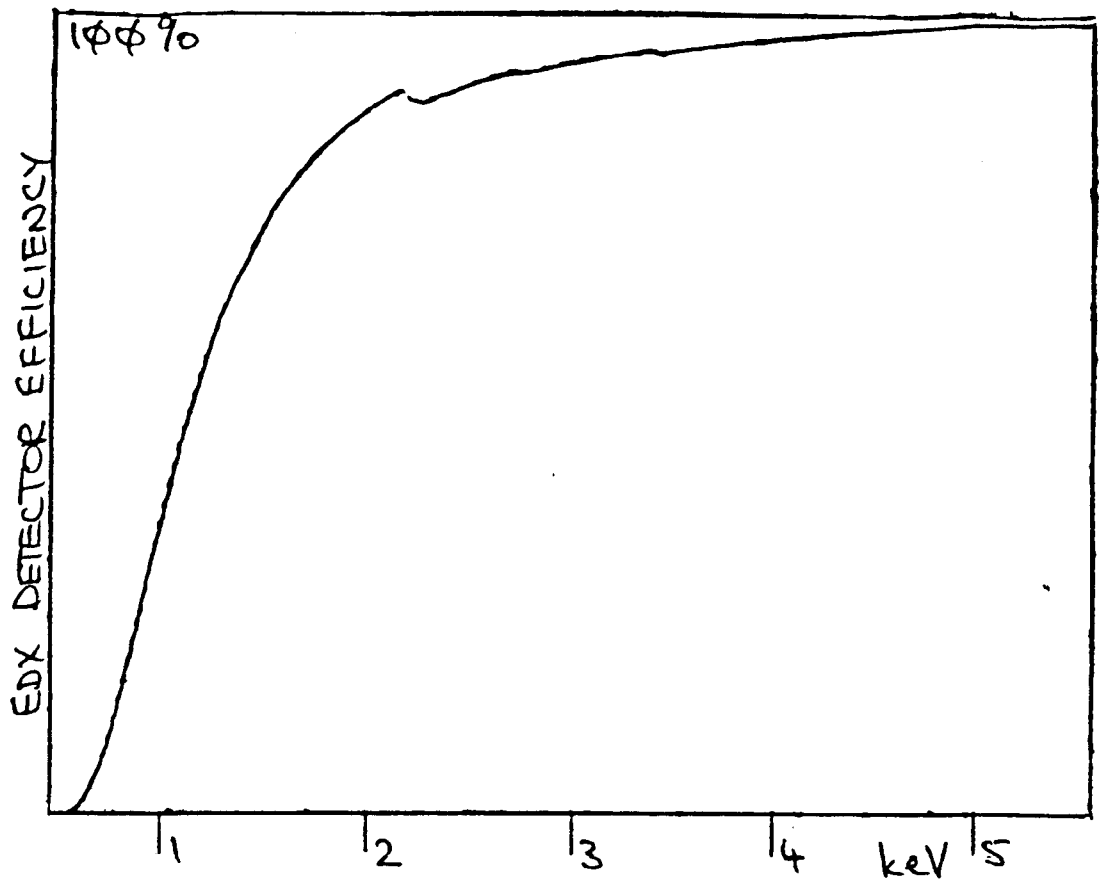
Figure 4.8

	Energy/keV				
	0.930	1.012	1.041	1.254	1.487
Springer and Nolan	576.75	452.49	417.78	245.31	150.67
Thinh and Leroux	699.08	541.17	496.77	282.61	168.69
Henke and Ebsu	745.0	578.3	530.0	300.5	178.7

Mass absorption coefficents/$cm^2 gm^{-1}$

Springer and Nolan	10.9	10.8	10.7	10.4	10.1
Thinh and Leroux	◁—————		—9μm—		————▷
Henke and Ebsu	8.4	8.4	8.4	8.5	8.5

Equivalent Be-window thicknesses/μm $\left(t_{Be}^{j}\right)$

Table 4.1

had been used, $t_{Be} \doteq 10.6 \mu m$. If the coefficients of Henke et al (1974) had been used, $t_{Be} \doteq 8.4 \mu m$. Clearly the optimum value of t_{Be} depends on the choice of coefficients. Thus, the optimum $t_{Be} = 9.0 \mu m$ value obtained in Section 4.2.2 should only be used with the mass absorption coefficients of Thinh et al (1979).

Finally, Adam (1985) also theoretically modelled the bremsstrahlung shape on a number of spectra (with substantial self-absorption corrections) which were acquired using the HB5 detector. Adam obtained an optimum t_{Be} window thickness of about 10 μm, using the mass absorption coefficients of Springer et al (1976). Clearly, this value is in reasonable agreement with the predictions shown in Table 4.1.

4.2.4   High Energy Detector Efficiency

Figures 4.9 and 4.10 show spectra recorded from evaporated Co on formvar and Ag. Scaled theoretical bremsstrahlung curves calculated from the parameterised MBH equation are also shown. A discrepancy between the theoretical and experimental spectral shapes is evident for X-ray energies above about 14 keV. The main cause of this discrepancy is due to the transmission of X-rays through the detector crystal. Thus, the high energy detector efficienty $\epsilon_H(E)$ can be written as (Zaluzec, 1979)

$$\frac{I_c(E)}{B_x(E)} = \epsilon_H(E) = \left[1 - exp \left(-\frac{\mu}{\rho}(E) \rho t \right)_{Si} \right] \qquad 4.8$$
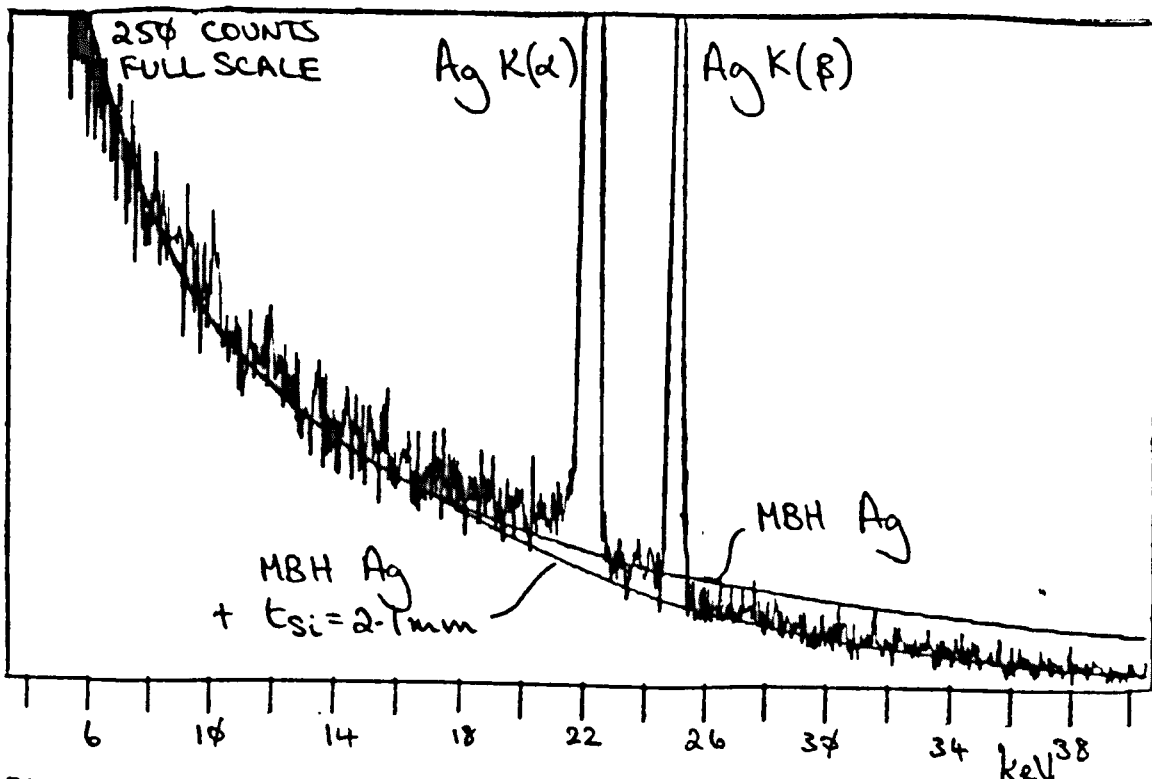
Figure 4.9   Ag spectrum.
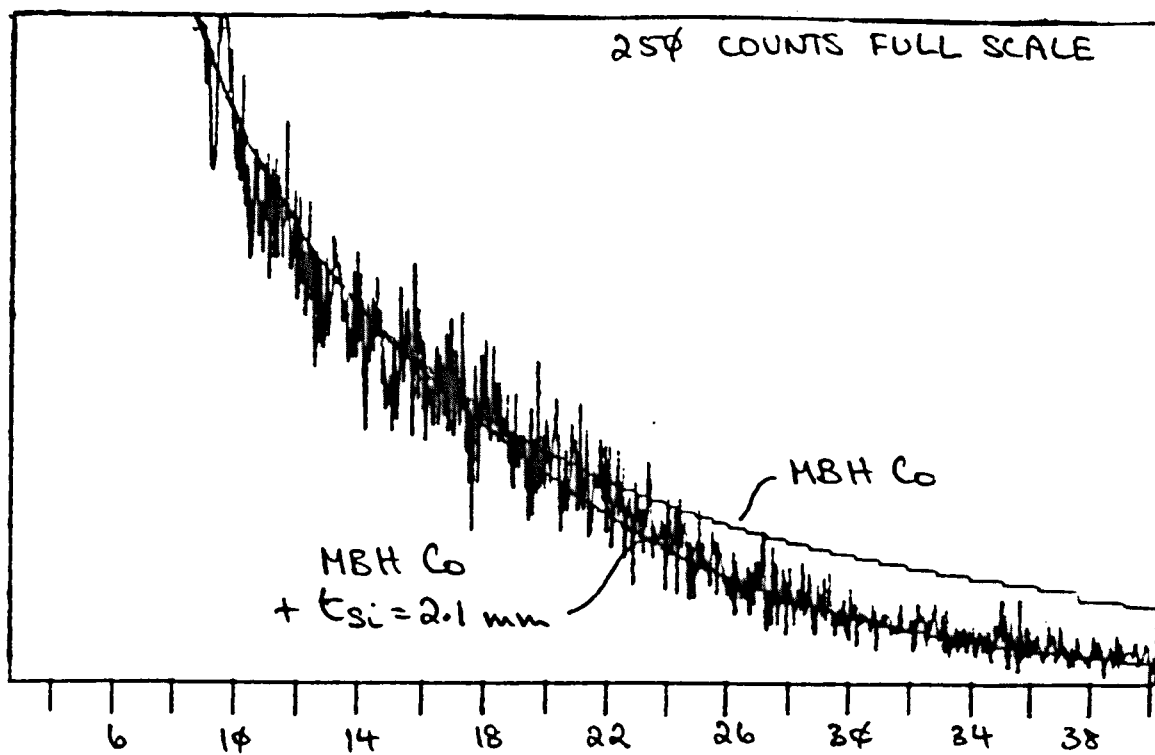
Figure 4.10   Co spectrum.

where the terms are as defined in Section 4.2.2. If t_{si} is regarded as a variable the best fit between $I_c(E)$ and the spectrum can be found by minimising a reduced chi-square function (summed over the fitting channels) of the form

$$\chi_r^2 = \frac{1}{d_r} \sum \frac{(I(E) - I_c(E))^2}{I(E)} \qquad\qquad 4.9$$

where d_r is the number of degrees of freedom (equal to n-3 in this case) and $I(E)$ is the number of counts in the experimental spectrum. A value of t_{si} = 2.1± 0.1 mm was obtained for both spectra with $X_r^2 \doteqdot 1$. The mass absorption coefficients of Springer et al (1976) were used. This value of crystal thickness is within the ~2-3 mm range of values quoted in the literature (Statham 1981). An estimate of the values of crystal thickness which would have been obtained if the coefficients of Thinh et al (1979) or Henke et al (1974) had been used can be estimated from an equation similar to Equation 4.7. These values lie within the range of crystal thicknesses quoted by Statham (1981). Since only light to medium atomic number elements were of interest here, only the low energy region of the EDX spectrum will be considered from now on. It should be noted that virtually all of the entire bremsstrahlung energy range of 0-40 keV can be accurately modelled using the scaled theoretical MBH equation when account is taken of detector and specimen absorption (following page 46) effects. Figure 4.11 shows the detector efficiency for the 0-40 keV energy region represented graphically. The only region where this modelling procedure does not describe the experimental bremsstrahlung

accurately is the region just below 2 keV where a count build-up is present (see Figure 4.6). This count build-up was assumed to be caused by the effects of count redistribution in the detector.

4.2.5   Count Redistribution in the X-ray Detector

Count redistribution within an EDX spectrum arises from several sources. Because of the uncertainty in the number of electron-hole pairs produced within the Si crystal by the incoming X-ray, the characteristic X-ray signal from an element becomes smeared out into a gaussian shape. However, this uncertainty has a negligible effect on the shape of the bremsstrahlung, except in the region of absorption edges where again the sharp change in intensity is smeared out (Gray 1981). Absorption edges were not present to any significant degree in the spectra examined.

Another effect causing a redistribution of counts which does affect the shape of the bremsstrahlung (and characteristic signals) is incomplete charge collection. If some fraction of the total charge produced by an X-ray in the detector is not collected, a count appears in a channel below that where it should. Such a process accounts for a low energy tail that is especially evident on characteristic signals occurring in the 2-4 keV energy range (Lacer et al 1977, Statham 1981). Photons in this range are absorbed heavily by the Si(Li) detector crystal and so the main interaction tends to occur close to the surface of the crystal where the charge collection is imperfect. This effect is called incomplete charge collection (ICC).

Incomplete charge collection was examined using the following method. (For a detailed study see Adam, 1986). A source producing characteristic X-rays without bremsstrahlung can be made using a strong

radioactive source (Shima et al 1983, Craven et al 1984). Figure 4.12 shows the experimental arrangement. An annular source emits Mn Kα and Kβ X-rays which can be used to produce X-rays of lower energy by fluorescence. The vacuum chamber was designed by WAP Nicholson and built in the Natural Philosophy department workshop. The chamber includes four adjustable screws which can be used to align the radioactive source with respect to the detector whilst the source is in vacuum.

Figures 4.13 and 4.14 show P and Ca characteristic peaks which were obtained by fluorescence of suitable samples. The P containing sample was made by embedding red phosphorus in paraffin wax. The Ca containing sample was made by similarly embedding Ca CO$_3$. The distortion of the X-ray peaks from the Gaussian shape is evident. The shape of the P and Ca characteristic peaks were important for the spectral processing described in Chapter 5.

Incomplete charge collection also affects the shape of the bremsstrahlung in the low energy region. Statham (1981) suggests that the buildup of counts below 2 keV, as indicated in Figure 4.6, is due to ICC. Craven et al (1984) have provided further quantitative evidence for this. They suggest that the effect of ICC on the bremsstrahlung shape can be calculated by redistributing the intensity in the theoretical bremsstrahlung distribution reaching the detector crystal. The theoretical bremsstrahlung distribution is defined to be that predicted by the modified Bethe-Heitler equation corrected for absorption in the specimen and detector. The redistribution of intensity is defined by an equation derived from a parametric fit to a series of fluoresced spectra ranging from Al to Mn. From this study

ADJUSTMENT
SCREWS

EDX DETECTOR

X-RAY SOURCE

VACUUM "POT"

PERSPEX LID

ANNULAR Fe^{55} SOURCE

SAMPLE

Figure 4.12

4∅∅∅ COUNTS FULL SCALE

P(k)

1   2   keV
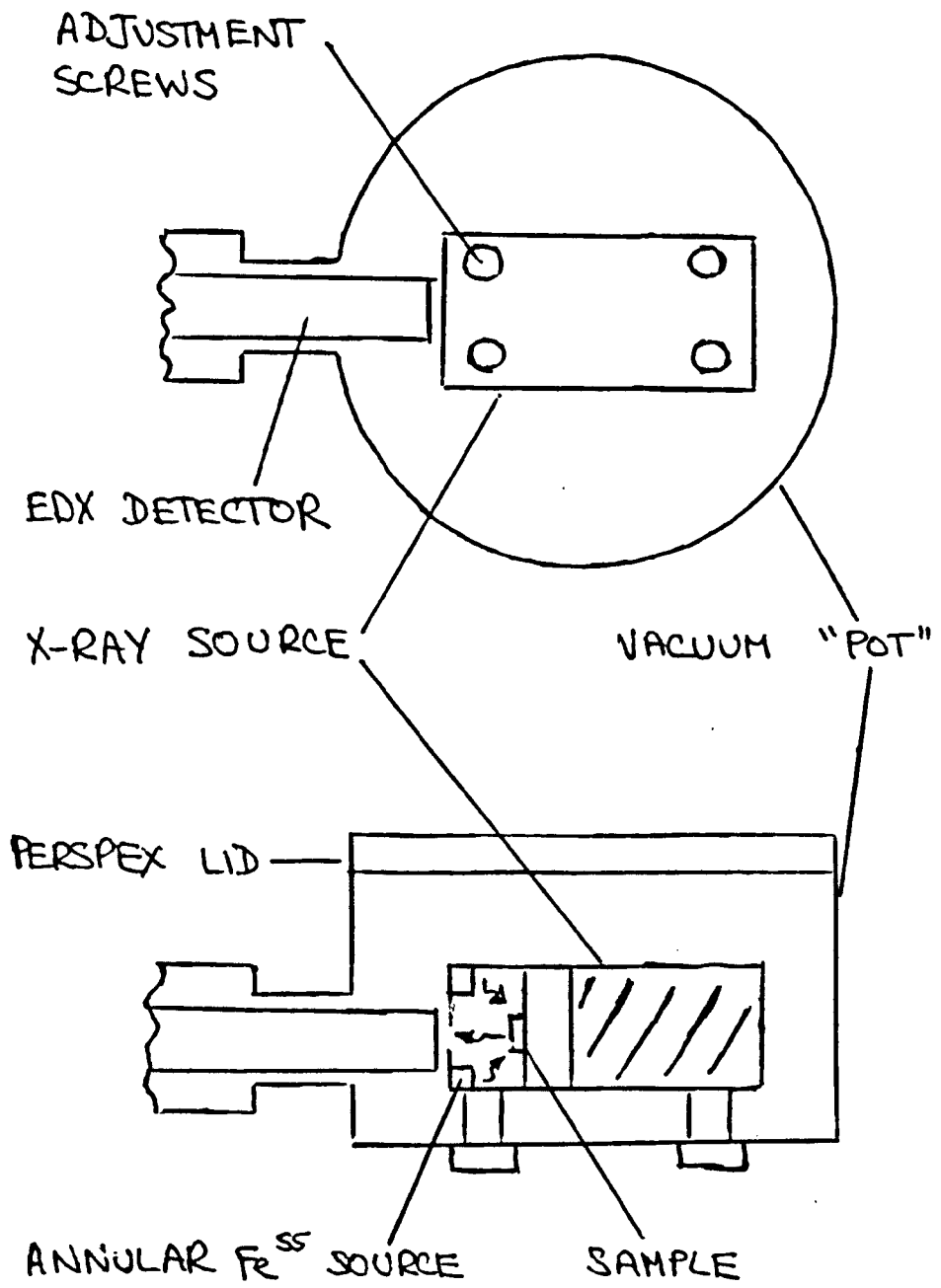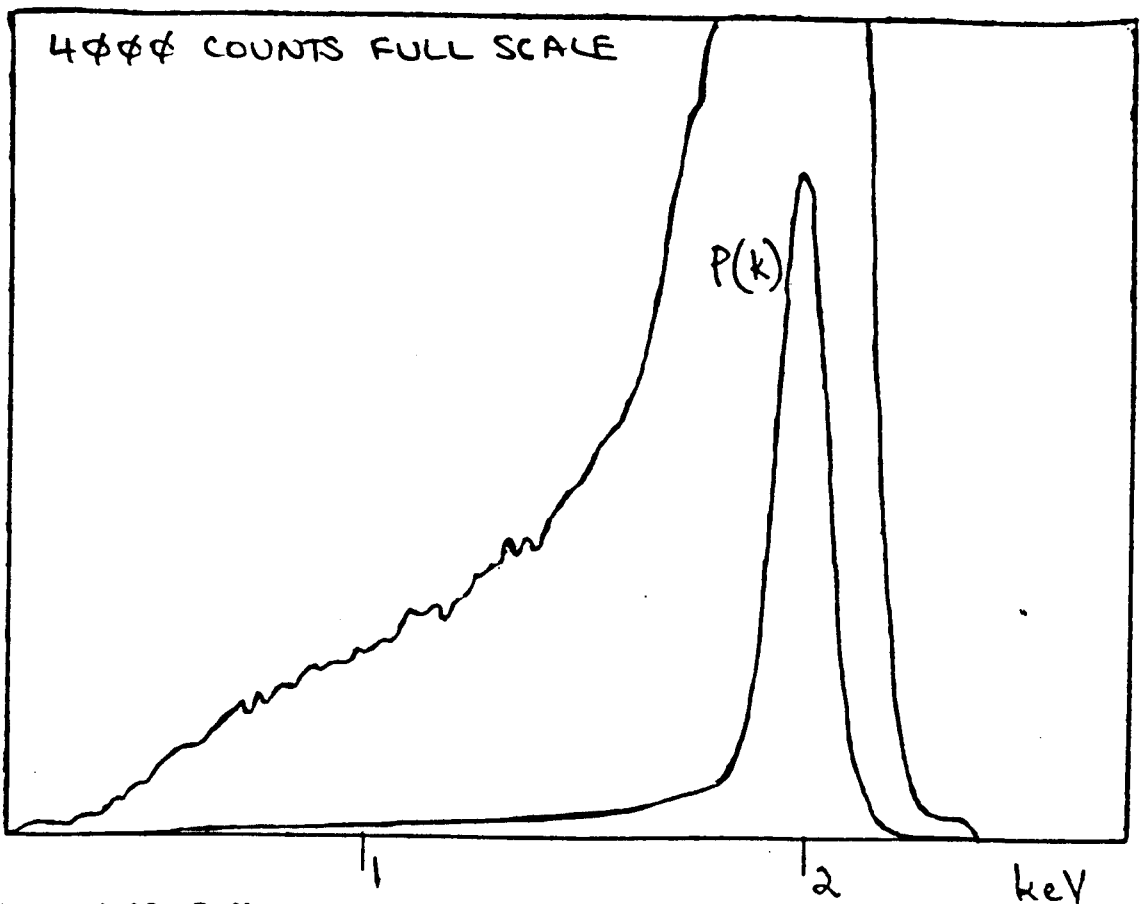
Figure 4.13 P fluoresced spectrum.

2∅∅∅ COUNTS FULL SCALE

Ca (Kα)

Ca (Kα) ESCAPE
PEAK

∅   1   2   3   4

keV
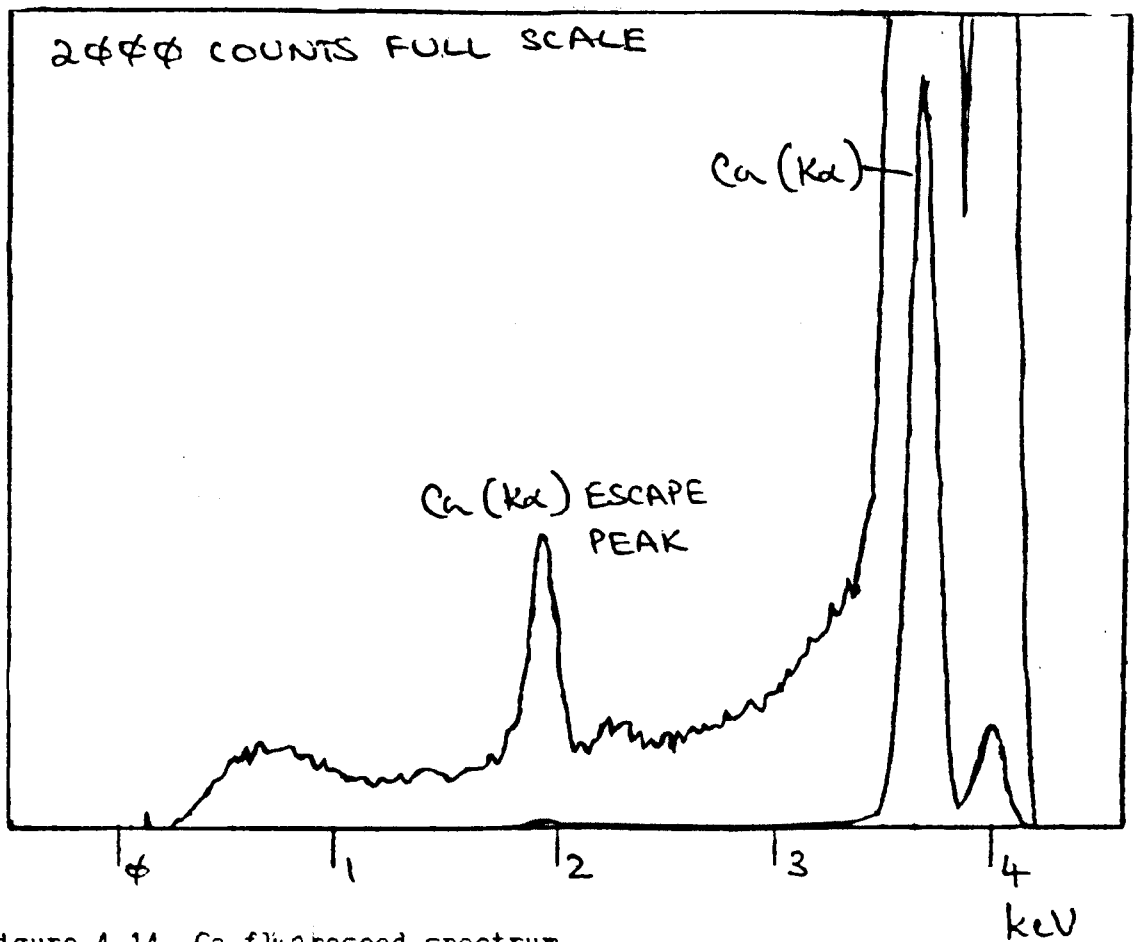
Figure 4.14 Ca fluoresced spectrum.

Adam (1985) and Craven et al (1984) predict that only the bremsstrahlung shape in the region of the Si absorption edge is affected, i.e. there is a loss of bremsstrahlung counts above the Si absorption edge and a nett gain of counts below the absorption edge. Whilst Adam (1985) had some success in predicting the bremsstrahlung shape close to the Si-absorption edge, Adam resorted to the use of a "bump" to model the ICC count redistribution when processing spectra (i.e. extracting the characteristic signals).

In conclusion, the buildup of counts on the low energy bremsstrahlung shape is probably due to ICC and not due simply to absorption in a Si dead layer. ICC need not affect the determination of detector efficiency described in Section 4.2.2 since care was taken to exclude this region.

4.2.6 SUMMARY

The efficiency of the EDX detector attached to the HB5 has been investigated and Figures 4.8 and 4.11 show this efficiency represented graphically. A significant discrepancy exists between the published values of mass absorption coefficients used to calculate the detector efficiency. Thus, the values of t_{Be} and t_{Si} derived are, to a limited extent, dependent upon the coefficients used when calculating the detector efficiency. Count redistribution in the spectra examined (due to ICC) need not affect this determination of detector efficiency since care was taken to exclude the region of the spectra near the Si absorption edge.
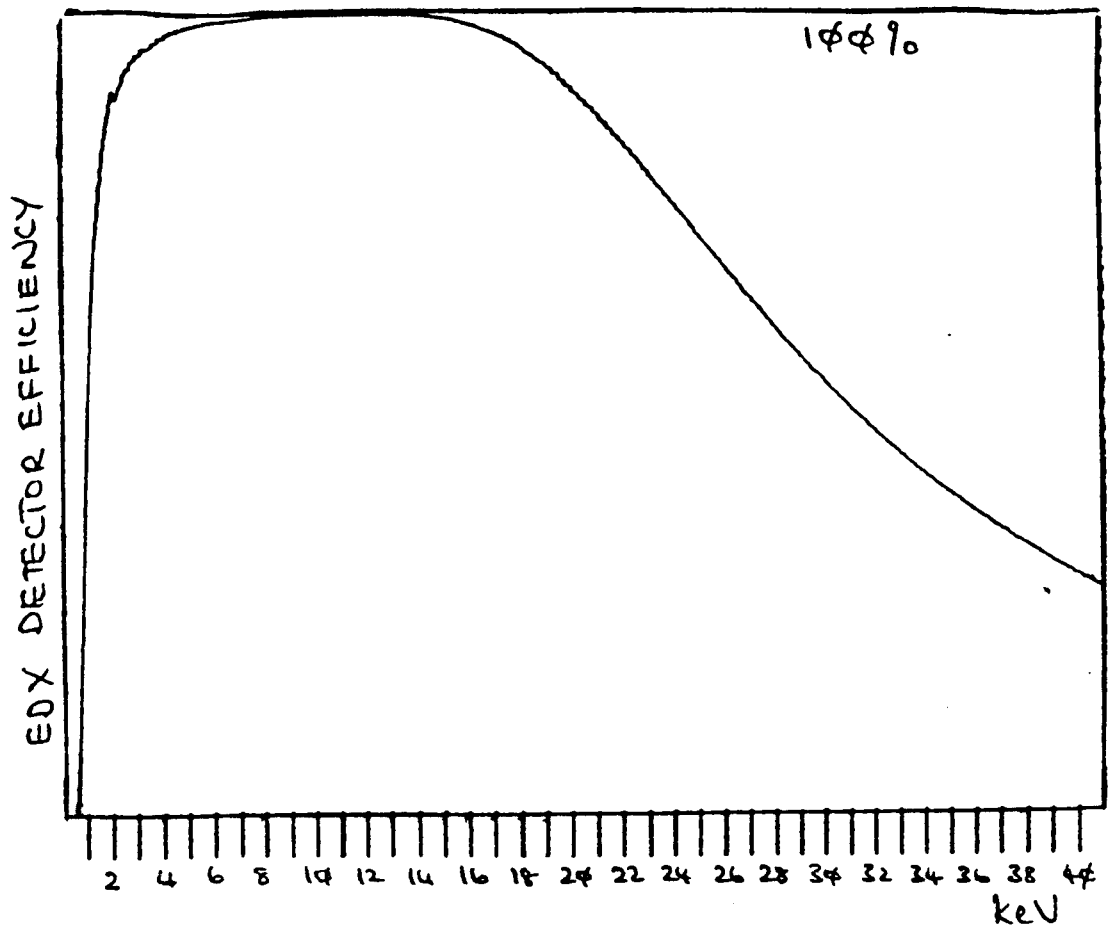
Figure 4.11

4.3 THE PARAMETERISATION OF CHARACTERISTIC CROSS-SECTIONS

Gray (1981) suggested using the ratio of the characteristic peak counts (Equation 4.1) to bremsstrahlung counts (Equation 4.2) in conjunction with the MBH equation to determine characteristic cross-sections. Thus, the cross-section may be determined from

$$\sigma_c = \frac{P}{B(E)} \, \frac{\sigma_B (E, \lambda) \, dE}{S} \qquad \qquad 4.10$$

where $\sigma_c = (\omega/4\pi)\sigma_k$ and $\sigma_B(E, \lambda)$ is the bremsstrahlung production predicted by the MBH equation. As discussed in Section 2.11, Chapman et al (1983) found that the MBH theory gives a satisfactory description of bremsstrahlung production in thin films. The advantage of using Equation 4.10 for calculating characteristic cross-sections is that the ratio P/B(E) may be determined with accuracy as it depends essentially on statistical fluctuations (which can be minimised by long spectral acquisition times) and the success with which spurious contributions to the background are removed. Gray et al (1983) succeeded in obtaining an agreement between theoretical and experimental characteristic cross-sections of typically 10%; however, it is of interest to see if other forms of the Bethe equation discussed in Section 2.5 could provide better agreement. The cross-section data of Gray (1981) has been used throughout (except where indicated).

4.3.1   Parameterisation Using the Non-relativistic Bethe Equation

The non-relativistic Bethe equation can be written as

$$\frac{\sigma_K I_K^2 U_K}{2\pi e^4} = b_K \ln U_K + b_K \ln c_K \qquad 4.11$$

where $U_K = T_0/I_K$ and T_0 has been substituted for E_0 ($T_0 = eV_0$; kinetic energy of electron, $E_0 = 1/2\, m_0 v_0^2$, see Section 2.5).   Figure 4.15 shows the characteristic cross-section data of Gray (1981) plotted in the manner described in Section 2.4.   The line corresponding to $b_K = 0.9$, $c_K = 0.65$ for the overvoltage range $4 \leq U_K \leq 25$ recommended by Powell (1976) is also shown.   With the exception of the Ti data, the line fits the points reasonably well, but only within the overvoltage range recommended.   The approach taken by Gray et al (1983) was to allow the Bethe parameters to vary until the best fit over the entire range of overvoltage was achieved.   If the parameters

$$y_i = \frac{\sigma_{Ki} U_{Ki} I_{Ki}^2}{2\pi e^4}$$ and $x_i = \ln U_{Ki}$ are defined then Equation 4.11 can be written

$$y_i = b_K x_i + b_K \ln c_K \qquad 4.12$$

The standard solution of a linear regression can therefore be written in this case as

$$b_k = \frac{\sum y_i \sum x_i - N \sum x_i y_i}{(\sum x_i)^2 - N \sum x_i^2}$$

4.13

$$c_k = \exp\left(\frac{1}{b_k}\frac{\sum y_i x_i - b_k \sum x_i^2}{\sum x_i}\right)$$

4.14

where the summation is carried out over all data points i up to the total N. In this case N=24. The values b_K = 0.6, C_K = 1.16 were obtained. A fractional variation F between the predicted cross-section σ_{Ki} and the experimental cross-section σ_{Ei} can be defined as

$$F = \frac{|\sigma_{Ki} - \sigma_{Ei}|}{\sigma_{Ei}}$$

4.15

σ_{Ki} can be written as

$$\sigma_{Ki} = (b_k x_i + a)/d$$

where a = $b_K \ln c_K$

d = $I_{Ki}^2 U_{Ki}/a\pi e^t$

x_i = ln U_{Ki}

Table 4.2(a) summarises the fractional variation in each of the data points. The average value of fractional variation is 11.8%. Gray

Element	(a)	(b)	(c)	(d)
Al:-				
TO= 40keV	10.0	13.3	1.2	7.7
60	7.1	11.3	2.3	9.7
80	9.7	14.6	8.6	17.1
100	4.6	9.7	7.5	16.4
Ti:-				
TO= 40keV	9.8	8.1	2.6	3.8
60	1.3	1.7	2.7	0.5
80	4.5	3.0	5.5	1.4
100	9.1	7.0	7.0	2.3
Co:-				
TO= 40keV	8.6	13.0	13.8	15.8
60	4.1	5.8	7.5	6.9
80	6.9	7.1	7.9	6.0
100	13.0	12.3	11.2	8.4
Cu:-				
TO= 40keV	6.2	12.2	16.5	21.0
60	9.6	12.2	17.1	18.3
80	9.5	10.4	14.5	14.2
100	10.5	10.4	8.8	6.7
Mo:-				
TO= 40keV	29.5	0.9	29.5	14.0
60	23.7	8.7	21.0	7.4
80	5.4	12.5	6.9	13.3
100	2.0	7.0	1.2	5.6
Ag:-				
TO= 40keV	62.2	1.1	68.1	8.9
60	16.1	4.7	14.8	5.6
80	16.5	3.5	14.7	1.7
100	3.3	4.8	3.5	4.8

Tables 4.2 (a) to (d)   PERCENT FRACTIONAL VARIATION

(1981) noted that the fit to the cross-section data can be improved by minimising the quantity R defined as

$$R = \sum_{i=1}^{N} \frac{[\sigma_{ki} - \sigma_{Ei}]^2}{\sigma_{Ei}^2}$$

This minimisation can be obtained by solving the simultaneous Equations

$$\frac{\partial R}{\partial b_k} = 0 \qquad \frac{\partial R}{\partial a} = 0$$

i.e.

$$b_k \sum \frac{x_i^2}{a^2 \sigma_E^2} + a \sum \frac{x_i}{a^2 \sigma_E^2} = \sum \frac{x_i}{a \sigma_E}$$

$$b_k \sum \frac{x_i}{a^2 \sigma_E^2} + a \sum \frac{1}{a^2 \sigma_E^2} = \sum \frac{1}{a \sigma_E}$$

$$\Rightarrow b_k = \frac{\left(\sum \frac{1}{a \sigma_E} \sum \frac{x_i}{a^2 \sigma_E^2}\right) - \left(\sum \frac{1}{a^2 \sigma_E^2}\right)\left(\frac{x_i}{a \sigma_E}\right)}{\left(\frac{x_i}{a^2 \sigma_E^2} \sum \frac{x_i}{a^2 \sigma_E^2}\right) - \left(\sum \frac{1}{a^2 \sigma_E^2} \sum \frac{x_i^2}{a^2 \sigma_E^2}\right)} \qquad 4.18$$

$$A = \frac{\sum \frac{x_i}{a \sigma_E} - b_k \sum \frac{x_i^2}{a^2 \sigma_E^2}}{\sum \frac{x_i}{a^2 \sigma_E^2}} \quad , \quad C_k = \exp\left(A / b_k\right) \qquad 4.19$$

The values b_K = 0.67, c_K = 0.89 are obtained and the fractional variation in the points are given in Table 4.2(b). The average value of F is 8.1% and none of the data points have a fractional variation greater than 14%. Clearly these Bethe parameters provide a more satisfactory parameterisation of the data. This parameterisation can be written explicitly as

$$\sigma_{ki} = \frac{2\pi e^4}{I_{ki}^2 U_{ki}} \, 0.67 \, \ln\left(0.89 \, U_{ki} / I_{ki}\right) \qquad 4.20$$

50

and is the "modified Bethe" equation defined by Gray et al (1983).

Figure 4.16 shows the cross-section data plotted as before but with $U_K = E_O/I_K$ in Equation 4.11. The values $b_K = 0.48$, $c_K = 1.43$ are obtained from a linear regression on the data and the fractional variations for each cross-section are summarised in Table 4.2(c). When R is minimised the values $b_K = 0.56$, $c_K = 1.05$ are obtained. The average fractional variation is 12.3% and the fractional variations in the cross-sections are summarised in Table 4.2(d). The average value of F is 8.5% and and none of the cross-sections have a fractional variation greater than 19.6%. The lines corresponding to both pairs of Bethe parameters are shown in Figure 4.16.

In conclusion, the modified Bethe equation marginally provides the best agreement between predicted and experimental cross-sections.

4.3.2 Parameterisation Using the Relativistic Bethe Equation

Since electrons with kinetic energy up to 100 keV were used to acquire the cross-section data, relativistic effects will be present to a limited extent. Therefore, the relativistic Bethe equation is probably a more appropriate guide to the parameterisation of these cross-sections. This relativistic equation can be written as

$$\frac{\sigma_K U_K I_K^2}{2\pi e^4} = b_K \left[\ln U_K - \ln(1-\beta^2) - \beta^2 \right] + b_K \ln c_K \qquad 4.21$$

The fractional variations in the cross-sections suggested by Zaluzec (1984) (Equation 2.8) for the elements of interest here are summarised in Table 4.2(e). Whilst good agreement between predicted and experimental cross-sections are

Element	(e)	(f)	(g)	(h)	(1)
Al:-					
T0= 40keV	33.9	1.2	7.1		
60	44.4	2.6	9.5		
80	55.6	9.3	17.3		
100	55.9	8.7	17.1	5.2	8.5
Ti:-					
T0= 40keV	20.5	2.3	3.4	17.3	15.8
60	18.6	2.4	0.5	11.6	9.6
80	17.7	4.7	0.9	6.6	3.8
100	17.8	5.7	1.2	2.5	0.2
Co:-					
T0= 40keV	5.8	14.1	16.2	7.1	7.4
60	5.9	7.2	6.8	2.3	1.2
80	8.3	7.0	5.1	1.3	0.6
100	6.5	9.8	7.1	3.9	5.9
Cu:-					
T0= 40keV	3.1	7.5	12.4	6.9	6.6
60	0.1	7.6	8.9	5.0	5.7
80	5.2	4.0	3.6	2.6	4.1
100	9.4	7.3	5.2	2.1	3.9
Mo:-					
T0= 40keV	57.8	28.2	1.5	6.5	1.9
60	48.8	21.7	8.7	11.9	14.8
80	15.3	5.4	11.4	8.3	7.6
100	25.3	1.1	2.8	1.0	1.2
Ag:-					
T0= 40keV	152.5	66.2	9.8	19.8	0.4
60	60.8	15.4	3.9	5.3	0.3
80	55.9	16.4	4.3	6.2	8.6
100	40.7	6.3	1.2	0.2	6.4

Tables 4.2 (e) to (1)   PERCENT FRACTIONAL VARIATION
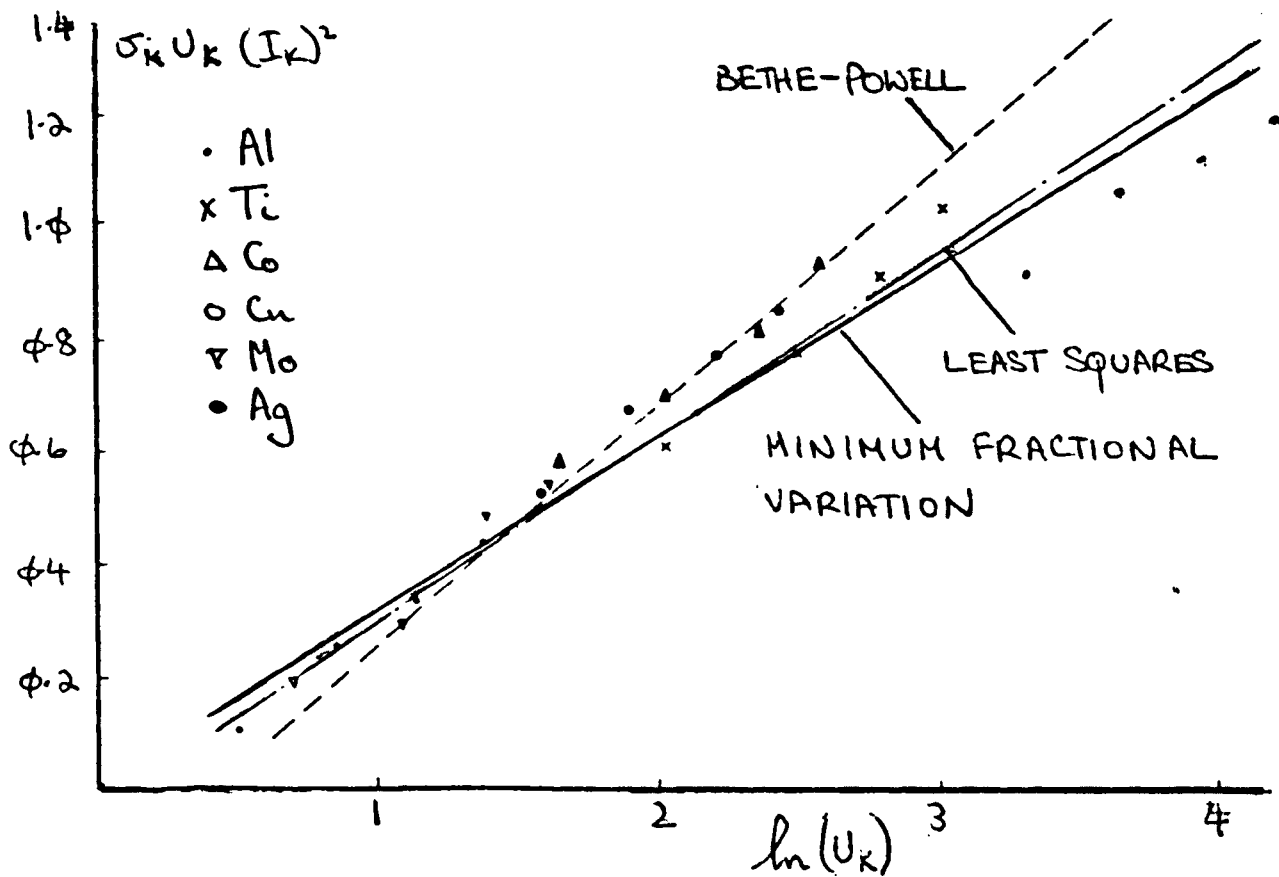
Figure 4.15 Non-relativistic Bethe, non-relativistic E_0.
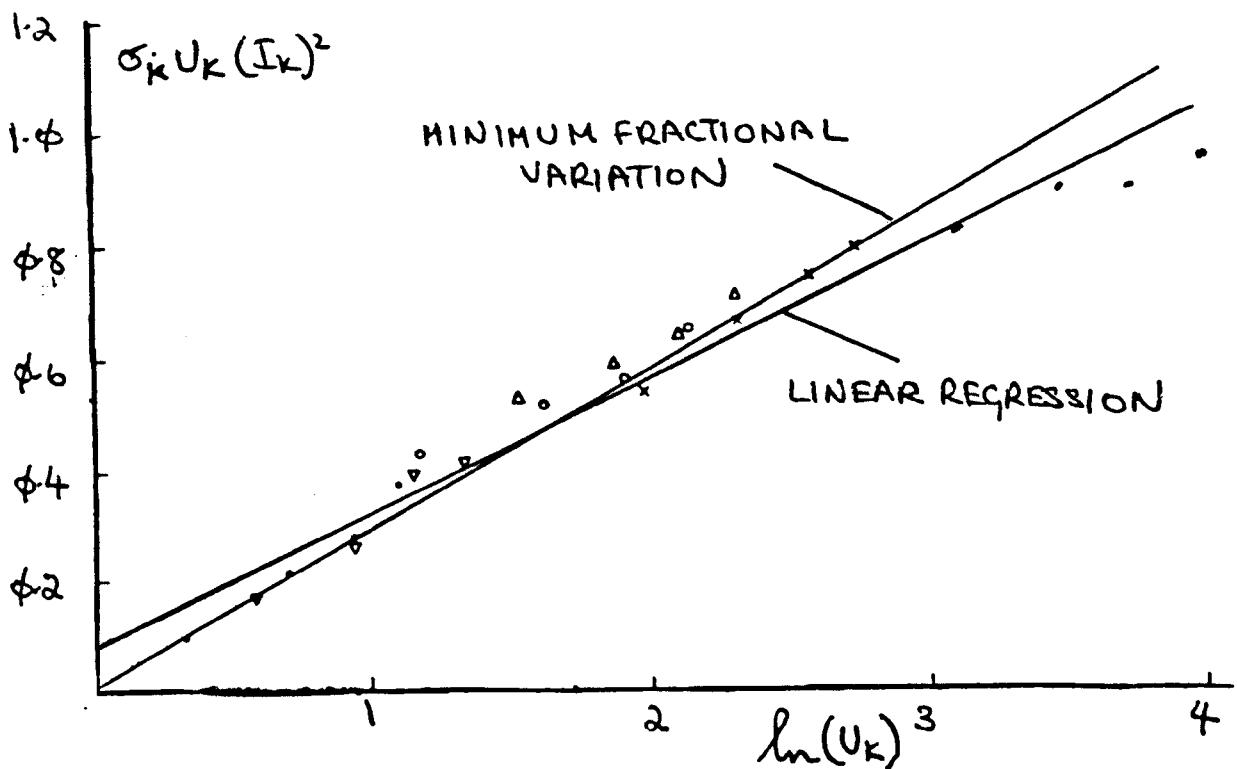
Figure 4.16 Non-relativistic Bethe, non-relativistic E_0.

obtained for Co and Cu (the average value of fractional variation is 5.5%); see Table 4.2(e), relatively poor agreement is obtained for the lowest and highest atomic number elements. The average value of fractional variation over the entire range of points is about 32%.

Better agreement can be obtained by allowing the Bethe parameters to vary as before. If the parameters $Y_i = \frac{\sigma_{Ki} U_{Ki} T_{Ki}^2}{2\pi e^4}$ and $x_i = \ln U_K - \ln(1 - \beta^2_i) - \beta^2_i$ are defined, then Equation 4.21 can be written in the form

$$Y_i = b_K x_i + b_K \ln c_K$$

and a linear regression performed on the points. The Bethe parameters can be calculated from Equations 4.13 and 4.14. The values $b_K = 0.48$, $C_K = 1.40$ are obtained and the fractional variation in the points are summarised in Table 4.2(f). The average value of F is 10.9%. Alternatively, the fractional variation in the points can be minimised and the Bethe parameters calculated from Equations 4.18 and 4.19. The values $b_K = 0.56$, $c_K = 1.04$ are obtained and the fractional variation in the points are summarised in Table 4.2(g). The average value of F is 6.9%. The lines corresponding to those parameters are shown in Figure 4.17.

In summary, the Bethe parameters of Zaluzec (1984) did not provide a very good fit to the cross-section data of Gray (1981). The best agreement between experimental and predicted cross-sections (using the relativistic Bethe equation) was obtained by minimising the fractional variation in the data. However, the fit to the data was not significantly better than that obtained when a similar minimisation was performed using the non-relativistic Bethe equation. Figures 4.15 to

4.17 show that one of the largest discrepancies between experimental and predicted cross-sections exists for Al, and Gray (1981) noted that the spectral processing technique used to obtain the data for Al might be suspect. Therefore, the cross-section for Al (T_o = 100 keV) was again determined using the knowledge of the low energy bremsstrahlung shape. In addition, an EEL spectrum was acquired simultaneously with the EDX spectrum allowing quantitative determination of any spurious light element contributions to the EDX spectrum; such as C contamination and O from aluminium oxide. Gray (1981) was not able to quantify (or detect) the presence of elements with Z<11 since an EEL system (or "windowless" EDX system etc.) was not available. The quantitation of C and O is especially important for a low Z thin foil such as Al since, from Equation 4.3, the efficiency of bremsstrahlung production varies as Z^2.

4.3.3 Determination of the Al Cross-section

4.3.3(a) Specimen Preparation and Spectral Acquisition

An Al thin foil was prepared by evaporation of Al onto a glass slide. The foil thickness was measured as 350$\pm$100Å. X-ray self-absorption by the specimen was considered negligible. The Al foil was floated off the glass slide (in distilled water) and supported on holey formvar on a Cu single hole mount. Simultaneous EDX and EEL spectra were acquired from a region of the Al foil which was over a hole in the formvar. The acquisition conditions used were VOA-250μm, CA-50 μm. The probe convergence semi-angle α, and electron collection semi-angle β were 25 m rad and 27 m rad respectively. This choice of α and β provide adequate counts in the EDX spectrum whilst minimising artefacts in the EDX spectrum (Crozier, 1985).
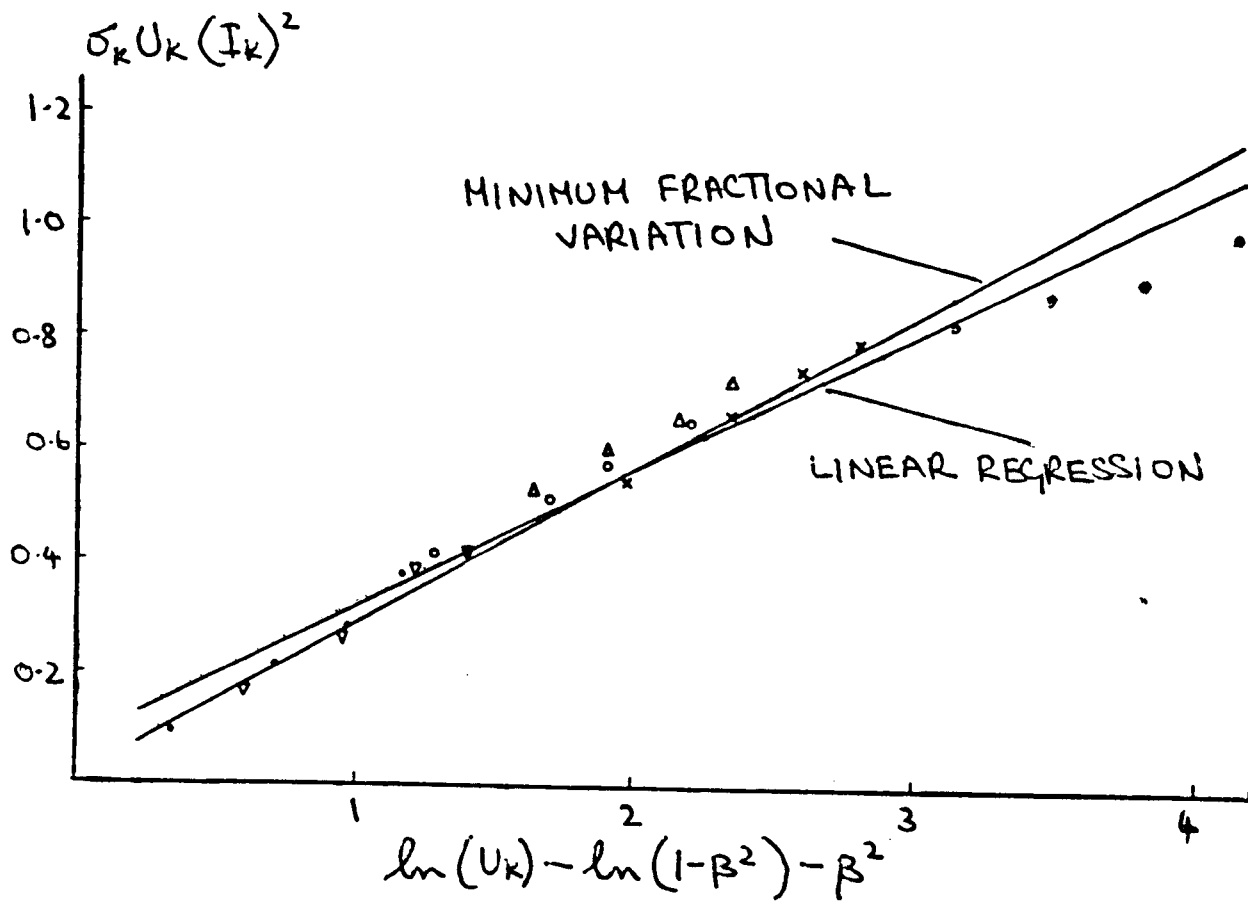
Figure 4.17   Relativistic Bethe.

4.3.3(b) Spectral Processing and Determination of the Al Cross-section

Figure 4.18 shows the Al EDX spectrum with a scaled theoretical background fitted to the spectrum.   The EEL Al spectrum (see Figure 4.15) clearly shows the presence of C and O.   Therefore, there will be a C and O bremsstrahlung contribution to the spectrum shown in Figure 7.13   The signals were extracted using the extrapolation method (see Chapter 6), allowance being made for a finite probe convergence angle and plural inelastic scattering.   (See Crozier (1985) for a description of these corrections).   The characteristic count ratios were quantified using the SIGMAK program of Egerton (1984), and the values obtained for the atomic C/O and O/Al ratios were 0.56 and 0.67 respectively.   The latter ratio indicates that all the Al had oxidised to Al_2O_3. Assuming that the specimen is composed entirely of Al, O and C, the characteristic Al peak to bremsstrahlung ratio, corrected for the C and O contribution, can be obtained from

$$F_{Al} = \frac{1}{1 + \dfrac{\sigma_o N_o}{\sigma_{Al} N_{Al}} + \dfrac{\sigma_c N_c}{\sigma_{Al} N_{Al}}}$$

where σ and N are the bremsstrahlung cross-sections (calculated from the MBH formula) and number of atoms of O, C and Al. F_{Al} is the fraction of total bremsstrahlung counts in the 20 eV channel at the Al characteristic peak energy which is due to Al alone.   An Al peak to background ratio which excludes the C and O bremsstrahlung can now be calculated then, using Equation 4.1, a value of σ_c can be determined.   A value of $\sigma_c = 8.05$ barns/sr was obtained by this method.   This value lies between that predicted by Powell (1976) and Rez (1984) and is significantly greater than the value obtained by Gray (1984).
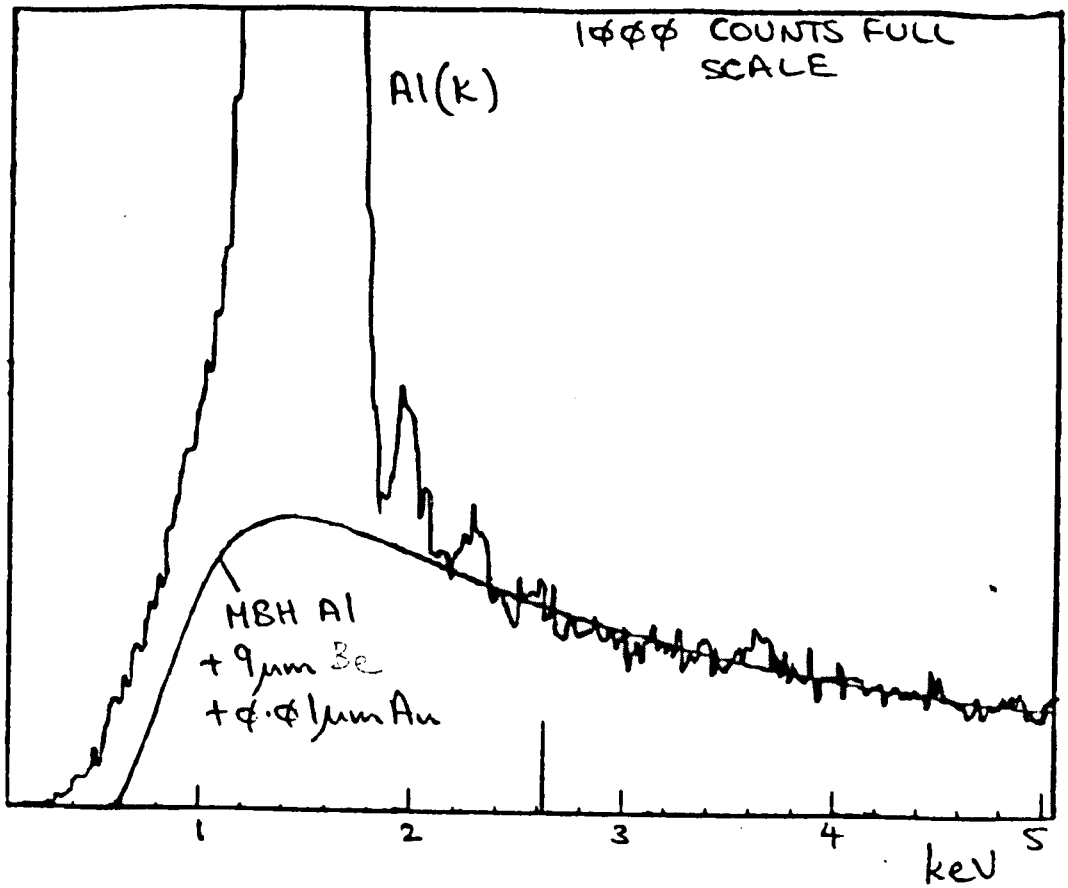
Figure 4.18 Al spectrum.

4.3.3(c) Parameterisation of the Cross-sections

A best fit to the cross-section data can again be calculated with the Al cross-sections determined by Gray (1981) excluded, and the 8.05 barns/str (T_O = 100 keV) value included.   If the fractional variation in the cross-sections are minimised, the Bethe parameters b_K = 0.73, c_K = 0.86 are obtained.   This parameterisation can be written explicitly as

$$\sigma_k = \frac{2\pi e^4}{I_k T_0} \, 0.73 \, \ln\left(0.86 \, T_0 / I_k\right)$$

4.23

and the fit to the data is as shown in Figure 4.19.

The fractional variations in the cross-sections are summarised in Table 4.2(i).   The average value of fractional variation is 5.5% and the fractional variation for the Al cross-section is less than 8.5%. Therefore, Equation 4.23 has achieved better agreement between experimental and predicted cross-sections than was obtained by Gray et al (1983).

4.3.4 SUMMARY

Parameterisation of the cross-section data of Gray (1981) has been examined in detail using different forms of the Bethe equation.   There was no advantage in using the relativistic, rather than non-relativistic form of the Bethe equation.   Gray (1983) noted that the Al cross-section data might be suspect.   When the Al cross-section was redetermined and substituted into the data of Gray, better agreement between experimental and predicted cross-sections was obtained.
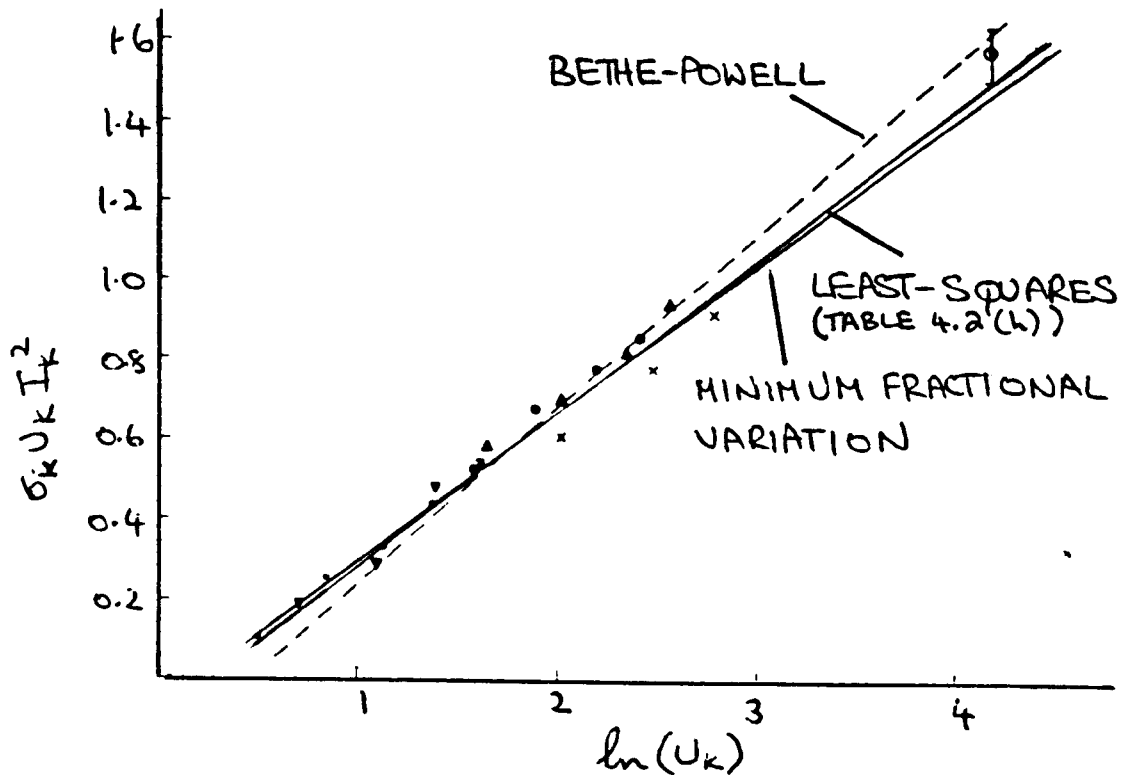
Figure 4.19 Non-relativistic Bethe, non-relativistic E_0.

CHAPTER 5

AN INVESTIGATION INTO THE QUANTITATION OF TRACE LIGHT
ELEMENT CONCENTRATIONS IN MINERALISED BONE.

5.1 INTRODUCTION

As described in Chapter 1 and Appendix 1, the presence of Al in the surface of mineralised bone is of physiological significance. This chapter describes an investigation into the quantitation and distribution of trace Al/Ca and Mg/Ca atomic ratios in mineralised bone. The samples investigated were obtained from an experiment performed by Dr H Y Elder. They consist of two groups; an "experimental" group of pathological samples containing trace concentrations of Al and a "control" group of samples which should not contain any Al. Sections of mineralised bone were prepared for EDX by the technicians in Dr Elders unit. The specimens were first cut to about 1500Å thickness using an ultramicrotome. They were then supported on formvar on a Cu single hole mount and finally carbon coated to make the specimens electrically and thermally conducting. Details of both the physiological experiment and the specimen preparation are given in Appendix 1.

The chapter begins with a description of a typical sample and the spectral acquisition conditions. Spectral processing (i.e. extraction of the characteristic signals) and quantitation (conversion of the characteristic intensity ratios to atomic ratios) are then discussed. Finally, some graphs of the distribution of the elements of interest are shown with the physiological interpretation being left to Appendix 1.

5.2 MINERALISED BONE SECTION

Figure 5.1a shows a typical section of mineralising bone. Soft tissue, osteoid, mineralisation nuclei and mineralised bone are indicated. It is generally accepted that the main constituent of mineralised bone is very similar to hydroxyapatite (Ca_{10} $(PO_4)_6(OH)_2$). Bone goes through a continuous remodelling process of bone formation (mineralisation), a dormant or resting stage and then resorption, and it was necessary to distinguish between these different stages when choosing where to acquire spectra. The most obvious difference between the experimental and control samples was that there was an almost complete lack of mineralising regions (generally characterised by the presence of mineralisation nuclei) in the experimental sections. Also, there was histochemical evidence of Al uptake into bone, only in the experimental samples (Elder, personal communication). The lack of mineralising regions was unexpected since they had been the regions chosen for investigation in previous human studies (e.g. Boyce et al 1981). Spectra were only acquired from regions of dormant bone (i.e. where mineralisation nuclei were not present) on both control and experimental sections. Care was taken to avoid regions of bone which may have been in the resorption stage. Figure 5.1b shows a typical region of dormant bone surface.

As decribed in Section 5.3.1, spectra were acquired from sites spaced at $1\mu m$ intervals into the bone from the dormant bone surface. The bone samples which were examined consisted of slices through roughly cylindrical bone trabecula. Due to the variable orientation of the trabecula it was never certain if the slice had been cut normal to the bone surface (Elder, personal communication).

57

(a)

MINERALISED
BONE

MINERALISATION NUCLEUS

1 μm

(b)

SOFT TISSUE / OSTEOID

1 μm
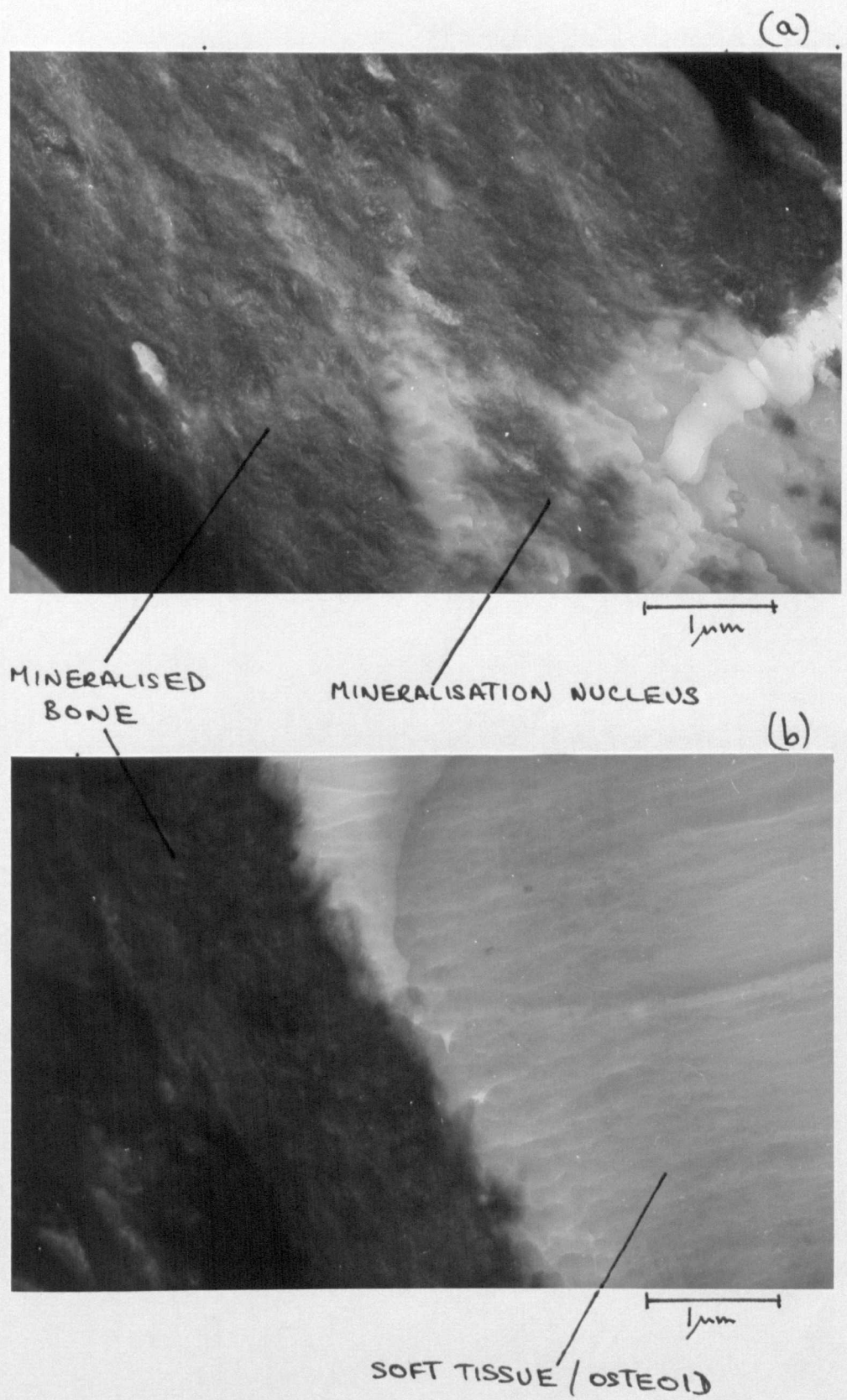
Figure 5.1

Thus, intervals of 1μm on the sample should be regarded as $\leqslant 1\mu$m at a true normal to the bone surface (see Figure 5.2). In an attempt to minimise the uncertainty in the intervals, spectra were acquired along the short axis of the typically oval region of bone examined.

5.3 SPECTRAL ACQUISITION

5.3.1 Choice of Microscope

Previous studies by Boyce et al (1981) involved determining the concentration of Al in three regions of bone; mineralisation nuclei, surface bone ($\leq 2\mu$m from the bone/osteoid interface) and deep bone ($>2\mu$m) from the interface). In the work described here, atomic Al/Ca, Mg/Ca and Ca/P ratios were determined from spectra acquired typically at 1μm intervals into the bone from the dormant bone surface. Trace concentrations of Al could often be detected 4μm from the surface; however, long spectral acquistion times (20-25 min) were required to obtain significant results. To minimise the acquistion time, the beam current on the specimen was maximised (about 8 nA on the HB5) and this was achieved by using the largest VOA (500μm). The probe size was therefore 0.26μm (see Section 3.4) which provided acceptable spatial resolution.

This is a relatively large probe which can be obtained using other instruments; a probe size of 0.2μm with a beam current of 0.3 nA can be obtained using a JEOL JEM 100C (Nicholson, personal communication). The advantages of using the HB5 were the following. Firstly, if the JEM was used it would take much longer than 25 min to acquire spectra with significant trace element signals. Secondly, the stray scattering contribution to a spectrum is smaller using the HB5
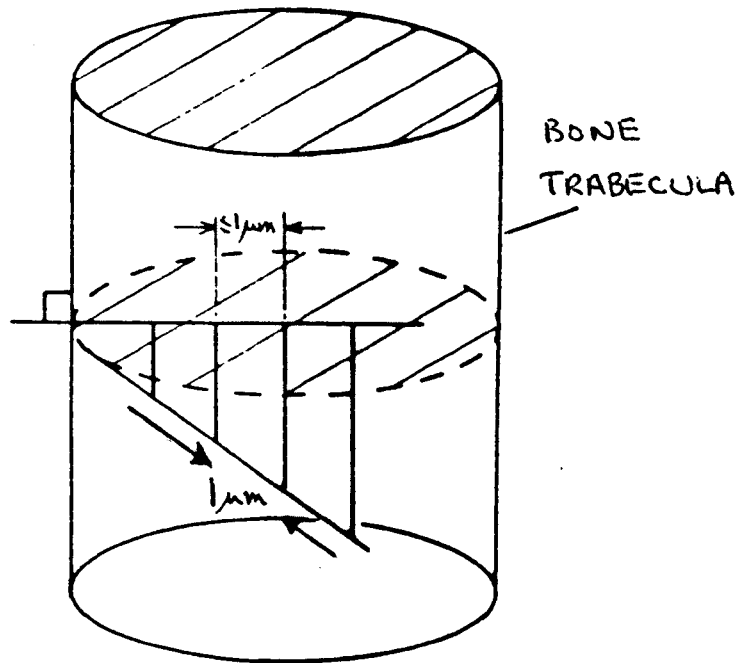
Figure 5.2

than using the JEM. From preliminary investigations it became clear that if a relatively large stray contribution was present, it was more difficult to extract the trace element counts. Thus the HB5 was used to acquire spectra since the beam current (for given probe size) was higher, and the stray scattering contribution lower, than could be obtained using the JEM.

5.3.2 X-ray Self-absorption Effects

One of the most important effects making extraction of the trace element counts difficult is variation in the specimen self-absorption. Care was taken to align each specimen in the microscope so that the major folds in the specimen pointed towards the X-ray detector. Thus there was a relatively clear path between the region of the specimen analysed and the detector (see Figure 5.3). Obvious regions of specimen which were folded or buckled were, of course, avoided. These constraints made it more difficult to move the probe during spectral acquisition.

5.3.3 Beam Damage to the Specimen

As stated in Section 5.3.1 spectral acquisition times of 20-25 min were required to obtain spectra with significant trace element signals. Clearly some precautions needed to be taken to avoid damage to the sample. It was important not to use a probe which was smaller than that required since although the current on the specimen would be less, the time taken to acquire spectra would have to be increased. Thus, the beam damage to the specimen would also be increased. To minimise the existing damage to the specimen, the probe was moved (parallel to the bone surface) every few minutes. For the reasons described in

59

DETECTOR

FOLDS

REGION CHOSEN FOR ANALYSIS

7 μm
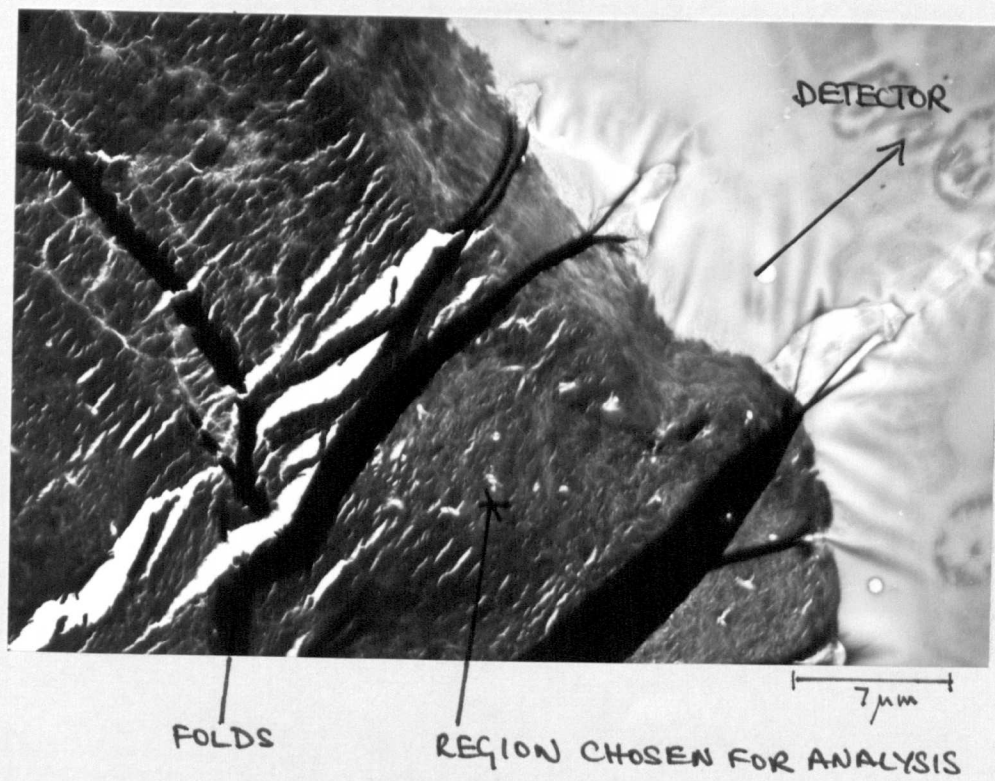
Figure 5.3

Section 5.3.2, the extent to which the probe could be moved was limited.

There is virtually no information in the literature about beam damage to mineralised bone. Mineralised tissues were one of the first biological specimens to be examined by EDX since they seemed the least likely to be damaged by the electron beam. Bres et al (1984) noted that biological hydroxyapatite crystals retained a recognisable structure even after one hour of high resolution lattice imaging. It was the crystalline component of bone which was of most interest in this study since Al is believed to be bound to the crystals (Boyce et al 1981). It should be noted that during spectral acquisition, no change in the appearance of the specimen or in the X-ray count-rate was observed, i.e. obvious damage to the bone was not present. The effects of possible damage to the bone are discussed in Appendix 1.

5.3.4   Summary

Spectra were acquired at typically 1 μm intervals into the bone from the bone surface. The probe size was 0.26 μm. The HB5 was used to acquire spectra since the beam current (for this probe size) was higher, and the stray scattering contributions lower, than could be obtained using the JEM. Care was taken to orientate each specimen in the microscope so that there was always a clear path between the region of specimen analysed and the X-ray detector. Spectra were acquired for 20-25 min. To minimise radiation damage to the specimen, the probe was moved during spectral acquisition. Obvious damage to the specimens was not present.

5.4 MINERALISED BONE SPECTRUM

Figures 5.4a and b show a typical mineralised bone spectrum. The object of this work is the extraction and quantification of the trace element peaks overlapped by the major P peak. The theoretical bremsstrahlung distribution has been calculated from Equation 4.4 assuming that mineralised bone has a composition of 22.7% Ca, 51.0% O and 13.6% P (the atomic fractions of hydroxypatite). Detector absorption and specimen self-absorption corrections have been included in this calculation. It should be noted that the background under the trace element peaks is not due to bremsstrahlung alone. Figure 5.5 shows Ca and P fluoresced spectra scaled to the characteristic peaks in a mineralised bone spectrum. Clearly a large amount of the P peak underlies the trace element peaks. The shape of the P peak has been discussed in Section 4.2.4. Some possible techniques for extracting the trace element counts will now be considered.

Statham (1976) has suggested the following methods for processing spectra. "Frequency filtering" relies on the fact that the background is a more slowly varying function of energy than the characteristic peaks. The fourier transform of the spectrum is first calculated and the low frequency components of the spectrum are removed. Only the characteristic signals should remain when the inverse transform is calculated. Another method called the "iterative peak stripping procedure" removes the characteristic peak in stages until no peak can be observed above the background. Both these methods do not require a detailed knowledge of the background shape in the region where the peak appears. Consequently these methods are less well suited for use in the low energy region of the spectrum where the background changes rapidly, and in situations where peak overlap is significant (Statham,

32ϕϕϕ COUNTS

P(K)   Ca(Kα)

Ca(Kβ)

Cu (Kα)

2   4   6   8   1ϕ   12   14   16   18   2ϕ   keV
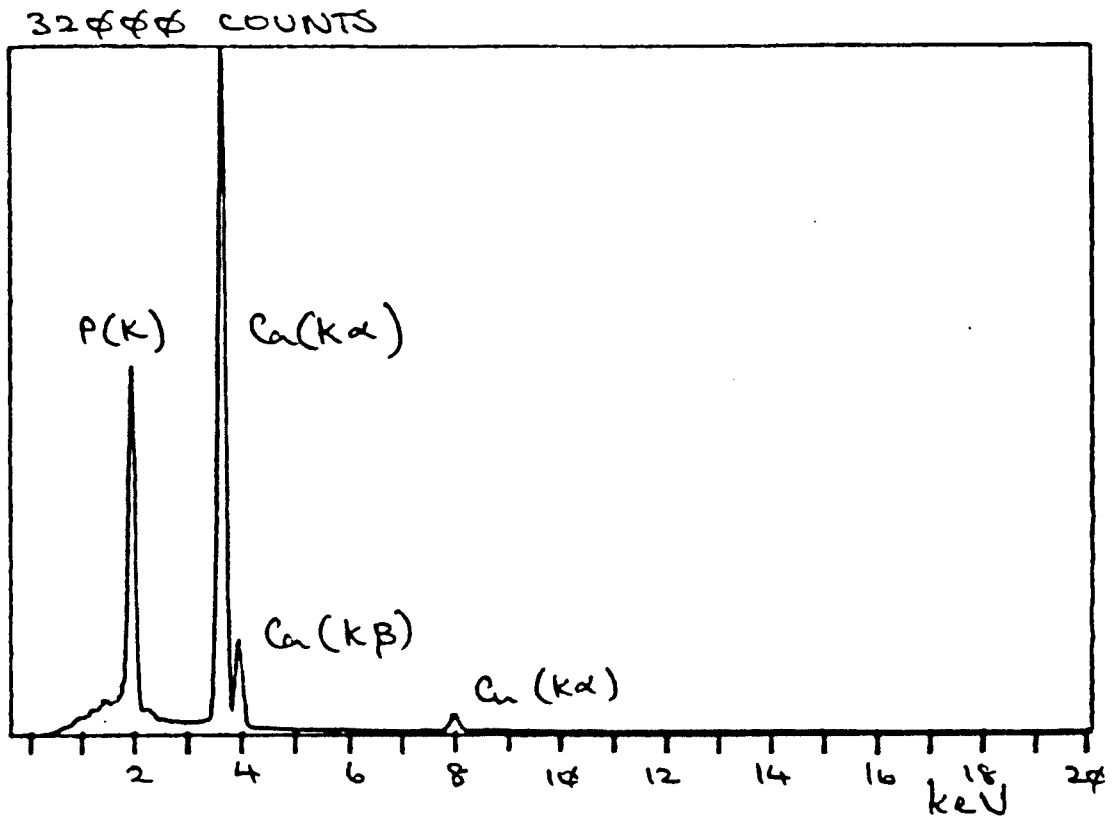
Figure 5.4(a) A typical MB spectrum. The Cu peak indicates the only bulk instrumental contribution.

2ϕϕϕ COUNTS

Al(K)   P(K)   Ca(K)

Hg(K)

S(K)

Na(K)

MBH HA + 9μm Be
+ ϕ.ϕ1μm Au
+ 15ϕϕ Å HA
(SELF-ABSORPTION)

2   4   6   8   keV 1ϕ
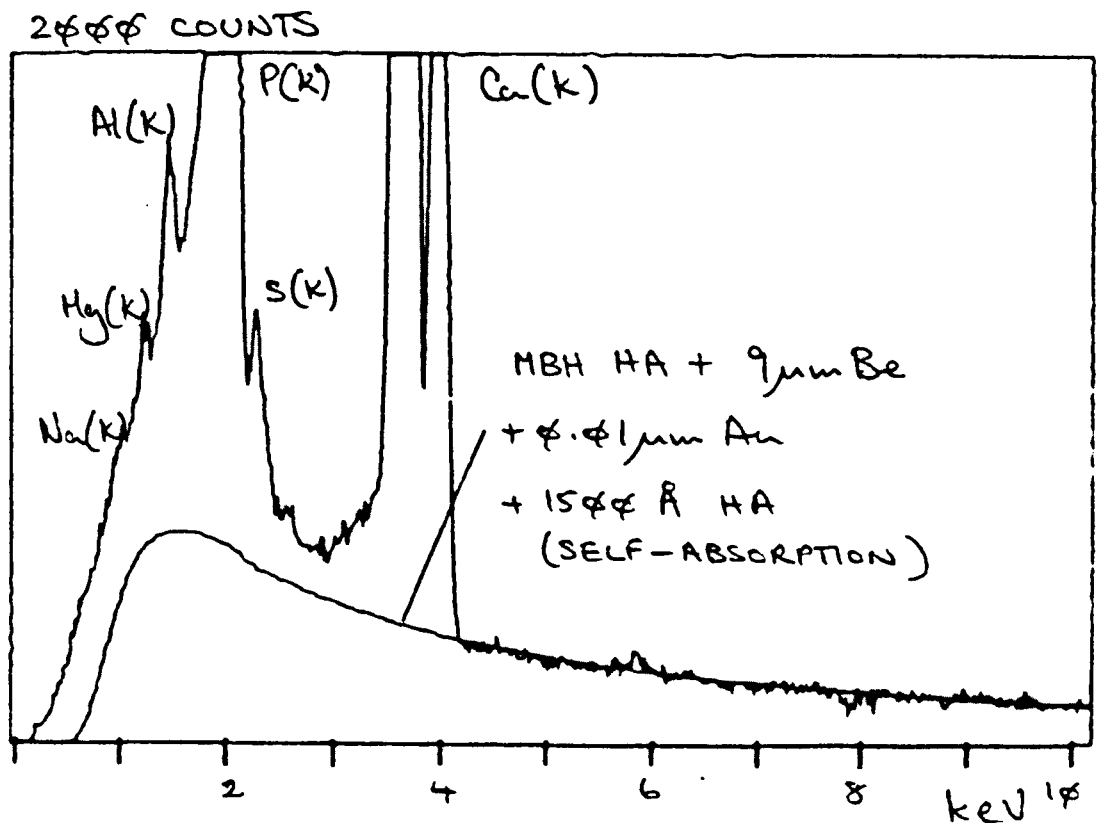
Figure 5.4(b) The bulk Cu contribution has been subtracted. The trace Na, Mg and Al signals are superimposed upon the P(K) low energy tail.
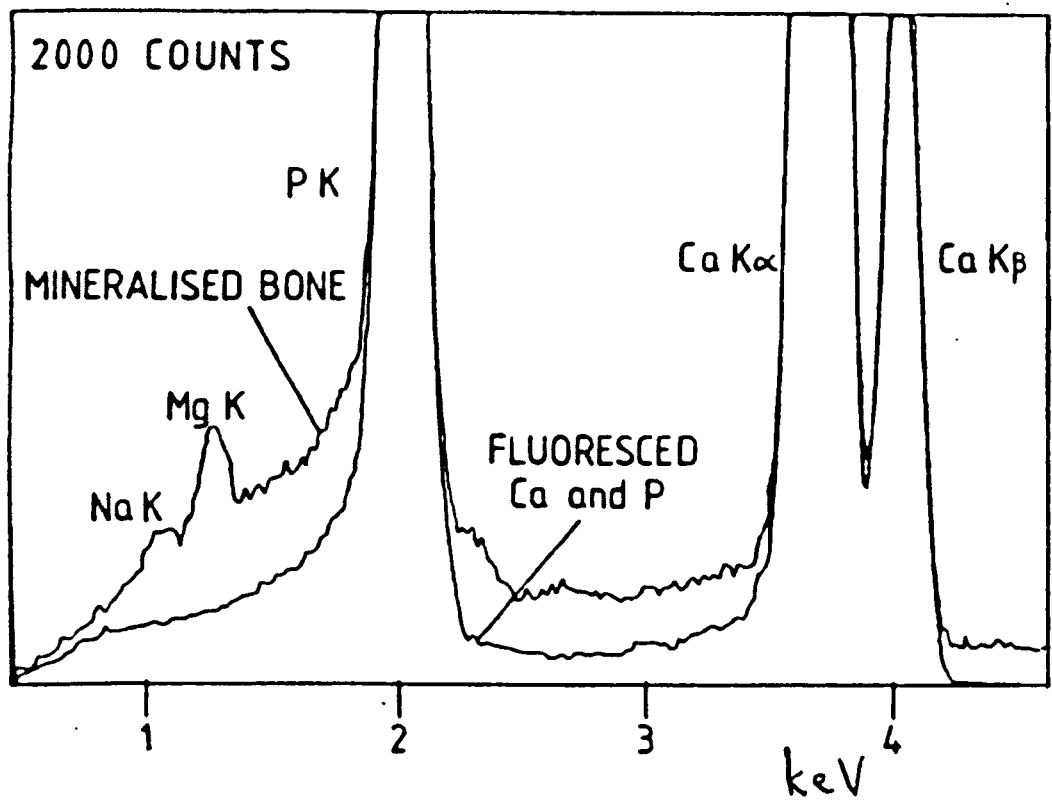
Figure 5.5 Ca and P fluoresced spectra scaled to the characteristic peaks in the MB spectrum.

1976). Thus, neither of these methods would appear to be particularly useful here. Most commercial spectrum analyser systems will perform an integration of the number of counts recorded in the peak by calculating a straight line background between two channels either side of the peak. This is usually sufficiently accurate for the extraction of counts in a large peak, but not for small overlapping peaks where there are no channels between the peaks (Nicholson et al 1980). The next Section describes the approach taken here to processing mineralised bone spectra.

5.5 SPECTRAL PROCESSING

Figure 5.6 shows the flow diagram of a program written to process the mineralised bone spectra so that the characteristic signals may be extracted. The program first subtracts the bulk Cu and the bremsstrahlung, then the Ca and finally the P peaks. Since the Al and Mg trace element peaks are superimposed upon the Ca and especially the P low energy tails, the accuracy of the subtraction of the Ca and P peaks is important. Statham (1981) suggests that it may be necessary to obtain about a 1 eV precision when attempting to extract trace element counts which are overlapped by a major characteristic peak. Since the mineralised bone spectra were acquired using a standard 20 eV/channel setting on the Link System computer, it was necessary to use an interpolation procedure to calculate peak alignment to better than 1 eV. Essentially, the fluoresced peak is aligned to one channel (20 eV) precision and scaled using the regions 3 and 4 shown in figure 5.7. A progressive series of peak shifts of less than 1/20 channel

1 Read in mineralised bone spectrum from disk.

2 Integrate gross counts I_G over regions 1 and 2 shown in figure 5.7

3 Scale and subtract bulk Cu contribution.

4 Scale and subtract theoretical bremsstrahlung distribution.

5 Calculate I_B under Ca and P peaks.

6 Subtract bremsstrahlung.

7 Scale and align Ca fluoresced spectrum, (using region 4, fig 5.7(a))

8 Integrate counts in fluoresced spectrum and subtract.

9 Scale and align P fluoresced spectrum, (using region 3, fig 5.7(a))

10 Integrate counts in fluoresced spectrum and subtract.

11 Integrate trace element counts P_x over regions 1 and 2 shown in figure 5.9 (The bremsstrahlung is assumed to be subtracted).

12 Calculate "statistical" uncertainty P_x^* in characteristic counts, $I_B = I_G - I_P$.

13 Output in the form of a table, P_x and P_x^*.

14 File to disk processed spectrum and scaled theoretical bremsstrahlung distribution for display on monitor.

Figure 5.6 Basic sequence of operations in processing a mineralised bone spectrum.
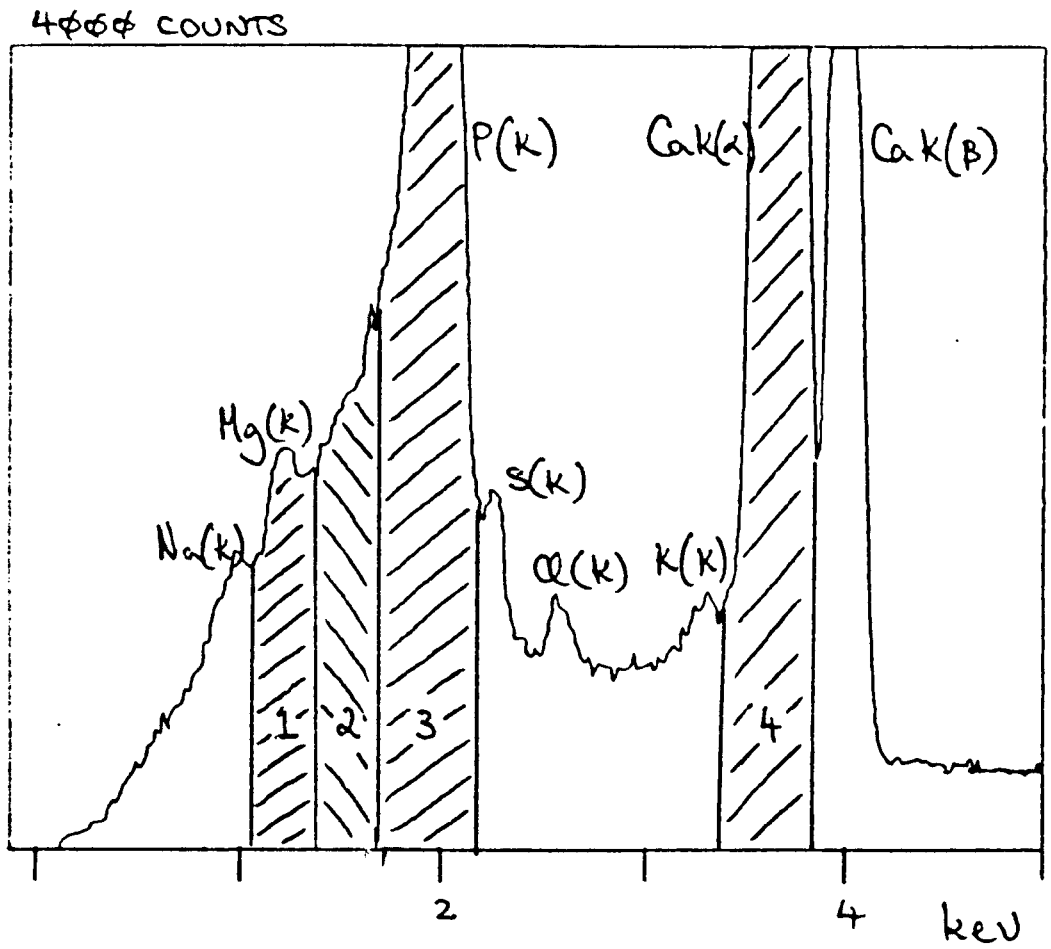
Figure 5.7(a) Energy regions defined in the MB spectrum.

(corresponding to shifts of <1 eV) are then calculated using an interpolation procedure, the optimum alignment of the peak being selected using a chi-square test (calculated over the same regions used for scaling the peaks). The peak alignment procedure is described in more detail in Section 5.6. A second fine rescaling of the fluoresced peak is performed and the peak is subtracted. This peak subtraction procedure was found to provide adequate results, and Figures 5.8a and b show an artificial mineralised bone spectrum which has been processed in this way. The artificial mineralised bone spectrum was made by adding Ca and P fluoresced peaks to a theoretical background. Difficulties were found in processing real mineralised bone spectra and these will be discussed in Section 5.7. The flow diagram also indicates how the counts are extracted from the spectrum during processing. The number of Ca and P characteristic counts is obtained by integrating over the scaled Ca and P fluoresced peaks before subtraction. Thus, counts which are lost from the central region of the peak by incomplete charge collection (and the escape peak), some of which underlie other peaks, are taken into account. The final number of counts in the residual trace element peaks is obtained by integrating over the regions 1 and 2 shown in Figure 5.9. (The bremsstrahlung distribution indicated is assumed to be subtracted).

Clearly some characteristic Al and Mg counts will be outside regions 1 and 2 due to incomplete charge collection. An estimation of those counts can be obtained from fluoresced Al and Mg spectra (see Figure 5.7(b)). To allow for these lost counts any Mg counts extracted from region 1 have to be multiplied by 1.13, and any Al counts extracted from region 2 have to be multiplied by 1.05. There is negligible uncertainty in these values which are included in the k factors (see
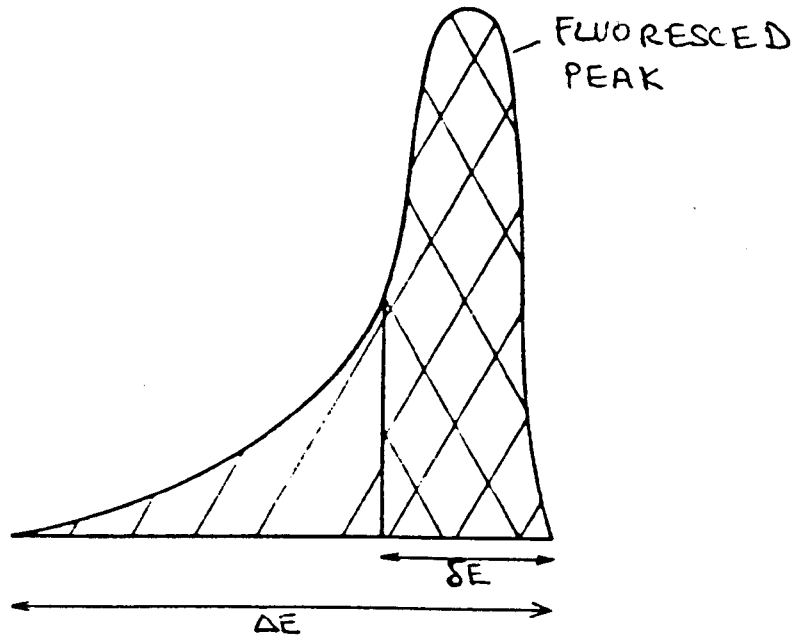
Figure 5.7(b) δI counts in energy region δE
                ΔI counts in energy region ΔE

Multiplying factor (m) defined as $\Delta I / \delta I$

$m_{Mg} = 1.13$ $m_{Al} = 1.05$
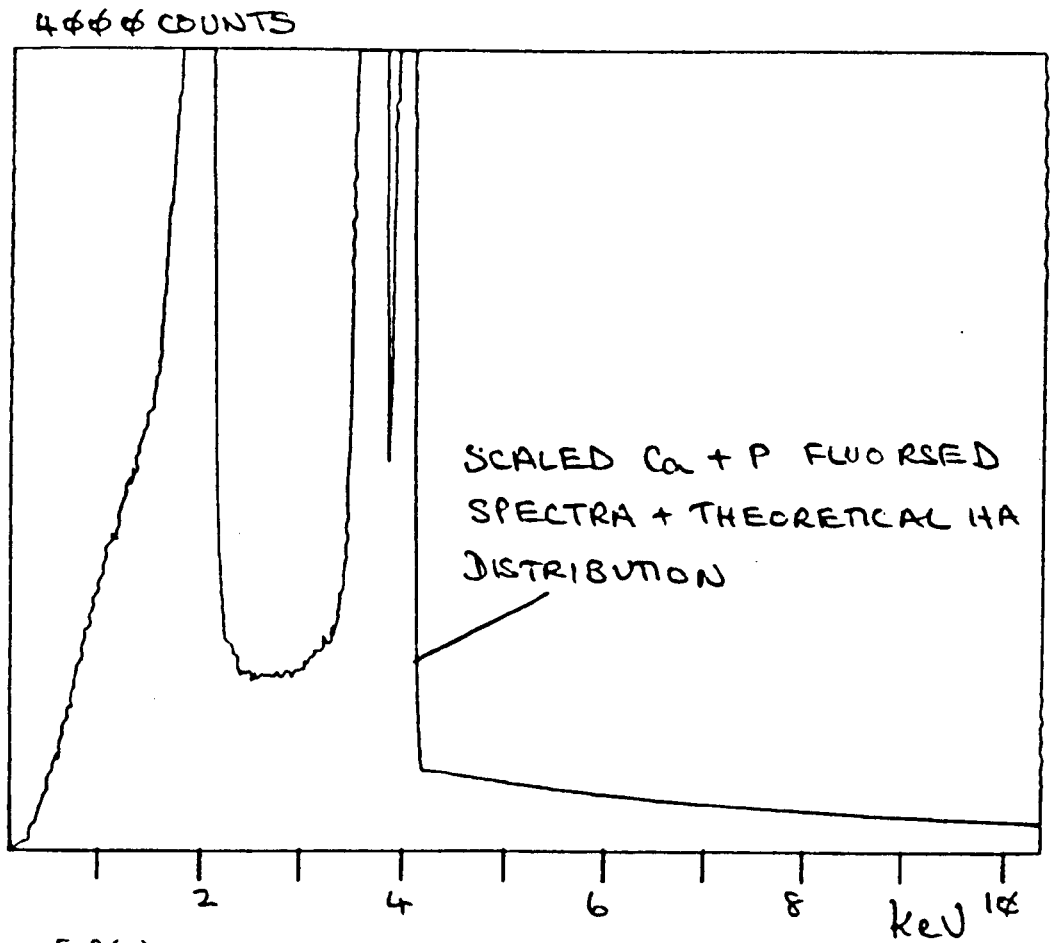
Figure 5.8(a)
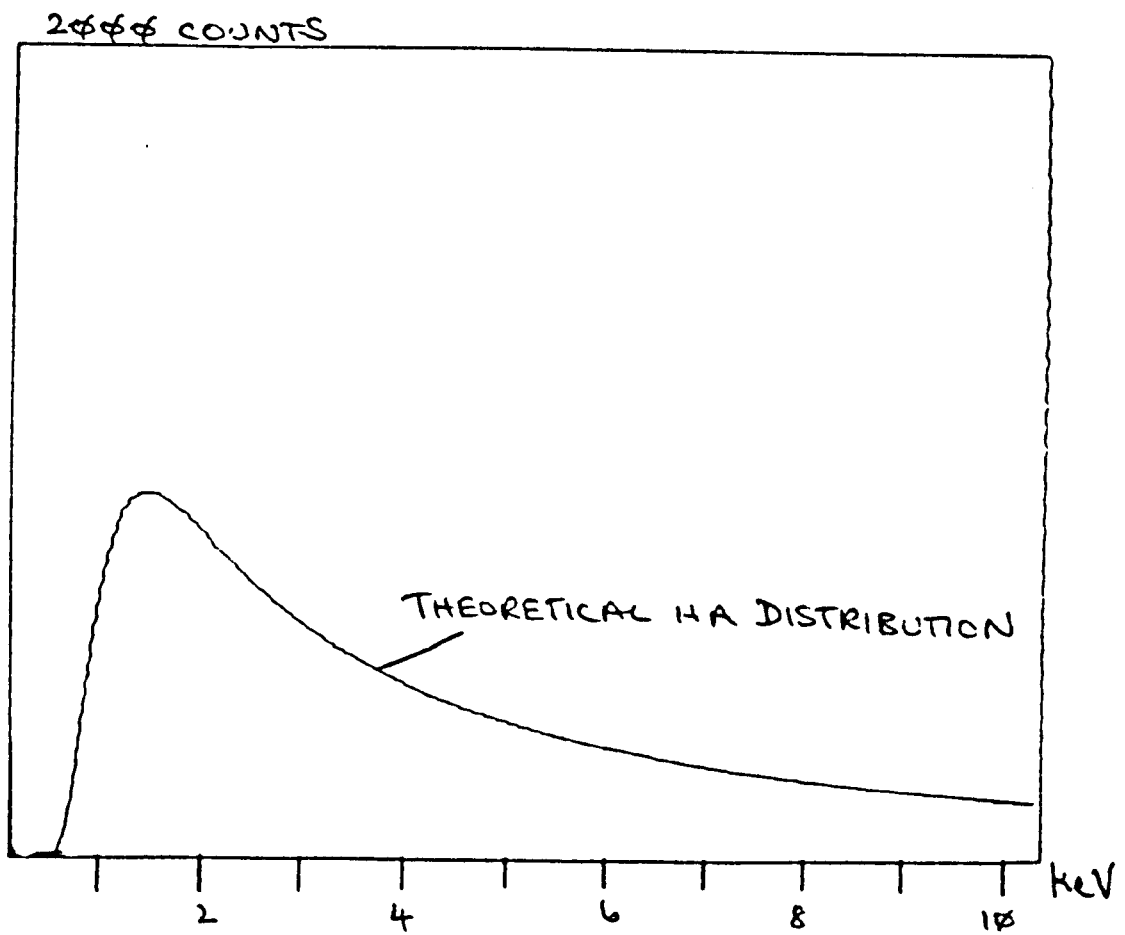
Figure 5.8(b) Ca and P fluoresced peaks subtracted from the artifical MB spectrum. No residual counts from the Ca and P peaks are present.
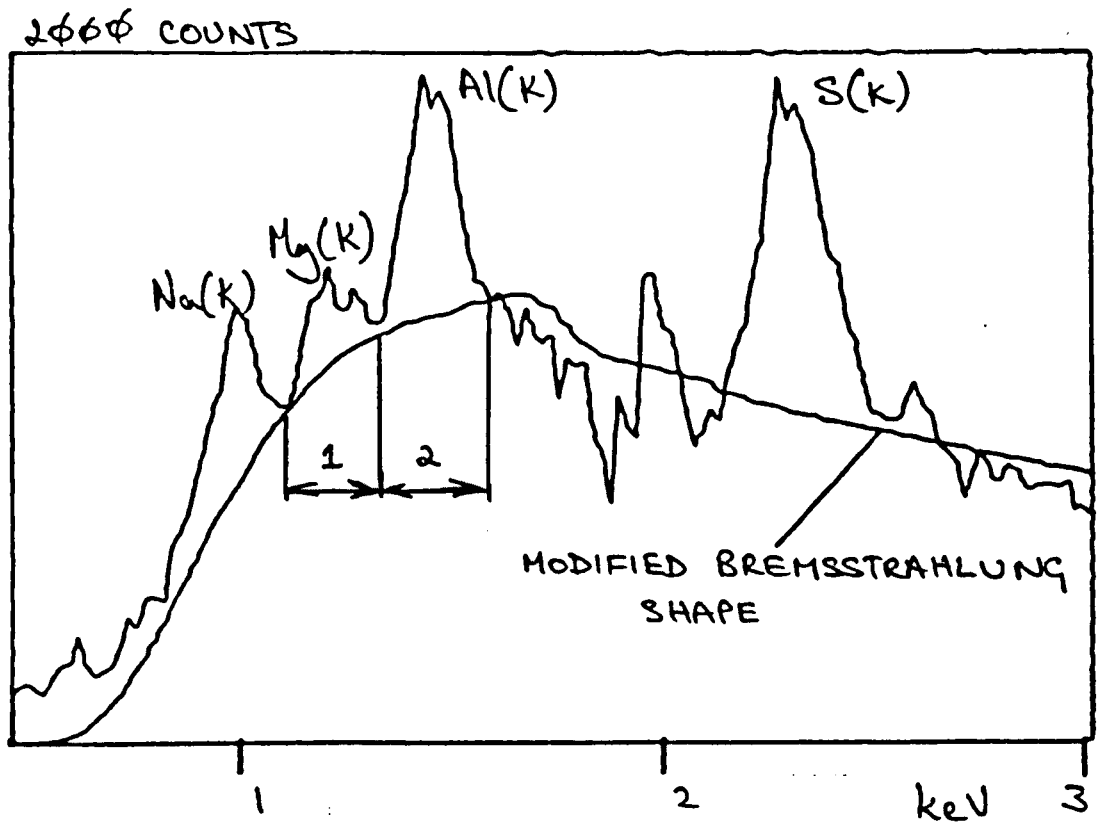
Figure 5.9 A typical MB spectrum after processing. The modified bremsstrahlung shape is discussed in section 5.7.1.

Section 5.10) used for transforming the characteristic intensity ratios to atomic ratios. The number of Al counts under the Mg peak is always less than 2% of the total Al signal and is generally insignificant compared to the other uncertainties involved in optimising the fit of the theoretical background beneath the Mg peak.

The uncertainty P_x in the integrated number of characteristic counts P_x can be calculated from the following equation (Zaluzec,1981).

$$\Delta P_x^S = \sqrt{P_x + h\,I_B}$$ 5.1

where I_B is the number of counts in the background and h is a constant. In the case of a spectrum consisting of a peak superimposed upon a background which can be estimated on both sides of the peak, Zaluzec (1981) suggests that $h \doteqdot 2$ is appropriate. This is adequate for determination of the "statistical" uncertainty in the large Ca and P signals; however, the total uncertainty in the trace element signals will be underestimated due to uncertainties in the spectral processing. Section 5.8 describes how an attempt was made to estimate this additional uncertainty.

5.6   PEAK ALIGNMENT

Figure 5.10 shows the effect of subtracting a slightly misaligned peak (shown dashed). The small spike labelled T indicates a trace element peak. If the alignment of the peak is not optimum (shown in Figures 5.10(a) and (c)) then the number of counts in a trace element

64
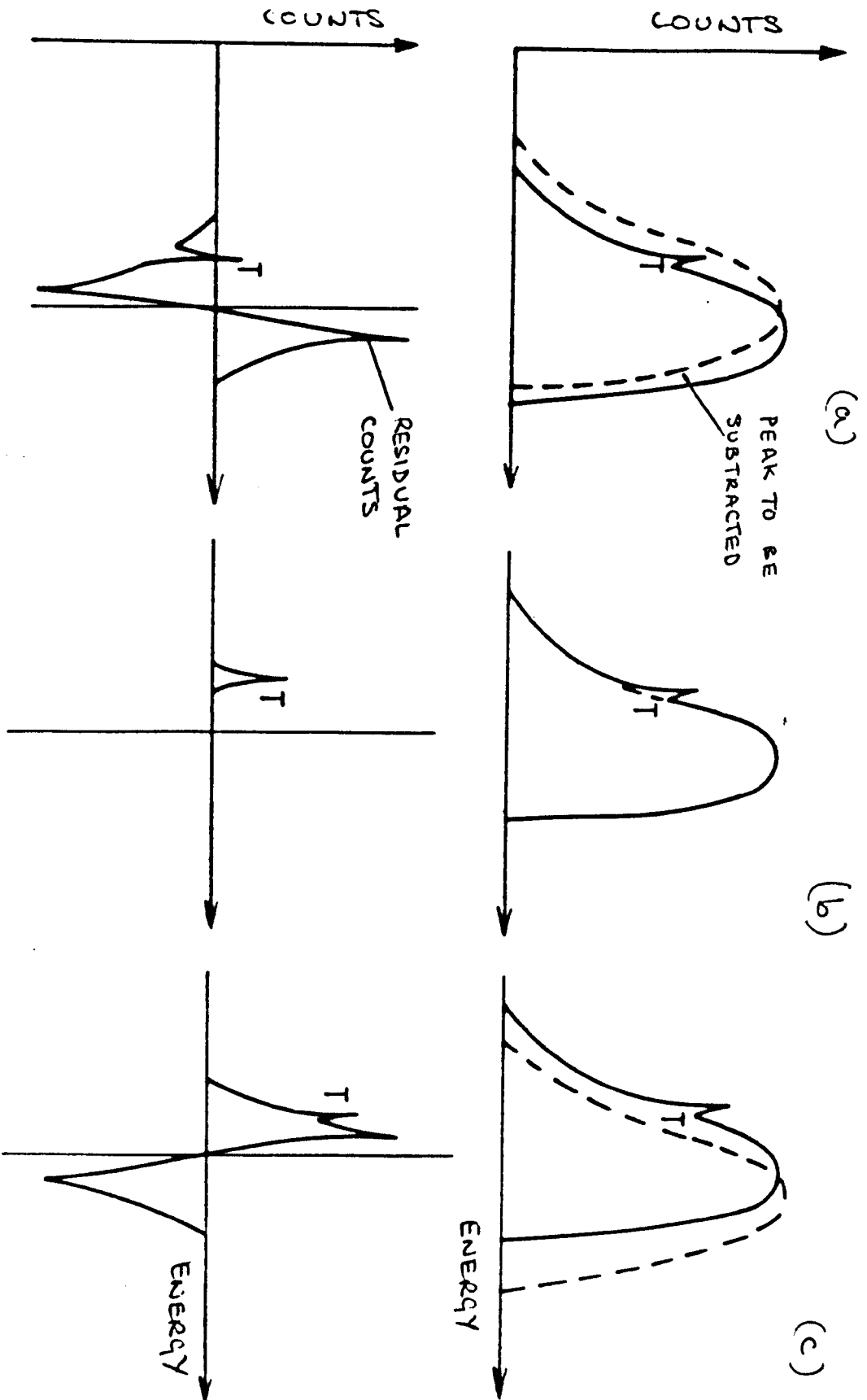
Figure 5.10   The residual counts for each alignment are indicated. The optimum alignment is in (b). In (a) the trace element counts would be underestimated, and in (c) they would be overestimated.

peak will be under or over estimated.

The simplest method of shifting a peak less than one channel can be described as follows. Figure 5.11 shows a schematic diagram of a region of a characteristic peak with $f(x_i)$ counts in channel x_i, $f(x_{i-1})$ counts in channel x_{i-1} etc. To calculate a peak shift of less than one channel, a constant k can be defined. i.e.

$$k = \frac{x - x_i}{x_i - x_{i-1}}$$

where $x < x_i$, is a constant, and k is negative if the peak is to be shifted to the right hand side. The number of counts $P(x_i)$ in channel x_i of the shifted peak can then be calculated from

$$P(x_i) = f(x_i) + k\left[f(x_i) - f(x_{i-1})\right]$$

and the counts for the other channels in the shifted peak calculated in a similar manner. This equation produces a shift because, (assuming k is a negative) $kf(x_{i-1})$ counts are subtracted from channel x_{i-1} and added to channel x_i, $f(x_i)$ counts are subtracted from channel x_i and added to channel x_{i+1} etc. To the left of the peak maximum more counts are typically transferred out of a channel than in. To the right of the peak maximum more counts are typically transferred into a channel than out. Therefore the peak shift is the nett effect of these transfer of counts. The above equation is the equation of a straight line; therefore, the unshifted peak is modelled as a series of straight lines. Clearly it should be more realistic to model the peak by a series of curves.
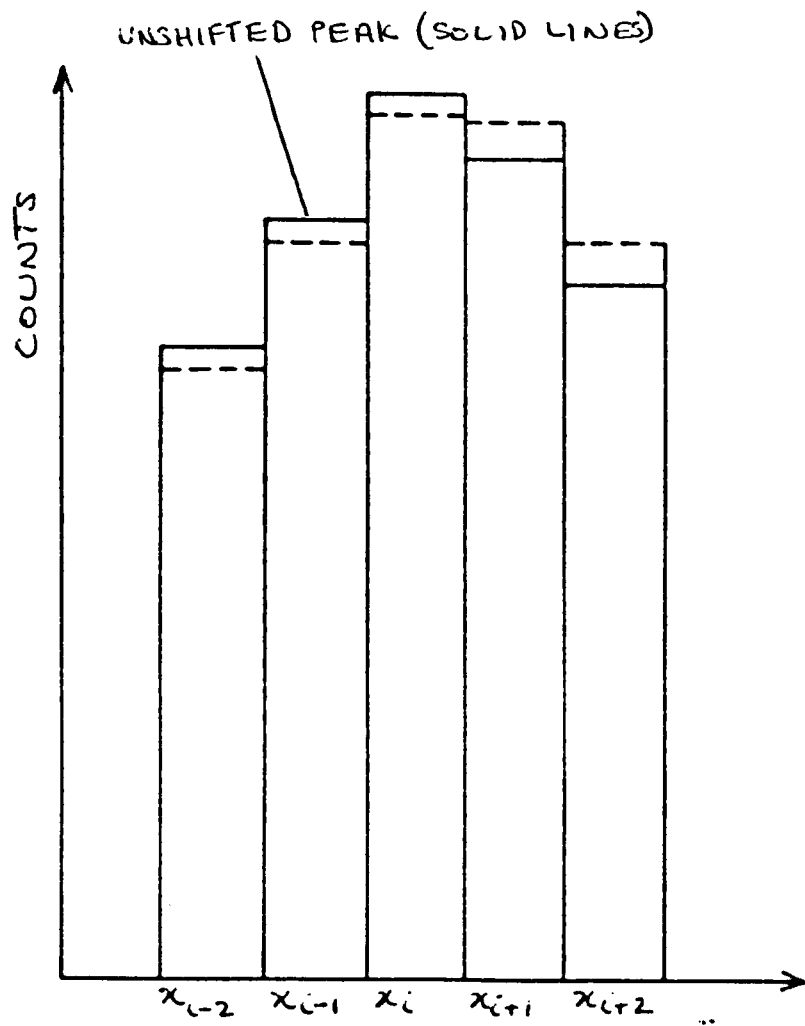
Figure 5.11   Unshifted peak f(x), shifted peak p(x).

The method that was used in practice was based on the Lagrange equation (e.g. Phillips et al 1973) of the form

$$P(x_i) = \sum_{i=i-2}^{i=i+1} k f(x_i)$$

where

$$k = \prod_{\substack{j=i-2 \\ j \neq i}}^{j=i+1} \left(\frac{x_i' - x_j}{x_i - x_j} \right)$$

and   is a constant.   To shift the peak, four points (e.g. x_{i-2} to x_{i+1}) are selected and $P(x_i)$ calculated.   Then the next four points (x_i-1 to x_i+2) are read in and $P(x_i+1)$ calculated.   However, it was later found that there was no practical advantage in using a series of curves to model a peak (since the peak looked identical after using either method).   Since the linear method is simplest it should be considered best for future work.

5.7   PRACTICAL PROCESSING OF MINERALISED BONE SPECTRA

Three factors are considered here; the self-absorption correction, the effect of incomplete charge collection on the bremsstrahlung and subtraction of the bulk Cu   contribution.

5.7.1   Optimising the Fit of the Theoretical Bremsstrahlung in the Low Energy Region

Figure 5.12a shows how the self-absorption correction was estimated for each spectrum.   The optimum fit to the spectrum lies within the curves calculated with self-absorption corrections for specimen thicknesses of 1000Å and 2000Å.   (The two theoretical bremsstrahlung

66

2000 COUNTS

Mg(K)

Na(K)

S(K)

Cl(K)

RESIDUAL P COUNTS

MBH HA + 9μm Be + 0.01μm Au
+ 1000 Å HA

MBH HA + 9μm Be + 0.01μm Au
+ 2000 Å HA

1   2   keV   3
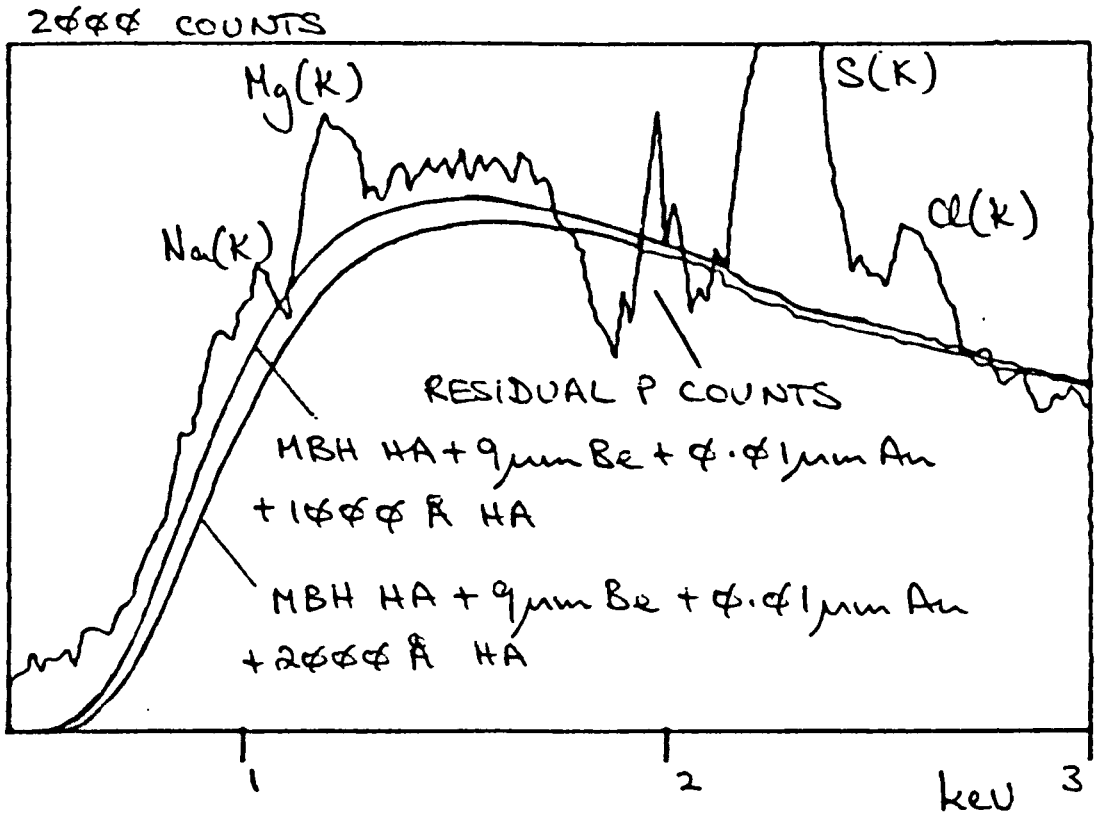
Figure 5.12(a)   The P (and Ca) peaks have been subtracted. (The spectrum was acquired from a control sample).

2000 COUNTS

Mg(K)

Na(K)

S(K)

Cl(K)

RESIDUAL COUNTS

MBH HA + 9μm Be + 0.01μm Au
+ 1500 Å HA

1   2   keV   3
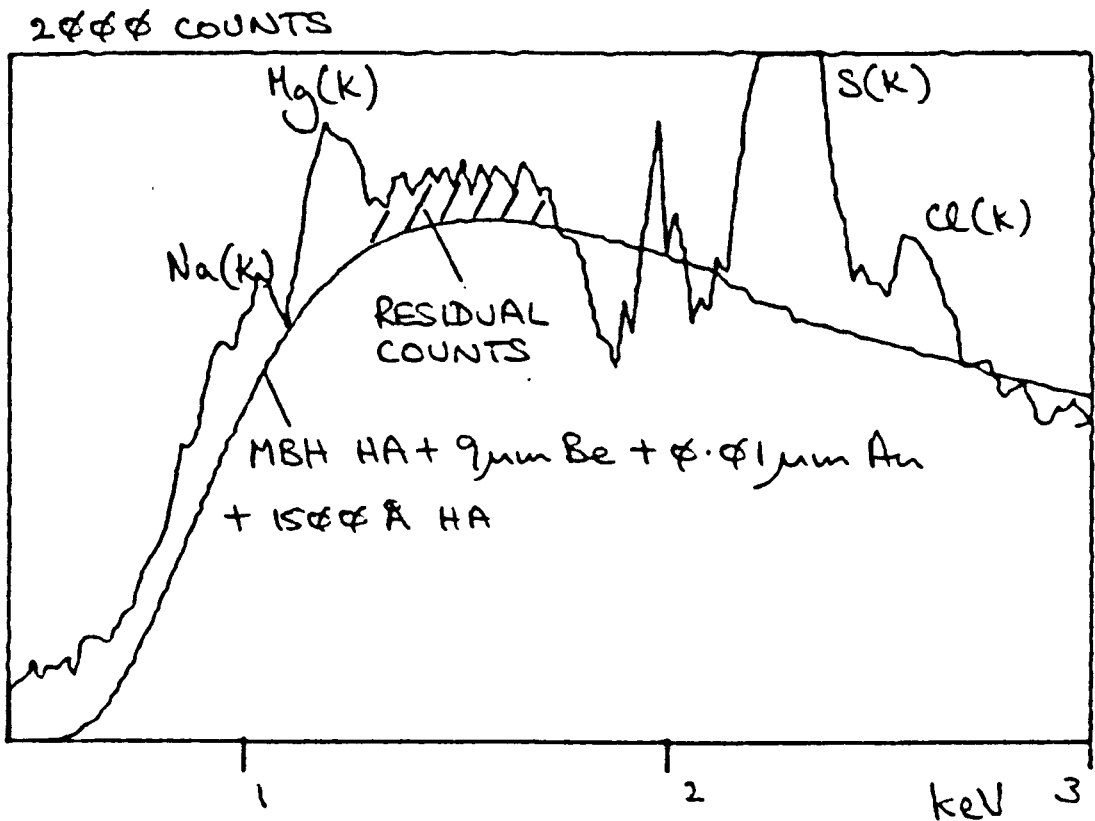
Figure 5.12(b)   The optimum fit to the spectrum. Residual counts are still present in the Al peak region.

curves can be superimposed since the shape of the mineralised bone spectrum is virtually identical after processing with either curve). The optimum fit to the spectrum (judged visually) is shown in Figure 5.12b and the corresponding uncertainty in the specimen thickness was estimated to be 1500± 500Å. Virtually all of the control and experimental sample spectra could be processed without changing the self-absorption correction much from 1500Å. This suggests that the precautions taken to experimentally minimise the variations in self-absorption (see Section 5.3.2) were successful. This typical self-absorption correction is in agreement with the nominal specimen thickness of 1500Å.

The majority of the background under the trace element peaks can be removed by the method described above; however, in Section 4.2.4 it was noted that incomplete charge collection in the detector distorts the bremsstrahlung in the low energy region. In particular, Figures 4.6 and 4.8 show two formvar spectra where there is a significant build up of counts above the theoretical bremsstrahlung shape. After processing all the spectra acquired from the "control" samples, (which are not expected to contain Al), it was clear that there were always residual counts above the optimum theoretical bremsstrahlung shape in the Al peak region (see Figure 5.12b). These residual counts were assumed to be due to the effect of incomplete charge collection on the bremsstrahlung (see Section 4.2.4); i.e. they are not Al counts. Clearly, if experimental sample spectra were processed, the Al counts would be overestimated. Therefore, an attempt was made to model the bremsstrahlung empirically with a "bump" to take account of these bremsstrahlung counts. Figure 5.12c shows the result of this modeling. This bump was not allowed to vary from spectrum to spectrum. Figures

67

2000 COUNTS
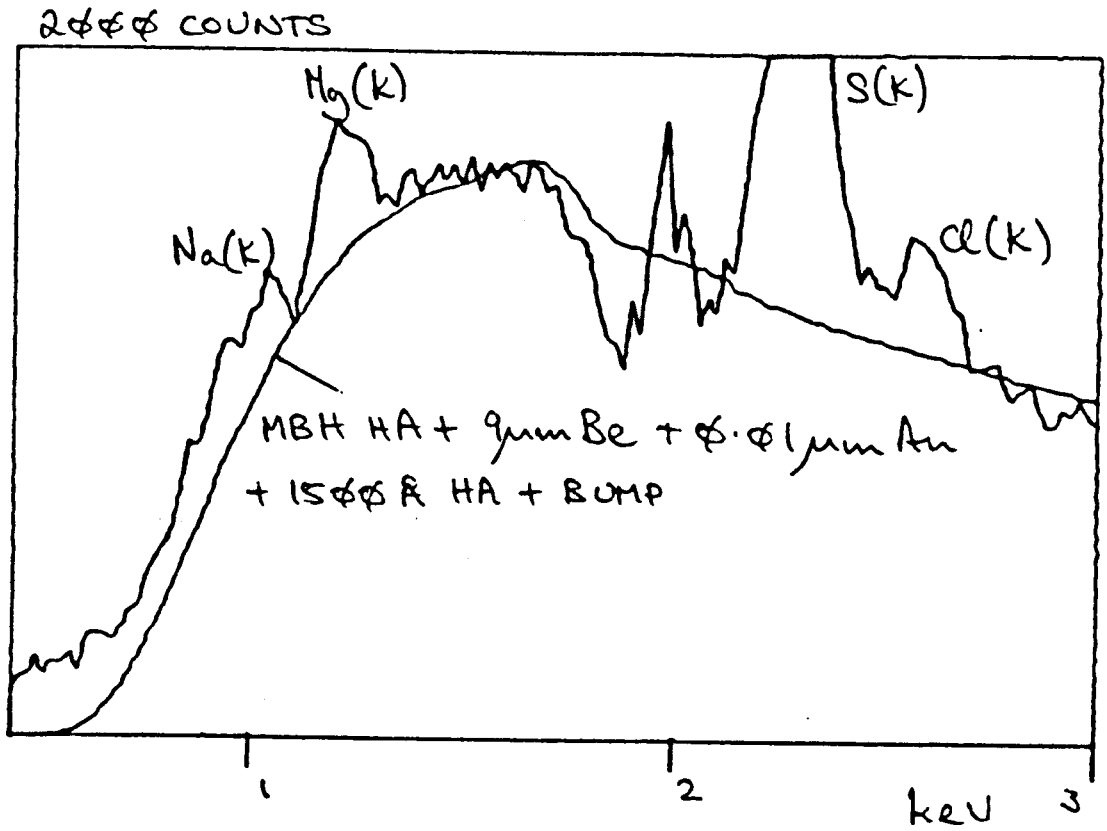
Figure 5.12(c) (Control sample spectrum.)

5.13a to 5.14c show some control and experimental sample spectra after processing. Difficulties arose when a self-absorption correction was required for a specimen thickness of other than 1500Å. The residual counts in the Al peak region are assumed to be due to a build up of counts from higher energies (where variations in self-absorption are much less significant). Thus the bremsstrahlung curves with different self-absorption corrections were modified (with the bump) assuming that the ratio of the counts in the bump to a given region of mid-energy bremsstrahlung was a constant. Figure 5.13b shows a spectrum with a self-absorption correction for 2000Å of hydroxyapatite and clearly an acceptable fit has been obtained.

5.7.2 Bulk Cu Subtraction

As stated in Section 5.3.1, it was more difficult to extract the trace element counts in mineralised bone spectra which contained a significant bulk Cu contribution. Such spectra had typically been acquired from regions of the specimen near the Cu single hole mount. The method for removing the bulk contribution to a spectrum (described in Section 4.2.2) assumes that the bulk spectrum recorded when the beam is directed onto bulk material is the same as that generated by stray electrons, some of which are scattered through wide angles and have energies less than the primary beam. Clearly this is an approximation. In some preliminary spectra (which had a large bulk Cu contribution) the fit in the low energy region was not as good as might be expected. In these cases changing the amount of bulk Cu subtracted by a few per cent improved the fit. It was therefore very difficult to process these spectra. Virtually all of the concentration ratios discussed in this

2000 COUNTS

Na(k) Mg(k) Si(k) S(k) Cℓ(k)

MBH HA + 9μm Be + 0.01μm Au
+1500 Å HA + BUMP

1   2   keV 3
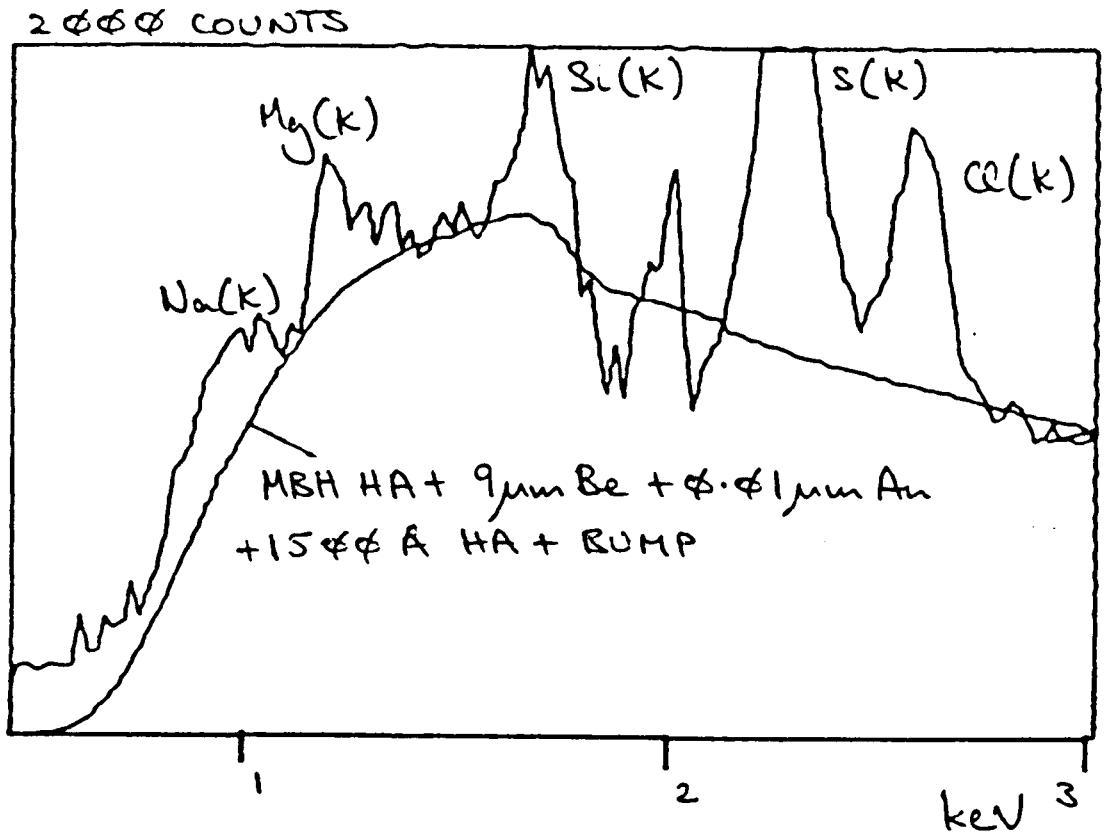
Figure 5.13(a) Control sample spectrum.

2000 COUNTS

Na(k) Mg(k) S(k)

MBH HA + 9μm Be + 0.01μm Au
+2000 Å HA + BUMP

1   2   keV 3
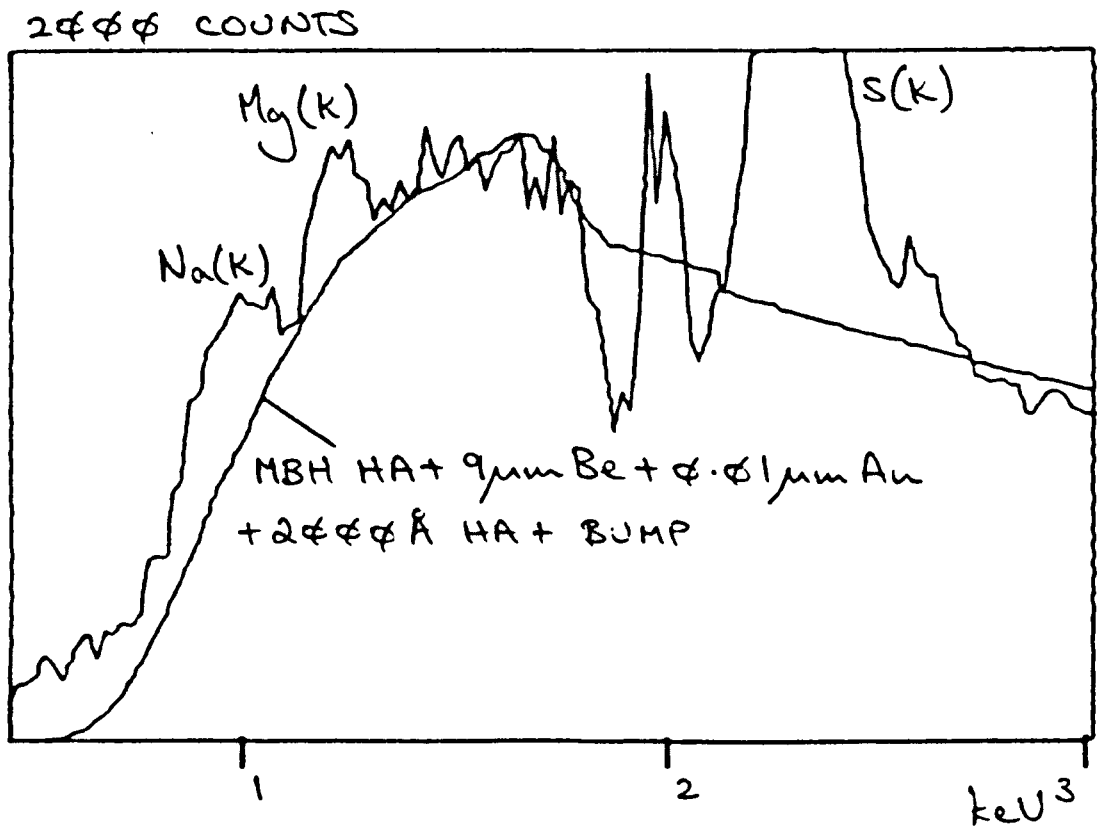
Figure 5.13(b) Control sample spectrum.
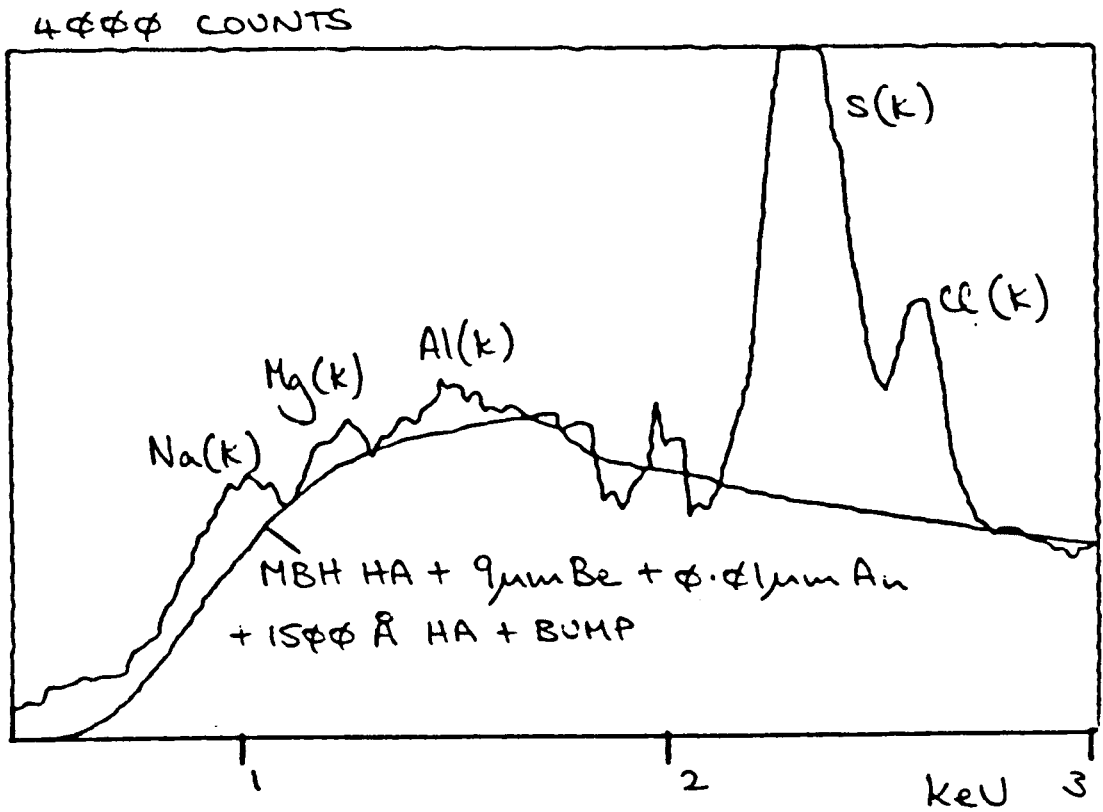
Figure 5.14(a)   Experimental sample spectrum.
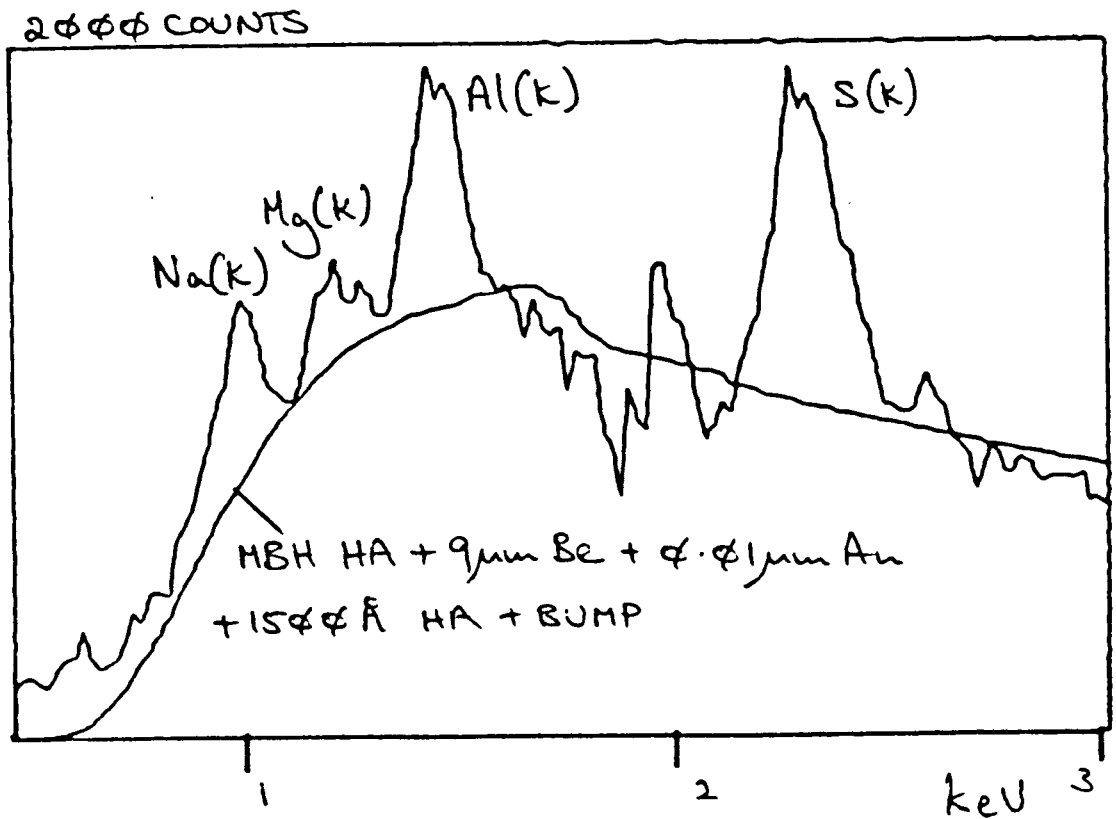
Figure 5.14(b)   Experimental sample spectrum.

2ØØØ COUNTS

Al(k)

S(k)

Mg(k)

Na(k)

Cl(k)

MBH HA + 9μm Be + Ø·Ø1μm Au
+ 15ØØ Å HA + BUMP

1   2   keV   3
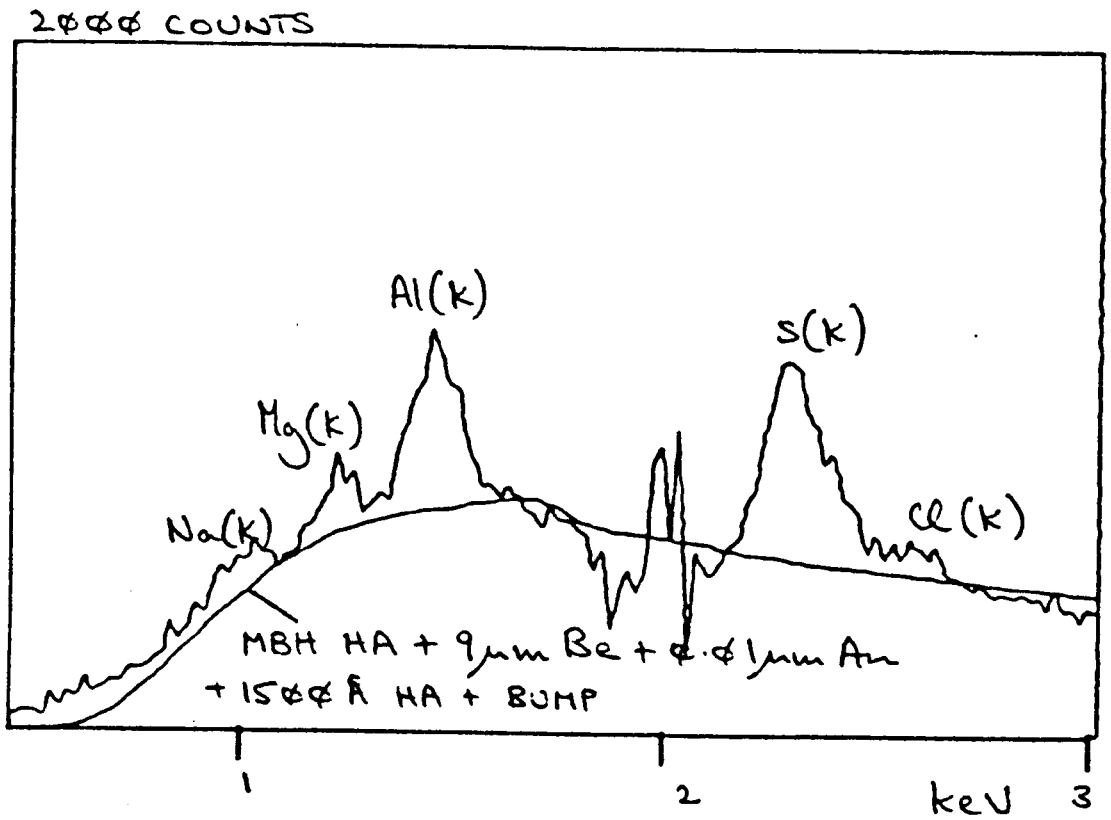
Figure 5.14(c)   Experimental sample spectrum.

Chapter and Appendix 1 have been obtained from spectra with a negligible bulk Cu contribution. Figure 5.15 shows a typical spectrum (before processing) with a bulk Cu spectrum scaled to the mineralised bone spectrum peak. Clearly there is very little bulk bremsstrahlung present.

5.8   STATISTICAL AND SPECTRAL PROCESSING UNCERTAINTIES

Two types of uncertainty will be considered here; "statistical" and those due to the limitations of the spectral processing technique. The statistical uncertainty $\Delta(P_x/P_y)^s$ can be expressed as

$$\frac{\Delta(P_x/P_y)^s}{P_x/P_y} = \left[\left(\frac{\Delta P_x^s}{P_x}\right)^2 + \left(\frac{\Delta P_y^s}{P_y}\right)^2 \right] \qquad 5.2$$

where ΔP_x^s and ΔP_y^s are the statistical uncertainties (defined by equation 5.1) in the individual signals. The uncertainties in the Ca/P intensity ratios were typically much less than 1% and therefore negligible. In addition, the Ca/P ratios were found to be independent of relatively minor variations in the estimation of the bremsstrahlung (due for example, to varying the self-absorption correction, and the addition of the bump). This was not the case with the trace Al and Mg signals although figures 5.12c to 5.14c show that a reasonably good fit to the experimental bremsstrahlung can be obtained. The apparent Al/Ca count ratios (obtained from processing all the control sample spectra) always lay in the range $\pm 0.8 \times 10^{-3}$. The experimental sample spectra were recorded under similar experimental conditions, contain approximately the same number of total counts, and were processed in an

69
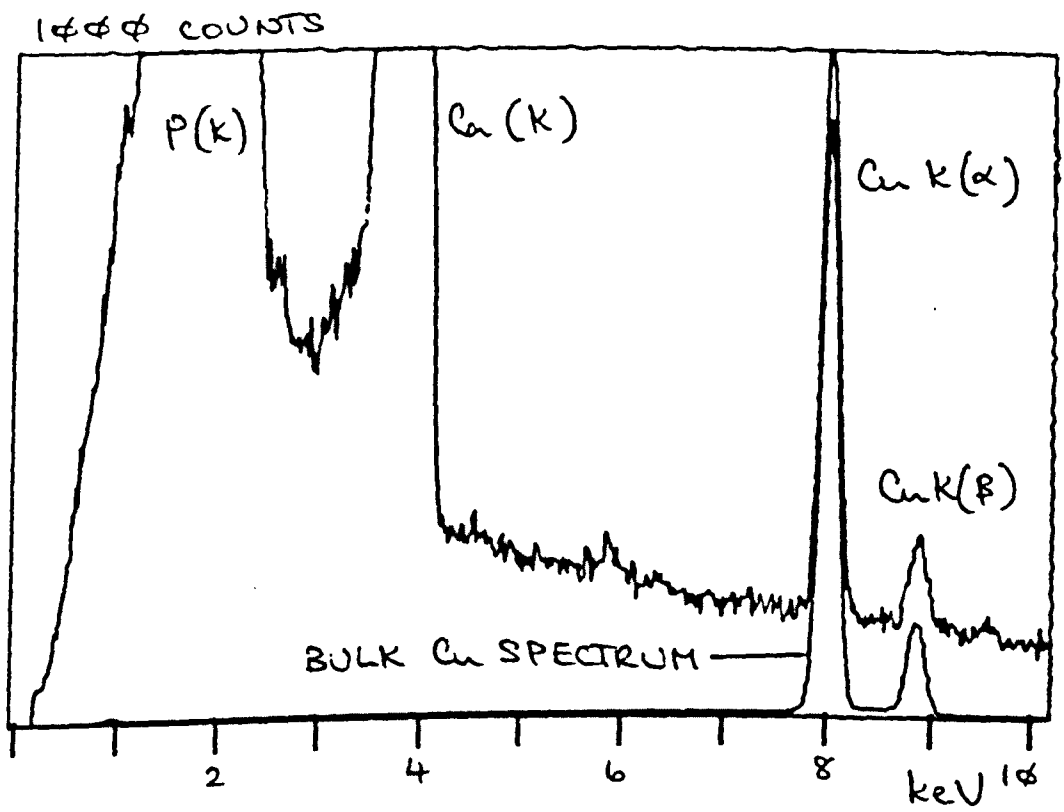
Figure 5.15

identical fashion. Thus an Al/Ca count ratio of less than 0.8×10^{-3} obtained from an experimental sample spectrum has doubtful validity.

Another indication of the spectral processing uncertainty was obtained. Upper and lower limits on the trace Al and Mg signals were estimated by allowing the self-absorption correction to the bremsstrahlung to vary about the optimum correction. Figure 5.16 shows two bremsstrahlung curves superimposed upon a processed control sample spectrum. In this case the lower limit for the trace counts was estimated using the bremsstrahlung curve with the correction for 1000Å of hydroxyapatite, and the upper limit estimated from the curve with the 2000Å corrections. The upper and lower Al/Ca count ratios differed from the optimum Al/Ca ratio by typically $\pm 1 \times 10^{-3}$ (in both control and experimental sample spectra). This range of Al/Ca ratios ($\pm 1 \times 10^{-3}$) is slightly larger than the range of apparent Al/Ca count ratios obtained from the control sample spectra (from 0.8×10^{-3} to 0.4×10^{-3}) and is due to the difficulty found in estimating the self-absorption correction to a spectrum to better than ± 500Å.

For the reasons described, $\pm 1 \times 10^{-3}$ is a good estimate of the uncertainty in the Al/Ca ratios due to spectral processing. The corresponding estimate for the uncertainties in the Mg/Ca ratios is about $\pm 1.2 \times 10^{-3}$ and is slightly larger than the value obtained for the Al/Ca ratios. An estimate of the total uncertainty in the Al/Ca and Mg/Ca ratios can be obtained from

$$\Delta\left(P_x/P_{Ca}\right)^T = \left[\left[\Delta\left(P_x/P_{Ca}\right)^S \right]^2 + \left[\Delta\left(P_x/P_{Ca}\right)^E \right]^2 \right]^{\frac{1}{2}}$$

where $\Delta(P_x/P_{Ca})^E$ is the uncertainty due to spectral processing.

2φφφ COUNTS

Mg(k)

S(k)

Na(k)

Cl(k)

MBH HA + 9μm Be + φ·φ1μm Au
+ 1φφφ Å HA + BUMP

MBH HA + 9μm Be + φ·φ1μm Au
+ 2φφφ Å HA + BUMP

1   2   keV   3
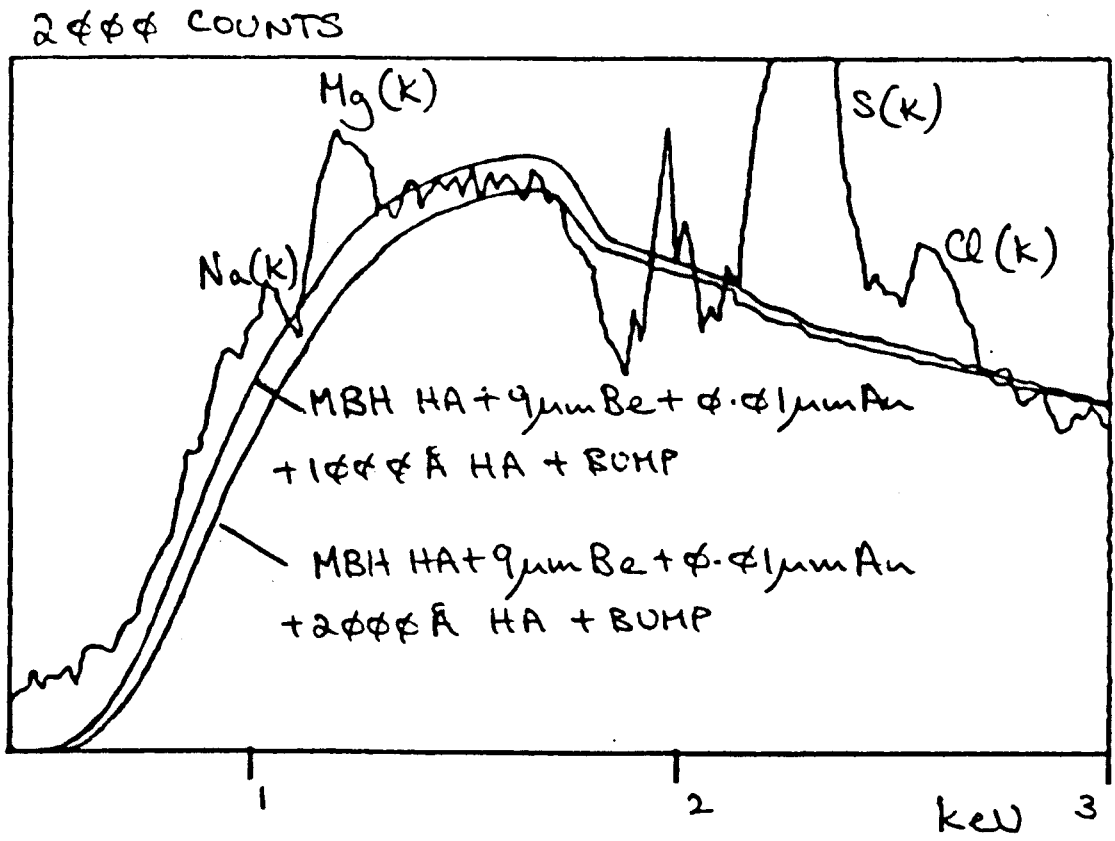
Figure 5.16

Figures 5.17a to 5.17e show a number of Al/Ca and Mg/Ca count ratios plotted against distance into the bone, from the bone surface. (The atomic ratio scales on the right hand side of the graphs will be discussed in Section 5.12). The statistical uncertainty $\Delta(P_x/P_y)^S$ is indicated by the error bars. The estimate of the total uncertainty $\Delta(P_x/P_y)^T$ in the ratios is indicated by the dots either side of the error bars.

The minimum detectable signal corresponds to the detection of a significant X-ray signal above the background. Since the total uncertainty in the Ca signal was always negligible, a criterion for detectability can be defined as

$$\frac{P_x}{P_{Ca}} > 3 \Delta \left(\frac{P_x}{P_{Ca}}\right)^T \qquad\qquad 5.3$$

Most of the residual Al/Ca ratios from the control sample spectra did not satisfy Equation 5.3, whilst virtually all of the Al/Ca count ratios obtained from the experimental samples did satisfy Equation 5.3. In Figure 5.17a to 5.17e, points indicated as ( ) do not satisfy equation 5.3 and the Al concentrations are below the level of detectability.

5.9 SUMMARY

Significant problems exist when attempting to extract trace Al and Mg counts from mineralised bone spectra. Essentially these are due to the extensive overlap between the major P peak and the trace element peaks. In addition, the bremsstrahlung background at these trace peak energies is changing rapidly due to absorption in the detector and
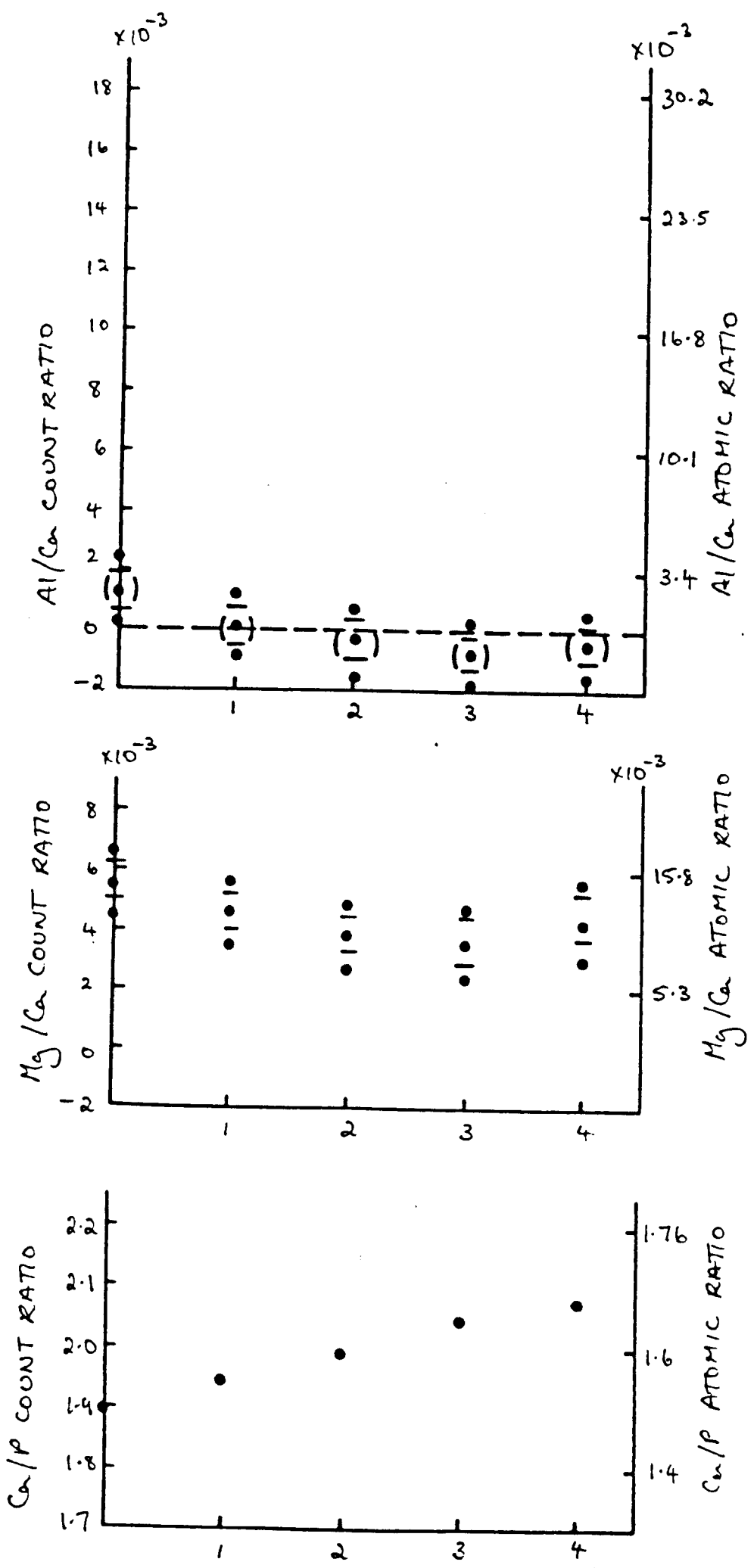
FIGURE S.17a CONTROL SAMPLE 1 (84/101)
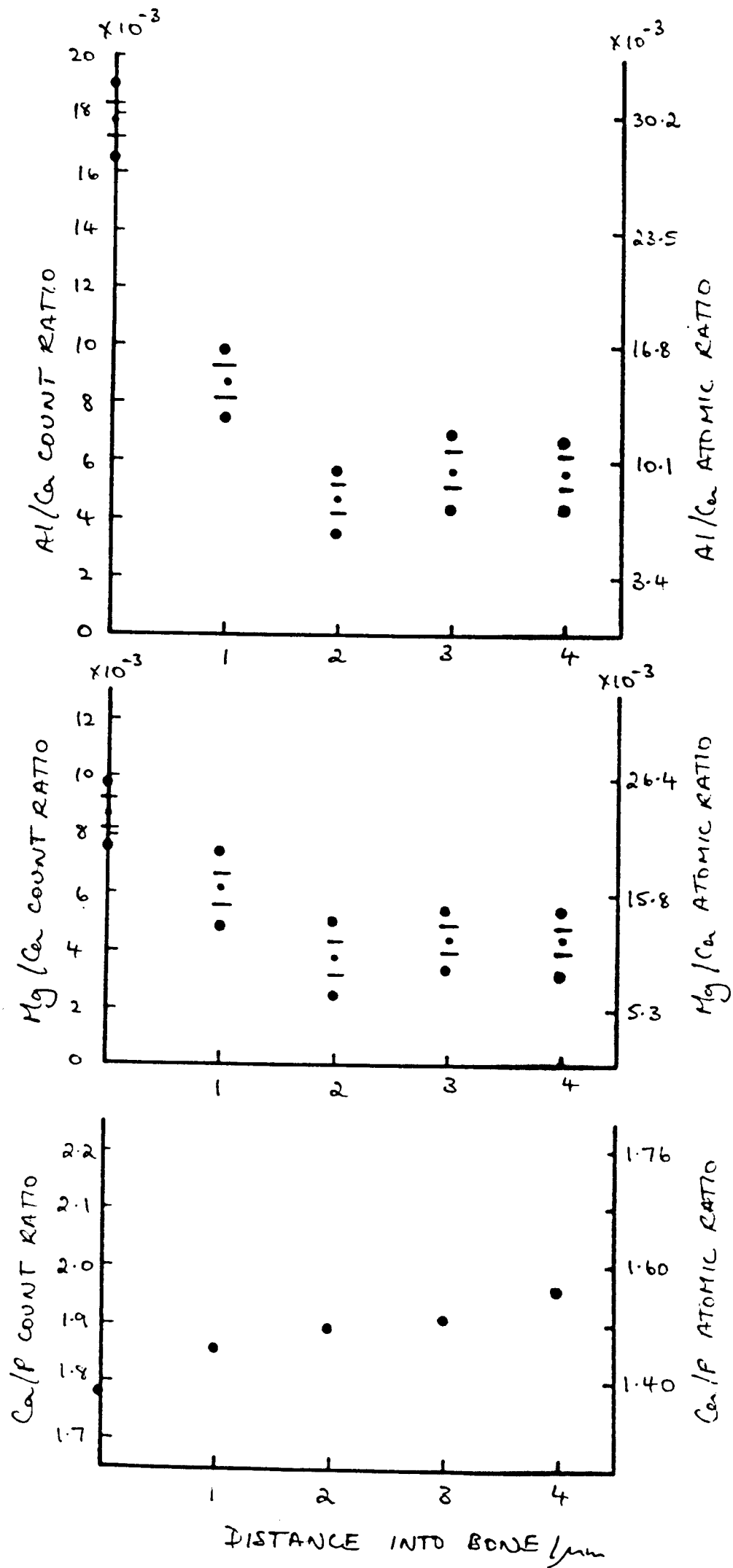
FIGURE S.176 EXPERIMENTAL SAMPLE I (84/106)
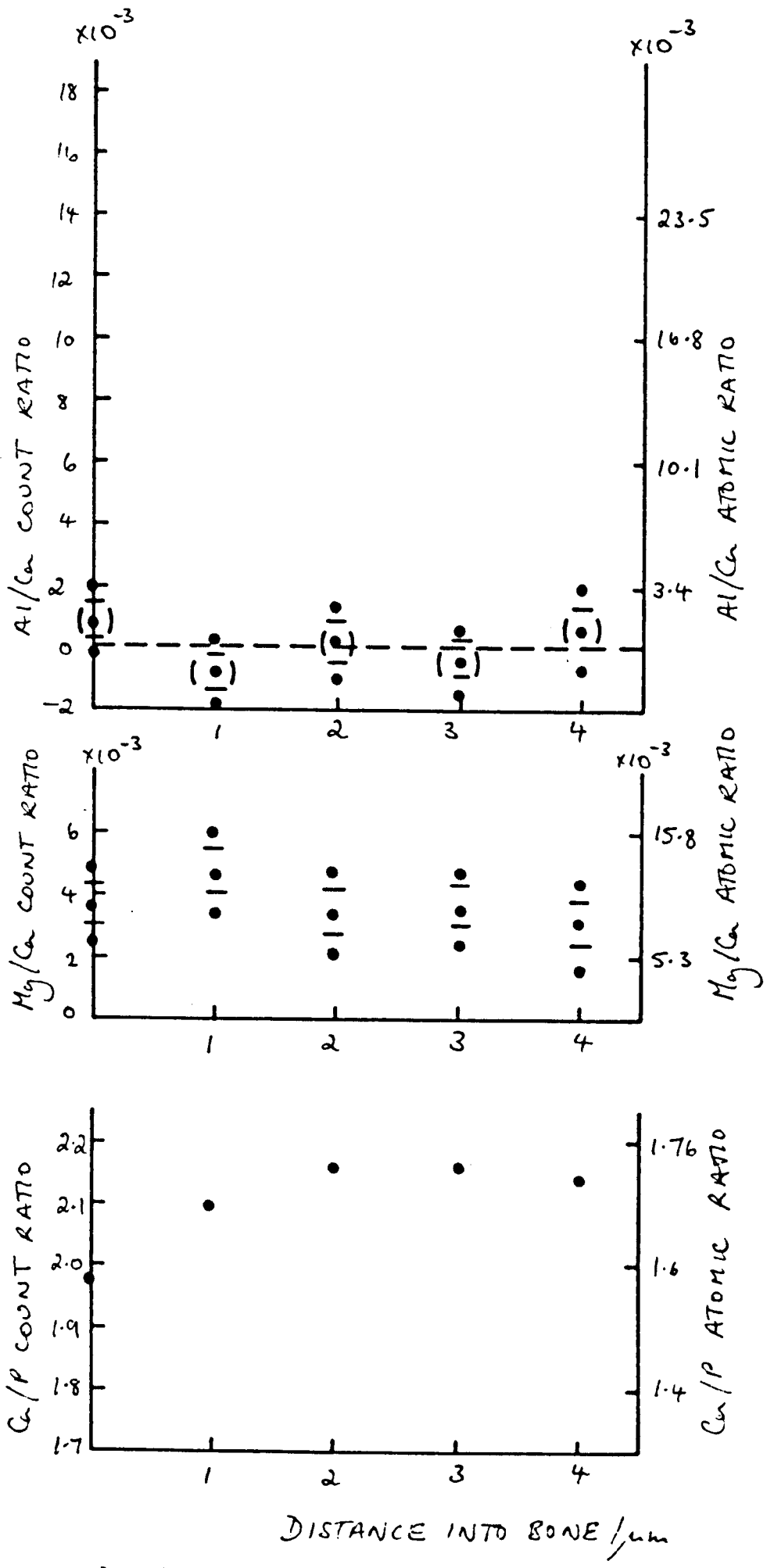
FIGURE 5.17c   CONTROL SAMPLE 2   (84/100)
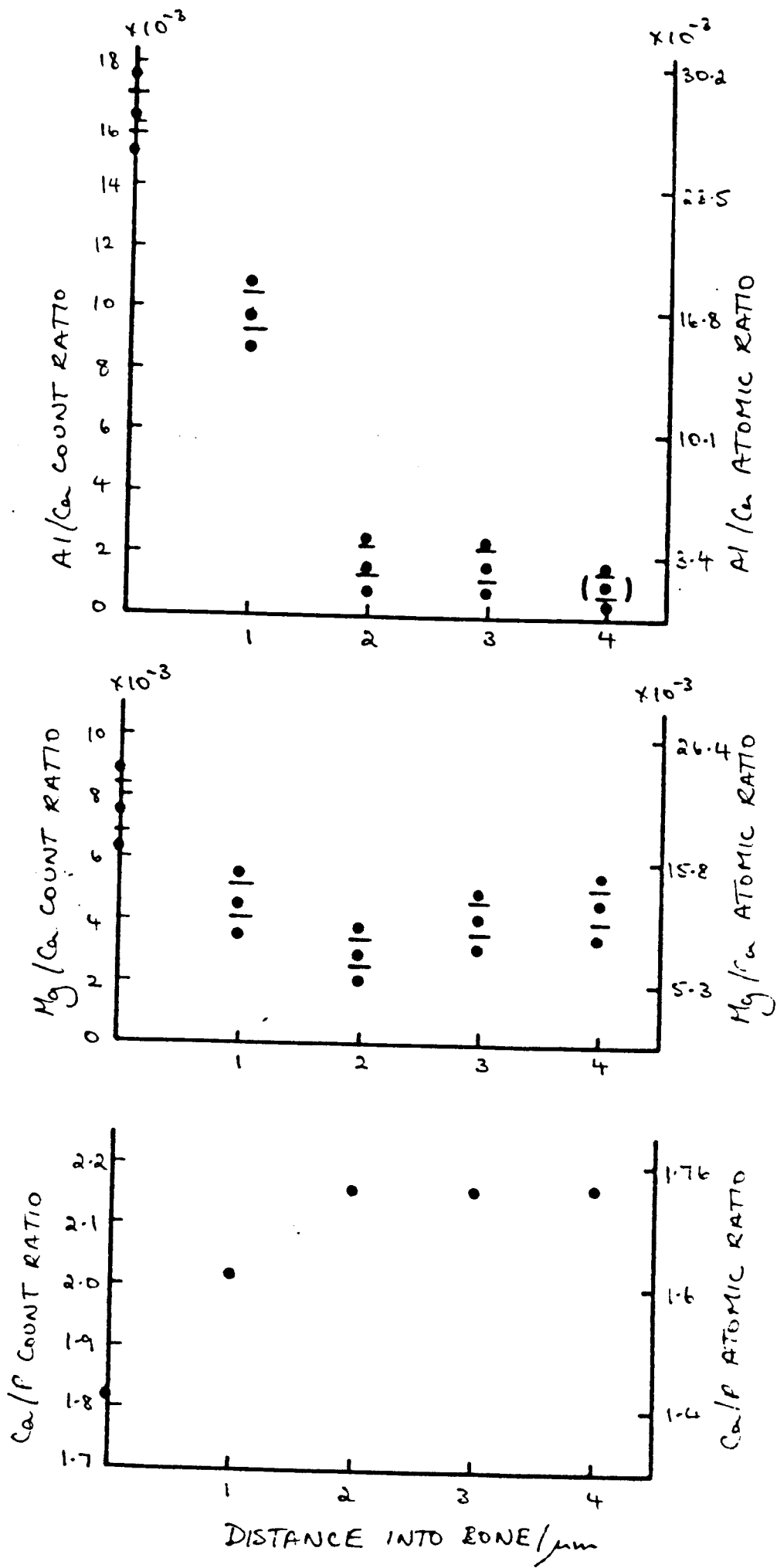
FIGURES.17d EXPERIMENTAL SAMPLE 2 (84/105)
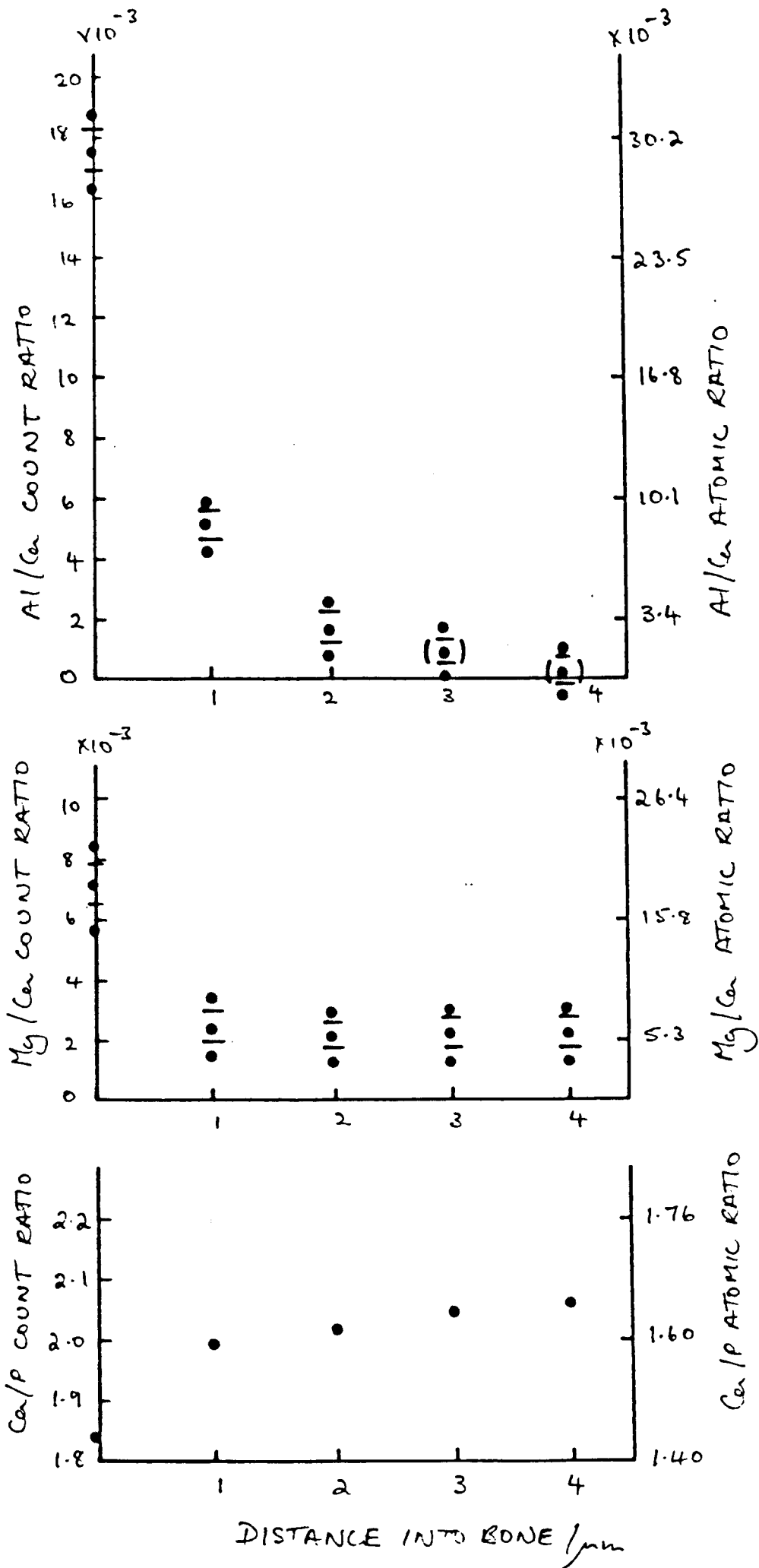
FIGURE 5.17e   EXPERIMENTAL SAMPLE 4   (84/105)

specimen.   The redistribution of counts due to incomplete charge
collection in the detector also affects the shape of the bremsstrahlung
in this energy region.   None of the established methods of spectral
processing appeared to be useful for extracting the trace element
counts.   The technique described here (Figure 5.6) did provide a method
of extracting these counts; however, the self-absorption correction to
the predicted bremsstrahlung had to be optimised for each spectrum.
The build up of counts due to incomplete charge collection had also to
be modelled.   Thus, each spectrum had to be processed and checked
visually several times.   Al/Ca and Mg/Ca count ratios have been graphed
against distance from the bone surface.

5.10   QUANTIFICATION OF THE CHARACTERISTIC SIGNALS

Equation 4.1 relates the number of atoms of type x to the intensity
of the signal detected.   For two elements x and y, the atomic ratio
n_x/n_y is related to the intensity ratio P_x/P_y by

$$\frac{n_x}{n_y} = k_{yx} \frac{P_x}{P_y} \qquad\qquad 5.4a$$

where

$$k_{yx} = \frac{\sigma_{ny} \, \omega_y \, S_y}{\sigma_{nx} \, \omega_x \, S_x} \cdot \frac{\epsilon(E_y)}{\epsilon(E_x)} \qquad\qquad 5.4b$$

Equations 5.4a and b assume that the incident electron interacts once
with the specimen.   It is also assumed that other effects due to a
finite specimen thickness are negligible (e.g. specimen self-absorption
and fluorescence).   These effects will be discussed in Section 5.11.

72

k_{yx} can be determined experimentally from standards of accurately known composition; however, suitable standards were not available for the elements of interest here (Elder, personal communication). Thus, Equation 5.4b allowed determination of theoretical k factors.

5.11   CORRECTION FOR SPECIMEN SELF-ABSORPTION AND FLUORESCENCE

The two most important corrections which are applied to X-ray spectra are for specimen self-absorption and fluorescence. As discussed in Chapter 4, self-absorption causes a reduction in the intensity of the X-rays incident upon the X-ray detector. Fluorescence occurs when an atom which has absorbed an X-ray de-excites by emitting a photon, thus enhancing the signal from these type of atoms.

Since atomic ratios are of interest, it is the relative self-absorption correction to an intensity ratio which is important. The intensity ratio P_x^1/P_y^1 obtained from a specimen of thickness t is related to the ratio P_x/P_y obtained from an infinitely thin film by (e.g. Goldstein et al 1977).

$$\frac{P_x}{P_y} = A_c \frac{P_x^1}{P_y^1} \qquad\qquad 5.5$$

$$\text{where } A_c = \frac{\mu/\rho_{spec}^x \left[1 - \exp\left(-\mu/\rho_{spec}^y \, \rho t \cosec\alpha'\right)\right]}{\mu/\rho_{spec}^y \left[1 - \exp\left(-\mu/\rho_{spec}^x \, \rho t \cosec\alpha'\right)\right]}$$

where μ/ρ_{spec}^x and μ/ρ_{spec}^y are the mass absorption coefficients for the characteristic X-rays from elements x and y respectively being absorbed by the specimen. ρ is the density of the specimen, and α' is the angle between the detector and the specimen surface. The mass absorption coefficients for hydroxyapatite were calculated from equation 4.5 using the mass absorption coefficients of Thinh et al (1979). The density of

73

mineralised bone is about 2.4 gm cm^{-3} (Elder, personal communication).
Equation 5.5b was evaluated for various specimen thicknesses and Table
5.1 summarises the values of A_c for Al/Ca, Mg/Ca and Ca/P intensity
ratios. If specimen thicknesses are defined as e.g. $1500 \pm 500\text{Å}$, $2500 \pm$
500Å etc, then the uncertainty in the self-absorption correction is
typically less than 2% for Mg/Ca, less than 2% for Al/Ca and about 1%
for Ca/P.

The characteristic X-ray intensity emitted by an element x may be
enhanced by secondary X-ray fluorescence from the characteristic X-rays
emitted by a second element z. Secondary X-ray fluorescence can only
occur if the energy of the z X-rays is greater than the excitation
energy of element x. Nockolds et al (1979) predict the fluorescence
enhancement is given by

$$\frac{P_x^f}{P_x^1} = C_z \omega_z \frac{r_x-1}{r_x} \frac{A_x}{A_z} \frac{\mu}{\rho}_x^z \frac{I_{cx}}{I_{cz}} \frac{\ln(E_0/x)}{\ln(E_0/z)} \frac{\rho t}{2}$$
$$\times \left[0.923 - \ln\left(-\frac{\mu}{\rho}_{spec}^z \rho t\right)\right] \sec\alpha \qquad 5.6a$$

where P_x^f/P_x^1 is the ratio of the fluorescence intensity to the primary
intensity, w_z is the fluorescence yield of element z, r_x is the
absorption edge jump ratio of element x, $\frac{\mu}{\rho}_x^z$ and $\frac{\mu}{\rho}_{spec}^z$ are the mass
absorption coefficients of element z radiation in element x and specimen
respectively, Ax and Az are the atomic weights, and I_{cx} and I_{cz} are the
critical excitation energies for the characteristic radiation of x and
z. The correction to an observed intensity P_x^1 is defined as

$$P_x = P_x^1 \left[1 - \sum \frac{P_{xj}^f}{P_{xj}^1} \right] \qquad 5.6b$$

where the summation is carred out for all characteristic peaks j, whose
energy is greater than the ionisation energy of radiation.

Intensity ratio	Specimen thickness				
	500	1500	2500	3500	4500
Mg/Ca	1.028	1.087	1.146	1.209	1.272
Al/Ca	1.016	1.048	1.082	1.116	1.151
Ca/P	0.995	0.985	0.975	0.965	0.956

Table 5.1 Absorption correction to the characteristic
intensities as a function of hydroxyapatite specimen
thickness($\overset{o}{A}$).

The ratio P_x^f/P_x^l is summarised in Table 5.2 for the Mg, Al and P signals. The mass absorption coefficents and jump ratios were calculated using the tables of Thinh et al (1979) and the fluorescence yields were taken from Table 2.6. Clearly, fluorescence effects in a mineralised bone section of thickness $1500\pm 500\text{Å}$ is of little significance since even the enhancement of the Mg signal by the P signal in a specimen of thickness 2500Å is less than 1%.

5.12   SUMMARY

Table 5.3 summarises the theoretical k factors for conversion of the characteristic intensity ratios to atomic ratios. The k factors have been calculated from the average of the predictions of Equation 5.5 and cross-section values given in Table 2.5. The values of fluorescence yield and partition function have been taken from Table 2.6, and the detector absorption, specimen self-absorption and fluorescence corrections have been taken from Tables 4.1 and 4.2. As discussed in Chapter 4, the cross-section ratios summarised in Table 2.5 agreed with the predictions of other published cross-section parameterisations to within 8% for Ca/Mg, 3% for Ca/Al and 2% for P/Ca. The uncertainty in the fluorescence yields are less than 2.5% and the uncertainty in the partition function should be negligible. The uncertainty in the X-ray absorption (due to both the detector and the specimen) is defined by the uncertainty in the self-absorption correction. As discussed in Section 5.11, this is estimated to be typically 2% for Mg/Ca and Al/Ca and 1% for Ca/P. Thus, for the reasons described, it seems likely that the Mg/Ca intensity ratios can be quantified to better than 9%, the Al/Ca ratios to better than 5% and

A fluoresing B	specimen thickness/Å				
	500	1500	2500	3500	4500
P, Al	6.19	15.0	22.3	28.7	34.5
P, Mg	2.34	5.69	8.45	10.9	13.1
Ca, P	4.87	8.57	18.6	24.4	29.7
Ca, Al	2.92	7.35	11.2	14.6	17.8
Ca, Mg	1.11	2.79	4.23	5.54	6.75

Table 5.2   The ratio $P_x{}''/P_x'$ in the units 10^{-4}.

	specimen thickness/Å	
	0	1500
$k_{Ca,Al}$	1.53	1.60
$k_{Ca,Mg}$	2.15	2.34
$k_{P,Ca}$	0.82	0.80

Table 5.3 k factors including corrections for X-ray self-absorption in specimens of 0 and 1500Å thickness.

the Ca/P ratios to better than 4%; (the uncertainties have been added in quadrature). The values of the atomic ratios obtained from the mineralised bone spectra are indicated by the scales on the right hand side of Figures 15.17a to e. The k factors used included corrections for 1500$\overset{\circ}{A}$ specimen self-absorption (this being the appropriate correction for the spectra) and a correction for the Al and Mg counts lost due to ICC. As stated in Section 5.6, there is negligible uncertainty in the latter correction.

5.13   CONCLUSIONS

As mentioned in Section 5.3.1, previous studies (e.g. Boyce et al (1981)) involved determining the concentration of Al in mineralisation nuclei, surface bone (<2 μm from the bone/osteoid interface) and deep bone (>2 μm from the interface). In this work atomic Al/Ca, Mg/Ca (and Ca/P) ratios were acquired from spectra acquired typically at 1 μm intervals into the bone from the dormant bone surface. The technique developed here for processing spectra is almost certainly more accurate than that suggested by Nicholson et al (1980), especially since (after processing) the fit of the theoretical to experimental bremsstrahlung was checked visually for each spectrum.

From Figures 5.17a to e, the Al/Ca ratios clearly decrease with increasing depth into the bone. This decrease is typically most rapid within the first 2 μm. The (atomic) Al/Ca ratios obtained at the surface of the bone are very similar (0.0299± 0.0014, 0.0272± 0.0017 and 0.0292± 0.0017 respectively) in experimental samples 1, 2 and 4 respectively. Trace concentrations of Al have been detected 4 μm from the bone surface (8 μm in one sample). In the study by Boyce et al

(1981) (using different samples), Al was detected in mineralisation nuclei and surface bone but not in deep bone. Thus in the work described here, Al/Ca gradients (with respect to distance into the bone) have been detected in finer spatial detail and quantified more accurately than, for example, Boyce et al (1981) and (1982). Other graphs of atomic Al/Ca, Mg/Ca (and Ca/P) ratios are shown in Appendix 1 together with a brief discussion on the overall physiological interpretation.

A SINGLE-STAGE PROCESS FOR QUANTIFYING ELECTRON ENERGY LOSS SPECTRA

6.1 INTRODUCTION

Electron energy loss spectroscopy (EELS) is a widely used technique for determining local elemented compositions (e.g. Egerton, 1984). In the case of two elements x and y, the ratio of elemental concentrations is given by

$$\frac{n_x}{n_y} = \frac{\sigma_y(\Delta_y)}{\sigma_x(\Delta_x)} \frac{I_x(\Delta_x)}{I_y(\Delta_y)} \qquad 6.1$$

where $I_j(\Delta_j)$ is the number of electrons which have lost energy within an energy window Δ_j due to ionisation of atoms of type j, and $\sigma_j(\Delta_j)$ is the relevant cross-section for the process. The cross-section models of Egerton (1979) and Leapman et al (1980) have been discussed briefly in Section 2.8. The $\sigma_j(\Delta_j)$ and $I_j(\Delta_j)$ terms in Equation 6.1 can be written as

$$I_j(\Delta_j) = \int_{\Delta E_j}^{\Delta E_j + \Delta_j} i_j(\Delta E)\, d(\Delta E) \qquad 6.2$$

$$\sigma_j(\Delta_j) = \int_{\Delta E_j}^{\Delta E_j + \Delta_j} \frac{d\sigma}{d(\Delta E)}\, d(\Delta E)$$

where $i_j(\Delta E)\, d(\Delta E)$ is the number of electrons losing energy between ΔE and $\Delta E + d(\Delta E)$ due to the particular ionisation of interest and $\frac{d\sigma}{d(\Delta E)}$ is the corresponding cross-section, differential in energy loss, but integrated

over the acceptance angle of the spectrometer. ΔE_j denotes the energy loss at the start of the _energy fitting window_ and can, but need not, be chosen to coincide with the edge onset.

Before Equation 6.1 can be applied it is necessary to separate the characteristic signal from the uninformative background in the recorded spectrum. The usual method for accomplishing this is to select a region before the edge and fit a curve of the form $A(\Delta E)^{-r}$ to it (e.g. Egerton 1983). Once A and r have been determined the curve is extrapolated beyond the edge to define the background which is then subtracted from the total spectrum leaving the desired signal. Then I_j is obtained by summing the counts in the selected energy window, and by using the relevant cross-sections, the ratio Λ_x/Λ_y is obtained.

Figure 6.1 shows an EEL spectrum acquired from mineralised bone. The specimen preparation technique used to obtain a sufficiently thin region of mineralised bone will be discussed in Chapter 7. The probe convergence semi-angle and electron collection semi-angle were 25 and 27 mrad respectively. The other spectra discussed in this chapter were acquired using these conditions. In the mineralised bone spectrum, extraction of the Ca signal is difficult because only a limited pre-edge fitting range is available. Structure from the C edge is also present in this range. The P signal is not very visible and is difficult to extract because the background preceding this edge only follows an $A(\Delta E)^{-r}$ form over a limited energy range due to the proximity of the low loss region.

A way of reducing these problems in signal extraction is to fit a curve to pre and post-edge regions _(J M Titchmarsh, personal communication)_ with the functional form

79
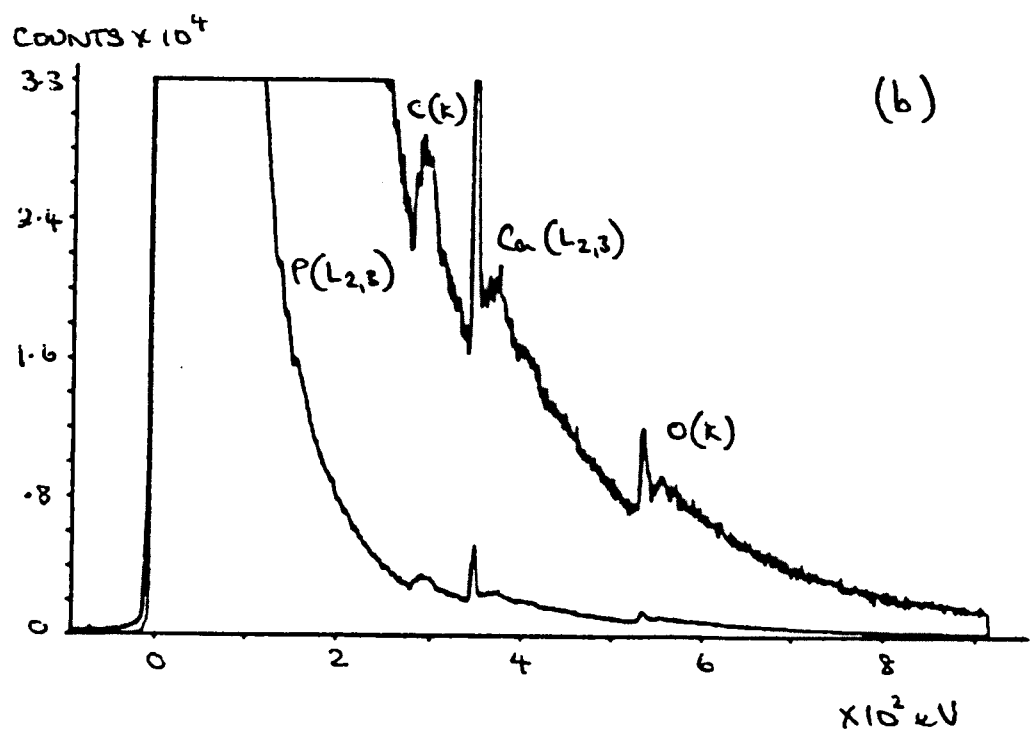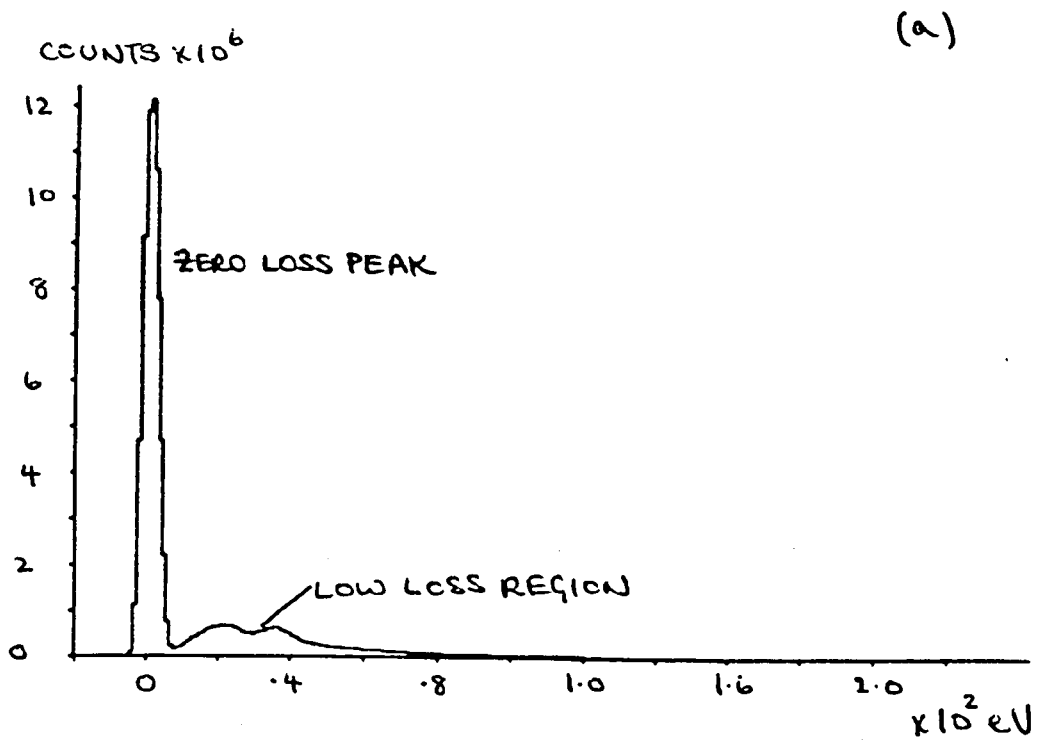
Figure 6.1 Mineralised bone spectrum.

$$A(\Delta E)^{-r} + k_j \frac{d\sigma}{d(\Delta E)_j} \qquad\qquad 6.3$$

where $\frac{d\sigma}{d(\Delta E)_j}$ is, of course, zero before the edge onset. In this way values of A and r are constrained to be acceptable over the total energy range of interest, rather than only in front of the edge. Furthermore, k_j is proportional to the number of atoms of type j present and Equation 6.1 reduces to

$$\frac{n_x}{n_y} = \frac{k_x}{k_y} \qquad\qquad 6.4$$

This chapter describes the latter "single-stage" technique and compares this method with the standard extrapolation technique.

6.2 BACKGROUND REMOVAL-EXTRAPOLATION TECHNIQUE

The general method used to remove a background is to define before the edge an energy range (typically 50 - 100 eV wide) and fit an $A(\Delta E)^{-r}$ curve. Once fitted, the curve is extrapolated under the edge over an energy window large enough to make solid state effects negligible (e.g. about 100 eV, Egerton, 1984). These effects will be discussed in Section 6.9.4. The fitting window must be sufficiently large to ensure reasonable precision, but not too large because the $A(\Delta E)^{-r}$ form is only valid over a restricted energy range (~200 eV) (Egerton, 1984). Different methods of curve fitting have been proposed by various

authors. Egerton (1983) suggests determining A and r from the following
equations

$$A = (I_1 + I_2)(1 - r) / (E_2^{1-r} - E_1^{1-r})$$

where   6.5

$$r \doteq 2 \log(I_1 / I_2) / \log(E_2 / E_1)$$

and the fitting window (E_1 to E_2) is divided into two halves with
integrated counts I_1 and I_2.   Colliex et al (1981) has proposed a more
complicated method where the A and r values calculated from Equation 6.5
are used as an initial estimate of the best fit curve, this being
obtained by minimising the function

$$\chi^2 = \sum_i \left(c_i - A(\Delta E)_i^{-r} \right)^2 / c_i^1$$ 6.6

where c_i^1 is the variance in c_i background counts and the summation is
carried out over all the fitting points.   The extrapolation routine
used for comparison with the single-stage technique was written by
P A Crozier.   It can be described as follows:

The function

$$z_i = A(\Delta E)_i^{-r}$$ 6.7

is written as the linear function

$$y_i = r x_i + \ln A$$ 6.8

81

where $y_i = \ln z_i$ and $x_i = \ln (\Delta E)_i$.   The parameters A and r are then obtained by minimising the following function

$$\chi^2 = \sum (y_i' - y_i)^2 \qquad\qquad 6.9$$

where $y_i' = \ln c_i$

and the summation is carried out over the fitting region.   The A and r values providing the minimum value of Equation 6.9 can be found by solving the simultaneous equations obtained from the following

$$\frac{\partial \chi^2}{\partial r} = 0$$

$$\frac{\partial \chi^2}{\partial A} = 0 \qquad\qquad\qquad 6.10$$

Crozier (1985) noted that very poor background fits were produced by the above procedure when using the Toltec Data Processing system.   All EEL spectra discussed here were processed using the Toltec system.   Crozier (1985) showed that the poor fits were due to "rounding error" in the Toltec system and as no double precision facility was available on this computer, normalised all the y_i data so that it lay in the region 0 to 2.   This effectively exaggerates the percentage difference between any two y_i points since the logarithm is changing rapidly in this range.   The rounding error was negligible with this restructured program.   When writing a program to fit Equation 6.3 to an edge it was necessary to check that rounding error was not present (to a significant extent).

6.3 THE SINGLE-STAGE FITTING TECHNIQUE - DEFINITION OF ENERGY REGIONS

Figure 6.2 shows the fitting ranges and offsets which are used in the single-stage technique.   In the program, all energy ranges and offsets are referred to the "bug" position which is set at the edge onset.   The pre-edge fitting range is defined in the same way as the extrapolation technique; however, the post-edge range is slightly more complicated.

An "alignment offset" is required because the onset of the ionisation edge is always smeared out due to the finite energy resolution of the electron spectrometer (see Section 3.6) and plural inelastic scattering within the specimen (see Section 2.10).   In addition, the exact position of the edge onset is uncertain due to near-edge fine structure (see Section 2.9).   Therefore an "alignment offset" between the edge onset and the "onset" of the cross-section is required. Typically an offset of only a few eV is required and varying this offset has little effect on the value of k extracted (usually about 1%).

A "convergence offset" is required since solid-state effects such as near edge fine structure dominate the shape of the edge near the edge onset.   These effects are not included in the calculation of the continuum cross-sections and, when calculating a fit to an edge, it is often necessary to exclude about the first 30 eV (from the edge onset) from the post-edge fitting range.   Section 6.6 discusses the effect of varying the convergence offset.

6.4 CONSIDERATIONS FOR CURVE FITTING

Equation 6.3 can be fitted to pre and post-edge regions by minimising a weighted least square function of the form

COUNTS

ENERGY LOSS /eV

IONISATION EDGE

$A(\Delta E)^{-r} + k \dfrac{d\sigma_u}{d(\Delta E)}$

BUG POSITION

$A(\Delta E)^{-r}$

ALIGNMENT OFFSET

PRE-EDGE FITTING RANGE (P)

CONVERGENCE OFFSET

POST-EDGE FITTING RANGE (W2)

W1
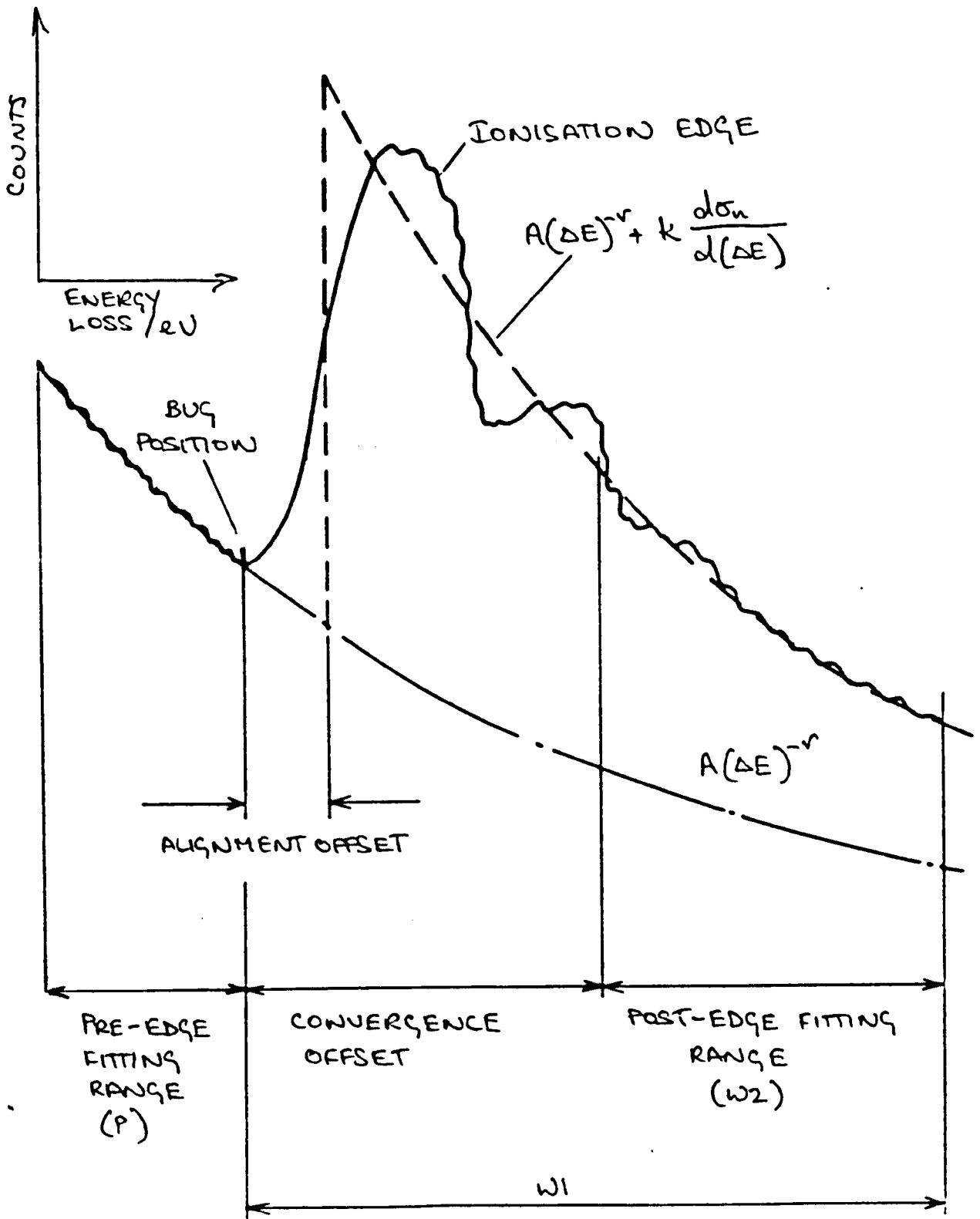
Figure 6.2   Energy regions used for curve fitting.

$$\chi^2 = \sum_i \left(S_i - \left[A(\Delta E)_i^{-r} + k \frac{d\sigma}{d(\Delta E)_i} \right] \right)^2 / S_i \qquad 6.11$$

where S_i denotes the number of counts in the pre and post-edge fitting ranges, and the summation is carried out over both these ranges. The initial approach was to use the "simplex" procedure (Nelder et al, 1965) which locates the minimum value of Equation 6.11 by varying r, A and k given starting values. The main problem with using this approach was that the simplex routine ran very slowly on the Toltec system (about 20 min). In addition, the background fits produced by Equation 6.11 sometimes did not pass through the pre-edge region when this range was short relative to the post-edge range. A different approach to curve fitting was taken based on the following considerations.

The $A(\Delta E)^{-r}$ curve was forced to pass through the pre-edge region. Other curves were clearly unacceptable. The simplex routine was not used due to the time required to run the program. In an ideal situation, when curve fitting, all possible combinations of r, A and k are examined (subject to the constraint that the $A(\Delta E)^{-r}$ curve passes through the pre-edge region) to remove the possibility of locating a local minimum in the chi-square function. However, to reduce the time required to fit the curve, only r, A and k values close to the best fit values should be tried. Finally, the curve fitting program must not produce significant rounding errors. The following sections describe the curve fitting procedure used to satisfy the above requirements, some of which are conflicting.

6.5 THE CURVE FITTING PROCEDURE

The best fit r value to an edge (r edge) is assumed to be between maximum and minimum values, r_{max} and r_{min}. r_{min} is first selected and an optimum A value for this r value selected by minimising a chi-square function of the form

$$\chi_1^2(A) = \sum_i \left(c_i - A\,(\Delta E)_i^{-r_{min}} \right)^2 / c_i \qquad 6.12$$

where A is the only variable and the summation is carried out over the pre-edge fitting range. Thus r_{min}, $A_{r\,min}$ and $(x_1^2)_{r\,min}$ are defined. An optimum k value for this r and A combination are determined by minimising another chi-square function of the form

$$\chi_2^2(k) = \sum_i \left(c_i - \left[A_{r_{min}}(\Delta E)_i^{-r_{min}} + k\frac{d\sigma}{d(\Delta E)_i} \right] \right)^2 / c_i \qquad 6.13$$

where k is the only variable and the summation is carried out over the post-edge fitting range. Thus a curve is defined by the parameters r_{min}, $A_{r\,min}$, $k_{r\,min}$, $(x_1^2)_{r\,min}$ and $(x_2^2)_{r\,min}$. The total chi-square value for this curve is then defined as

$$\left(\chi_T^2 \right)_{r\,min} = \left(\chi_1^2 \right)_{r\,min} + \left(\chi_2^2 \right)_{r\,min} \qquad 6.14$$

The r value is now progressively incremented and a series of curves calculated by this method up to r = r_{max}. The values r, A_r k_r and $(X_T^2)_r$ are output from the program in the form of a table. The "best" fit to an edge corresponds to the minimum value of $(X_T^2)_r$. The r range (r_{max} to r_{min}) is then contracted about the previous best r value and another series of curves calculated at finer increments. The final best fit is obtained when the k_r values have ceased to vary significantly over the r range examined. Details of this fitting procedure will now be described.

6.5.1 Calculating the A_r and k_r values

As discussed in Section 6.5, the A_r value (for each r value) is obtained by minimising Equation 6.12. To reduce computational time a minimum number of A values should be examined. An initial estimate of the A_r value is calculated from

$$A_I^r = \frac{\sum S_i}{\sum (\Delta E)_i^{-r}}$$

6.15

where the summations are only carried out over the pre-edge range. Equation 6.15 assumes that the area under the best fit A_r value curve and the energy loss counts, in the pre-edge range, are equal. This approximation is best when r = r edge, as will be shown.

Colliex et al (1981) note that there is the following approximate relation between the area under the data (i.e. energy loss counts) and the area under a best fit curve determined by a least square procedure.

86

Equation 6.16 suggests that as the X^2 value for a curve increases, the area under the data is increasingly underestimated by a chi-square fit. When calculating A_r and $(X_1^2)_r$ values it was noted that for $r < r$ edge and $r > r$ edge $A_I^r > A_r$ but for $r = r$ edge, $A_I^r \doteq A_r$. This trend is expected from Equation 7.6 since $(X_1^2)_r$ is greatest for $r < r$ edge and $r >$ edge. For the edges examined $X^2/$Area (data) $\leq 1\%$ typically when $r = r$ edge, thus A_I^r is clearly a good initial approximation to A_r.

The A_r value is obtained from locating the minimum value of Equation 6.12 by varying the A value between $A_I^r \pm \Delta A$. The ΔA value is input to the program and Section 6.5.2 discusses the choice of this value. Figure 6.3 shows schematically the effect of varying A for $r_1 < r$ edge $r_2 = r$ edge and $r_3 > r$ edge. Figure 6.5(a) shows a typical variation of $X_1^2(A)$ with A using an experimental edge. The A_I^r and A_r values are indicated. It should be noted from Figure 6.5(a) that the difference between the A_I^r and A_r values is less than 0.1% and that $(X_1^2)_r$ is changing slowly in the region of the minimum value. The importance of these two observations will be discussed in Section 6.5.2.

The k_r values are calculated by a method similar to that used to obtain the A_r values. Again, an initial estimate of the k_r value is calculated from

$$k_I^r = \frac{\sum (S_i - A(\Delta E)_i^{-r})}{\sum d\sigma/d(\Delta E)_i} \qquad 6.17$$

87
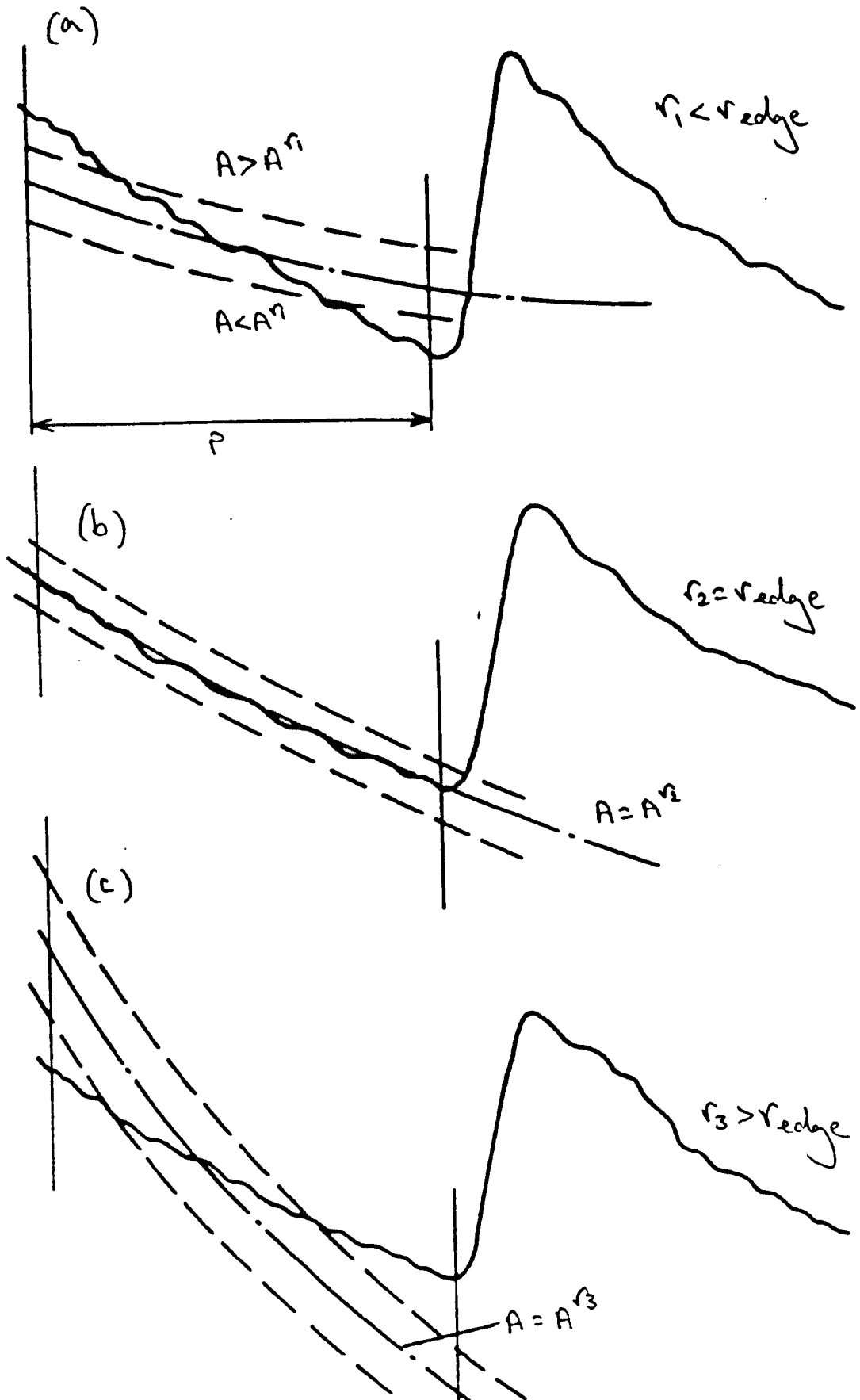
Figure 6.3   Varying r and A in the pre-edge region. Curves corresponding
to different combinations of r and A are shown. The best fit is in (b).

(a)

$k > k_{r_1}$

$k < k_{r_1}$

$r_1 < r_{edge}$

$A(\Delta E)^n$

(b)

$k = k_{r_2}$

$r_2 = r_{edge}$

(c)

$k = k_{r_3}$

$r_3 > r_{edge}$
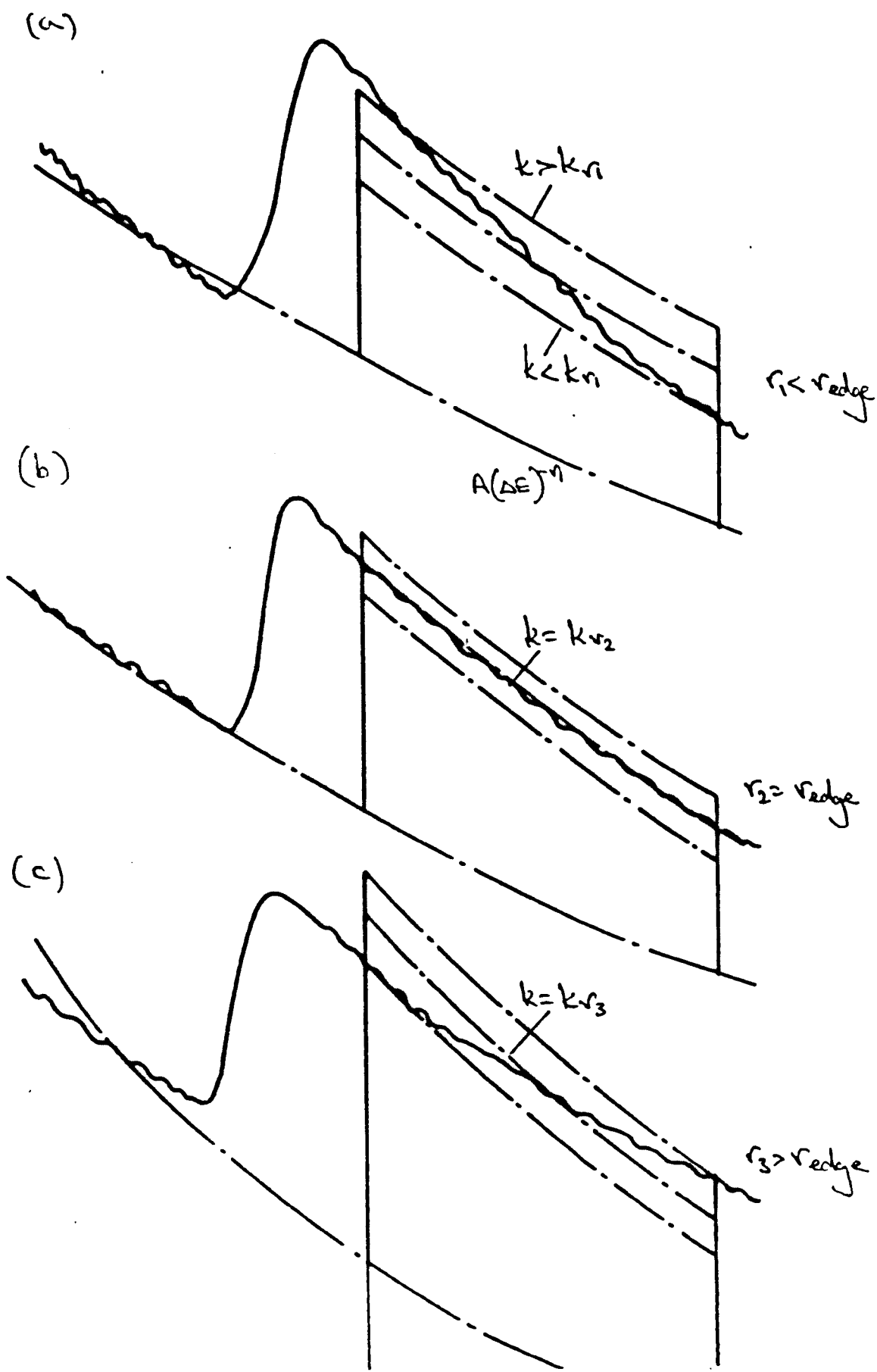
Figure 6.4   Varying r and k in the post-edge region. The curves corresponding to different combinations of r and k are shown. In all cases $A = A_r$. The best fit is in (b).
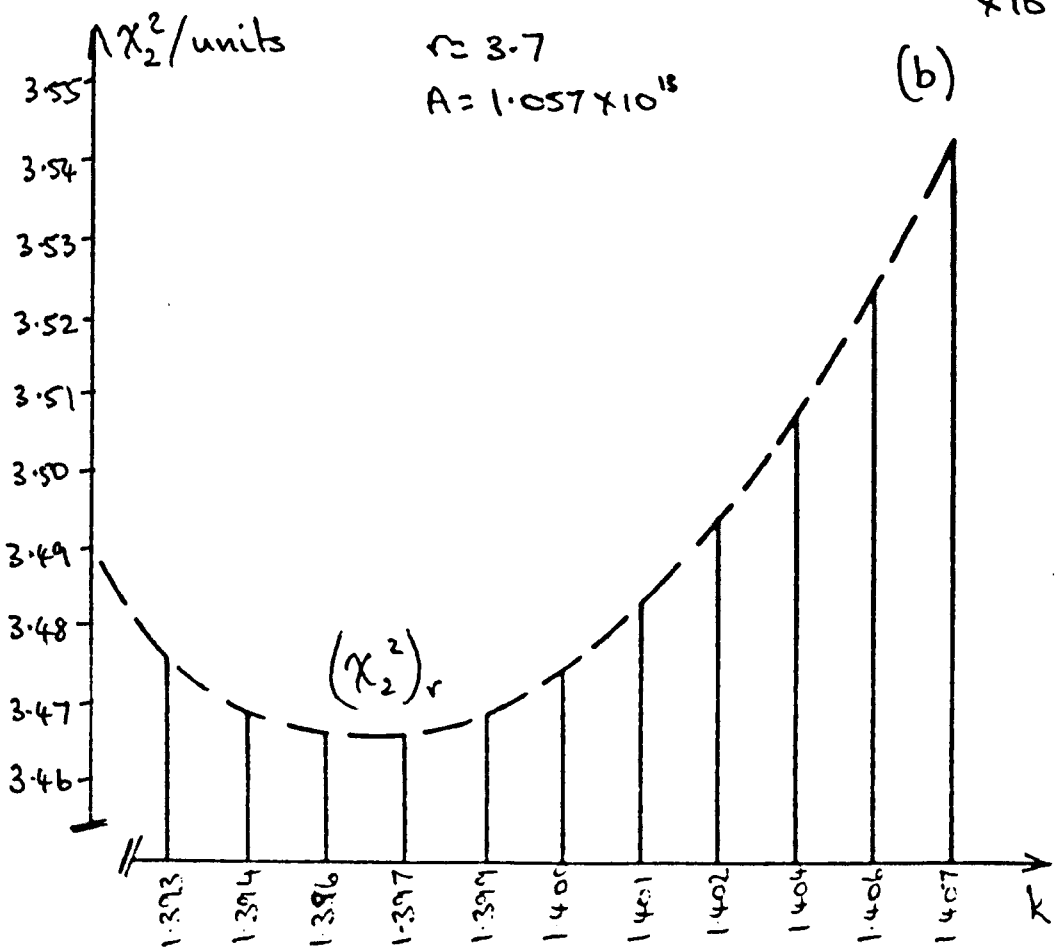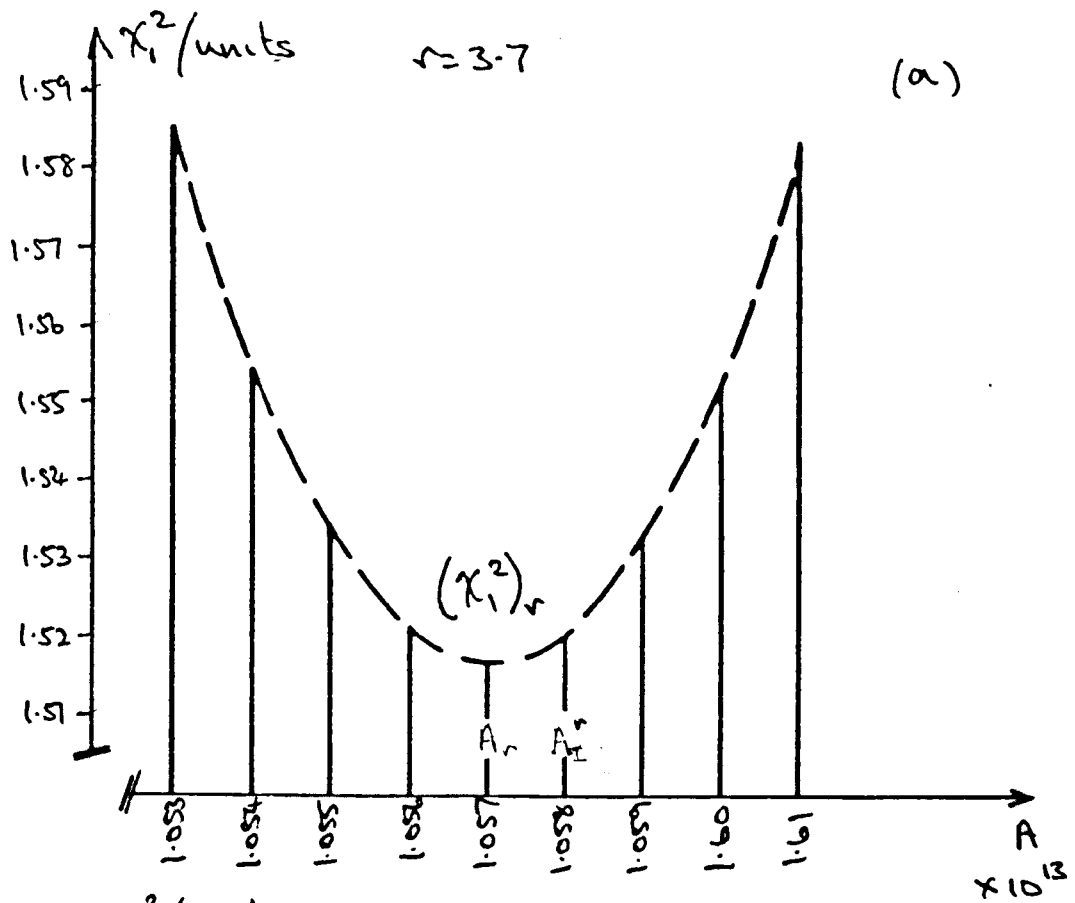
Figure 6.5

where the summations are only carried out over the post-edge range. Equation 6.17 assumes that the area under the best fit k_r curve and the energy loss counts in the post-edge range are equal. The relation between the k_I^r and k_r values is similar to that between the A_I^r and A_r values.

The k_r value is obtained by allowing the k value to vary between $k_I^r \pm \Delta k$ so that Equation 6.13 is minimised. Again, Δk is input to the program and Section 6.5.2 discusses the choice of this value. Figure 6.4 shows schematically the effect of varying k for $r_1 < r$ edge, $r_2 = r$ edge and $r_3 > r$ edge. In all cases $A = A_r$. Figure 6.5(b) shows a typical variation of (X_2^1) with k for given r and A. The k_I^r and k values are indicated. Again, it should be noted that the difference between k_I^r and k_r is less than 0.2% and that $(X_2^2)_r$ is changing slowly in the region of the minimum value. The choice of ΔA and Δk will now be discussed.

6.5.2   The Choice of ΔA and Δk

When optimising the A value for any particular r value there are two basic considerations. Firstly, a minimum value of $X_1^2(A)$ (i.e. $(X_1^2)_r$) must be found within the $2\Delta A$ range of A values examined. The program indicates if a minimum has been found. Secondly, the $X_1^2(A)$ function must be evaluated at sufficiently fine A value intervals within the $2\Delta A$ range examined. The significance of the second criterion is indicated by Figure 6.6. If the interval A´ (A´ $= \Delta A/2$ in the program) is chosen to be too large, then the minimum chi-square value obtained will be larger than the "true" minimum value (also indicated). Thus, the A_r value obtained may be significantly different from the "true" A_r value. It is necessary to choose a ΔA value (and therefore and A´
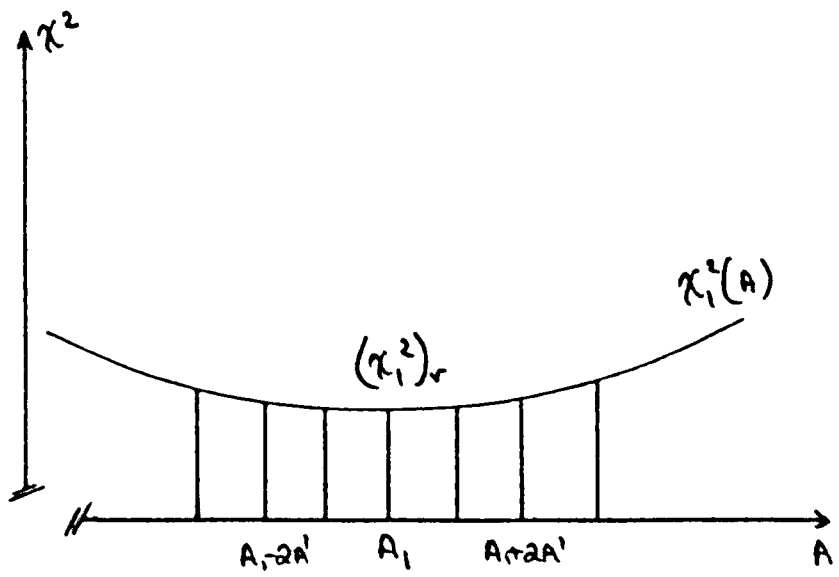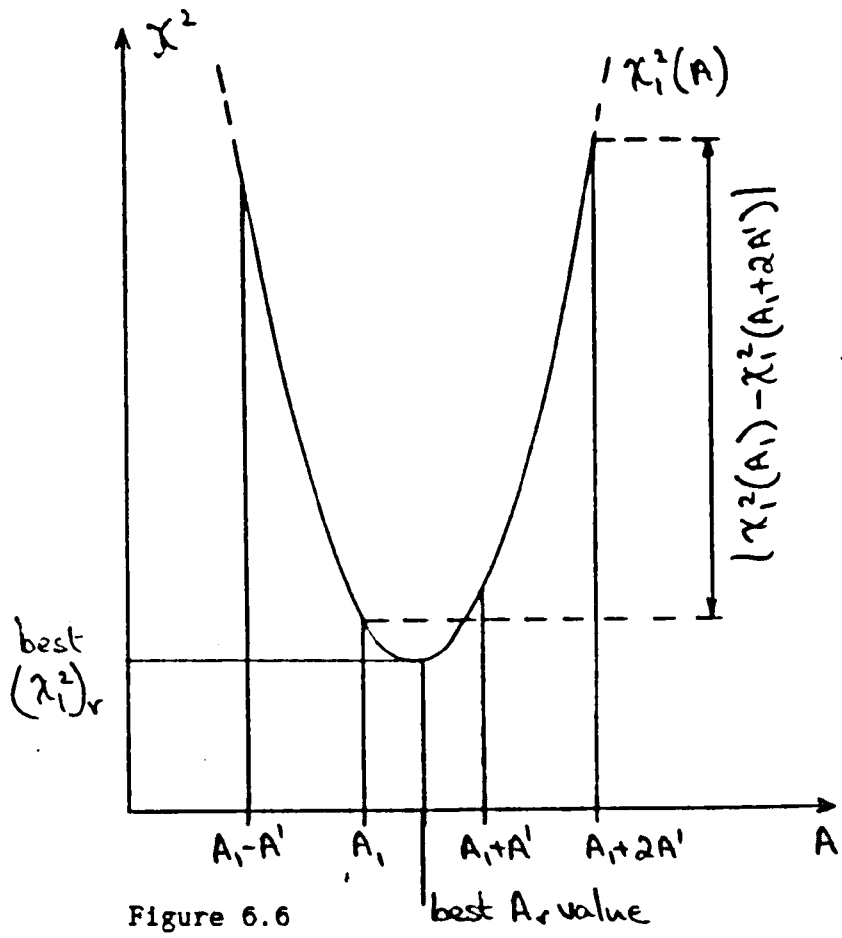
Figure 6.6

Figure 6.7

value) so that there is no significant variation of $X_1^2(A)$ about the $(X_1^2)_r$ value (Figure 6.7). A parameter can be defined which indicates the variation of $X_1^2(A)$ about $(X_1^2)_r$ i.e.

$$P_A = \left| \chi_1^2(A_1)_r - \chi_1^2(A_1 + A') \right| / \chi_1^2(A_1) \qquad 6.18$$

where $X_1^2(A_1)_r = (X_1^2)_r$ (see Figure 6.6). Since typically $P_A \ll 1\%$ for the A values chosen (usually, $\triangle A \doteq 0.5 \times 10^{-2} A_I^r$), $X_1^2(A)$ does not vary significantly about $(X_1^2)_r$. In addition, A is only varied by about 0.5%. It is therefore very likely that the situation shown in Figure 6.7 occurs, i.e. a good final estimate of the optimum A value, for each r value, is obtained.

When optimising the k value for any r and A_r combination, the same two criteria used for obtaining the A_r values apply, i.e. a minimum value of $X_2^2(k)$ must be found within the $2\triangle k$ range of k examined and the $X_2^2(k)$ function must be evaluated at sufficiently fine intervals. A parameter P_k, similar to Equation 6.18 can be defined which indicates the variation of $X_2^2(k)$ with k around $(X_2^2)_r$. Since typically $P_k \ll 1\%$ for the values of k chosen (usually, $\triangle k \doteq 0.5 \times 10^{-1} k_I^r$), $X_2^2(k)$ does not vary significantly about $(X_2^2)_r$. Again, k is only varied by about 0.5%. Thus it is likely that a good final estimate of the optimum k value, for each r and A_r combination is obtained.

6.6 PROGRAM CHECKS

Figure 6.8 shows the edge which was produced by adding a suitably
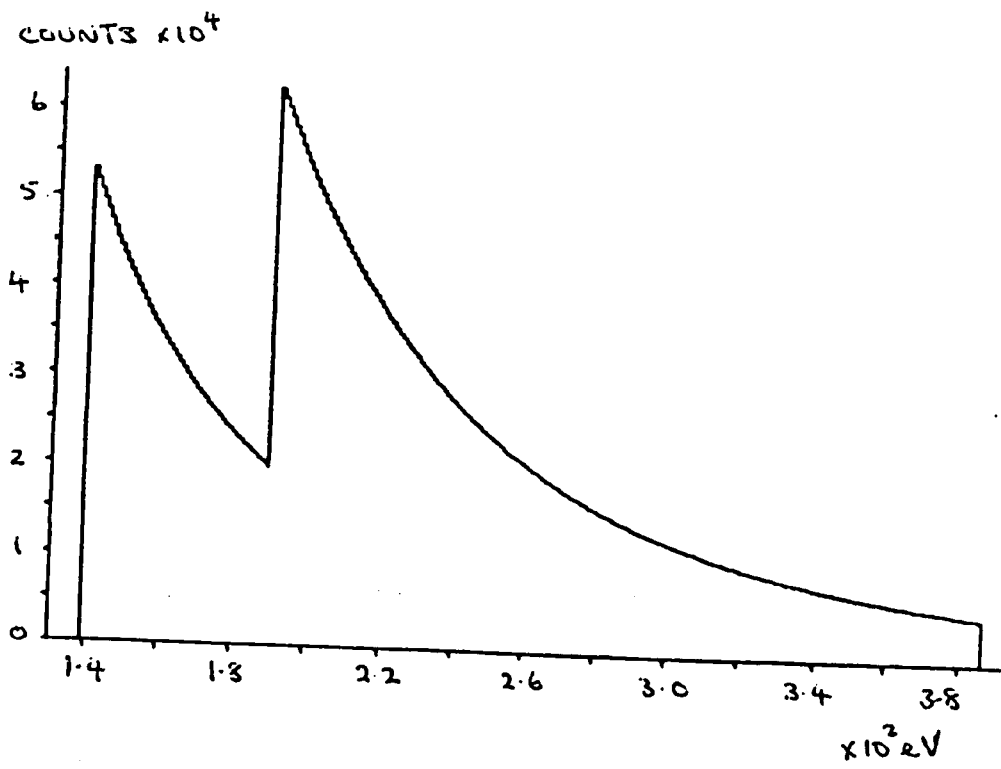
Figure 6.8

scaled cross-section to an $A(\Delta E)^{-r}$ background. The edge was calculated with $r = 3.177$, $A = 3417 \times 10^{12}$ and $k = 10.0$. Since a chi-square from the pre-edge region is added to a chi-square from the post-edge region it was of interest to examine the variation of both with r.

Figure 6.9 shows the variation of $(X_1^2)_r$ and A_r with r for various pre-edge fitting ranges (P). It should be noted that an overall minimum of $(X_1^2)_r$ was always obtained at $r = 3.177$ (i.e. the correct r value). Table 6.1 summarises the r, A_r and $(X_1^2)_r$ values obtained as best fits to the pre-edge ranges. Clearly these values are in agreement with the known values. These $(X_1^2)_r$ values should be zero since there is no noise in the edge, and they are very small. Figure 6.10 shows a typical fit to the pre-edge range. It should be noted from Figure 6.9 that the variation of $(X_1^2)_r$ with r is less rapid when the pre-edge fitting range is decreased. It is important to have a well defined minimum $(X_1^2)_r$ value since the corresponding r and A values will also be well defined for obtaining the best k value. Thus, the extent of the pre-edge fitting range should be maximised.

Figures 6.12(a) and (b) show the variation of $(X_2^2)_r$ and k_r with r for several different post-edge fitting ranges. A small (10 eV) pre-edge fitting range was used. Table 6.1 summarises the r, A_r and k_r values obtained at the minimum $(X_2^2)_r$ values. These chi-square values are very small, as expected. Figure 6.11 shows a typical fit obtained by minimising $(X_2^2)_r$ and Figure 6.13 shows the cross-section scaled to the edge. The edge is obtained by subtracting the best fit $A(\Delta E)^{-r}$ background. Clearly there is a good fit between the edge and the scaled cross-section. It should be noted from Figures 6.12(a) and (b) that the change in $(X_2^2)_r$ with r is less rapid when the post-edge
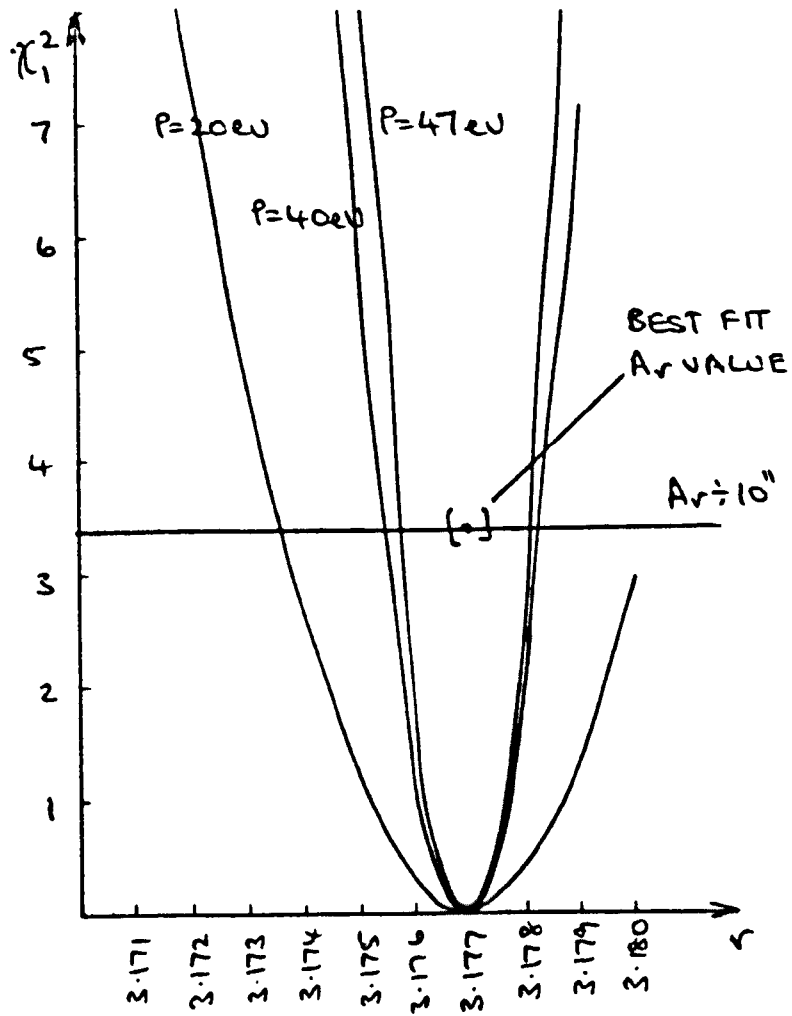
Figure 6.9 The variation of $(X_1^2)_r$ and A_r with r for several different pre-edge fitting ranges.

fitting region	r	A	k	$\langle \chi^2_T \rangle_r$	
20/-/-	3.177	.3414	10.0	$.46 \times 10^{-5}$	PRE-EDGE.
40/-/-	"	10 "	"	$.60 \times 10^{-5}$	FITTING ONLY
47/-/-	"	"	"	$.67 \times 10^{-5}$	$\left(\chi^2_T = \chi^2_1 \right)$
10/90/10	"	"	"	$.48 \times 10^{-5}$	POST-EDGE
10/60/40	"	"	"	$.39 \times 10^{-5}$	FITTING ONLY
10/20/80	"	"	"	$.48 \times 10^{-5}$	$\left(\chi^2_T = \chi^2_2 \right)$
10/170/10	"	"	"	$.37 \times 10^{-5}$	
10/80/100	"	"	"	$.27 \times 10^{-5}$	

Table 6.1   Best fit curves fitted to the artifical edge shape.

The fitting regions (expressed in eV) are defined as:-

pre-edge fitting range/post-edge range/convergence offset
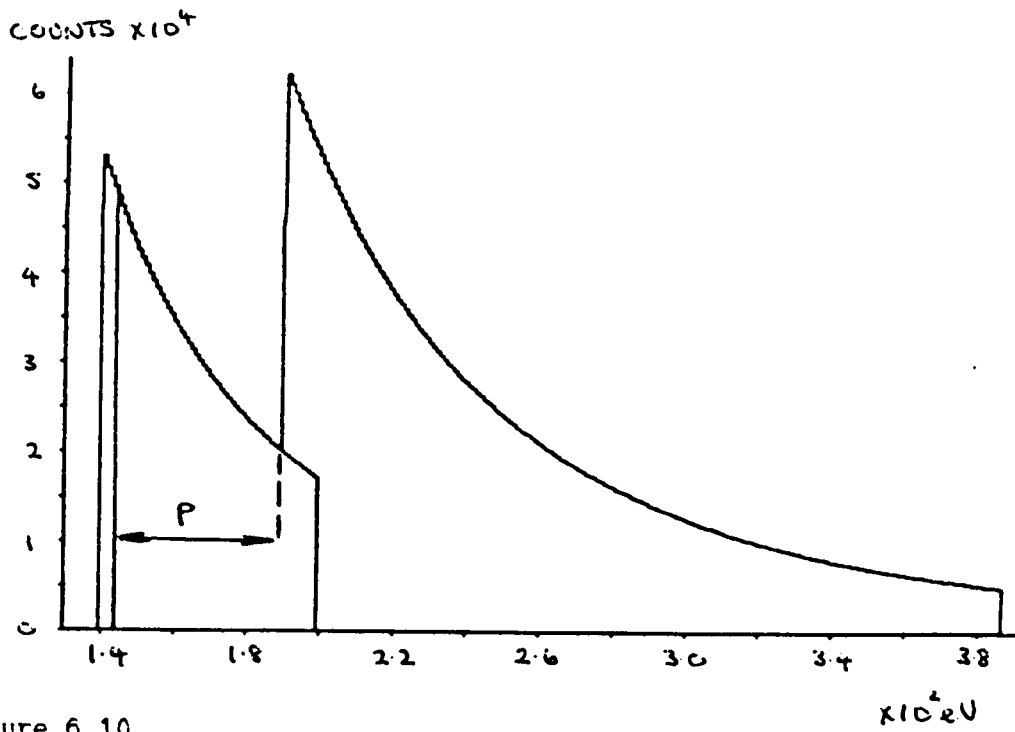
Figure 6.10
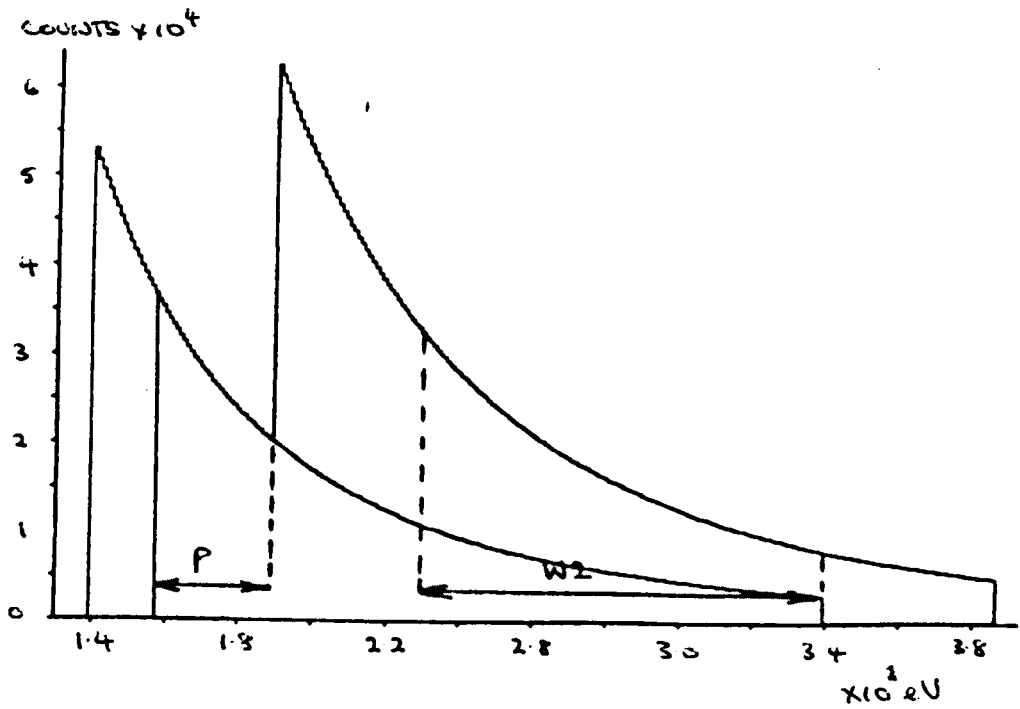
Figure 6.11   P:- pre-edge region
   W2:- post-edge fitting range
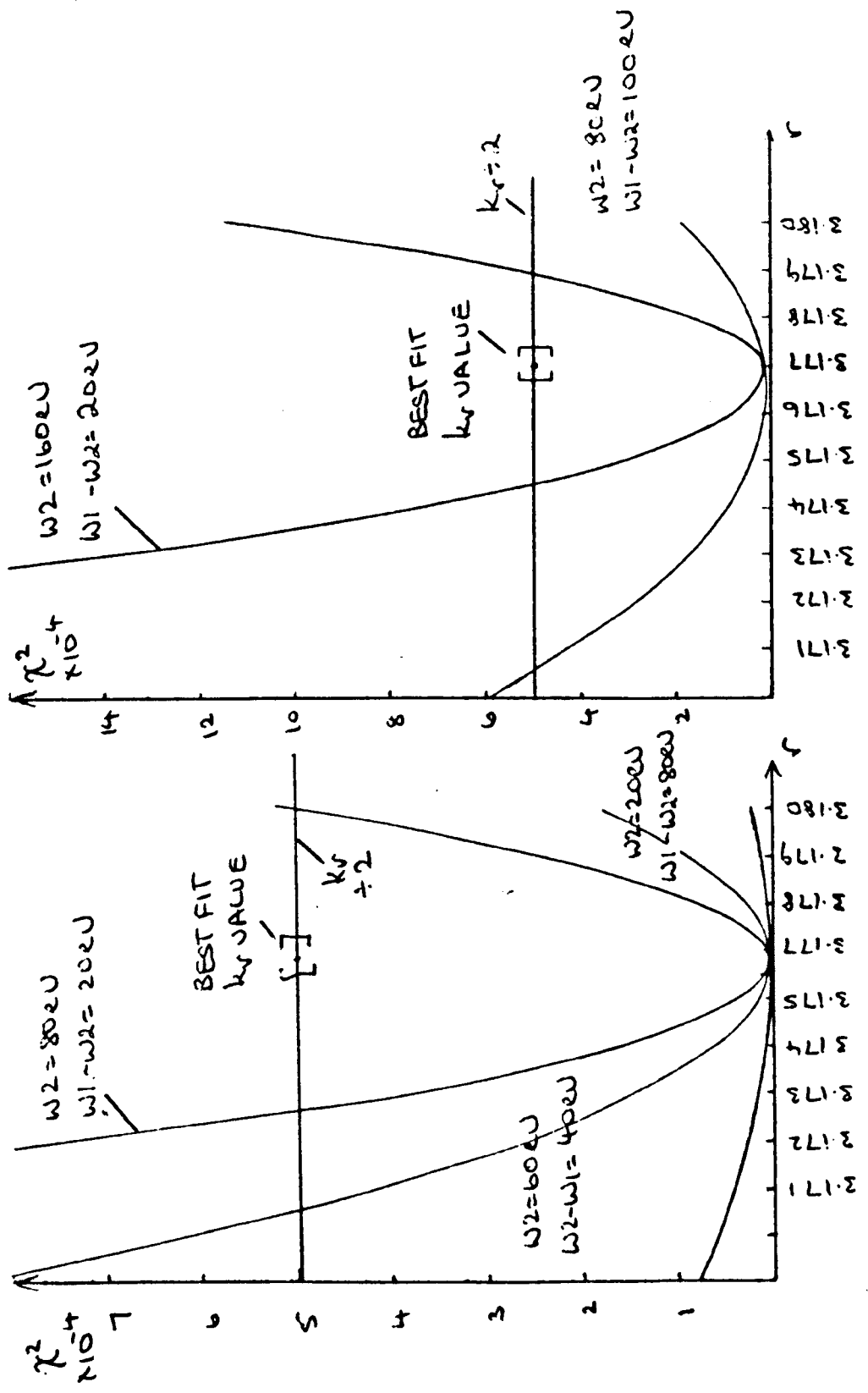
Figure 6.12   The variation of $(X_2^2)_r$ and k_r with r as the post-edge fitting range is varied.
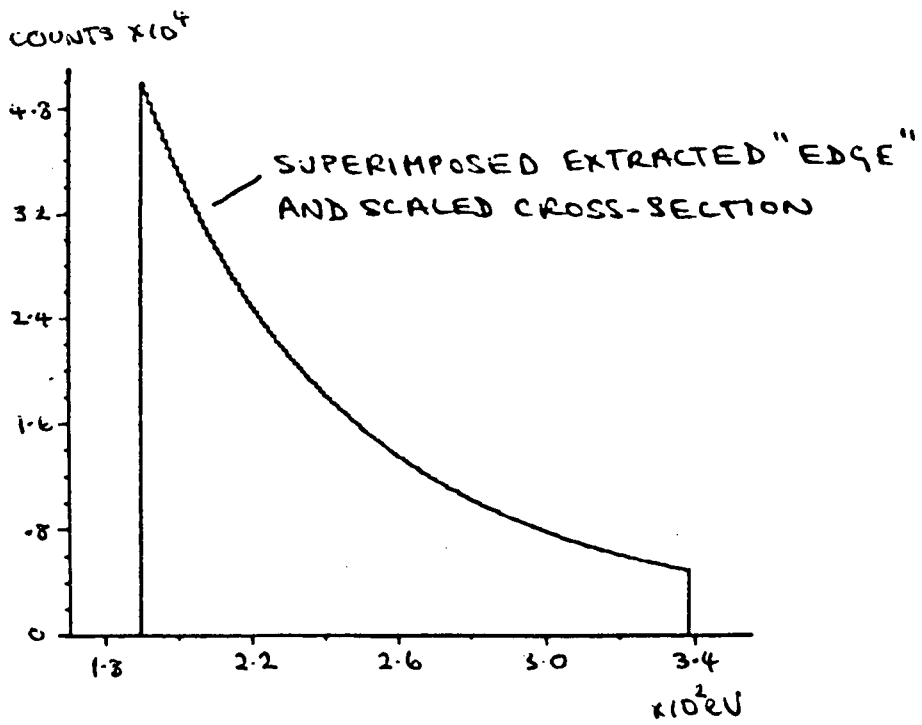
Figure 6.13

fitting range is decreased by increasing the convergence offset. Since k_r varies (almost linearly) with r it is important to have a well defined minimum in the $(X_2^2)_r$ curve so that the best fit k_r value will also be well defined. Thus, it is important to maximise the post-edge fitting range by minimising the convergence offset.

When a $(X_1^2)_r$ graph is superimposed on a $(X_2^2)_r$ graph (shown schematically in Figure 6.14(a)) the minima should coincide at the same r value. This r value would therefore correspond to the value of r obtained if $(X_T^2)_r$ were minimised, and this was found in practice. However, when minimising $(X_T^2)_r$ on a real ionisation edge the position (with respect to r) of the $(X_1^2)_r$ and $(X_2^2)_r$ minima are never identical and one chi-square curve can be significantly higher than the other (e.g. Figure 6.14(b)). This is especially evident when the background does not precisely follow an $A(\Delta E)^{-r}$ form (due, for example, to structure from a preceding edge) and structure is present on the edge of interest. In such circumstances the r value corresponding to the minimum $(X_T^2)_r$ value will always be between the minimum $(X_1^2)_r$ and $(X_2^2)_r$ values, although one chi-square curve can dominate the other. This will be discussed briefly later in this section.

So far the fitting routine has been tested on an edge without noise. It is therefore of interest to run the program using only the $(X_1^2)_r$ minimisation to fit an $A(\Delta E)^{-r}$ curve to the pre-edge region of a real spectrum. The signal extracted by extrapolation of this curve can then be compared with the signal extracted (using the same fitting range) by the extrapolation routine written by Crozier (1985).

Figure 6.15 shows the O(K) edge from the mineralised bone spectrum. Table 6.2 summarises the pre-edge fitting range, post-edge signal integration range and signal extracted. The characteristic signals

91
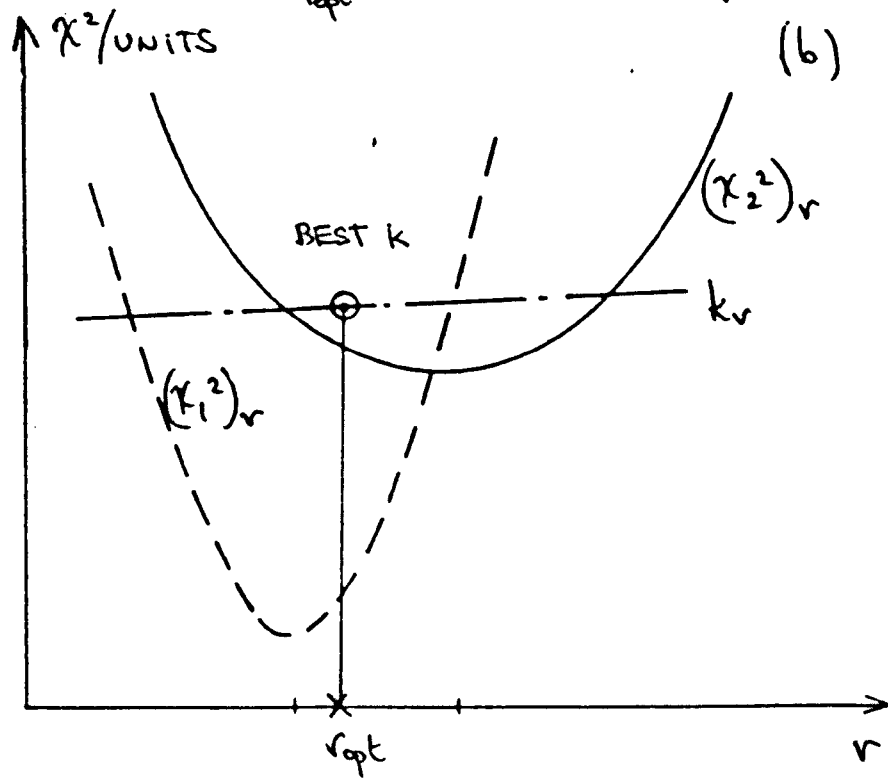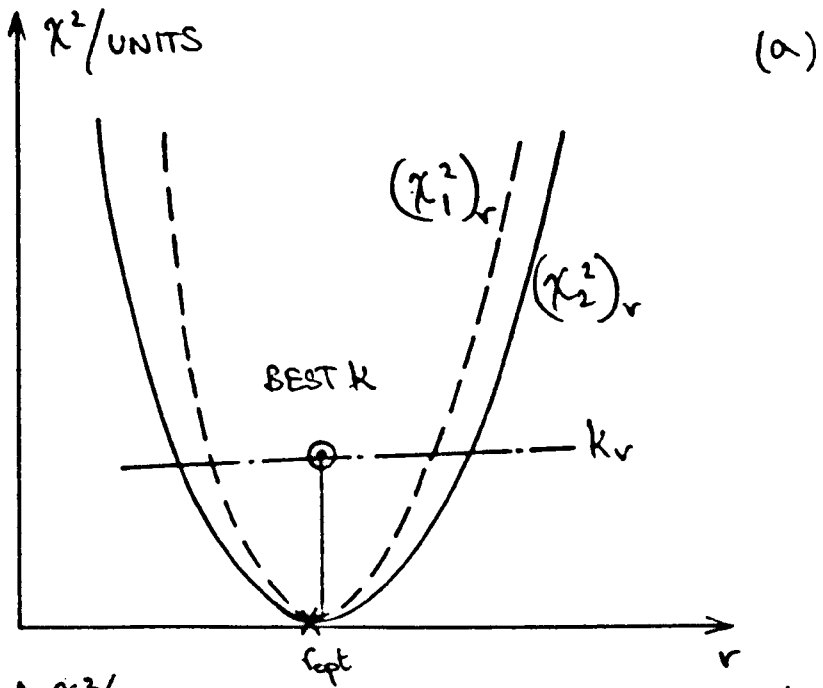
Figure 6.14

Fitting Routine	Fitting range	Post-edge integrated signal counts	Difference
Extr. Single-St.	50/50/0	0.1809×10^{10} 0.1821×10^{10}	$\langle 0.7\%$
Extr. Single-St.	30/30/0	0.1804×10^{10} 0.1810×10^{10}	$\langle 0.5\%$
Extr. Single-St.	40/40/0	0.1564×10^{10} 0.1573×10^{10}	$\langle 0.6\%$

Table 6.2

extracted (for given pre-edge fitting range) agree to better than 1%.
This discrepancy is less than the uncertainty in the signals predicted
by the extrapolation routine of Crozier (1985) (typically about 2%).
Figure 6.15 shows two curves superimposed calculated using the $(X_1^2)_r$
minimisation and the routine written by Crozier (1985). It is not
possible visually to tell the difference between the two curves.

The O(K) edge has a background which follows the $A(\Delta E)^{-r}$ form
reasonably well, i.e. although Ca and P edges will contribute to the
O(K) background $A(\Delta E)^{-r}$ fits with reduced chi-square values of ~1 can
be obtained. In addition, the O edge does not have a lot of structure
present and, since it results from a K shell ionisation, the hydrogenic
cross-section is expected to describe the edge shape reasonably well.
Therefore, this edge was used to investigate the variation of chi-square
with r.

Figure 6.17 shows a graph of $(X_1^2)_r$, $(X_2^2)_r$ and $(X_T^2)_r$ versus r for
the O edge. The pre-edge fitting range was 40 eV and the post-edge
range was 50 eV. As expected, there is a small difference between the
r values (and therefore the $A(\Delta E)^{-r}$ backgrounds) which individually
best fit the pre and post-edge ranges. Figure 6.16 shows these two
backgrounds. The solid line has been calculated with r=3.57 (the
optimum value for the pre-edge range) and the dotted line with r=3.32
(the optimum value for the post-edge range). There is little
difference between the integrated number of edge counts (less than 1 %
when either curve is used to model the background). As expected, the r
value corresponding to the minimum of the $(X_T^2)_r$ curve was found to lie
between the minima of the $(X_1^2)_r$ and $(X_1^2)_r$ curves and so the $A(\Delta E)^{-r}$
curve obtained by the single-stage technique (i.e. using $(X_T^2)_r$
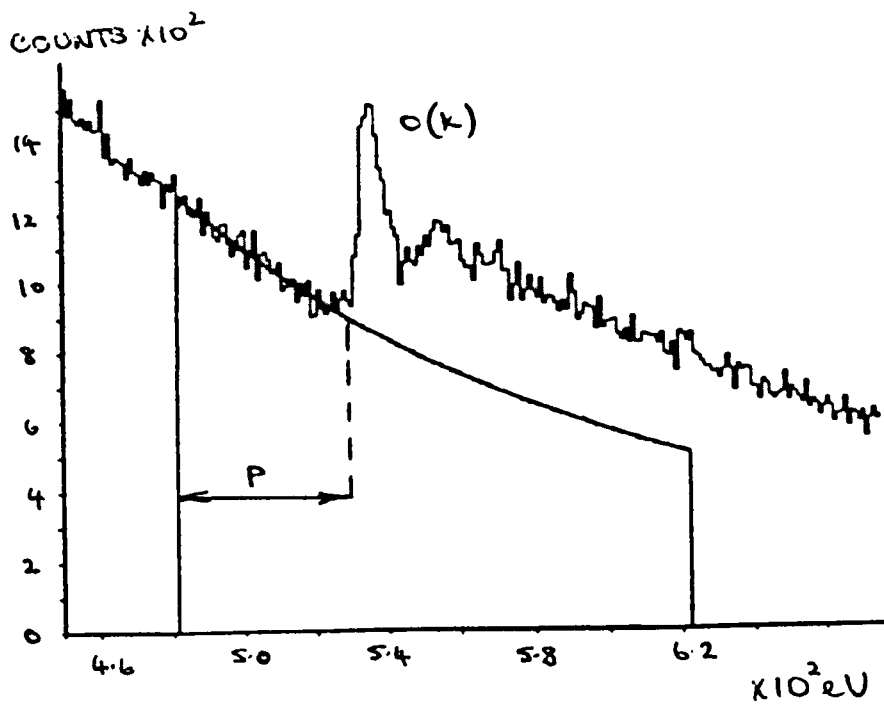
Figure 6.15
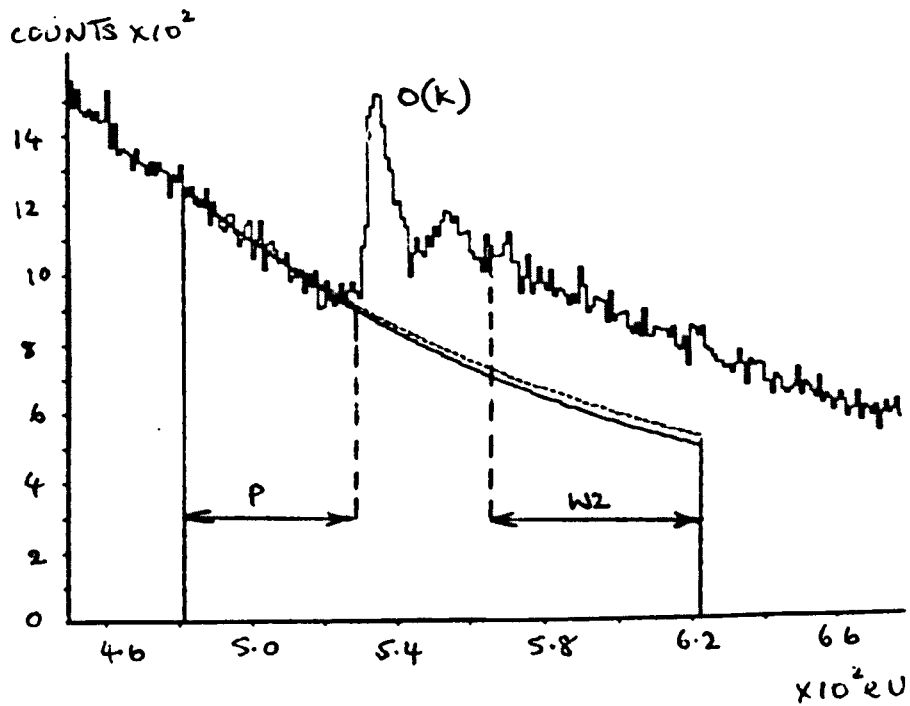
Figure 6.16
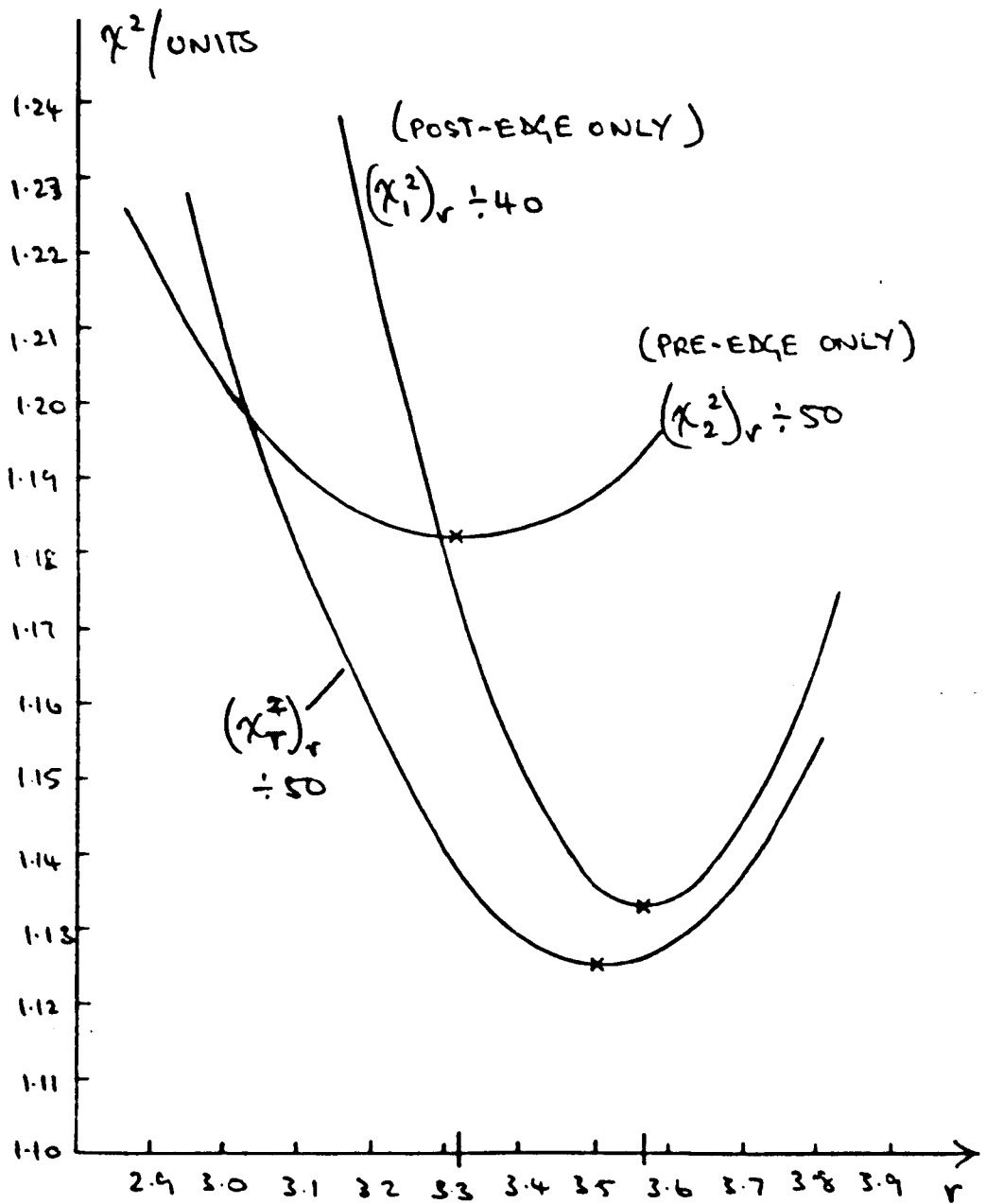
FIGURE 6.17

minimisation) lies between the two $A(\Delta E)^{-r}$ curves superimposed on Figure 6.16. The former curve represents a compromise between the curves best fitting the pre and post-edge ranges. Thus, using the single-stage technique, r, A and k values have been obtained which are acceptable over the total energy range of interest, rather than only in front of the edge. Examples of curve fitting on a number of edges are given in Section 6.8, together with the match between the scaled cross-section and the stripped-edge shapes.

6.7 SUMMARY

A new method of analysing electron energy loss spectra has been suggested in which the characteristic signals are separated from the total spectrum and quantified in a single process. When fitting the $A(\Delta E)^{-r} + k\dfrac{d\sigma}{d(\Delta E)}$ function to an ionisation edge the $A(\Delta E)^{-r}$ curve was forced to pass through the pre-edge region. The A value is calculated using the pre-edge region and the k value, as expected, from the post-edge region. The curve fitting procedure has been tested on artificial and real ionisation edges with satisfactory results. Rounding error was not obviously present. The program produces a fit to an edge in 2-3 min (dependent upon the size of the fitting ranges); however, the program usually has to be run twice so that $A(\Delta E)^{-r} + k\dfrac{d\sigma}{d(\Delta E)}$ curves are calculated at sufficiently fine intervals.

6.8 SPECTRAL PROCESSING USING THE SINGLE STAGE TECHNIQUE

As will be described in Chapter 7, very few spectra were acquired from mineralised bone due to the difficulties involved in specimen

preparation. Thus, in addition to the mineralised bone spectra, three other spectra were used to investigate the single-stage technique. The first two spectra were acquired by P A Crozier from samples of a second phase carbide precipitate in a ferritic steel and from boron nitride. The third spectrum was acquired by S Duckworth from a sample of vanadium carbide. Extraction of the signals in the mineralised bone, ferritic steel, and vanadium carbide spectra present difficulties if the standard extrapolation method is used.

Figures 6.18 to 6.20 show the P, Ca and O edges of the mineralised bone spectrum. Extraction of the Ca edge is difficult because of structure present in the carbon edge. The background preceding the P edge follows an $A(\Delta E)^{-r}$ form over a limited energy range because of the proximity of the low-loss region of the spectrum. As a result, the P signal tends to be underestimated when the background is extrapolated under the edge. Figures 6.18 to 6.20 show backgrounds fitted to the P, Ca and O edges using the single-stage technique. The pre-edge (P) and post-edge (W2) fitting regions are indicated. The stripped edge shapes and scaled theoretical edge shapes are also shown. The theoretical edge shapes will be discussed in Section 6.9. As shown, satisfactory agreement exists between the theoretical and experimental edge shapes provided the regions close to the edge onsets are ignored.

Figure 6.21 shows the ferritic steel spectrum. Here the close succession of $O(K)$, $Cr(L_{2,3})$, $Mn(L_{2,3})$ and $Fe(L_{2,3})$ edges means that limited pre-edge fitting ranges are available. In addition, the post-edge regions of the Cr and Mn edges are also small, the Cr (L_1) edge underlies the $Fe(L_{2,3})$ edge, and there is structure present in all the pre-edge fitting regions due to preceding edges. Using the pre-edge
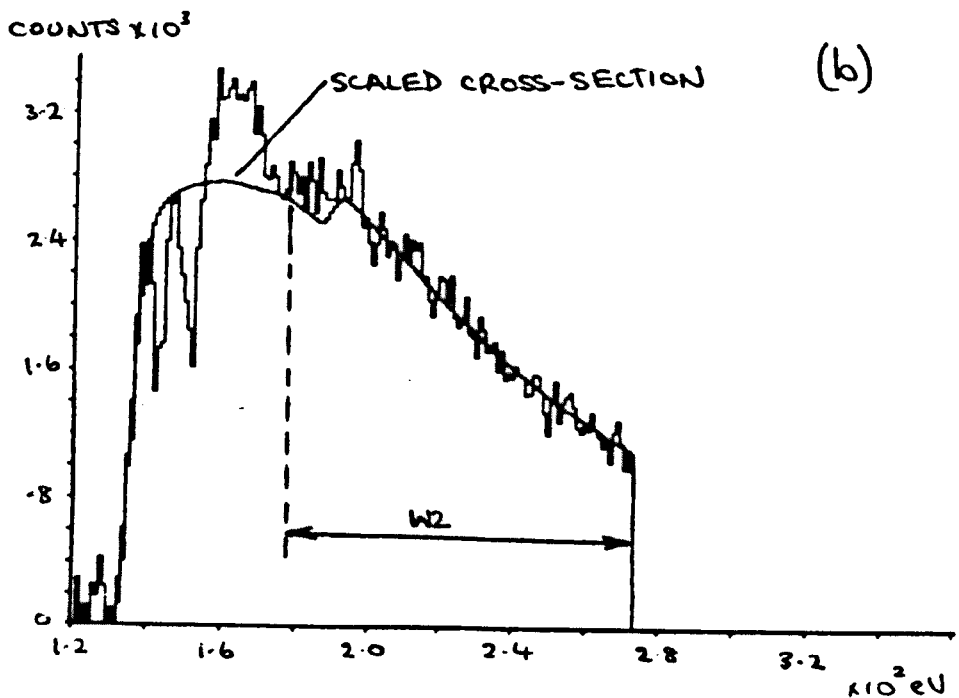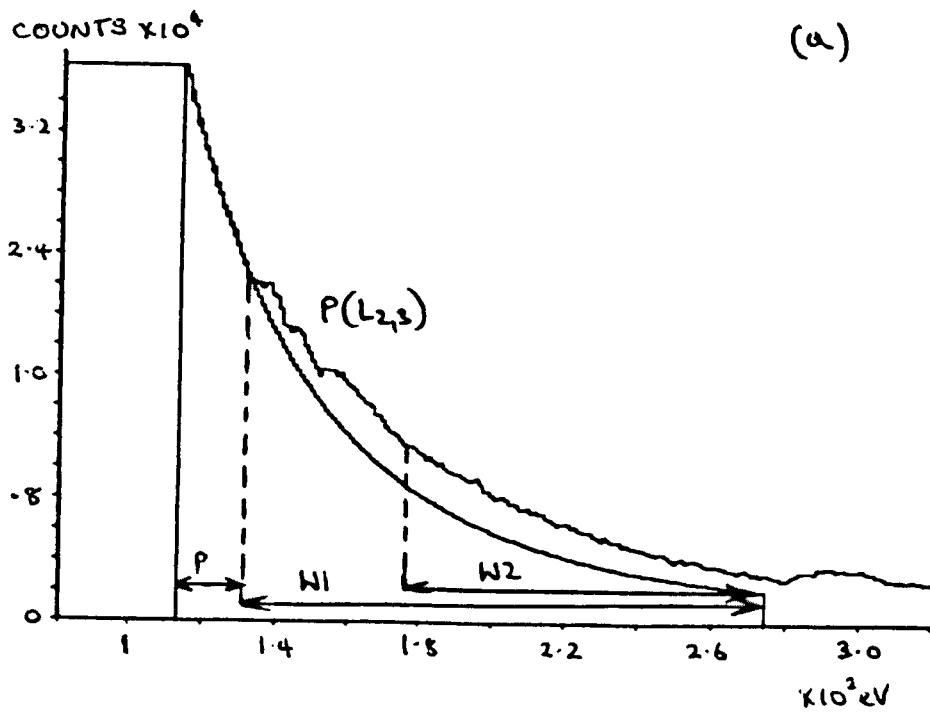
Figure 6.18   Mineralised bone spectrum, P edge.
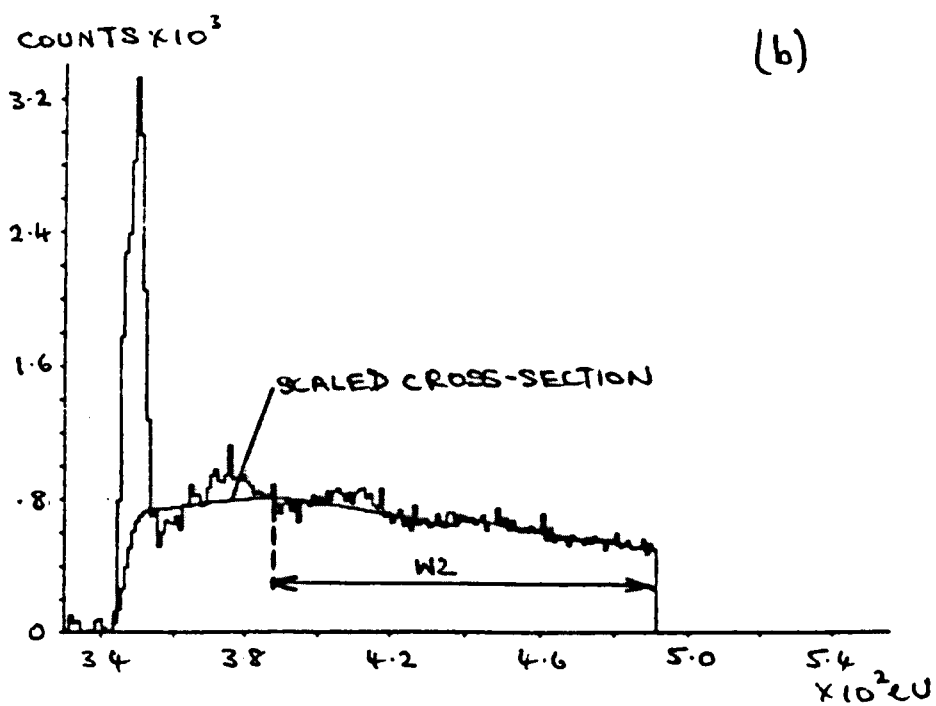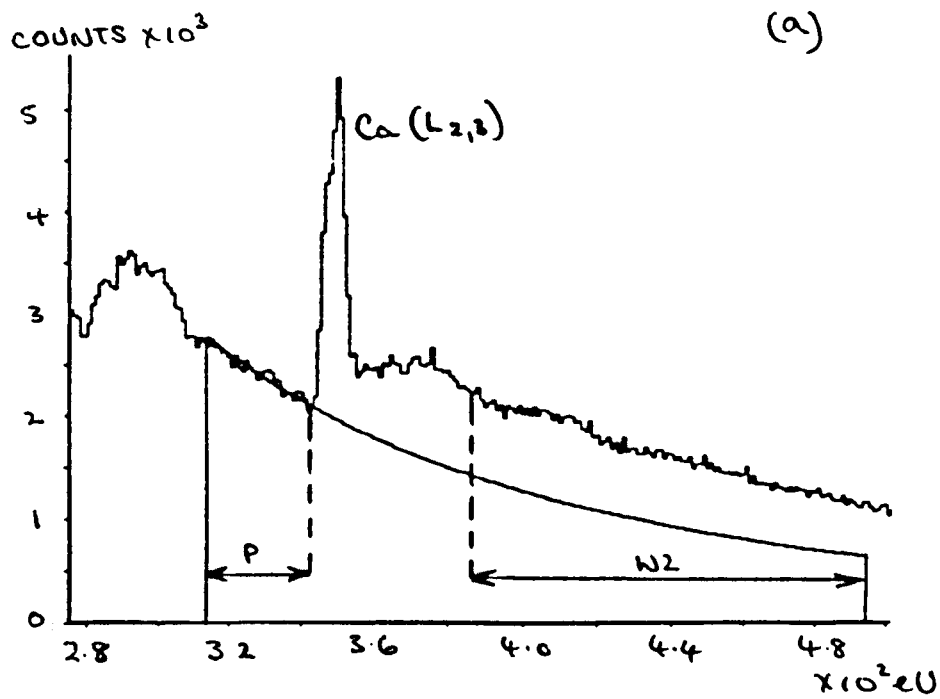
Figure 6.19   Mineralised bone spectrum, Ca edge
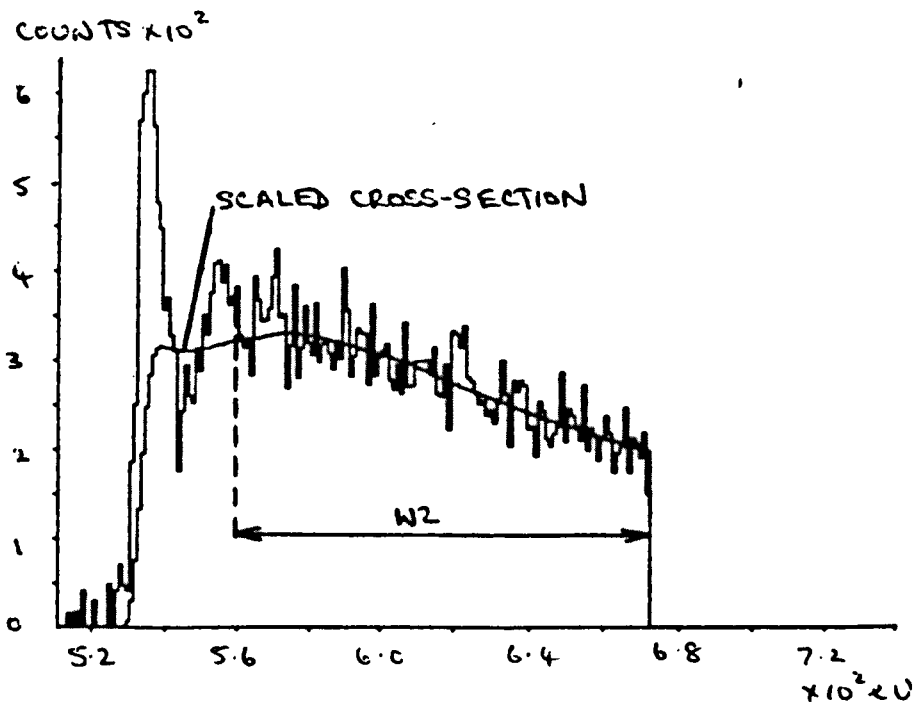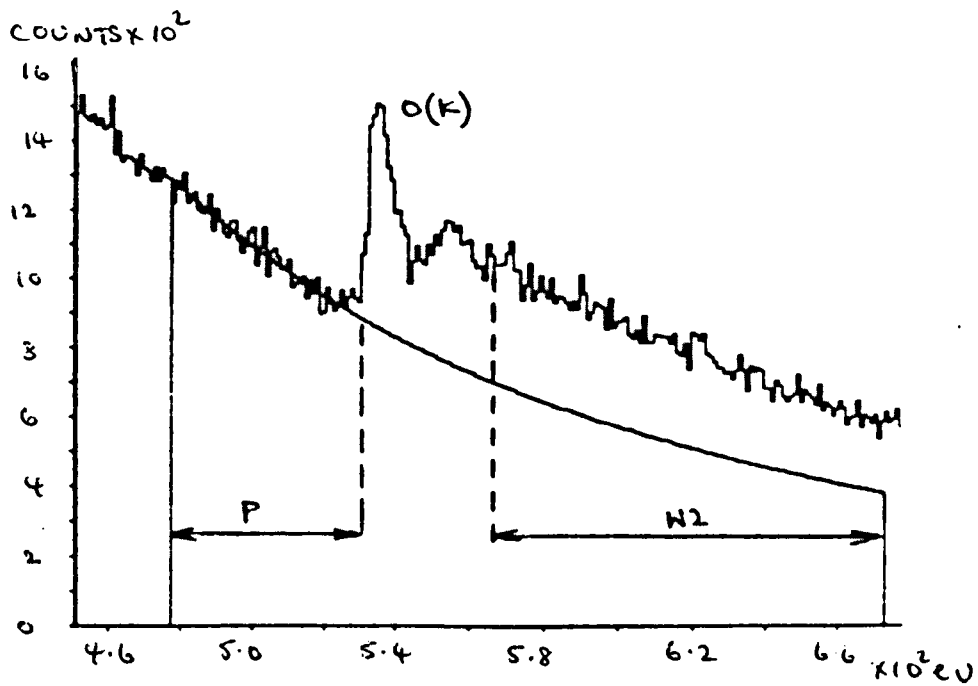
Figure 6.20   Mineralised bone spectrum, O edge
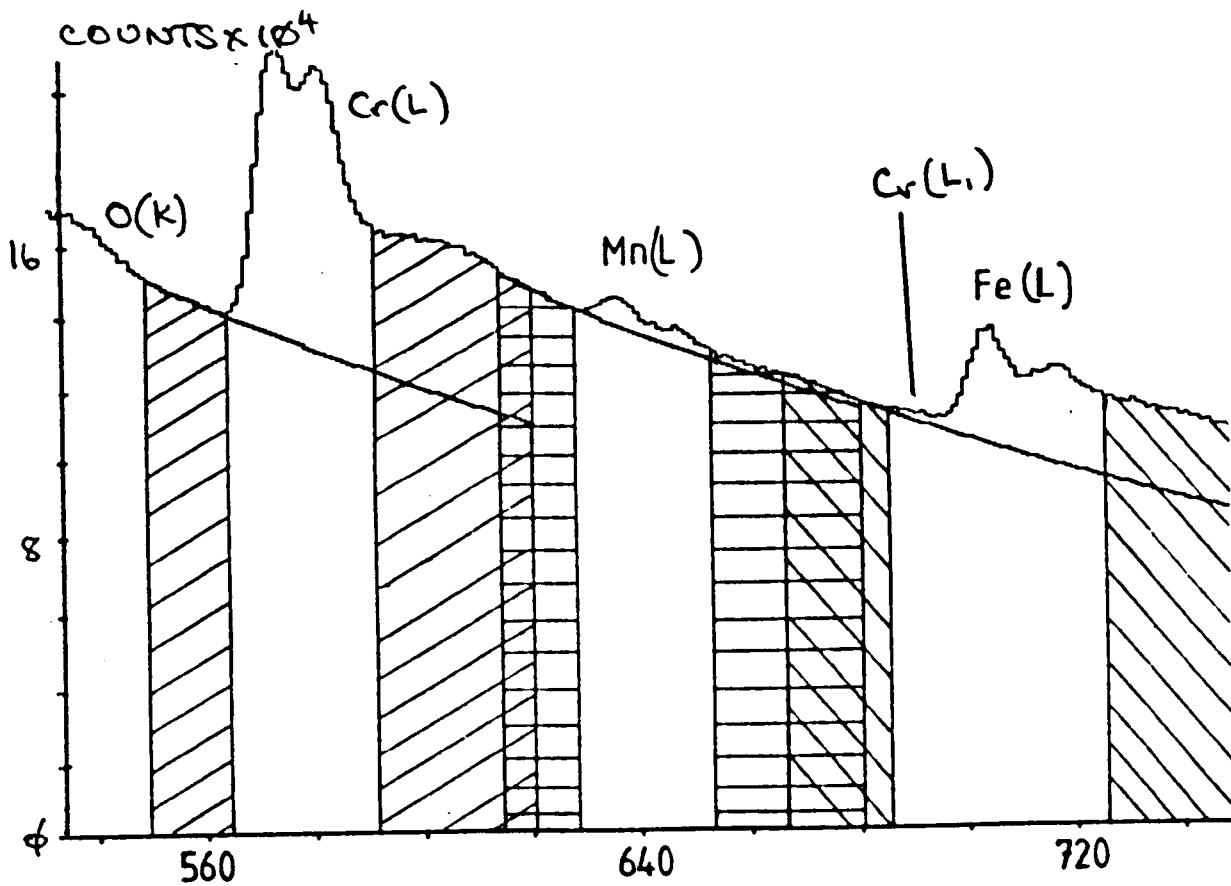
Figure 6.21   Ferritic steel spectrum

(a)
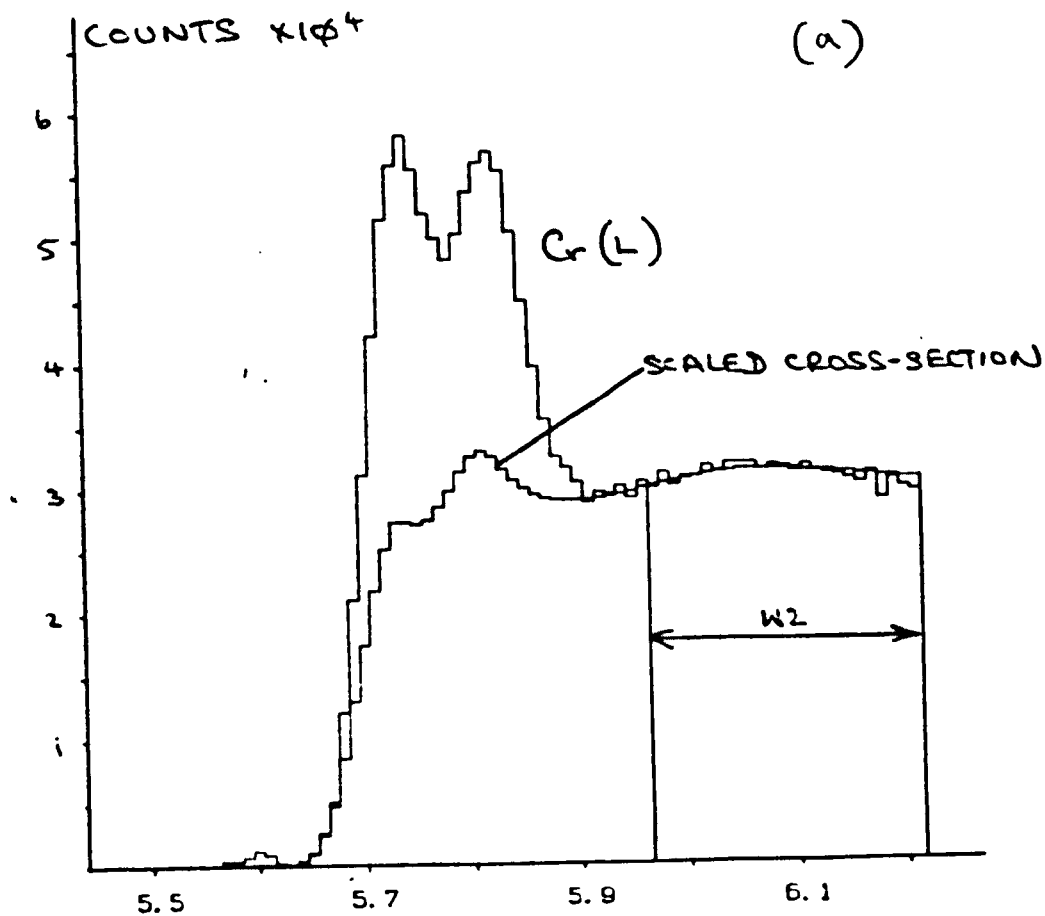
Ferritic steel spectrum, Cr edge

FIGURE 6.22
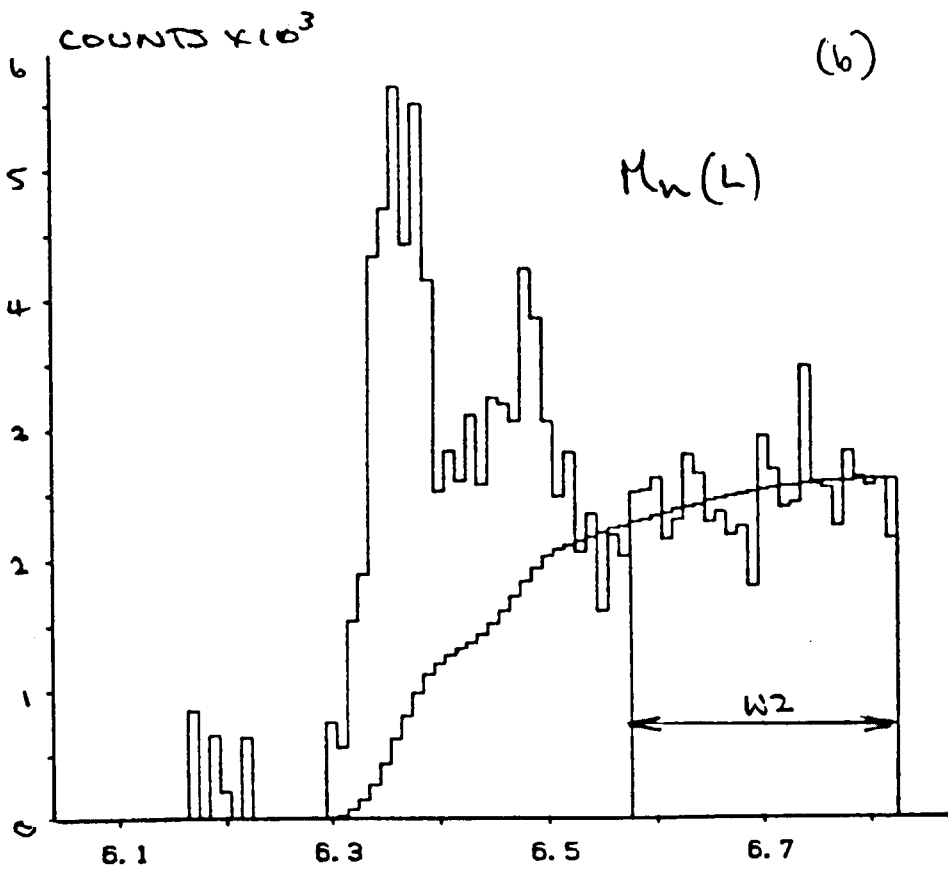
Ferritic steel spectrum, Mn edge
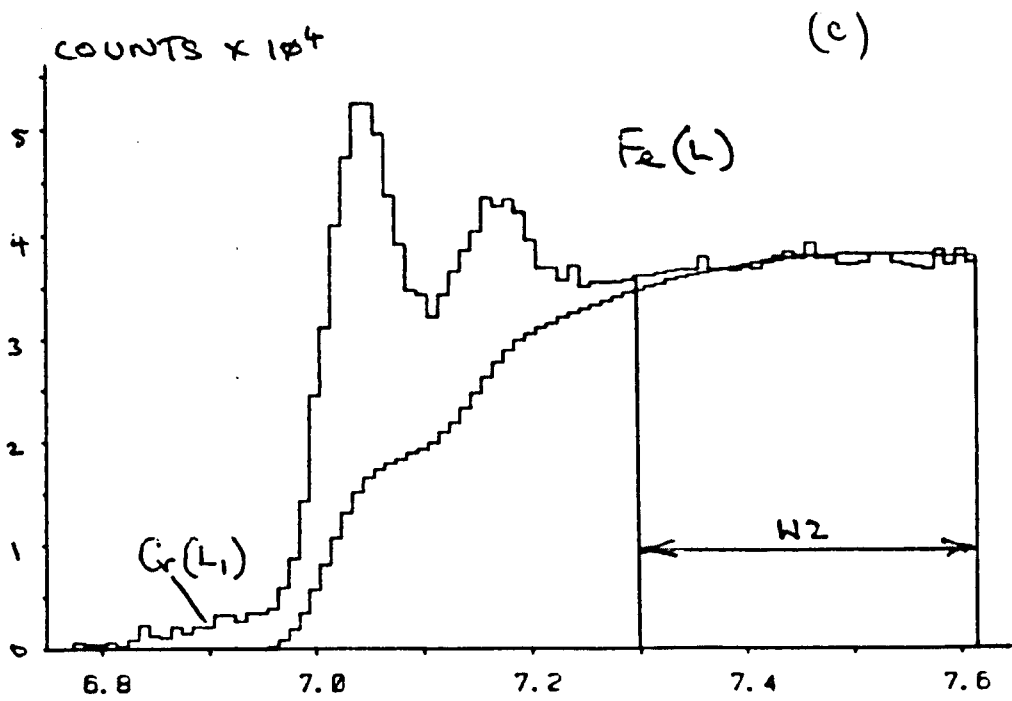
Ferritic steel spectrum, Fe edge

and post-edge fitting regions shown in Figure 6.22, stripped edge shapes were obtained which, away from their onsets, again follow the theoretical expectation (see Figures 6.22(a) to (c)).

Figures 6.23 and 6.24 show the B(K) and N(K) edges in the boron nitride spectrum. Large pre-edge regions are available here (and therefore the extrapolation procedure could be carried out with some confidence). The backgrounds shown in Figures 6.23 and 6.24 have been fitted using the single-stage routine. Again, the pre-edge and post-edge fitting ranges are indicated. The stripped edges and the theoretical edge shapes are also shown.

Figure 6.25(a) shows a spectrum acquired from a vanadium carbide (VC) spectrum. Extraction of the C signal presents particular problems since the background follows an $A(\Delta E)^{-r}$ form over a very limited energy range. There is no obvious reason for this change in background form; e.g. a closely preceding edge, plasmon counts significantly underlying the edge etc. (Duckworth, personal communication). A background fitted using the extrapolation routine is also shown in Figure 6.25(a). The pre-edge fitting range was chosen by Duckworth because, in a range of VC spectra, it provided VC ratios closest to the expected values. However, the extracted C signal appears to be underestimated. In contrast, Figure 6.25(c) and (d) show the signal extracted using the single-stage technique, and clearly a better match between experimental and theoretical edges has been achieved. A comparison of VC ratios obtained from a series of spectra using both extrapolation and single-stage techniques would be useful.
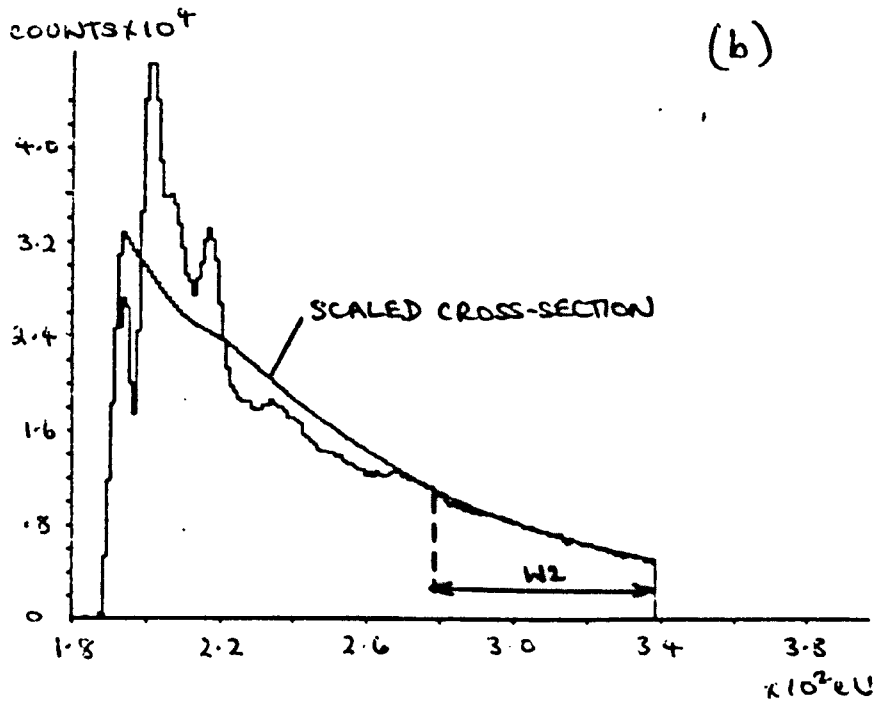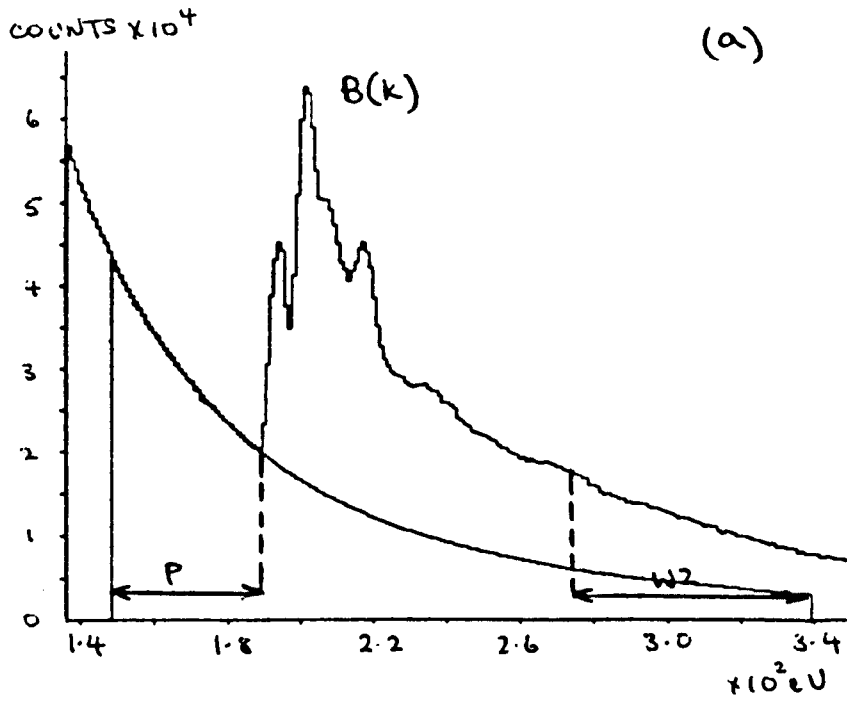
Figure 6.23 Boron Nitride spectrum, B edge
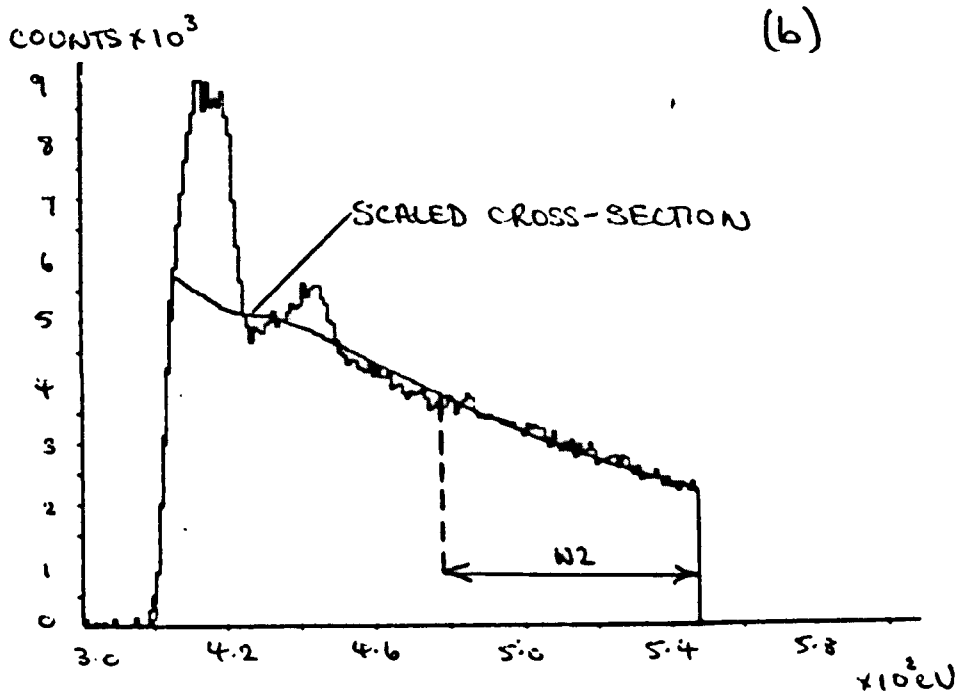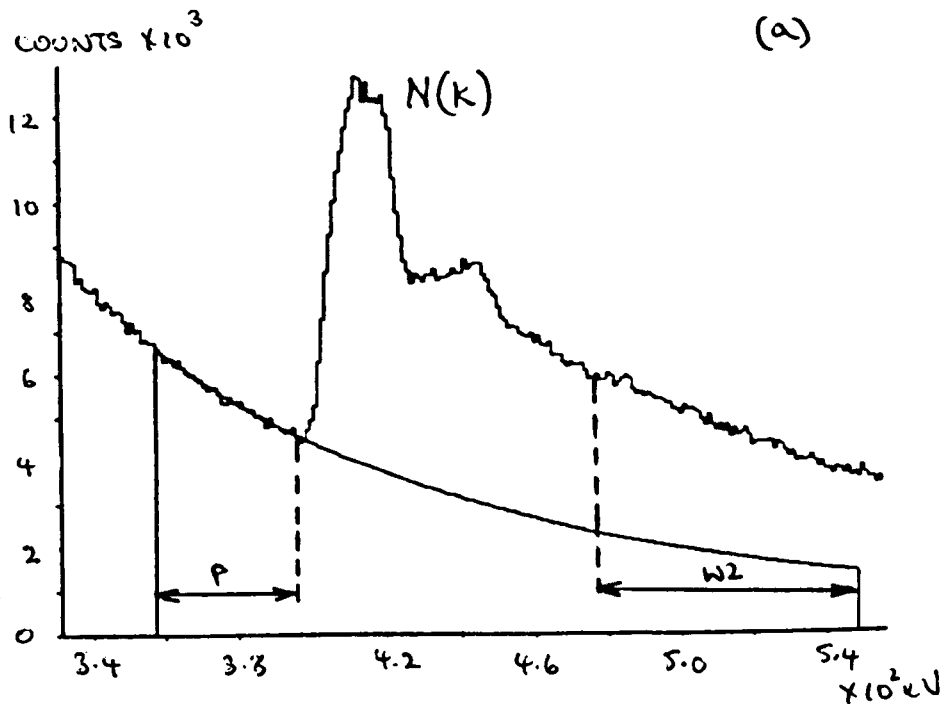
Figure 6.24 Boron Nitride spectrum, N edge
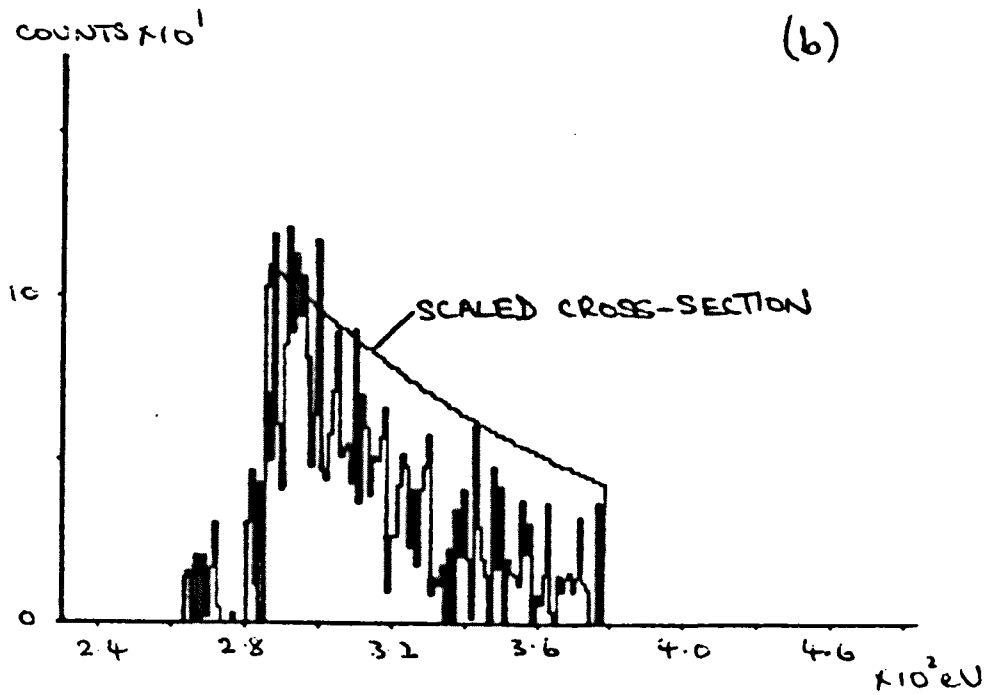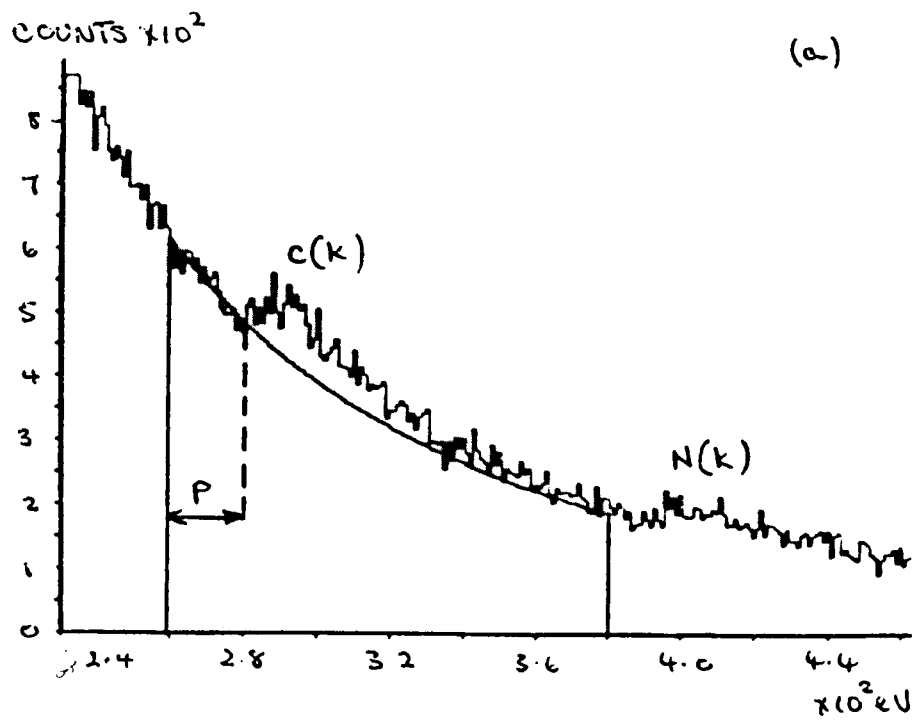
Figure 6.25(a),(b)   Vanadium Carbide spectrum, C edge

The spectrum has been processed using the extrapolation
technique.
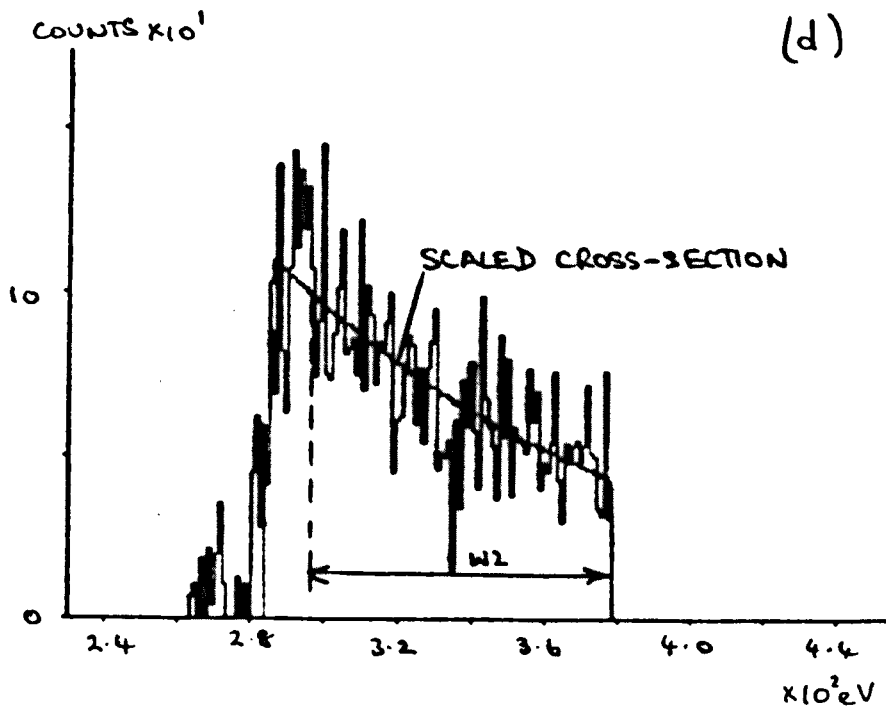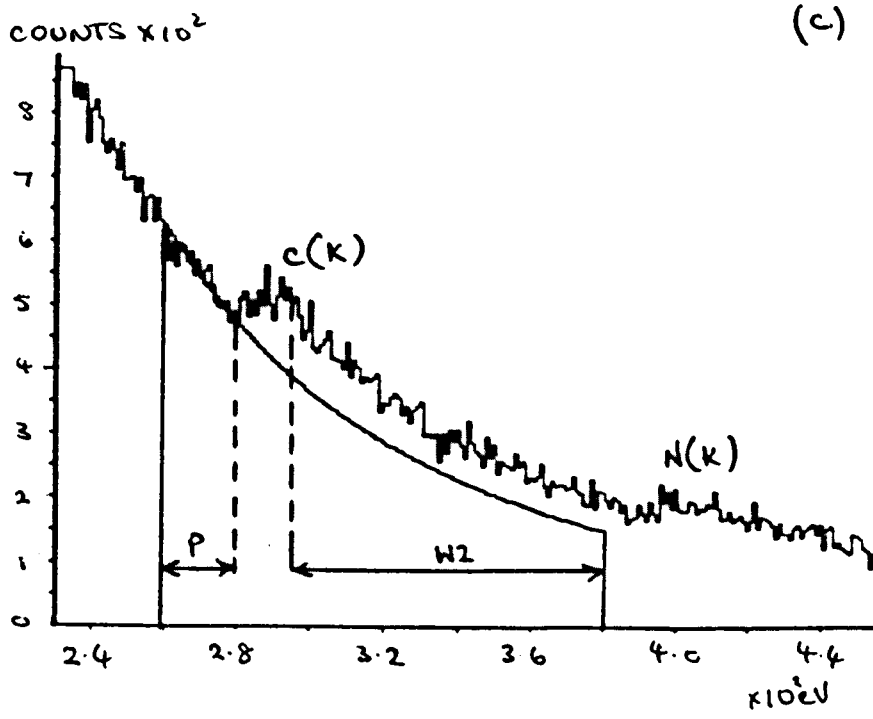
Figure 6.25(c),(d)   Vanadium Carbide spectrum, C edge

The spectrum has been processed using the single-stage technique.

6.9 EDGE SHAPES-THE THEORETICAL CROSS-SECTION MODELS

As discussed in Section 2.8, two cross-section models are available for calculating theoretical edge shapes, the Hartree-Slater (HS) model of Leapman et al (1980) and the semi-analytic modified hydrogenic (H) model of Egerton (1983). The shape of energy differential cross-sections for the L-shell is correctly predicted by the HS model (Rez 1984); however, the H model requires the use of an empirical factor. As expected, the edge shapes predicted by either model differ, e.g. Figure 6.26 shows the Cr $(L_{2,3})$ edge calculated using the HS and H models. Although the most significant differences between the HS and H edge shapes occur within the first 30 eV, the edges also differ within the energy region W2. Thus different results are obtained when H cross-sections, rather than those predicted by HS, are used for quantitation.

Crozier (1985) has compared experimental EDX and EEL Cr/Fe ratios calculated using both HS and H cross-sections and suggests that the HS are more accurate. It was not possible to directly compare HS and H cross-sections for most of the edges of interest here (e.g. $P(L_{2,3})$, Ca were not available. Egerton(1984) has compared cross-sections $(L_{2,3})$, O(K), N(K) and B(K)) since the HS cross-sections calculated for these elements and found good agreement. Table 6.3 summarises this comparison. Clearly these predictions of cross-section for O(K), N(K) and B(K) by both models are very similar. This is not surprising since the overall shape of the K-shell cross-sections are predicted well by both models (Egerton, 1979, Rez 1984), although the theoretical H K-edge shapes are slightly lower at threshold (Leapman et al, 1980). Egerton (1979) has compared H K-shell cross-section with photoabsorption data and found good agreement over the entire atomic number range.

96
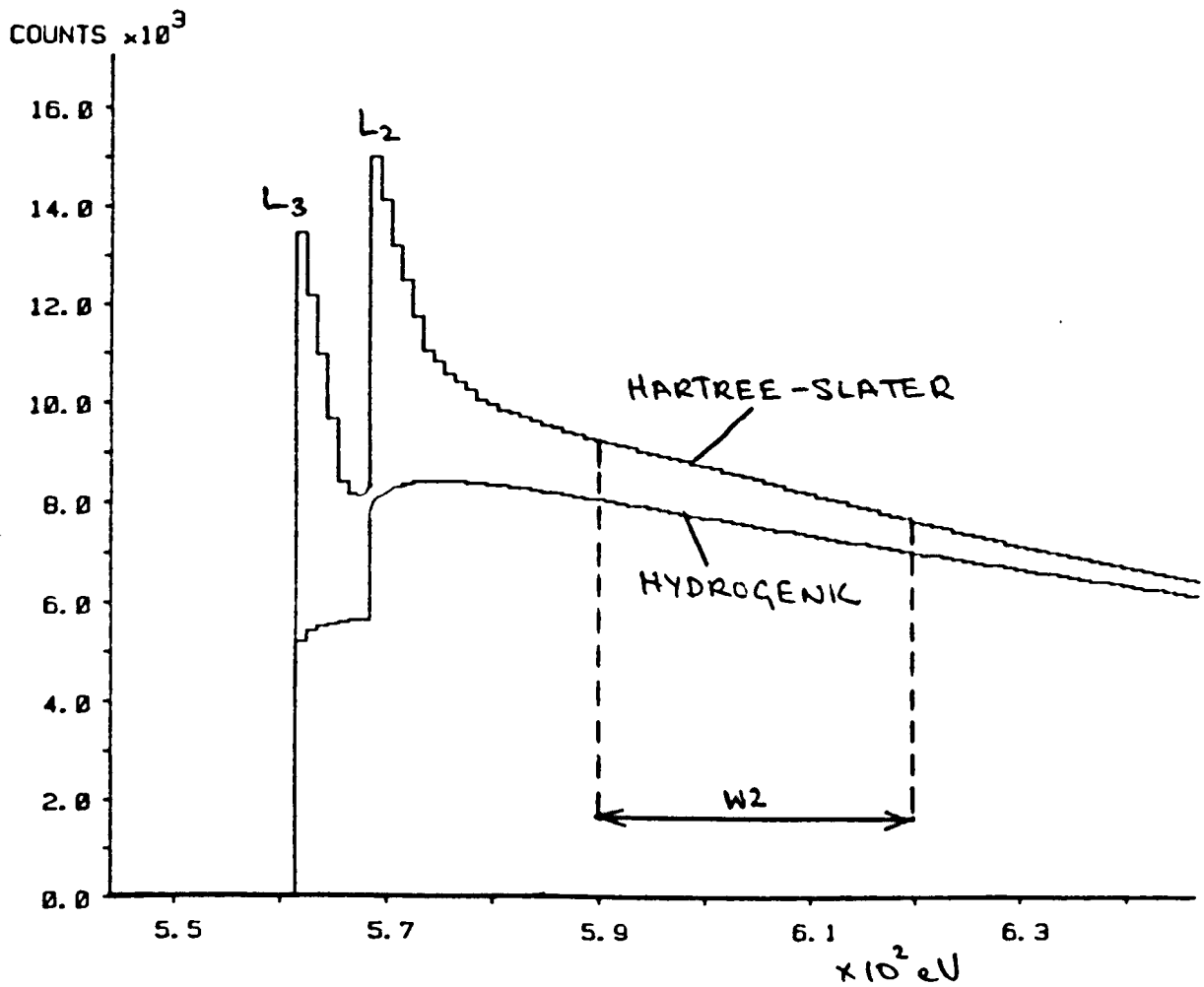
Figure 6.26 Cr edge calculated using the HS and H cross-section models. Collection semi-angle 27mrad. The HS cross-section was supplied by Dr P Rez.

Edge	Δ /eV	β/mrad	cross-section/m^2 HS	H
P(L)	50	10	5.0	5.0
Ca(L)	70	10	1.2	1.2
O(K)	100	3	4.0	3.7
Co(L)	100	10	0.15	0.17
Cr(L)	100	10	0.48	0.42

Table 6.3 A comparison between HS and H cross-sections for several of the elements of interest here (from Egerton (1984)).

β:- electron collection semi-angle
Δ:- cross-section integration range

6.9.1 Spin-orbit Splitting

L-shell cross-section calculated from HS and H generalised oscillator strengths do not take account of spin-orbit splitting; i.e. the 6 states available to the 2p orbital are considered degenerate. Spin-orbit splitting results from the interaction of the electron spin magnetic dipole moment and the internal magnetic field of the atom. The latter is related to the electrons orbital angular momentum. It can be shown (e.g. Eisberg et al, 1974) that spin-orbit splitting causes the L_2 edge to appear at a slightly higher energy loss than the L_3 edge. Ahn et al (1985) take account of spin-orbit splitting by first calculating the L_3 edge and then adding the contribution from the L_2 edge (starting at the L_2 edge threshold energy) with a weighting factor of 0.5. The HS and H edge shapes shown in Figure 6.26 have both been calculated using the procedure described above. Spin-orbit splitting is only significant for the transition metals (e.g. Cr, Mn and Fe) and not for the P and Ca edges.

6.9.2 Plural Inelastic Scattering

As discussed in Section 2.10, plural inelastic scattering by valence electrons within a sample causes a redistribution of intensity within the energy loss spectrum. Egerton (1983) has shown that the contribution to an ionisation edge from electrons which have caused a valence shell excitation (in addition to the inner-shell excitation) can be removed by first subtracting the background from the edge and then deconvoluting the edge signal using the intensity distribution in the low loss region and zero loss peak as a deconvolution function. Egerton (1983) suggests replacing the zero loss peak by a delta function of magnitude equal to the sum of the counts in the zero loss peak. This avoids any

attempt to correct the signal for the energy width of the zero loss peak since this would result in the deconvoluted edge being dominated by noise.

The procedure adopted here was to convolve the energy differential cross-section with the low loss region and zero loss peak before processing each experimental edge of interest. The convolution routine was written by J H Paterson. As an example, Figure 6.27(a) to (c) show the P, Ca and O hydrogenic cross-sections before and after convolution with the low loss (and zero loss peak) of the mineralised bone spectrum (Figure 6.1(a)). Clearly these convolved edge shapes can only be used to process this particular spectrum. Each of the edge shapes are scaled so that, if they were extended up to a high enough energy loss, the areas under the convolved and unconvolved edges would be the same. As expected, plural inelastic scattering removes counts from the edge onset and there is a nett gain in counts at higher energy losses. Convolution of the cross-section is simpler than deconvolution of the experimental edges and does not result in an increase in noise. This was especially important when extracting the small Mn signal from the ferritic steel spectrum.

6.9.3 Theoretical and Experimental Edge Shapes

As discussed in Section 2.9, solid-state effects such as ELNES and EXELFS are not taken into account in the atomic cross-section models. The clear peak at the Ca edge onset (Figure 6.19) is due to transitions to empty d-states (Ahn et al 1985). In the transition metals (e.g. Figure 6.22) the two peaks at threshold are again due to transitions to unoccupied bound d-states. Ahn et al (1985) note that although the

Figure 6.27

Figure 6.27
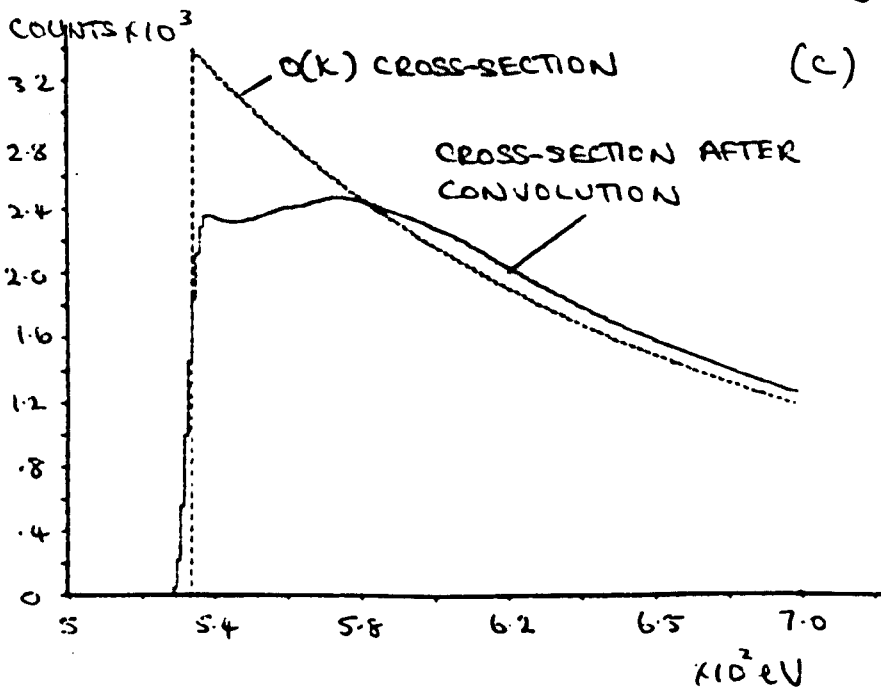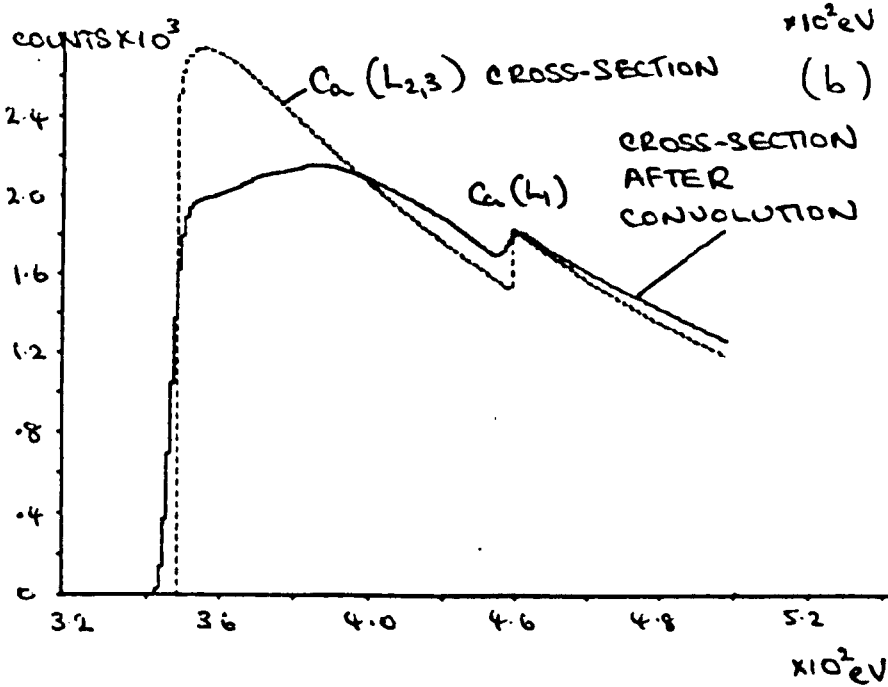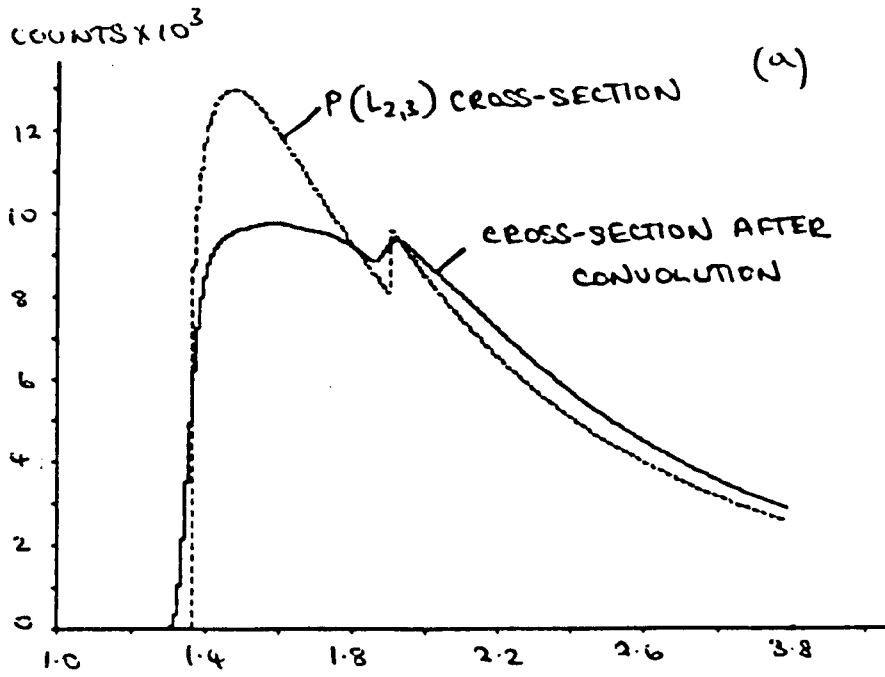
ratio of such peaks is generally not 2:1, the calculation of the transitions to the continuum are in the expected 2:1 ratio. EXELFS modulation extending up to ~150 eV past the edge onset is pronounced in the B(K) edge; however, statistical fluctuations in the O(K) signal (Figure 6.20) obscure similar detail. In the case of the B(K) edge, the structure at threshold is due to transitions to σ and π antibonding orbitals (Ahn et al 1985).

Comparison between experimental and theoretical edge shapes could be used to isolate the oscillatory EXELFS intensity. Once isolated, these data can then be used to calculate radial distribution functions (e.g. Csillag, 1984). Thus, a single-stage EELS/EXELFS analysis procedure is possible; however, the problems associated with standard EXELFS analysis would still be present; i.e. statistical noise in the data and adjacent edges. The former problem would be increased if a deconvolution procedure to remove plural scattering was employed.

6.10 COMPARISON BETWEEN THE EXTRAPOLATION AND SINGLE-STAGE TECHNIQUES

As discussed earlier, extraction of the Ca and P signals in the mineralised bone spectrum, and the Cr, Mn and Fe signals in the ferritic steel spectrum provides problems if the extrapolation technique is used. It was therefore of interest to compare the single-stage and extrapolation techniques to see if the former technique offered any advantages. To determine to what extent choice of the background fitting region affects the magnitude of the characteristic signals extracted (using both techniques), the number of counts in the signals were calculated as the pre-edge fitting ranges were varied. The mineralised bone spectrum is considered first.

The post-edge fitting ranges were kept at 150 eV for the Ca and O signals and 140 eV in the case of the P signal. The pre-edge range was extended from 20-35 eV (5 eV steps) in the case of the P signal and from 20 to 50 eV (10 eV steps) in the case of the Ca and O signals. Table 6.4(a) shows the mean number of counts in the entire post-edge regions (W1) and the post-edge fitting ranges (W2). Also shown is the standard deviation in the means from which it can be seen that the extracted signals varied less when the single-stage technique was used.

Quantitation of the characteristic signals in the ferritic steel spectrum presents difficulties because both pre and post-edge fitting ranges are limited. Again, variation in the characteristic signals were determined by varying the pre-edge fitting range (from 15 to 30 eV in 5 eV steps) whilst keeping the post-edge fitting ranges constant. (Typically 25 eV windows displaced beyond their edge onsets by the same amount). Table 6.4(b) shows the mean number of counts in the entire post-edge regions (W1) and the post-edge fitting ranges (W2). From the standard deviation in the means it can be seen that for Cr and Fe (the larger signals), the variations obtained using either processing technique were <10%, but considerably greater for the smaller Mn signal. In the latter case, the spread obtained using the constrained fitting of the single-stage technique was significantly smaller than when the extrapolation method was used.

In summary, the single-stage and extrapolation techniques have been compared on two spectra where the background (i.e. pre-edge) fitting regions were restricted. In the case of the mineralised bone spectrum long post-edge regions were available. Extraction of the Ca, P (and O) signals was significantly less dependent upon the choice of the

	$W1 \times 10^{+5}$		$V2 \times 10^{+4}$	
	Extr.	Single-St.	Extr.	Single-St.
Ca	1.12±0.75	1.20±0.37	6.21±0.57	6.75±0.30
P	2.41±0.36	2.62±0.34	1.38±0.21	1.51±0.20
O	0.44±0.01	0.43±0.0002	0.29±0.01	0.27±0.001

Table 6.4(a)   Mineralised bone spectrum

	$W1 \times 10^{5}$		$V2 \times 10^{4}$	
	Extr.	Single-St.	Extr.	Single-St.
Cr	18.1±0.7	19.3±0.8	61.0±4.0	68.0±4.0
Mn	1.25±0.21	1.09±0.12	4.2±1.1	3.3±0.7
Fe	15.3±0.5	16.4±0.9	81.0±5.0	88.0±9.0

Table 6.4(b)   Ferritic steel spectrum.

background fitting region when the single-stage technique was used. In the case of the ferritic steel spectrum, only short pre and post-edge fitting ranges were available and the single-stage technique did not offer significant advantages when dealing with the Cr and Fe edges. This is partly attributable to the inadequacy of the cross-sections when only small energy windows close to the edge onsets are avilable. However, the single-stage technique did appear to be better for extracting the small Mn signal. In the case of the VC spectrum, the extracted signal followed the form expected theoretically when the single-stage technique was used, and in comparison the extrapolation method underestimates the C signal.

6.11 ESTIMATION OF THE UNCERTAINTY IN THE k VALUES

In any characteristic signal Ic extracted from a spectrum, there is a statistical uncertainty and an uncertainty due to the limitations of the spectral processing. The uncertainty in the signal extraction procedure will be especially significant when the fitting regions are small and do not exactly follow the form expected; e.g. the pre-edge range used for extracting the Ca signal has structure present from the C signal. An estimate of the uncertainty in the k values was obtained as follows. Once the cross-section has been scaled to an edge

$$k \frac{d\sigma}{d(\Delta E)} = I_c \qquad \text{6.19}$$

101

where I_c is the total number of counts in the extracted signal within the range. Thus the uncertainty Dk_s in the k value due to the statistical nature of the EEL acquisition can be described by

$$\frac{Dk_s}{k} = \frac{DI_c^s}{I_c} \qquad\qquad 6.20$$

where

$$DI_c^s = \sqrt{I_c + 2I_B}$$

and I_B is the number of background counts in the range W2. The additional uncertainty in the k value due to the limitations of the signal extraction procedure can be estimated by varying the pre and post-edge fitting ranges and calculating the standard deviation in the mean of the k values (Dk_m). The total uncertainty in the k value is then obtained from

$$Dk = \sqrt{(Dk_s)^2 + (Dk_m)^2} \qquad\qquad 6.21$$

6.12 QUANTITATION USING THE SINGLE-STAGE TECHNIQUE

The atomic Ca/P ratio obtained from the mineralised bone spectrum (Figure 6.11) was 1.56± 0.26 which compares reasonably well with the value expected for hydroxyapatite (1.67). The O/Ca ratio obtained was 3.38± 0.17 which is higher than the value expected (2.6). The uncertainties in the ratios quoted here do not include an estimate of

the systematic uncertainties in the theoretical cross-section ratios. Egerton (1984) suggests that predictions of cross-section by the H model may only be accurate to about 20%. Crozier (1985) suggests that for many pairs of elements not widely spaced in atomic number, the H and HS L-shell cross-section ratios agree to within 20%. Malis et al (1985) have compared experimental and theoretical K/K, L/L and L/K H cross-section ratios and found agreement within 10% for the K-edges, but significantly worse agreement in the case of L edges. Thus the discrepancy between experimental and predicted Ca/P and O/Ca ratios described above is probably due in part to systematic uncertainties in the theoretical cross-sections used. The B/N ratio obtained from the spectrum shown in Figure 6.23, was 0.90 ± 0.04 which is less than the 1.0 value expected. Crozier (1985) notes that atomic B/N ratios calculated using HS cross-sections, and assuming similar experimental conditions, are about 15% higher than the ratios calculated using H cross-sections. It is therefore likely that if HS cross-sections had been used for quantifying the B/N ratio, a value nearer unity would have been obtained.

Finally, to give an indication of the reliability of the single-stage technique, J H Paterson calculated Cr/Fe and Mn/Fn ratios from a number of ferritic steel spectra. Crozier (1985) describes the spectra acquistion conditions. The concentration ratios obtained from the EEL spectra were compared with those obtained from simultaneously recorded EDX spectra. The latter were expected to be accurate to 4% (Crozier, 1985). The concentration ratios obtained using the HS and H cross-sections differed from each other as expected; however, they were in everyway comparable with those described previously by Crozier et al (1983, 1984) and Crozier (1985).

6.13 SUMMARY

From the comparison of the single stage and extrapolation techniques presented here, it would appear that the characteristic signal extracted is less dependent upon the choice of the pre-edge fitting range when using the single-stage technique. However, difficulties still exist when trying to analyse spectra containing a series of adjacent edges. This is partly attributable to the inadequacy of the cross-sections when only small energy windows close to the edge onsets are available. Despite this, the single-stage technique offers an internally consistent approach and appears to offer some advantages when dealing with relatively small signals on large backgrounds.

CHAPTER 7

THE APPLICATION OF EELS TO THE STUDY OF TRACE Al CONCENTRATIONS IN MINERALISED BONE.

7.1   INTRODUCTION

This chapter consists of two parts.   The first part discusses the problems associated with EEL specimen preparation.   The second part describes a method of estimating the minimum trace Al concentration in mineralised bone which could be detected using EELS assuming adequate specimen preparation techniques were available.   In addition, the advantages and disadvantages of the EEL and EDX techniques are discussed and compared.

7.2   SPECIMEN PREPARATION REQUIREMENTS FOR EELS

Specimen preparation for EELS is more difficult than for EDX because of the need to prepare thinner specimens.   This is because plural inelastic scattering by valence electrons redistributes the counts within the EEL spectrum and tends to obscure the characteristic signals (see Chapters 2 and 6).   The specimen thickness t is related to the total inelastic mean free path λ by (e.g. Raether, 1980)

$$\frac{t}{\lambda} = \ln\left(\frac{I_{Tot}}{I_o}\right)$$

7.1

where I_{tot} and I_o are the total intensity in the spectrum and zero loss peak respectively.   As stated in Section 2.10, if $t/\lambda \ll 1$, then the

majority of electrons only undergo one inelastic scattering event or pass through the specimen without losing appreciable energy.   In practice $t/\lambda \leq 0.5$ is acceptable for quantitation (Egerton, 1984). Equation 7.1 allows estimation of specimen thickness assuming λ is known.   This can be estimated as follows.   An expression for the total inelastic scattering cross-section $\sigma_T{}^A$ from an atom can be expressed as (e.g. Leapman et al, 1984).

$$\sigma_T{}^A = \frac{3c^2 \lambda_c^2}{4\pi v_o^2} \, z^{1/2} \, \ln\left(\frac{2}{\theta_E}\right)$$

where λ_c is the Compton wavelength and θ_E is the characteristic angle of the most probable energy loss $\overline{\Delta E}$.   An approximation to the total inelastic cross-section for a sample $\sigma_T{}^S$ can be obtained by summing the individual cross-sections, i.e.

$$\sigma_T{}^S = \sum \sigma_T{}^A$$

The total mean free path for inelastic scattering can then be expressed as

$$\lambda = \frac{4\pi v_o^2 M}{3c^2 \lambda_c^2 \rho A_v \ln(2/\theta_E)} \; \frac{1}{\sum z^{1/2}}$$

where M is the molecular weight of the sample, ρ is the density and A_v is Avogadros number.   The mean free path for 100 keV electrons in a MB sample obtained by this method is about 1000Å.   As expected, this value lies within the $1500 > \lambda > 500$Å range which is typical for most specimens when $T_o = 100$ keV (Egerton, 1983).

Three methods of specimen preparation were investigated here, "wet-cutting", "dry-cutting" and "ion-beam thinning". Only the wet-cutting procedure has been used successfully by previous workers, (e.g. Arsenault et al, 1983) for preparing mineralised bone sections for EELS. The reason for trying other specimen preparation methods is that wet-cutting may significantly alter the specimen composition. These alterations will be discussed further in Section 7.2.2.

7.2.1 Dry-Cutting

In the dry-cutting technique the bone was first chemically fixed and then embedded in a block of methyl-methacrylate resin. Sections were cut from the block using a dry diamond knife in an Ultramicrotome. The sections were manipulated by means of eyelashes mounted on an orange stick, onto the formvar in the centre of a Cu single hole mount. Finally, a layer of C was evaporated onto the section to make it thermally and electrically conducting.

A significant amount of skill is required to cut sections of mineralised tissue and place them on single hole mounts. Since the technicians in the Physiology Department do this work routinely for EDX specimen preparation, they attempted to cut the sections thin enough for EELS.

The standard dry cut specimen preparation method (as described above) was altered to ensure that electrons would not pass through any material (e.g. formvar support) other than the section. Thus unnecessary (plural) electron scattering was significantly reduced. Firstly, 400 mesh holey carbon grids were used to support the specimen instead of the Cu single hole mounts. Spectra were only acquired from regions of specimen overlying the holes in the support film. Secondly,

a C coating was not added to the specimens after they were placed on the grids. When the specimens were observed in the microscope they usually remained well attached to the support film and specimen charging effects were not obvious; i.e. the image of the specimen remained stationary on the screen. Figure 7.1 shows a typical section of dry cut mineralised bone and holes in the support film under the specimen are visible. Figure 7.2 shows a typical spectrum taken from this specimen. Plural inelastic scattering by valence electrons has virtually obscured the major Ca and O signals. Using Equation 2.15, the ratio t/λ was calculated to be 0.9 and this suggests a specimen thickness of $\sim 900 \text{Å}$. Significantly thinner sections were not obtained by the dry cut method since they tended to crumble.

7.2.2 Wet-cutting

Wet-cutting is essentially the same as dry-cutting except that the diamond knife is kept in contact with a liquid (e.g. distilled water) which acts as a lubricant during sectioning. Consequently, thinner sections can be obtained than when dry-cutting. Immediately after cutting, the sections float on the surface of the liquid prior to being placed on the specimen supports. White light interference gives the sections an apparent colour which is dependent upon the section thickness. Only specimens appearing light grey to transparent ($\leq 400 \text{Å}$) were chosen for EELS.

The wet-cutting method has the disadvantage that significant translocation of elements within a section may occur when it is in contact with the liquid; e.g. Nicholson et al (1977) state that, whilst

15 µm
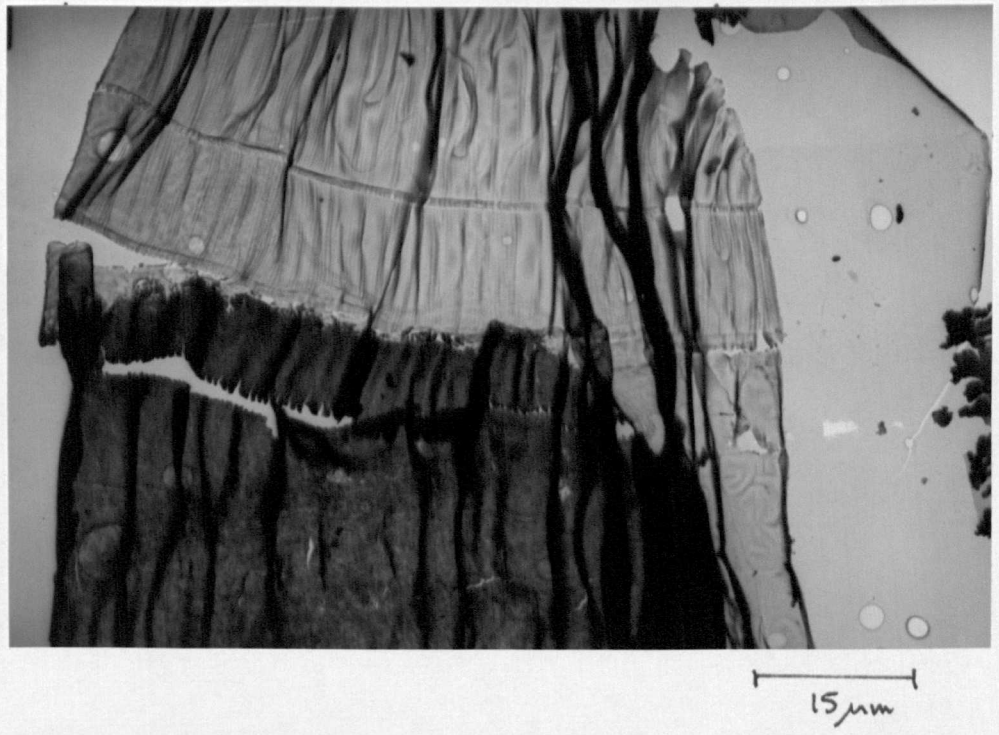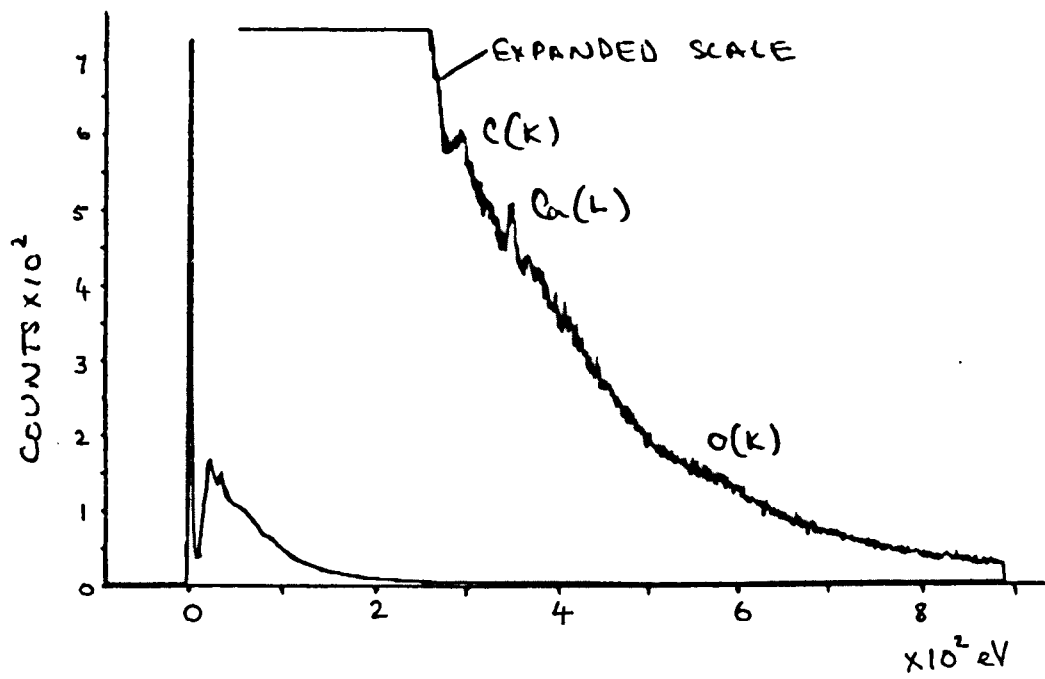
Figure 7.1

Figure 7.2

Ca is tightly bound to the hard tissue matrix, P can be easily washed out.

Figure 7.3 shows an EEL spectrum $(t/\lambda = 0.4)$ obtained from one of the thinnest specimens. The Ca and O signals are clearly present; however, the P signal is not visible. Figure 7.4 shows an EDX spectrum acquired simultaneously with the EEL spectrum. The Ca/P count ratio in the EDX spectrum is significantly greater than the ~2:1 ratio expected. This may be attributed to loss of P by the specimen preparation procedure. It should be noted that alteration in the Ca/P count ratio was not observed for the 1500Å thick EDX specimens. This is probably due to the latter specimens having a higher volume/surface ratio, i.e. loss of P from the sample surface will be less significant for thicker specimens. Effort was made to ensure that each specimen was in contact with the sectioning liquid for the shortest possible time; however, the EEL sections were always in contact with the liquid for the longest time because of the difficulty in sectioning them.

7.2.3(a)   Ion Beam Thinning-apparatus

The apparatus used for this process was an Ion Tech Limited Microlap B304 ion beam thinning unit. Morrison (1981) discusses this equipment in some detail and therefore it will only be described briefly here. An aluminium alloy high vacuum chamber contains two B11 saddle field ion sources. The sources are mounted on a supporting arm that tilts about the specimen plane so that both sides of the specimen may be thinned simultaneously at any angle (from about 5° to 60°) to the specimen plane. The specimen is clamped between two Ta plates and mounted in a toothed stainless steel wheel which is rotated by a small electric motor inside the vacuum system. A binocular microscope situated above the

(a)

(b)

Figure 7.3

COUNTS
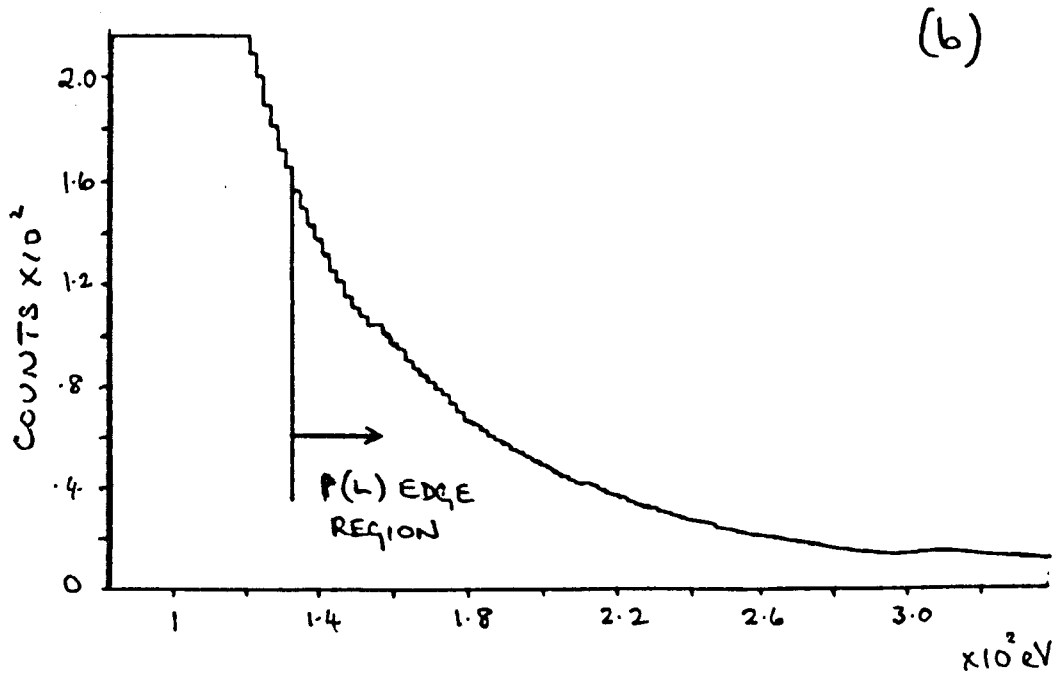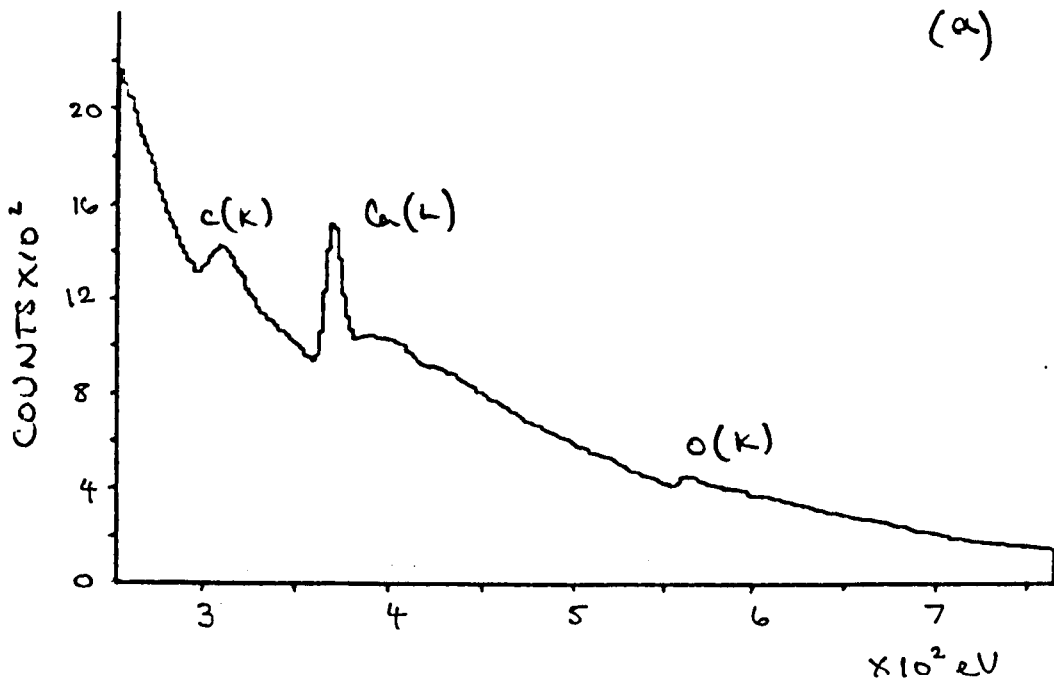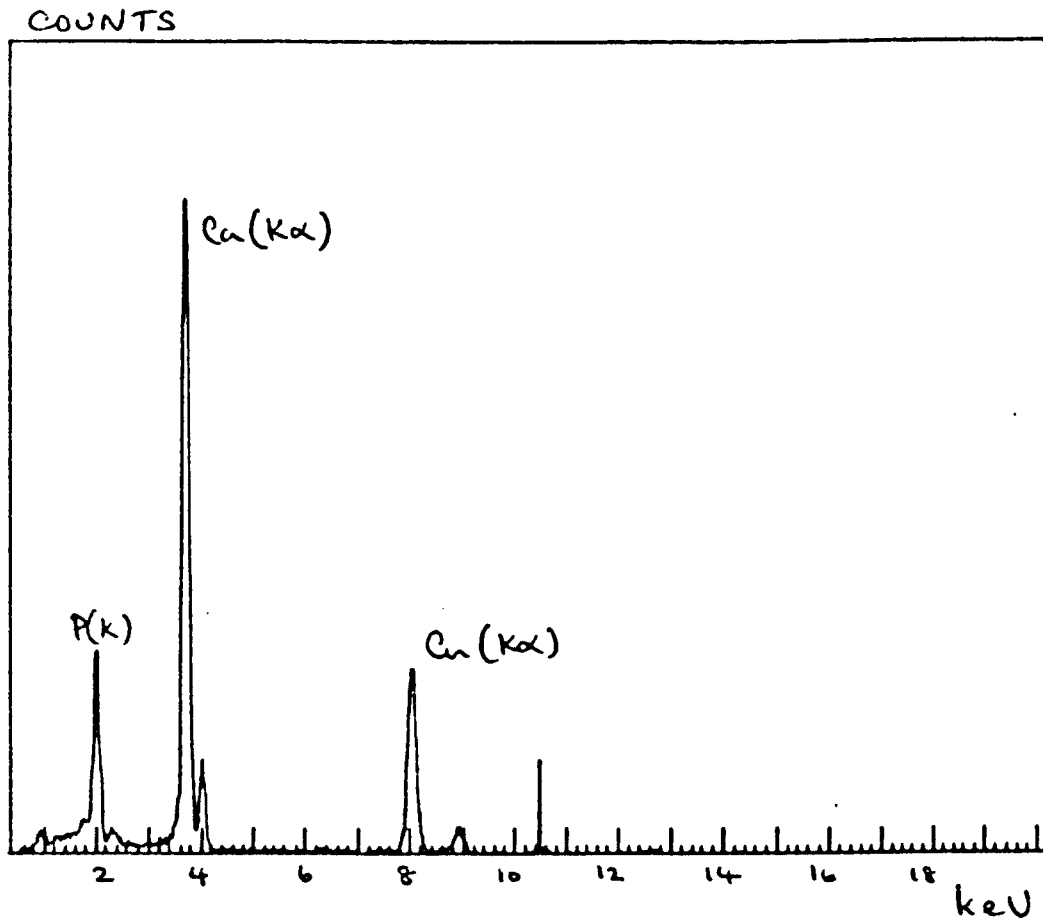
Figure 7.4   Spectrum acquired from the wet cut mineralised bone section.
The large bulk Cu contribution is due to a fine mesh Cu grid being used
to support the specimen.

illuminated specimen allows observation of the specimen during thinning.

The ion sources are routinely operated at 6 keV and 1.5 mA emission current. An ion current of up to 100μA can be obtained. High purity Ar was used as the bombarding gas. The output from the ion guns was controlled by varying the flow of Ar into the chamber (by needle valves) and by controlling the current to the ion sources. Two difficulties were found when using this equipment to thin the mineralised bone samples. Firstly the mechanism for rotating the specimen easily jams. Secondly, so much light is transmitted through a biological specimen that observing changes in the specimen appearance during thinning is difficult.

When using a gas such as Ar, the thinning rate is dependent upon many factors such as the energy of the incident ion and relative masses of ion and target atom; however, for most specimens the minimum thinning rate generally occurs when the ion beam is set at a glancing angle to the specimen surface (e.g. Morrison, 1981). It was found that the thinning rate of mineralised bone was relatively high, around 0.1 μm/min, even when a single beam angled at about 5° to the specimen surface was used.

7.2.3(b) <u>Ion Beam Thinning</u>

Clearly, specimens of mineralised bone could not be supported on formvar (or carbon) for thinning since the support film thins as well as the specimen. Therefore ~5000Å thick sections of sample were dry cut and "sandwiched" between the two sides of a 400 mesh folding grid. No carbon was present on the grid and since the section was 5000Å thick (initially) it was easily self-supporting.

Two main problems were encountered when attempting to ion beam thin mineralised bone. Firtly, due to the relatively high thinning rate, the specimens easily became fragile with numerous large holes and few regions thin enough for EELS. Secondly, those regions found suitable for EELS rarely occurred at the mineralised bone/osteoid border which was of most interest here. The EEL spectra which were shown in Figures 6.18 to 6.20 were obtained from a region of deep bone.

Figure 7.5 shows a region of ion beam thinned mineralised bone. The scanning attachment on the JEM 1200EX was used to obtain these micrographs. Figure 7.5 shows that after thinning, the surface of the bone is rough. Boyde (1963) notes that structure present after thinning mineralised bone should be interpretated in terms of (a) differences in the rate of removal of surface layers which are no longer there, (b) the rate of depostion of "sputtered" material and (c) the effects of local electrostatic charging by the ion beam which deflects the beam from the charged areas so that they are eroded less. It seems likely that the structure seen here is composed mainly of heavily mineralised regions with the relatively softer organic components of bone near the surface of the sample having been removed.

7.2.4 Summary

Three methods of preparing mineralised bone specimens for EELS have been investigated. Suitably thin specimens were obtained by either wet-cutting or ion beam thinning. The former technique has the disadvantage that significant alteration of specimen compostion may occur. The latter technique was of limited use because thin regions of specimen were rarely produced in the areas of most interest.
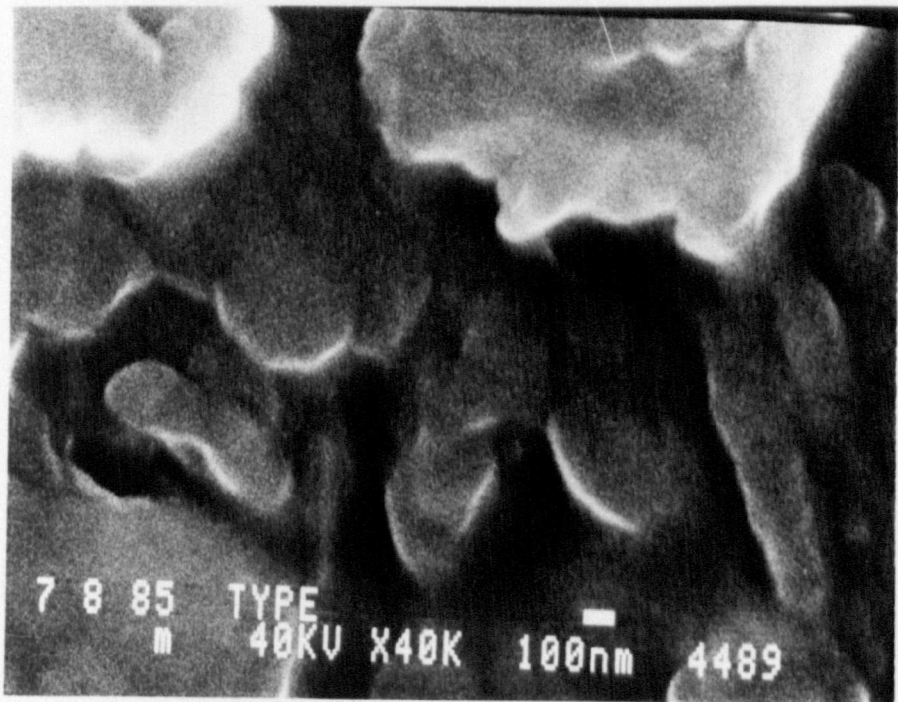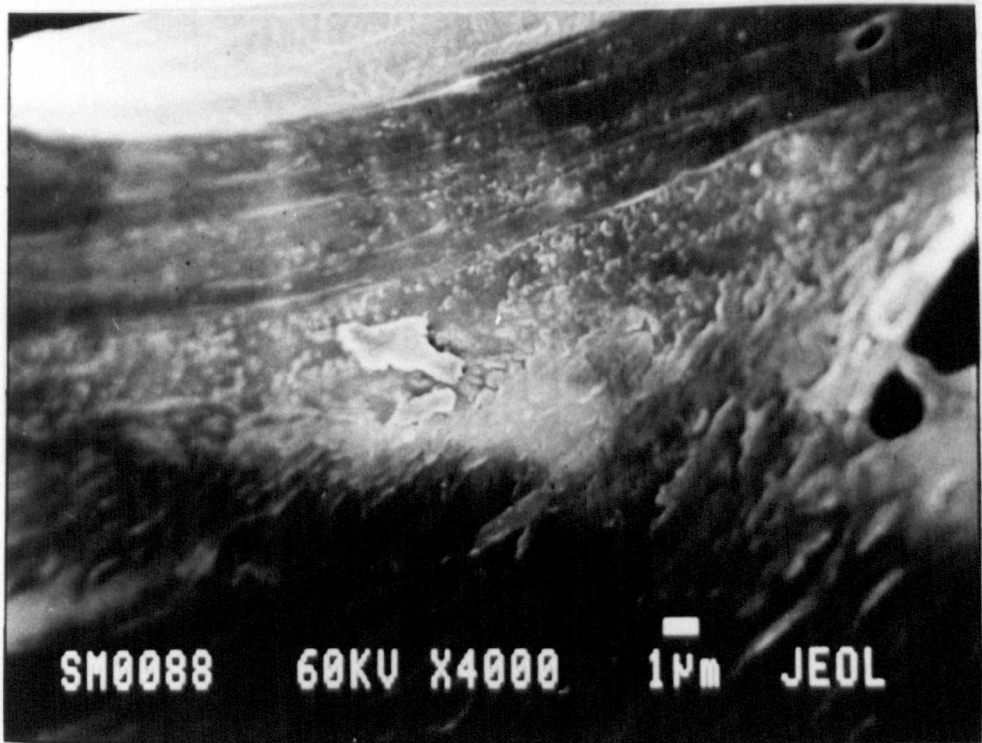
Figure 7.5

7.3 DETECTION OF TRACE Al CONCENTRATIONS IN MINERALISED BONE USING THE EEL TECHNIQUE

The remainder of this chapter describes and applies a method for determining the minimum trace Al concentration in mineralised bone which can be detected using EELS, assuming adequate specimen preparation methods are available. The method can be summarised as follows.

If it is assumed that the Al atoms are uniformly distributed within the electron probe diameter, then the characteristic EDX and EEL signals from these atoms are related by

$$I_{X,Al} = C_{Al} I_{E,Al} \qquad\qquad 7.3$$

where $I_{X,Al}$ and $I_{E,Al}$ are the EDX and EEL signals and C_{Al} is defined in the next section. C_{Al} was determined experimentally from a pair of EDX and EEL spectra simultaneously acquired from an Al thin foil. The C_{Al} value can then be used to predict $I_{E,Al}$ values in an EEL MB spectrum using the integrated number of Ca counts in a simultaneously acquired EDX MB spectrum as follows. In Chapter 5, Al/Ca count ratios were graphed (as a function of distance from the mineralised bone surface.) Therefore, it is possible to determine $I_{X,Al}$ values corresponding to Al/Ca ratios, for the EDX MB spectrum. By using the C_{Al} value, $I_{E,Al}$ values can be calculated which correspond to given Al/Ca EDX count ratios. Since both $I_{E,Al}$ and the corresponding EEL background signal are known, it is possible to estimate both the minimum trace Al concentration detectable using EELS, and the corresponding minimum spectrum acquisition time.

7.3.1 The Relation Between Characteristic EDX and EEL Counts in Spectra Acquired under Identical Instrumental Conditions

As described in Chapter 2, the characteristic Al EDX and EEL counts ($I_{X,Al}$ and $I_{E,Al}$ respectively) detected from a sample can be described as

$$I_{X,Al} = t_X \frac{N_X}{\gamma_X} \frac{I_0}{e} \sigma_{X,Al} \omega_{Al} S_{Al} \frac{d\Omega}{4\pi} \epsilon(E_{Al}) S(E_{Al}) \qquad 7.4$$

$$I_{E,Al} = \frac{N_E}{\gamma_E} Q \sigma_{E,Al} \qquad 7.5$$

where $\dfrac{N_X}{\gamma_X}, \dfrac{N_E}{\gamma_E}$ number of Al atoms per unit area detected by EDX and EELS respectively.

I_0/e total number of incident electrons.

Q counts in the zero loss peak and low loss region of the EEL spectrum integrated over the same energy loss range used to obtain $I_{E,Al}$.

$\sigma_{X,Al}, \sigma_{E,Al}$ cross-sections for production of Al characteristic X-ray and EEL counts (taking account of the experimental conditions).

W, S fluorescence yield and partition function.

$d\Omega$ solid angle subtended by the X-ray detector.

$\epsilon(E_{Al})$ correction factor for absorption of Al X-rays by the detector.

113

$S(E_{A1})$ correction factor for absorption of Al X-rays by the specimen

Assuming that the Al atoms are uniformly distributed within the electron probe diameter at the specimen

$$\frac{N_x}{q_x} = \frac{N_E}{q_E} \qquad\qquad 7.6$$

so the characteristic signals in the EDX and EEL spectra are related by

$$I_{x,A1} = \left\{ t_x \frac{I_o}{e} \frac{\sigma_{x,A1} \omega_{A1} S_{A1}}{\sigma_{E,A1}} \frac{d\Lambda}{4\pi} \epsilon(E_{A1}) S(E_{A1}) / q \right\} I_{E,A1} \qquad 7.7$$

where the term in brackets is equal to C_{A1} in Equation 7.3. Assuming that the EDX and EEL spectra are acquired from the mineralised bone and Al samples under identical experimental conditions, and that $(S(E_{A1}))_{A1}$ = $(S(E_{A1}))_{MB}$ = 1.0, then

$$\frac{(I_{x,A1})_{A1}}{(I_{x,A1})_{MB}} = \frac{(t_x I_{E,A1}/q)_{A1}}{(t_x I_{E,A1}/Q)_{MB}} \qquad 7.8$$

where the subscripts Al and MB outside the brackets indicate the terms for the Al foil and mineralised bone samples respectively. It should be noted that a knowledge of theoretical cross-sections, X-ray

absorption corrections and the EDX and EEL detector geometrics are not required for evaluation of Equation 7.8. The main assumption is that the spectra must be acquired under identical experimental conditions and Craven et al (1981) suggest that the standard acquisition conditions used here are highly reproducible. Thus, by determining a given number of Al EDX counts in the mineralised bone spectrum (corresponding to a given Al/Ca ratio) it is possible using Equation 7.8, to calculate a corresponding number of EEL Al counts in the simultaneously acquired spectrum.

7.3.2 The Signal/background and Signal/noise Ratios

To estimate the minimum trace Al concentration which is detectable using EELS, it is necessary to take account of the following two factors; the signal/background and signal/noise ratios.

The signal/background ratio $R_{S,B}$ is important because if it is too low, it will never be possible to extract a signal, no matter now high the signal/noise ratio is, due to the limitations of the spectral processing techniques. This ratio can be defined as follows (see Figure 7.6)

$$R_{S,B} = \sum_{j=\Delta E_1}^{j=\Delta E_1+\delta} s_j \bigg/ \sum_{j=\Delta E_1}^{j=\Delta E_1+\delta} b_j = \frac{S}{B} \qquad 7.9$$

where s_j and b_j are the number of signal and background counts in a channel j, and S and B are the respective integrated counts within the energy region ΔE_1 to $\Delta E_1 + \delta$.

Clearly, the signal/noise ratio is also important since if the signal level is below the noise level, the signal is not significant.

115
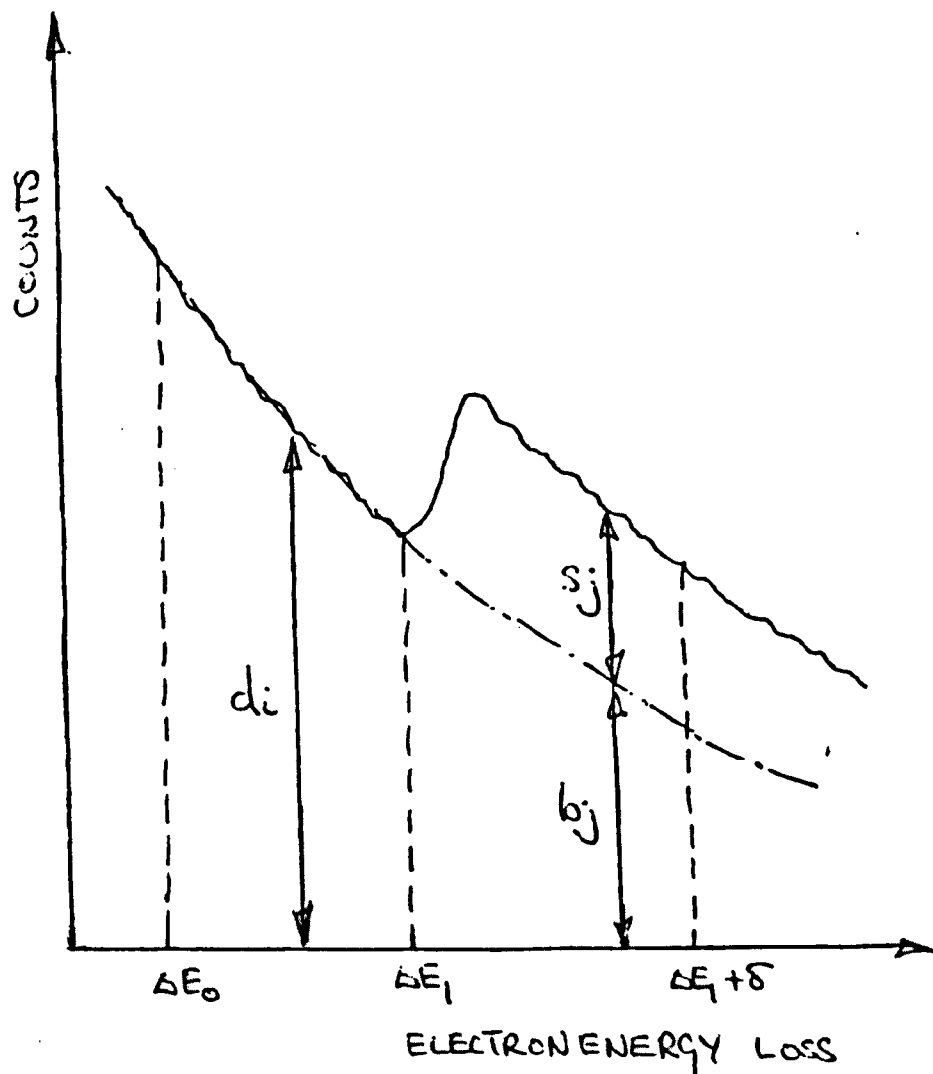
Figure 7.6

As stated in Chapter 6, Egerton (1982) defines the signal/noise ratio R_{SN} as

$$R_{SN} = \frac{S}{\sqrt{S + hB}} \qquad 7.10$$

where h is a parameter which can be expressed as

$$h = 1 + var(B)/B \qquad 7.11$$

Egerton (1982) defines var(B) so that account is taken of the statistics of background fitting and extrapolation. The extrapolation routine written by PA Crozier numerically evaluates var(B) following the method of Egerton, and so it was possible to determine h values for calculation of the signal/noise ratios.

7.3.3 The Al(L) and Al(K) Signal/background Ratios

The minimum acceptable signal/background ratio can be determined by investigating the accuracy of the theoretical background modelling when the signal from the trace Al concentration is not present. The MB spectrum (obtained from a control sample) shown in Figure 7.3 was found to be typical, i.e. the background count distributions within the Al(L) and Al(K) edge regions are similar to those in most other MB spectra. Therefore, this spectrum was used to estimate the limitations of the spectral processing techniques.

The extrapolation technique was used for signal extraction; however, another technique based on the following equation was briefly considered (see Figure 7.6)

$$S = T - \phi D = T - B \qquad\qquad 7.12$$

where ϕ is a constant and D is defined as

$$D = \sum_{i=\Delta E_o}^{i=\Delta E_1} d_i$$

Equation 7.12 assumes that the ratio of the integrated background counts B/D are constant for all spectra; i.e. that variations in specimen mass thickness (which produces a variable redistribution of counts in the specimen, see Chapter 2) are not significant. Clearly this assumption is only valid in the case of a very homogeneous specimen. Since mineralising tissue is relatively inhomogeneous there will be a significant uncertainty in the ϕ term, limiting the usefulness of Equation 7.12.

7.3.3(a) Al(L) Signal/background

Figure 7.7 shows the Al(L) signal region. The background counts are due to valence shell excitation and the Ca $M_{2,3}$ edge. As expected, the $A(\Delta E)^{-r}$ background fitted using the extrapolation method do not model the background well. A much better fit was achieved using the single-stage technique, however, the goodness of fit was found to be
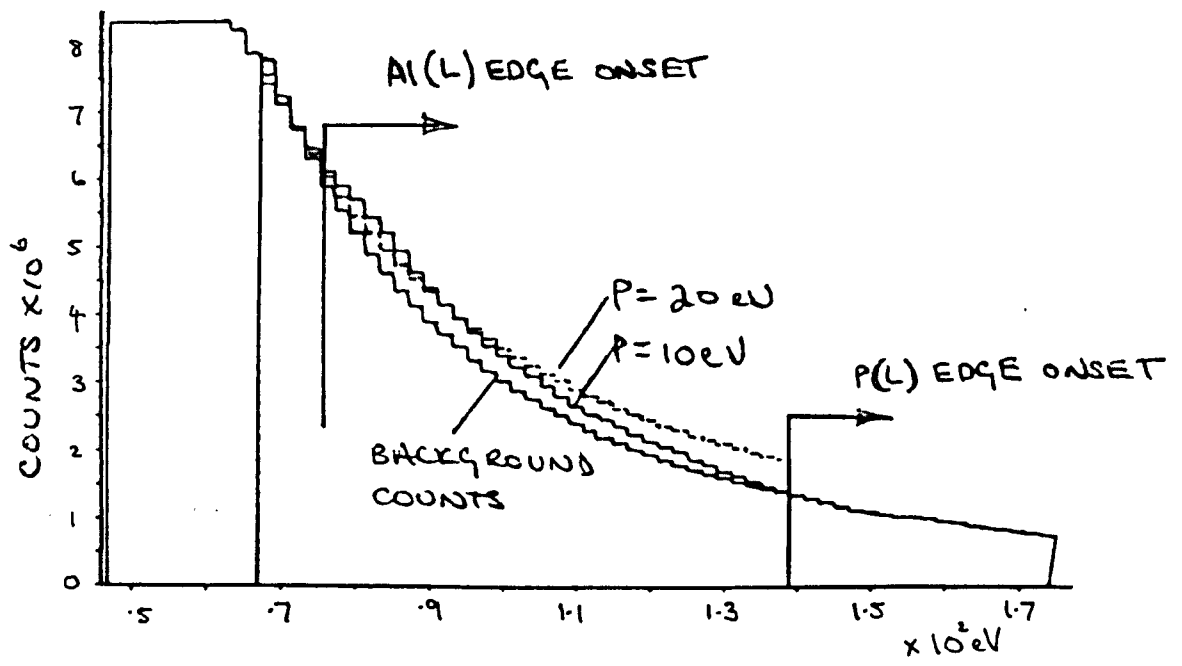
Figure 7.7   Extrapolated backgrounds.

very dependent upon the choice of pre and post-edge fitting ranges. This effect has been described previously – see Section 6.6.

The advantage of using Equation 7.12 is that a specific functional form is not assumed for the background. To determine ϕ, a number of MB spectra were acquired from the same wet cut control sample that was used previously. Table 7.1 summarises the ϕ values for each spectrum.

A criterion for detection of signal S above the background B can be defined as

$$S = 3\Delta B$$

7.13

where ΔB is the uncertainty in the background counts B which can be estimated from

$$\Delta B = B \sqrt{\left(\frac{\Delta \phi}{\phi}\right)^2 + \left(\frac{\Delta D}{D}\right)^2}$$

7.14

If ΔD is defined as $\sqrt{D}$, and $\Delta \phi$ is the standard deviation of the mean of the ϕ values then $\Delta \phi / \phi \doteqdot 3\% \gg \Delta D_i / D_i$, and therefore

$$S = 3B\Delta \phi / \phi$$

7.15

for signal detection.

118

EEL MB spectrum	¢ Al (L)
1	1.42
2	1.29
3	1.59
4	1.12
5	1.24
6	1.30
7	1.26
8	1.37

Table 7.1

Consequently, the Al(L) signal from the trace concentrations is only significant if the integrated signal counts S are greater than 15% of the background counts B.

Since an Al(L) signal/background ratio of about 16% was obtained from a thin Al_2O_3 foil (see Section 7.3.5), it is most unlikely that the corresponding ratio for the Al(L) signal in an EEL MB spectrum will approach 16%. Therefore Equation 7.12 would not be practical for signal extraction and the extrapolation or single-stage techinques might prove more useful. Alternatively, the signal extraction method described by Equation 7.9 could be improved by the method suggested by Colliex (1984); ie the pre-edge region (ΔD to ΔE, see Figure 7.6) is considered to be split into two equal regions and the integrated counts in these regions used to estimate the integrated backround counts in the signal region. Account is therefore taken of the change in curvature of the background due to mass thickness effects. The reason for considering a technique based only on Equation 7.12 will be described in Section 7.3.8.

7.3.3(b) <u>Al(K) Signal/Background</u>

Figure 7.8 shows the Al(K) energy region of the MB spectrum. The $A(\Delta E)^{-r}$ backgrounds have been obtained using the extrapolation method and long post-edge regions have been chosen because characteristic signals tend to be smeared out at high energy loss due to defocus of the post-specimen lenses (due to chromatic aberration). The extrapolated backgrounds were found to lie increasingly above the true background counts as the total pre-edge fitting range and post-edge extrapolation range was increased. This is probably due to the fact that an EEL
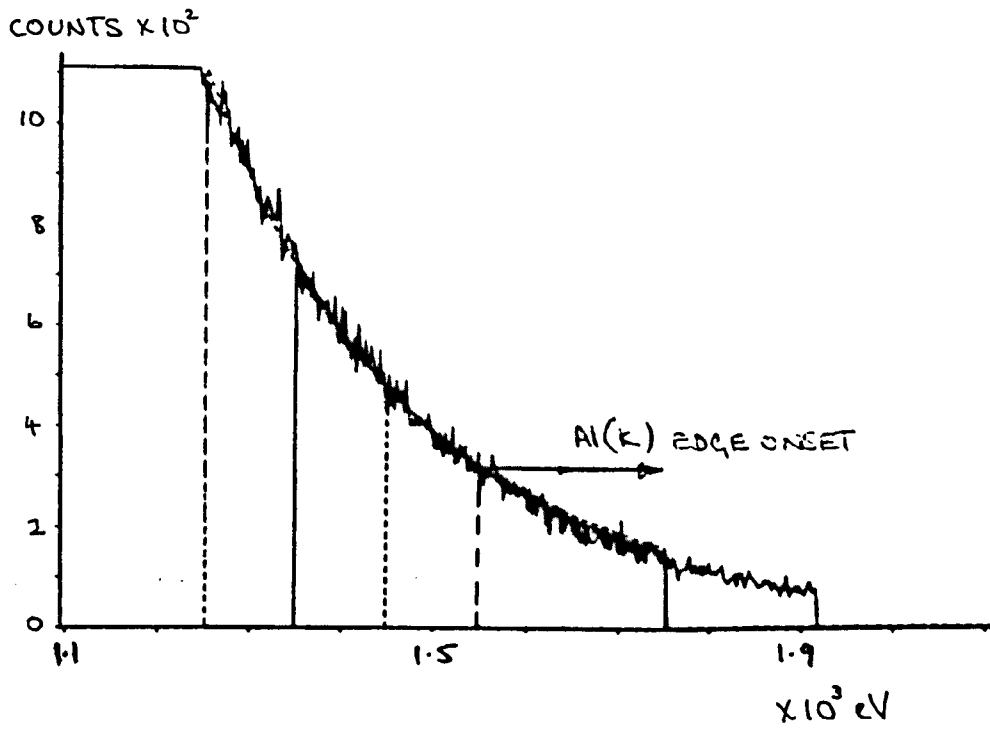
Figure 7.8   Extrapolated backgrounds.

spectrum only follows an $A(\Delta E)^{-r}$ form over a limited energy range – about 180 eV (Egerton, 1982).   For simplicity therefore, the systematic uncertainty in the background modelling will be considered negligible if the total pre and post-edge range does not exceed 180 eV.   The detection of signals using a total range exceeding 180 eV will not be considered.

7.3.4 The Signal/noise Ratio

Assuming that the Al(L) and Al(K) signal/background ratios satisfy the criteria defined in the previous section, the signal/noise ratio can be calculated from Equation 7.10

In the case of the Al(K) edge, it was shown that the background count distribution could be accurately modelled using the extrapolation routine.   Figure 7.9 shows a graph of h values versus post-edge integration range, for various pre-edge fitting ranges.   Clearly the signal/noise ratio can be minimised by using a large pre-edge fitting range and a short post-edge signal integration range (since h is smallest under these circumstances).   This is in agreement with the observation by Egerton (1983).

It is useful to be able to estimate the minimum spectrum acquistion time t^1 which is required to detect a signal above the noise level.   A time dependence t can be introduced into Equation 7.10, i.e.

$$R_{SN} = \frac{s(t/t_n)}{\sqrt{s(t/t_n) + h\, B(t/t_n)}}$$

7.17
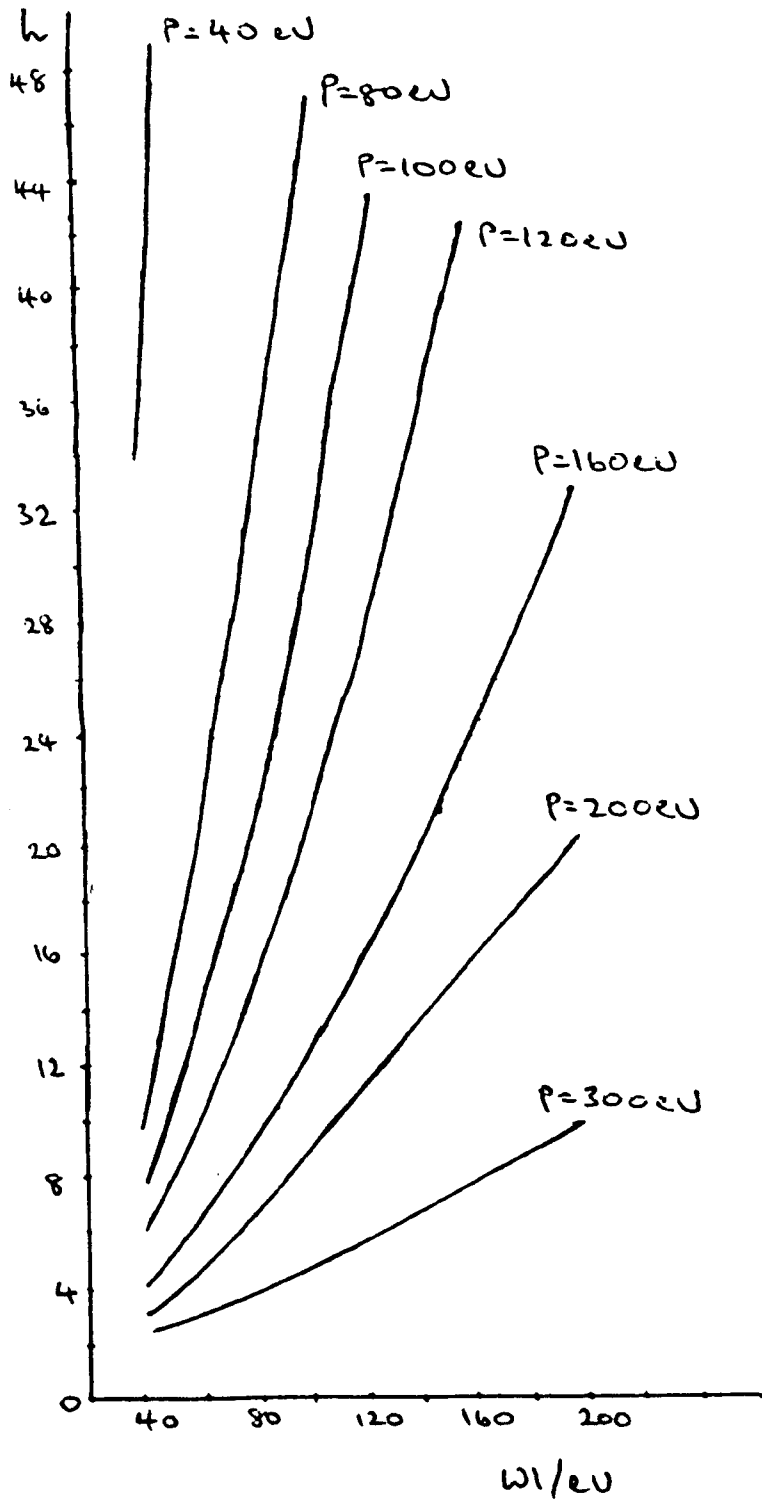
Figure 7.9   Experimentally derived h values for the Al(K) edge signal in mineralised bone spectra.

where t_n is the acquistion time of the EEL MB spectrum shown in Figure 7.8 (i.e. 184 sec). A criterion for detecting a signal above the noise level can be defined as;

$$R_{SN} > 3$$

therefore, Equation 7.17 can be rewritten as

$$t' \leq \frac{9(S/t_n + hB/t_n)}{(S/t_n)^2}$$

7.18

7.3.5 Spectral Processing

The following two sections describe the processing (i.e. characteristic signal extraction) of the two pairs of simultaneously acquired MB and Al EDX and EEL spectra.

7.3.5(a) Mineralised Bone Spectra

As stated in Section 7.3.3, the EEL MB spectrum shown in Figure 7.3 was found to be typical. Therefore, this spectrum was used to estimate the minimum trace Al concentration detectable using EELS.

The simultaneously acquired EDX spectrum has been shown previously (Figure 7.4) and Figure 7.10 shows this spectrum in more detail together with a scaled theoretical background. Extraction of the characteristic $Ca(K\alpha)$ EDX counts is relatively straightforward. Using these number of Ca counts, a range of possible Al EDX counts can be predicted (which

COUNTS

P(K) Ca(Kα) Ca(Kβ)

MBH HA
+ 9μm Be
+ 0.c1μm Au

Si(K)

Na(K)

S(K)

1   2   3   4   keV
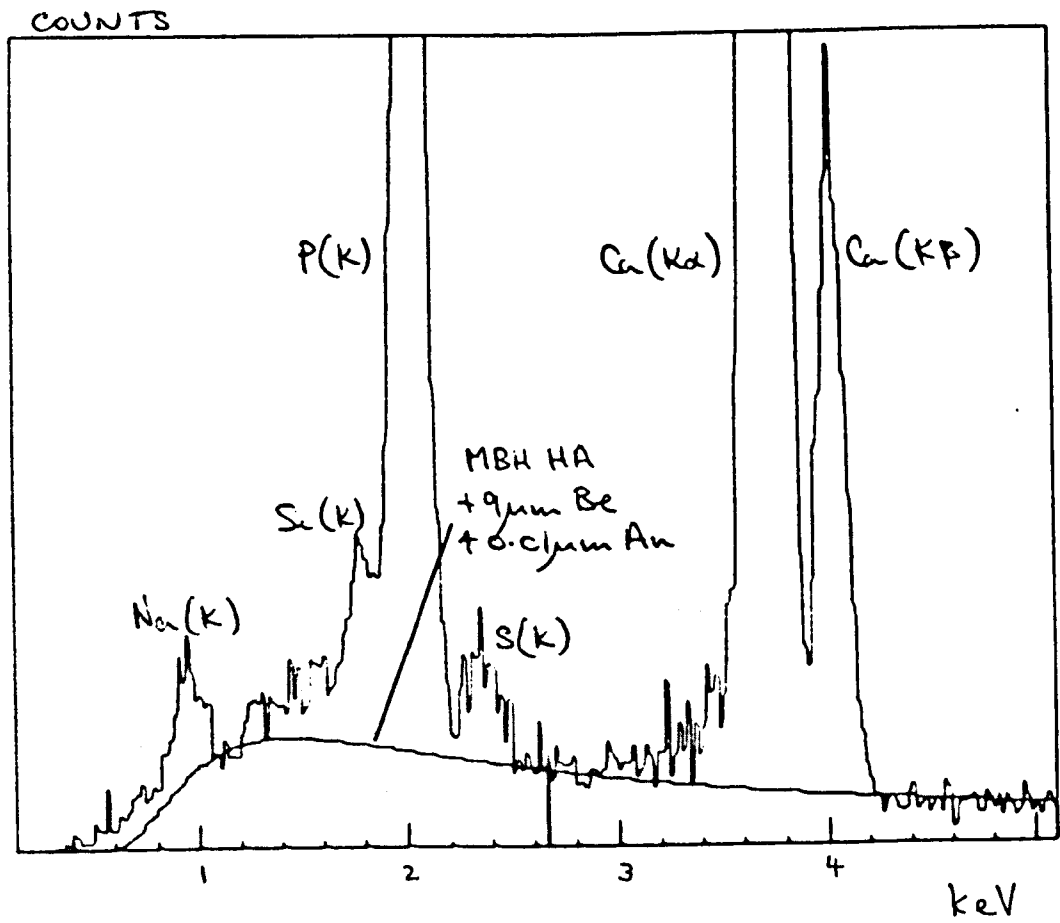
Figure 7.10

would be present if the spectrum was acquired from an experimental sample) using the Al/Ca (EDX) count ratios determined in Chapter 5.

Two count ratios were chosen. The first was the highest ratio (2×10^{-3}) determined in the EDX study. The second ratio (0.2×10^{-3}) was more typical and found in most experimental samples about 1 to 2 μm from the MB surface.

7.3.5(b) Aluminium Spectra

The simultaneous EDX and EEL Al spectra which were used to determine the minimum trace Al concentration were also used to determine the Al EDX peak/bremsstrahlung ratio. Extraction of the characteristic EDX Al counts was described in Chapter 4.

Figure 7.11 shows the EEL Al spectrum with two extrapolated backgrounds calculated for the Al(L) edge. Clearly there is a significant difference between the predicted background when the pre-edge fitting range is changed by only a small amount. It has been shown in Chapter 6 that it is better to use the single-stage technique when attempting to extract a signal which is close to the low-loss region. Figure 7.12 shows the background fitted using the single-stage technique.

It should be noted that the Al(L) signal/background ratio is about 16%. The background under the Al(L) signal mainly arises from valence shell excitation and the background under the signal was found to follow an $A(\Delta E)^{-r}$ form reasonably well; i.e. better than the same energy region in the MB spectrum. Unfortunately, because of the low signal/background ratio, the extracted signal could be varied by about 10% by varying the pre and post-edge fitting ranges. However, it is likely that the Al(L) signal has been extracted here with reasonable
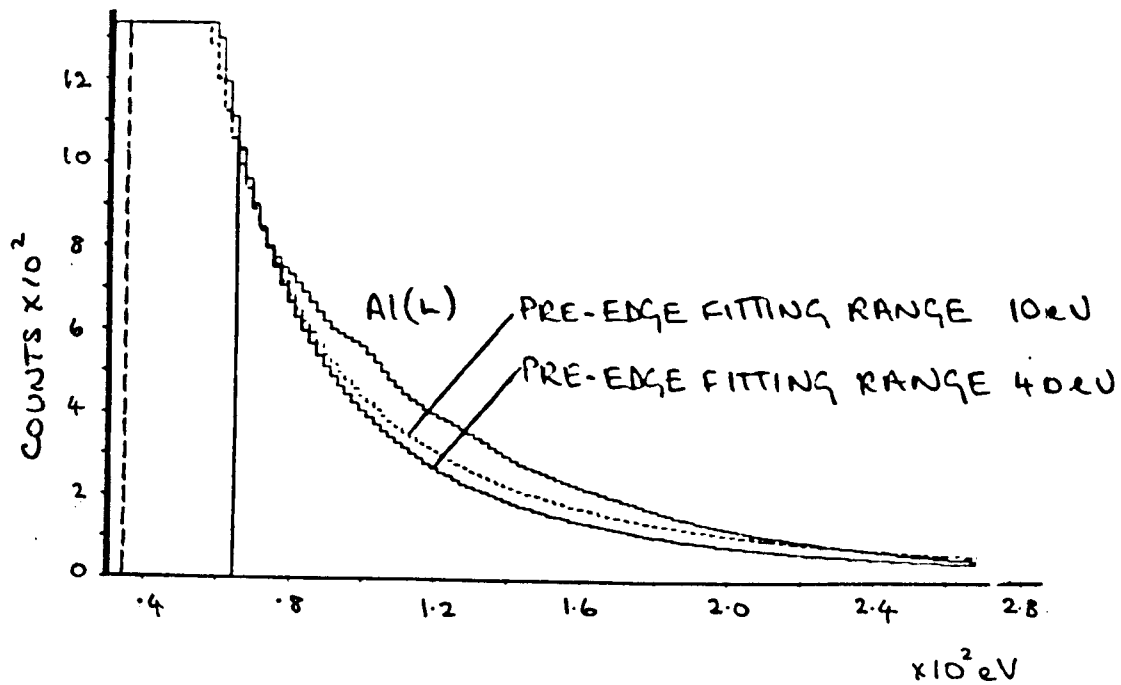
Figure 7.11
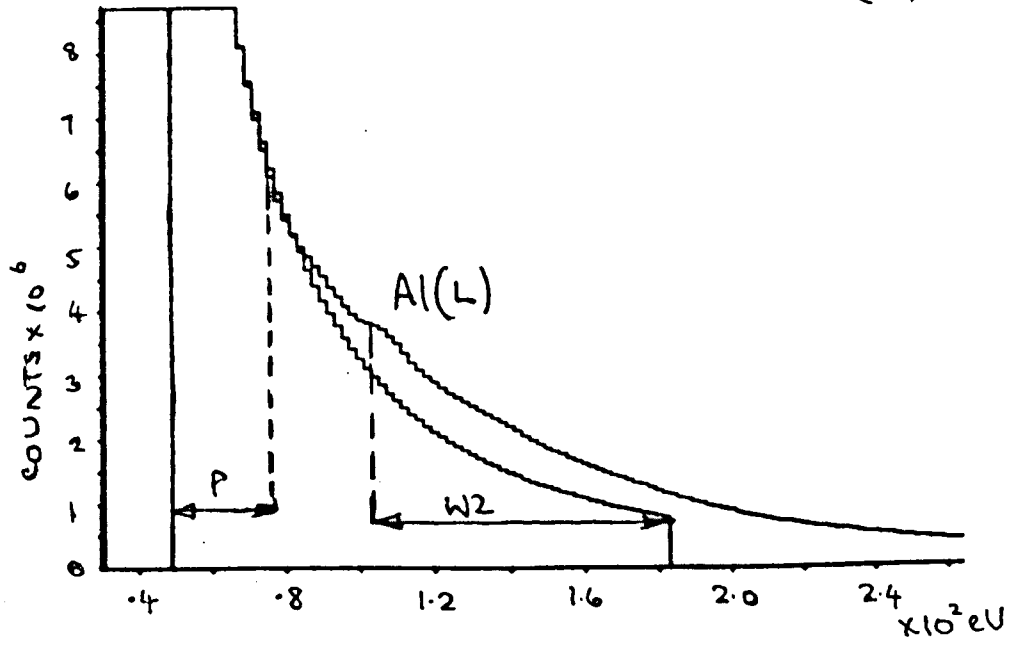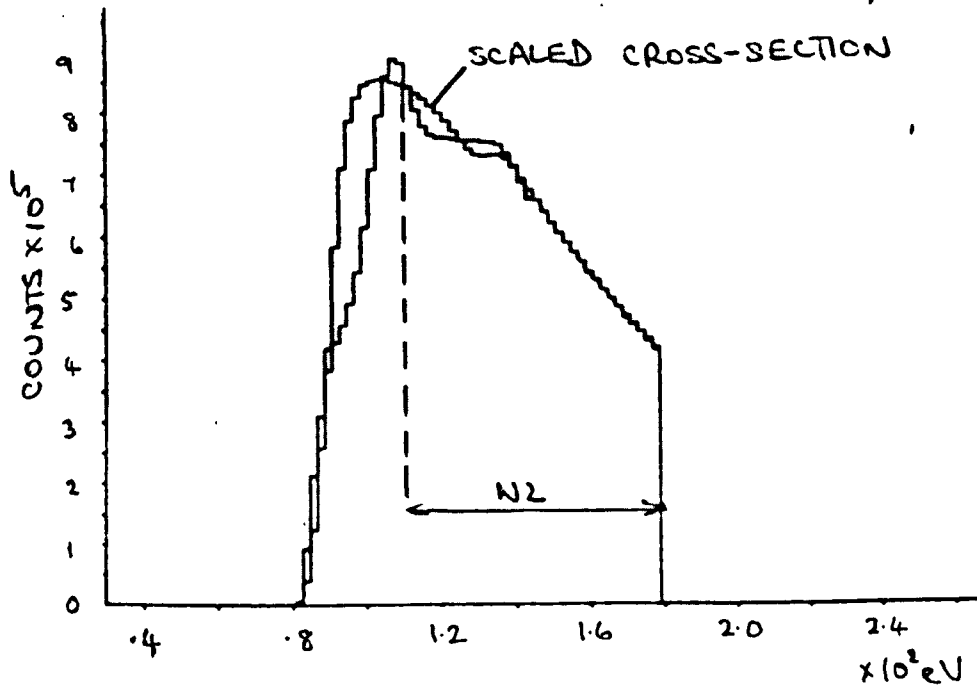
Figure 7.12

accuracy for two reasons. Firstly, as will be shown, it is possible to extract the Al(K) signal with negligible uncertainty, and the L/K count ratio agrees with the predictions of Egertons SIGMAL and SIGMAK programs to within 10%. Secondly, Figure 7.12(b) shows the extracted Al(L) edge and the scaled hydrogenic cross-section. The cross-section has been convolved with the zero-loss and low-loss regions of the Al spectrum. A good match between experimental and theoretical edge shapes has been obtained provided the region close to the edge onset is ignored.

Figure 7.13 shows the Al(K) edge with an extrapolated background. As in the case of the MB spectrum, a long post edge signal integration range was chosen because of defocus of the spectrum at high energy. The uncertainty in the extracted signal was estimated to be $< 1\%$. and, as expected, there was no significant difference between the signal extracted using the extrapolation and single-stage techniques.

7.3.6 Estimation of the Minimum Trace Al Concentration which can be Detected Using EELS

The minimum trace Al concentration which can be detected using EELS can now be estimated. The Al(L) and Al(K) signals will again be considered separately.

Table 7.2 summarises the Al(L) signal/background ratios. Even the ratio for the high trace concentration is less than 1%. Clearly this signal is not really visible. In view of this and the discussion in the preceding sections, it is not possible to extract the Al(L) signal from the trace Al concentrations due to the limitations of the signal extraction procedures. The Al(K) signal will now be considered.

Figure 7.14 shows the time t^1 (Equation 7.18) plotted for various

(a)
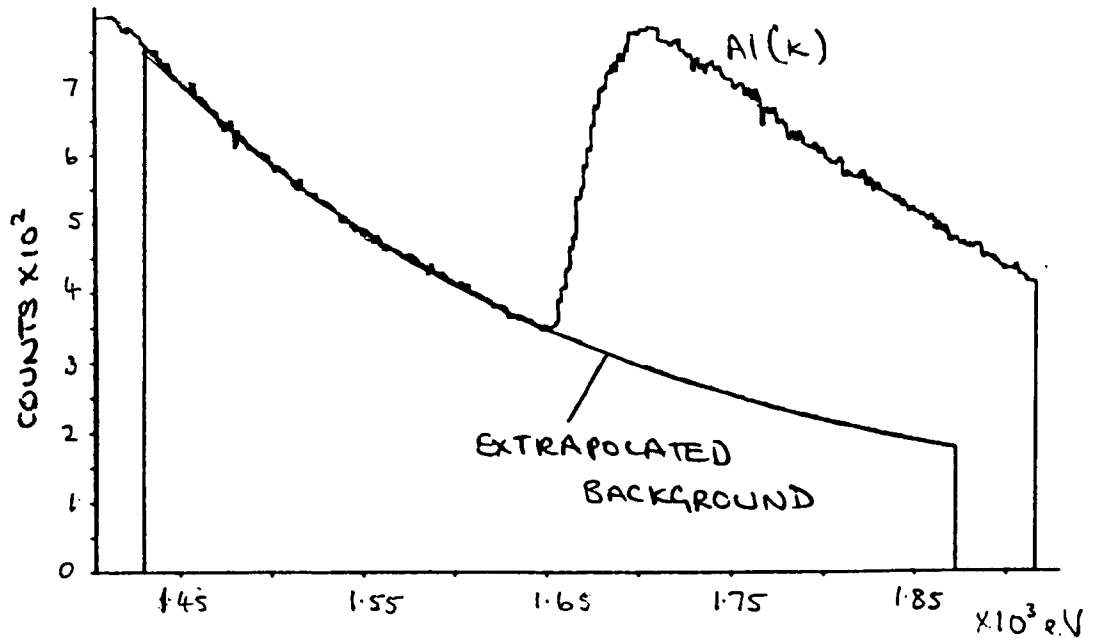
(b)
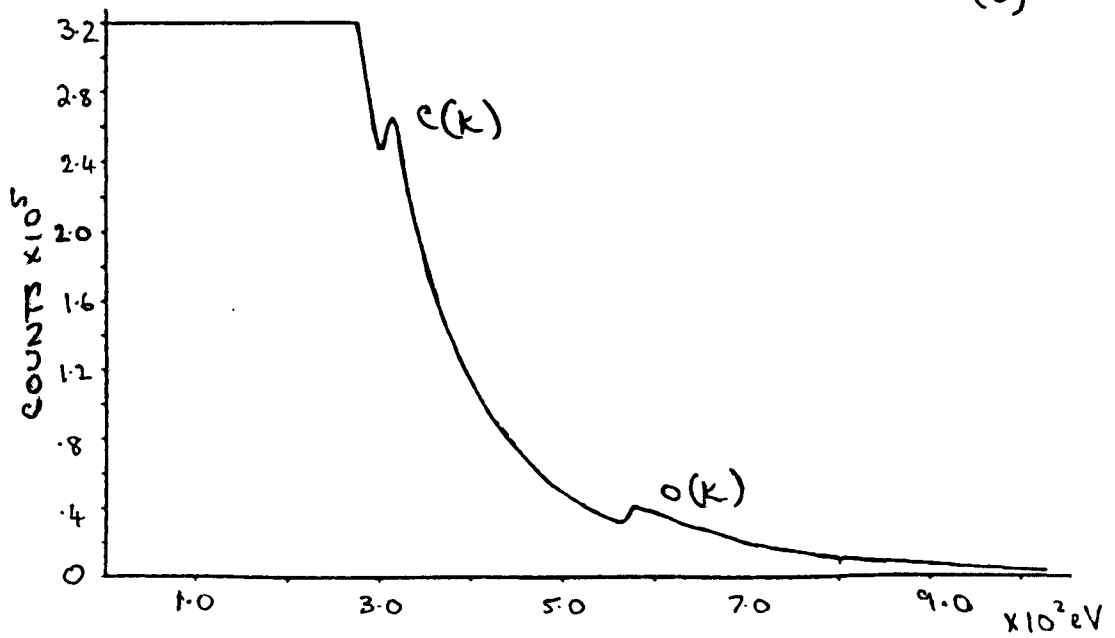
Figure 7.13

	Signal/Backround ratio (%)
low Al concentration	0.05
high Al concentration	0.54

Table 7.2
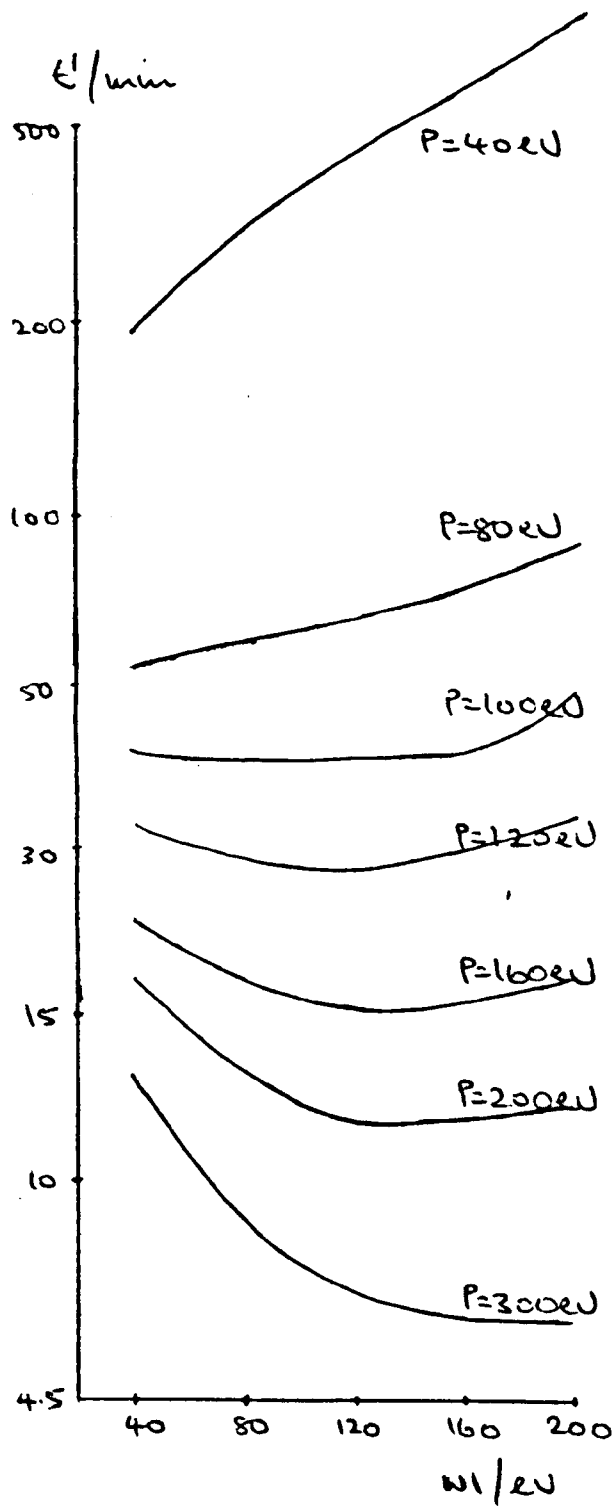
Figure 7.14 Experimentally determined t' values for the high trace Al concentration, Al(K) edge signal.

values of P and W1 for the Al(K) edge signal. As expected, the choice of P significantly influences the time t^1. Egerton (1983) noted that the signal/noise ratio (Equation 7.10) typically decreased or remained constant for increasing W1. To follow this trend, t^1 should increase or remain constant with increasing W1. Figure 7.14 shows that this occurs for P$\leq$160 eV. For longer values of P there is a decrease in t^1 with W1; however, as stated in Section 7.3.3, an EEL spectrum only follows an $A(\Delta E)^{-r}$ form over a limited energy range.

As stated in Section 7.3.3(b), the systematic uncertainty in the background modelling will only be considered negligible if the total pre-edge fitting range and post-edge signal integration range do not exceed 180 eV, i.e. P+W1 $\leq$ 180 eV. If it is also assumed that W1 has to exceed 40 eV because the region close to edge onset is not described well by theory (see Figure 7.12), then for P+W1 $\leq$ 180 eV and W1 > 40 eV, from Figure 7.14, $t^1 \geq$ 30 min. Clearly the t^1 values for the low trace Al concentration will be much greater than 30 min.

7.3.7 Summary

It is not possible to extract the Al(L) signals from the trace concentrations due to the limitations of the signal extraction procedures. If the extrapolation method was used to extract the Al(k) signal, then $t^1 \geq$ 30 min for the high trace Al concentration, and $t^1 \gg$ 30 min for the low trace concentration. Since the low trace Al concentration could be quantified using an EDX spectrum which was acquired for 20-25 min (see Chapter 5), there was no advantage in using EELS, even if suitable samples could have been prepared. However, it might be possible to improve on this level of detectability by

optimising the experimental conditions. This is discussed in the next section.

7.3.8 Optimising the Experimental Conditions for Detection of the Al(L) and Al(K) Signals

It should be noted that EEL Al signals were never observed in sections cut from the experimental sample blocks used in the EDX study. In addition, the same samples were sent to the Carl Zeiss Laboratories, Oberkochen, West Germany, and EEL signals from the trace concentrations were not detected either (Hetzel, personal communication).

Arsenault et al (1983) show electron spectroscopic images (ESI's) of trace Al concentrations in MB. The ESI's were obtained using the Al(L) signal and the Al concentrations were probably very similar to the concentrations used here because the basic physiological experiments were essentially identical. The ESI technique used by Arsenault et al (1983) is based on Equation 7.12. Thus, Arsenault's study appears to contradict the predictions in this chapter. Since Leapman (1980) has suggested that, in general, mass thickness artefacts are unavoidable in Arsenault's type of ESI technique, even when attempting to image a relatively high concentration element such as P in MB, it was of interest to consider the effects of optimising the experimental conditions; i.e. to see whether the trace Al signals could ever be detected using EELS.

Clearly it is the low signal/background ratios which limits the applicability of EELS to the study of trace Al concentrations. There are two ways to increase the signal/background ratios, decrease the specimen thickness t, or optimise the electron collection semi-angle β.

7.3.8(a) Al(L) Signal/background Ratio

It is unlikely that removal of the plural inelastic scattering in the spectrum shown in Figure 7.3, (e.g. by deconvolution) would significantly increase the peak/background ratios stated in table 7.2 since, from Equation 2.15, the probability of plural inelastic scattering is less than 9%.

Egerton (1983) notes that the signal/background ratio typically is at a maximum for $10 < \beta < 30$ mrad when the background counts arise from both the plasmon interaction and a closely preceding edge. This is the case for the Al(L) signal in a MB spectrum since almost half the background counts are due to the Ca $M_{2,3}$ edge. It should be noted that electrons which have been scattered through greater than 27 mrad can be detected since $\alpha = 25$ mrad. An estimate of the "Effective" electron collection semi-angle can be obtained from $\beta^1 = \sqrt{\alpha^2 + \beta^2}$. Therefore, $\beta^1 = 38$ mrad. There is nothing in the literature (e.g. Egerton (1983), Crozier (1985)) which suggests that the peak to background ratios stated in Table 7.2 would be more than doubled if β^1 was reduced to the 10 to 30 mrad range.

Since the signal/background ratio would only be ~2% if β^1 was reduced, it is still not possible to extract the Al(L) signal from a trace concentration in MB, even if optimum experimental conditions had been used.

7.3.8(b) Increasing the Al(K) Signal/background Ratio

Since there are no counts from the valence shell interaction underlying the Al(K) signal and the plural inelastic scattering is negligible, it is not possible to increase the signal/background ratios

by decreasing the specimen thickness.

However, it is possible to theoretically calculate the variation in this ratio as β is changed since the cross-sections for Al(K), O(K), Ca(L) and P(L) can be calculated from the SIGMAK and SIGNAL programs of Egerton. The Al(K) signal/background ratio is proportional to

$$\frac{\sigma_{Al}}{\sigma_T} = \frac{\sigma_{Al}}{\sigma_{Ca} n_{Ca} + \sigma_P n_P + \sigma_o n_o} \qquad 7.19$$

for element K integrated over an energy window 1.56 - 1.71 keV where σ_K are the cross-sections and n_K are the atomic fractions for these elements. The n_K values were calculated assuming the specimen was composed of hydroxyapatite.

Figure 7.15 shows the ratios $\dfrac{\sigma_{Al}}{\sigma_o}$, $\dfrac{\sigma_{Al}}{\sigma_P}$ and $\dfrac{\sigma_{Al}}{\sigma_{Ca}}$

As expected, these ratios decrease with increasing β due to the characteristic Al(K) signal being more forward peaked than the background signal. There is no change in these ratios for $\beta \leq 13$ mrad and this is because, in Equation 2.13, the kinematical term dominates the generalised oscillator strength for small scattering angle. The decrease in the cross-section ratios continues for $\beta \geq 100$ mrad and this is since at high scattering angles, the generalised oscillator strength dominates the kinematical term and the former continues to increase with β for characteristic signals with $E_K \geq 700$ eV (e.g. Egerton, 1983). The ratio σ_{Al}/σ_T (Equation 7.19) is at a plateau for $\beta < 27$ mrad and as

127
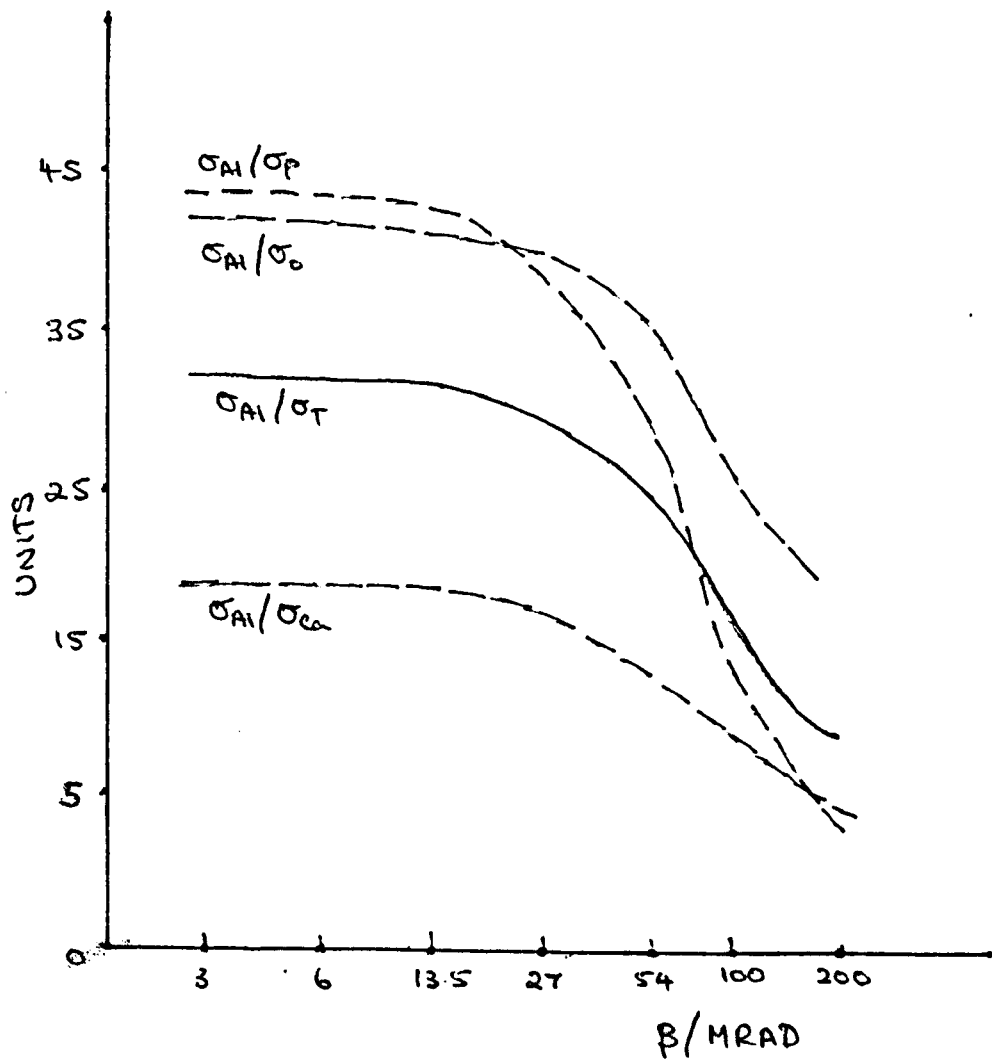
FIGURE 7.15

stated previously, $\beta^1 \doteqdot 54$ mrad. Figure 7.15 shows that the signal/background ratio will be increased by about 28% by reducing β to ~13 mrad. However, the signal from the trace Al concentrations will still probably be easier to extract and quantify using EDX.

7.3.9   CONCLUSION

The Al(L) signal from the high trace Al concentrations can not be extracted from an EEL MB spectrum assuming the experimental conditions defined in Section 7.3.1 are used. Even if the experimental conditions were optimised for detection of this signal, it would still not be possible to extract the signal from the background counts. This contradicts the finding of Arsenault et al (1983).

The Al(K) signal from the high and low trace concentrations could be separated from the MB background using the extrapolation method. There is little improvement in signal detectability (signal/background ratio) if optimum experimental conditions for Al(K) signal detection had been used.

In view of the preceding discussion, and the fact that EEL MB specimen preparation introduces artefacts and is more difficult than EDX specimen preparation, EDX is clearly the better technique for studying the distribution of trace concentrations of Al in MB. The ESI images of the trace Al distribution in MB samples obtained by Arsenault et al (1983) were probably produced by variations in specimen mass thickness.

CONCLUSIONS AND FUTURE WORK

8.1 INTRODUCTION

The major part of this thesis has been concerned with the detection and quantitation of trace concentrations of Al and Mg in mineralised bone. There were two motivations for this work; the first one being to develop and extend the techniques available for quantifying, at high spatial resolution, trace concentrations of low atomic number elements in a mineral/organic matrix. The second motivation was to further elucidate the modes of action of Al poisoning in interfering with the bone mineralising process. The latter is discussed in Appendix 1.

The EDX technique was chosen for this study because the signals from the trace concentrations were never detected using EELS. The main aspects of the EDX study consisted of:

a) Theoretically modelling the experimental MB bremsstrahlung distribution to allow extraction of the characterisic signals and determination of the specimen self-absorption correction. The approach taken here was to first characterise the detector efficiency using the simplest possible spectra, i.e. spectra with minimal or negligible self-absorption corrections, and with no major characteristic peaks in the low energy region.

b) Attempting to minimise the uncertainty in the theoretical total ionisation cross-section ratios by further investigating the parameterisation of the cross-section data of Gray (1981).

The main aspects of the EEL study consisted of:

a) The development of a new technique of EEL spectral processing which
    appears to have some advantages over the standard extrapolation
    method.

b) An investigation into the problems associated with EEL MB specimen
    preparation, and the application of EELS to the study of trace Al
    concentrations, assuming adequate specimen preparation techniques
    had been available.

8.2 EDX DETECTOR EFFICIENCY

X-ray spectra from simple thin foil samples were acquired and
analysed to determine the efficiency of the HB5 EDX detector. The
efficiency was determined by scaling the theoretical MBH bremsstrahlung
distribution to the spectrum mid-energy region, and then optimising the
fit to the low and high energy regions by regarding the Be-window and
Si-crystal thickness (t_{Be} and t_{Si}) as variables. The t_{Be} and t_{Si}
values obtained by this method lay within the range of values quoted in
the literature. In addition, these thicknesses were found to be
completely independent of the specimen atomic number, clearly suggesting
that the thicknesses were representative of the detector. However,
some discrepancy exists between published values of mass absorption
coefficients and so the t_{Be} and t_{Si} values are, to a limited extent,
dependent upon the choice of coefficients. The uncertainty in the
coefficients was not significant for this particular study because the
t_{Be} (and t_{Si}) thicknesses were always used with the coefficients chosen
originally for the determination of detector efficiency. The only
region which could not be modelled well theoretically was the region
just below the Si-absorption edge. Future work in the following areas
would be useful:

a) Redetermination of the mass-absorption coefficients in an attempt to improve their accuracy.

b) Further investigation of the bremsstrahlung count redistribution at the Si-absorption edge. The use of a detector with a relatively small amount of incomplete charge collection (if available) is preferable. With such a detector, the count redistribution may be almost negligible (e.g. see Gray, 1981).

8.3 EDX CHARACTERISTIC CROSS-SECTION PARAMETERISATION

Parameterisation of the cross-section data of Gray (1981) has been examined in detail using different forms of the Bethe equation. There was no clear advantage in using a form of equation different to that chosen by Gray. When examining the parameterisation of the data it became clear that the discrepancy between experimental and parameterised cross-sections was largest for the Al cross-sections, irrespective of the form of the parameterisation functions. Gray (1981) noted that these data might be suspect and therefore the Al(K) (T_o = 100 keV) cross-section was redetermined. The EEL Al spectrum acquired simultaneously with the EDX Al spectrum indicated the presence of a significant C and O light element contribution to the "Al" bremsstrahlung. Closer agreement between experimental and parameterised cross-section was achieved when the corrected Al cross-section was substituted into Gray's data.

More work in the following areas would be useful:

a) The specimen used to redetermine the Al cross-section was not ideal because of the significant C and O contribution. Therefore,

131

another specimen should be prepared and the cross-sections for $T_o =$ 40, 60, 80 and 100 keV recalculated.

b) The presence of O and C contamination would have been less significant for the higher Z elements in Grays data (since the efficiency of bremsstrahlung production varies approximately as Z^2); however, these other cross-sections could be checked also.

c) Egerton (1979) and Rez (1984) suggest that the hydrogenic model is adequate for determining total ionisation cross-sections. Egerton's SIGMAK program can be used to calculate these cross-sections and a preliminary investigation showed good agreement between the values of cross-section obtained from the SIGMAK program, and those published by Rez (1984). However, since Rez had only calculated the Bethe parameters for three elements in Grays cross-section data, Rez's parameters were of limited use. The SIGMAK program should allow calculation of total ionisation cross-sections for most elements. This would be useful for providing additional cross-sections for elements not included in Gray's basic experimental data. Cross-section ratios could also be determined from commercially available standards.

8.4 INVESTIGATION OF TRACE Al CONCENTRATIONS IN MINERALISED BONE EDX SIGNAL EXTRACTION AND QUANTITATION.

A number of significant problems exist which complicate the extraction of the signals from trace Al and Mg concentrations. These are due to:

a) Extensive overlap between the major P peak and the trace element peaks.

b) The bremsstrahlung background at the trace peak energies is changing rapidly due to absorption in the detector and specimen.

c) The redistribution of counts in the detector also affects the shape of the bremsstrahlung in the trace element region.

The technique of spectral processing which was developed did allow extraction of the characteristic Al counts. However, it does have the following disadvantages:

a) The self-absorption correction to the bremsstrahlung had to be optimised for each spectrum. Therefore, it was necessary for each spectrum to be processed and checked visually several times, which was time consuming since over 100 spectra were acquired.

b) The (ICC) count build-up on the bremsstrahlung had to be modelled empirically.

A "windowless" EDX detector with minimal incomplete charge collection would have the following advantage for future work:

a) Less change in the MB bremsstrahlung shape at the trace peak energies since there is no absorption in a Be-window.

b) Much less overlap between the P peak and the trace Al (and Mg) peaks. In addition, the bremsstrahlung count redistribution would be less.

The MB Mg/Ca, Al/Ca and Ca/P count ratios were quantified to better than 9%, 5% and 3% respectively. The uncertainty in the total ionisation cross-sections are the main cause of these uncertainties; therefore, the work suggested in the previous section may improve the accuracy of quantitation.

8.5 EEL SPECIMEN PREPARATION

Specimen preparation for EELS is more difficult than for EDX because of the need to prepare thinner specimens. Suitably thin specimens were obtained by either wet-cutting or ion beam thinning. The former technique has the disadvantage that significant alteration of specimen composition may occur. The latter technique was of limited use because thin regions of specimen were rarely produced in the areas of most interest.

8.6 AN INVESTIGATION INTO THE APPLICATION OF THE EEL TECHNIQUE TO THE STUDY OF TRACE Al CONCENTRATIONS IN MB.

In Chapter 7, the application of EELS to the study of trace Al concentrations in MB was discussed. Even if suitable specimen preparation techniques were available, the Al(L) signal could not be extracted from the MB spectrum when the "standard acquisition conditions" (defined in Chapter 3) were used. If the experimental conditions were optimised for detection of the Al(L) signal, signal extraction would still not be possible. This contradicts the finding of Arsenault et al (1983) and is in agreement with the prediction of Leapman (1980). Using the extrapolation technique, it should be possible to extract the Al(K) signal from the EEL background counts. If "parallel" EEL data acquisition equipment had been available, then the Al(K), t^1 values quoted in Chapter 7 would, of course, be significantly reduced. However, there is still no clear advantage in using EELS rather than EDX because the signal/background ratio is so low.

8.7   THE EEL SINGLE-STAGE TECHNIQUE.

A new method of analysing electron energy loss spectra has been suggested in which the characteristic signals are separated from the total EEL spectrum and quantified in a single process.   When fitting a background curve it was necessary to force the curve to pass through the pre-edge region.   The curve fitting procedure was tested on artificial and real ionisiation edges with satisfactory results.   From the comparison of single-stage and extrapolation technique, it would appear that when using the single-stage technique, the extracted signal is less dependent upon the choice of pre-edge fitting range.   Difficulties still exist when trying to analyse spectra containing a range of adjacent edges.   This is partly attributable to the inadequacy of the cross-sections close to the edge onsets.   Despite this, the single-stage technique appears to offer some advantages when dealing with relatively small signals on large backgrounds.

PHYSIOLOGICAL INTERPRETATION

A.1 Introduction

A number of studies has shown that Al can produce a form of osteomalacia occuring in patients with chronic renal failure and on regular haemodialysis (Ellis et al 1979, Druke 1980, Boyce et al 1981, 1982). It is frequently associated with a severe form of dementia in which high concentrations of Al have been found in blood, bone, and brain tissue (Alfrey et al 1972, 1976, Elliot et al 1978, Pierides et al 1980, Parkinson 1979). Epidemiological studies originally suggested that the source of the Al was dialysate prepared from tap water, and it was shown that removing Al from the dialysate greatly reduced the incidence of the disease. It was then believed that, with the establishment of permissible levels of the metal, Al toxicity would no longer occur. This was not the case, and Ward et al (1979) and Rottenbourge et al (1980) provided evidence that some remaining cases of Al poisoning were due to the patients' medication; Al based phosphate binding drugs. This Appendix describes a further investigation into the toxic effects of Al on bone mineralisation.

A.2 Bone mineralisation and the effects of Al

Amorphous calcium phosphate (ACP) or poorly crystaline hydroxyapatite (PCH) comprise a significant portion (about 40%) of the mineral in adult femurs of several species (eg Harper et al, 1966) and in young animals up to about 70% can occur (Termine et al, 1967). The latter authors have suggested that ACP, PCH (+ octacalcium phosphate etc) may be the initial form of mineral deposited during nucleation,

most of which is subsequently converted to crystaline HA. More recently,
Blumenthal et al (1984) studied the effect of Al on three _in vitro_ test
systems considered to be analogous to biological mineralisation: (a)
direct HA precipitation, (b) transformation of ACP to HA and, (c) growth
of HA seed crystals. They found that in all three systems the initial
time from mixing of reagents to the initial time for formation of HA
(the induction time) was not affected by the presence of Al, clearly
suggesting that _in vitro_, Al has negligible involvement with the
chemical processes that occur initially in HA nucleation. Al was found
to slow the rate of crystal growth, only once it had begun. Blumenthal
et al (1984) suggested that Al ions and/or $AlPO_4$ may adsorb onto the
surface of already formed HA nuclei, poisoning growth sites and
inhibiting HA proliferation. However, it is also possible that Al may be
incorporated into the HA crystals, since Al rich apatites may contain
more than 25% of Al (Fisher et al, 1969).

In vivo mineralisation, of course, depends on osteoblast activity.
Osteoblasts synthesise calcifiable matrix as well as a number of
specific factors which inhibit or promote mineralisation (eg Bernard,
1982). In embryonic bone the initial site of apatite nucleation is
located in structures which derive directly from these cells; ie
vesicles or osteoblast extrusions (Bonucci, 1971). In mature bone, most
mineral deposition occurs on collagen fibrils (Bonucci, 1971) and pre-
existing crystals (Anderson et al, 1981), although the presence of
vesicles near the osteoblasts have been reported (Anderson et al, 1981).
Therefore, intact osteoblast activity is essential not only for matrix
deposition but also for matrix mineralisation. Vernejoul et al (1985)
have recently provided histomorphometric evidence of the deleterious

effect of Al on osteoblasts. Other toxic effects of Al have been reported: eg Boyce et al (1981) found that in preliminary in vitro studies, Al inhibited the action of alkaline phosphatase, an enzyme closely associated with mineralisation. Clearly Al exerts toxic effects on a variety of mechanisms important for mineralisation.

The following section discusses the experimental animal protocol used for the study described in this thesis. (The experiment was performed by Dr H Y Elder).

A.2.1 Experimental animal protocol

Standard laboratory rats (Wistar, starting at about 90g wt.) male, were put in single cages and put on a normal animal house diet (food and water ad libitum).

An experimental group consisting of 8 rats (2 died of infections during the course of the 10 week experiment) received daily (5 days per week) intraperitoneal (IP) injections of AlCl₃ solution at a concentration of 1 mg/ml and rising over the first 10 days to 5 mg/ml. The rats were weighed before each injection and the volume of the solution was varied according to the weight of the rat.

A control group of 4 rats received daily (5 days per week) IP injections of distilled water. Again the volume of the solution was varied according to the weight of the rat.

A.3 Results

Figures A.1 to A.9 show Al/Ca, Mg/Ca and Ca/P atomic (molar) ratios for the experimental and control samples which were determined using the experimental technique described in chapter 5. Each set of ratios will be discussed separately.

A1.3
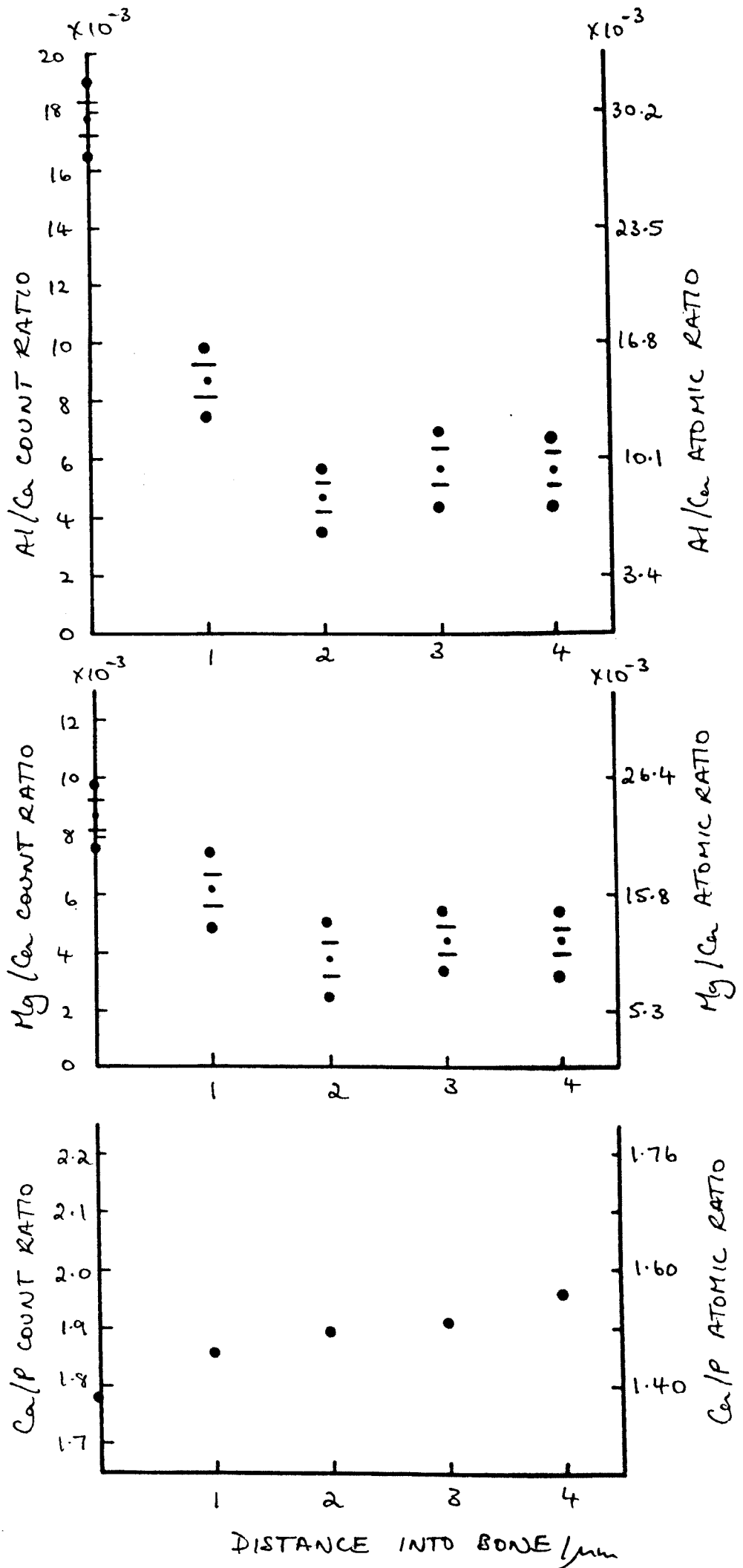
FIGURE A.1 EXPERIMENTAL SAMPLE 1 (84/106)
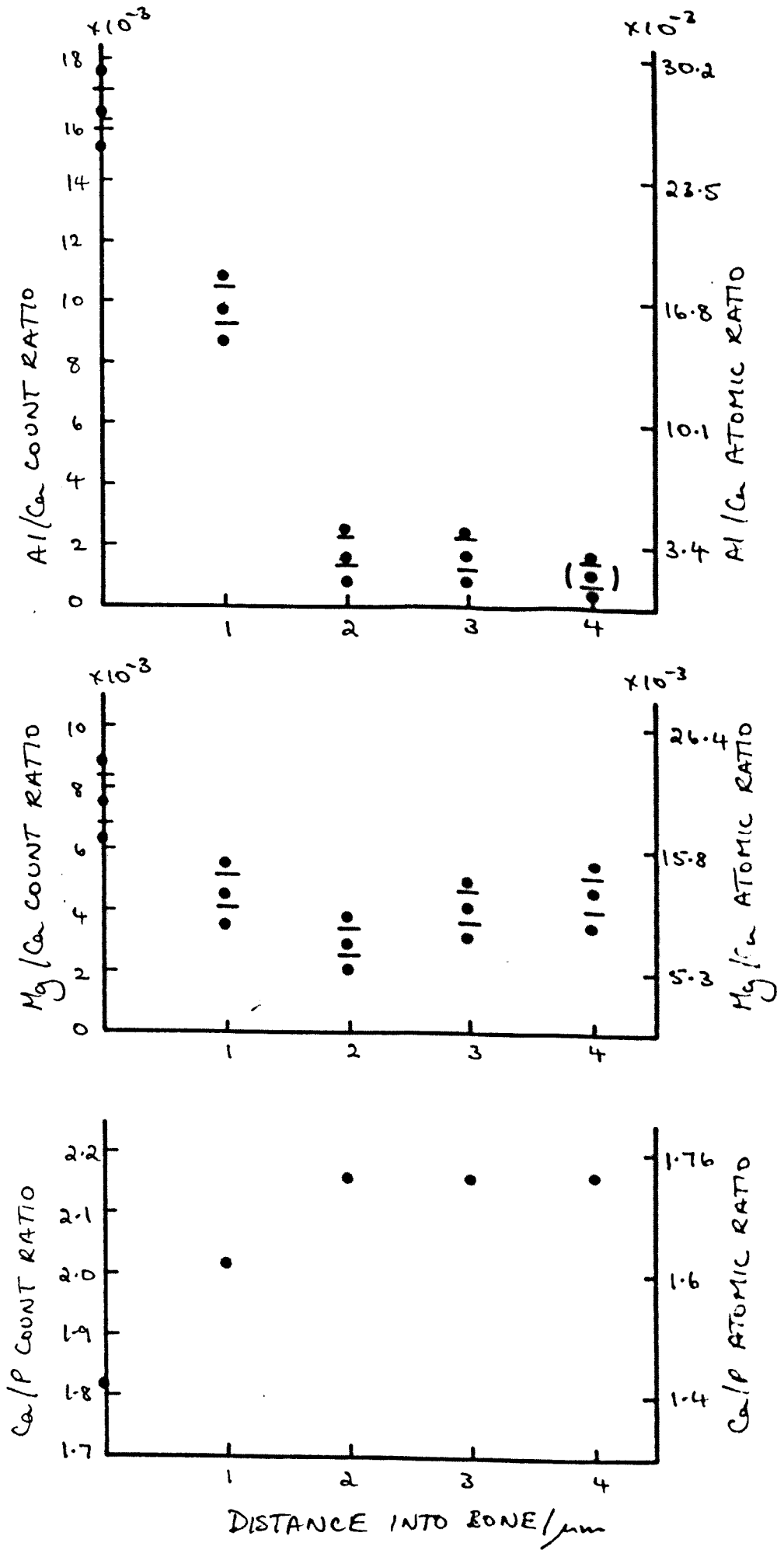
FIGURE A3 EXPERIMENTAL SAMPLE 2 (84/105)
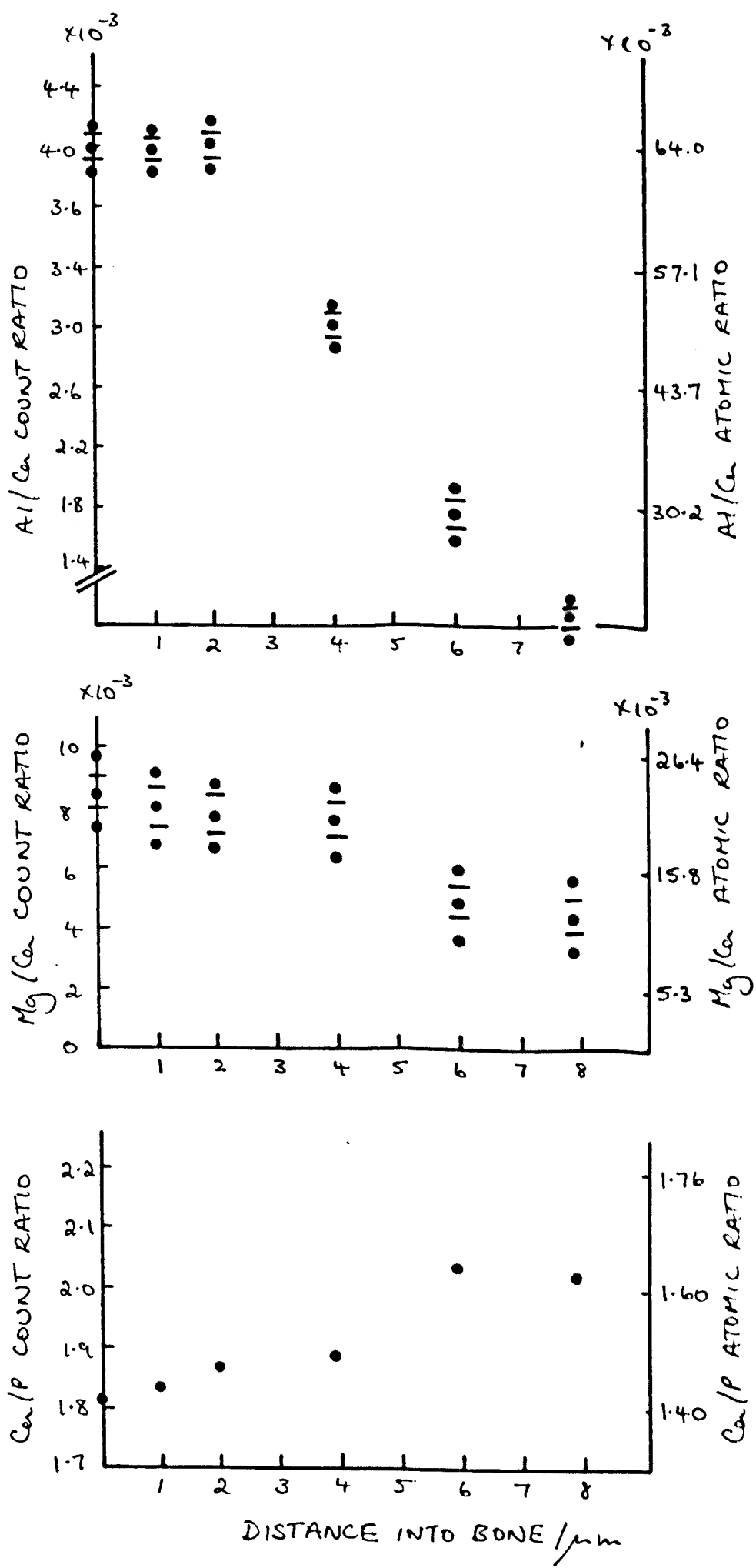
FIGURE A.3 EXPERIMENTAL SAMPLE 3 (84/108)
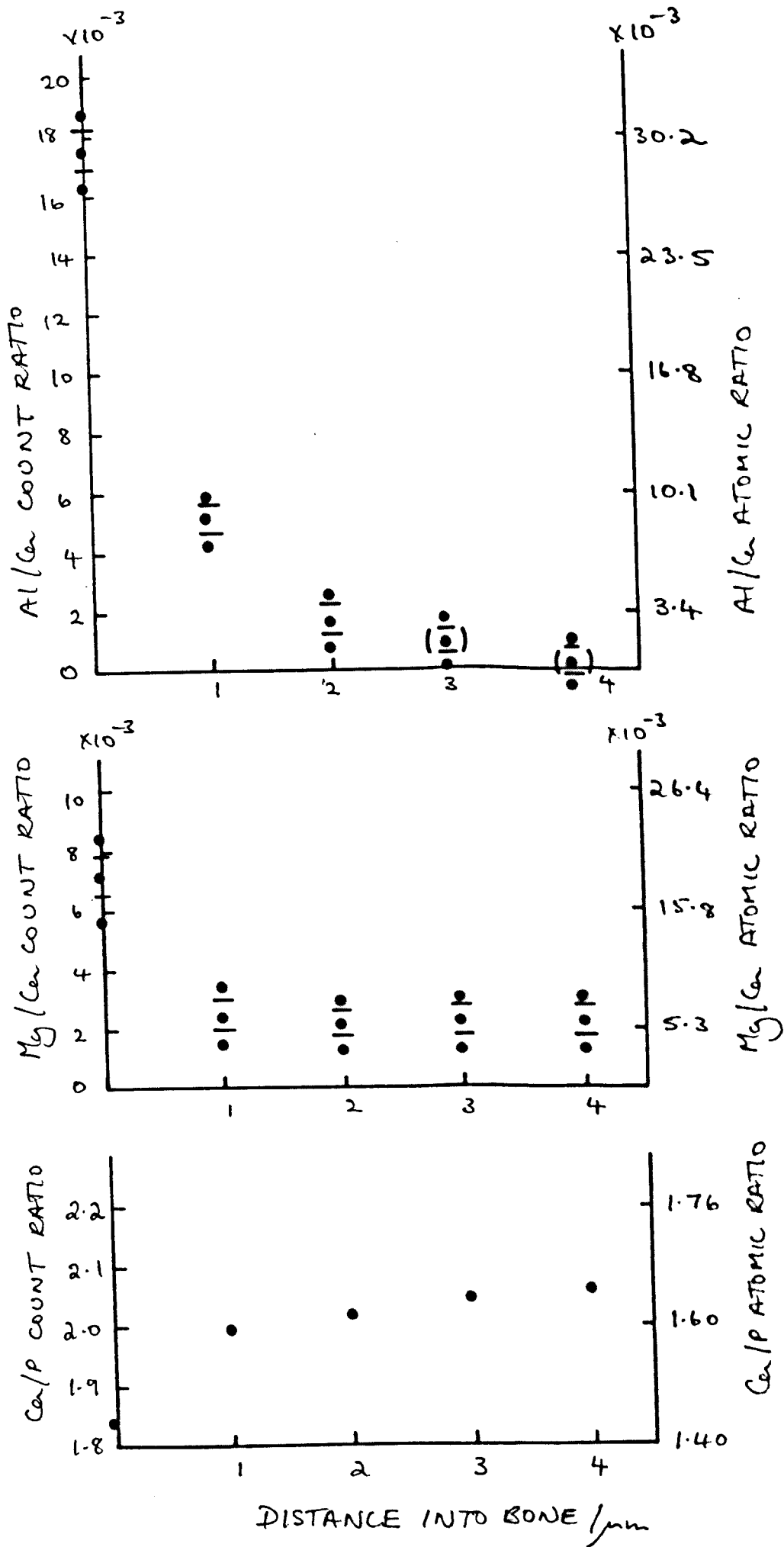
FIGURE A.4 EXPERIMENTAL SAMPLE 4 (84/108)
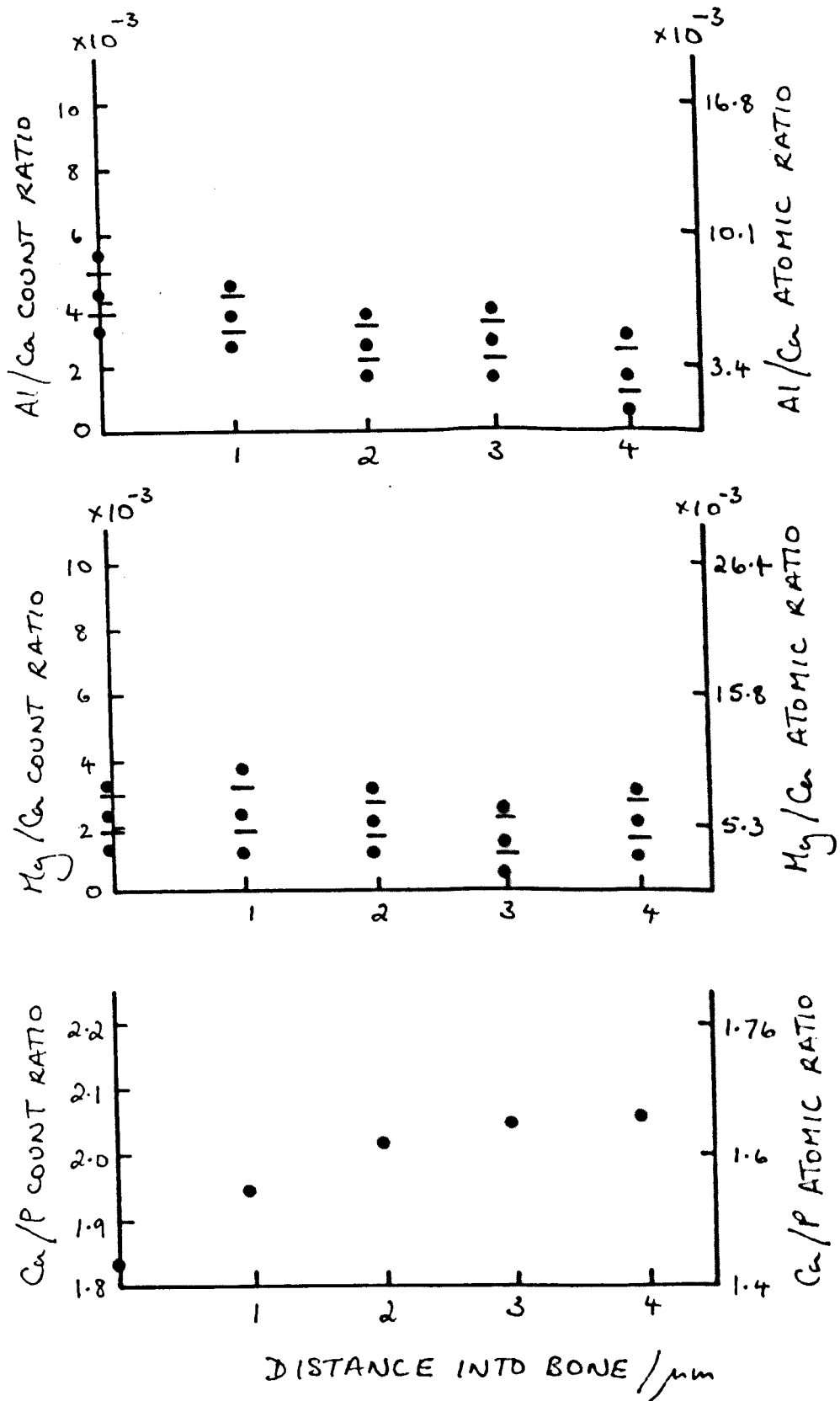
FIGURE A.5 EXPERIMENTAL SAMPLE 5 (84/104)
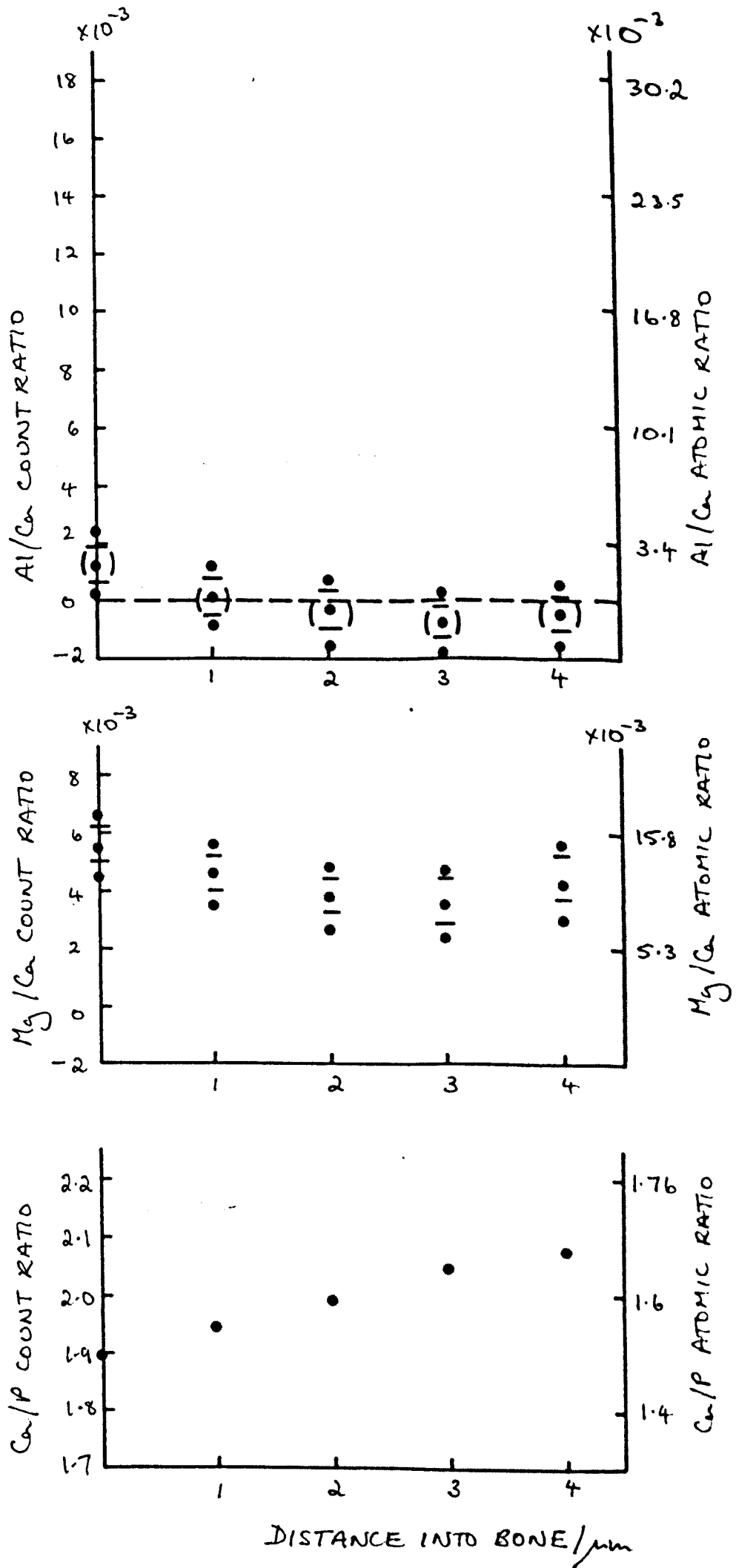
FIGURE A.6   CONTROL SAMPLE I   (84/101)
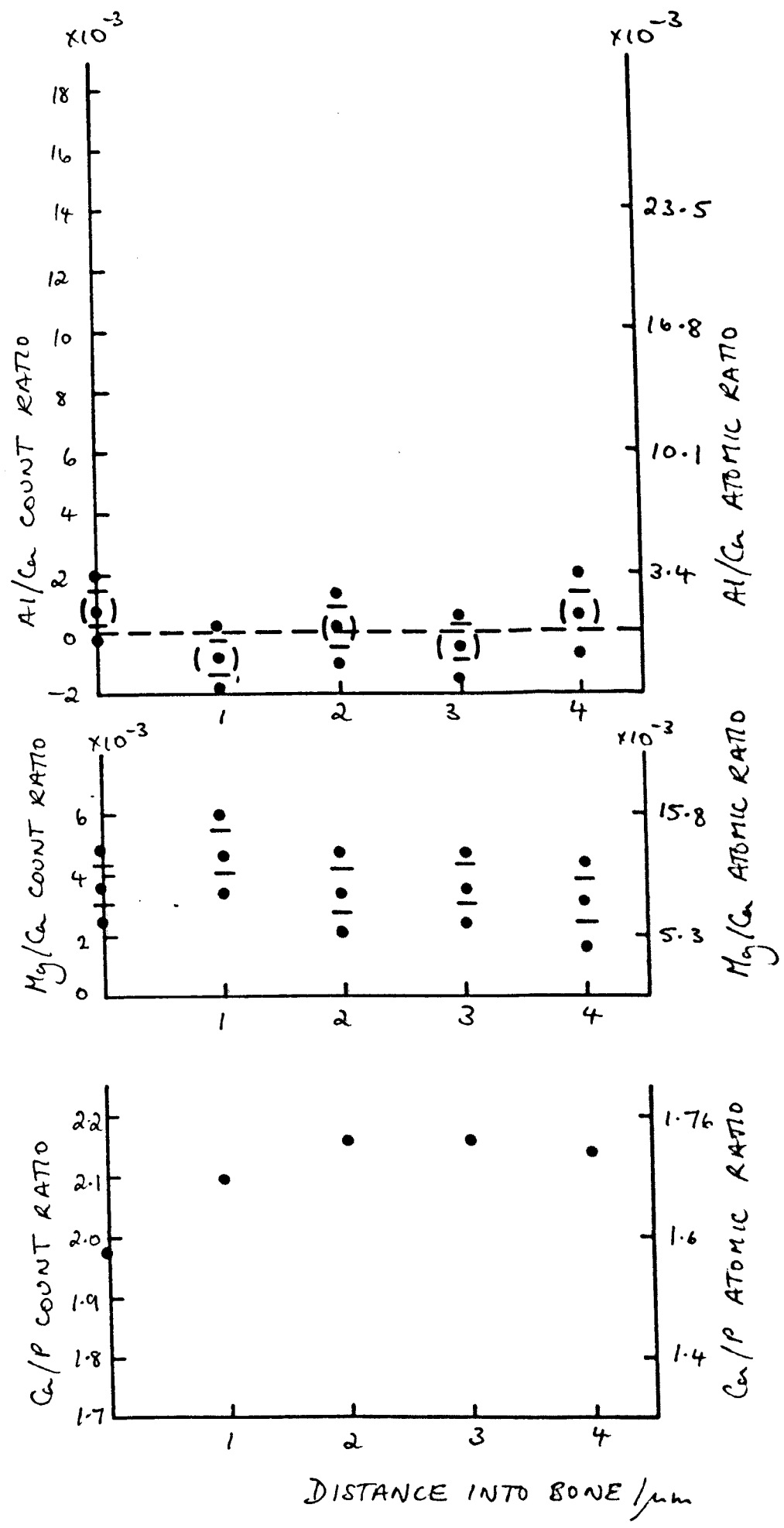
FIGURE A.7 CONTROL SAMPLE 2 (84/100)
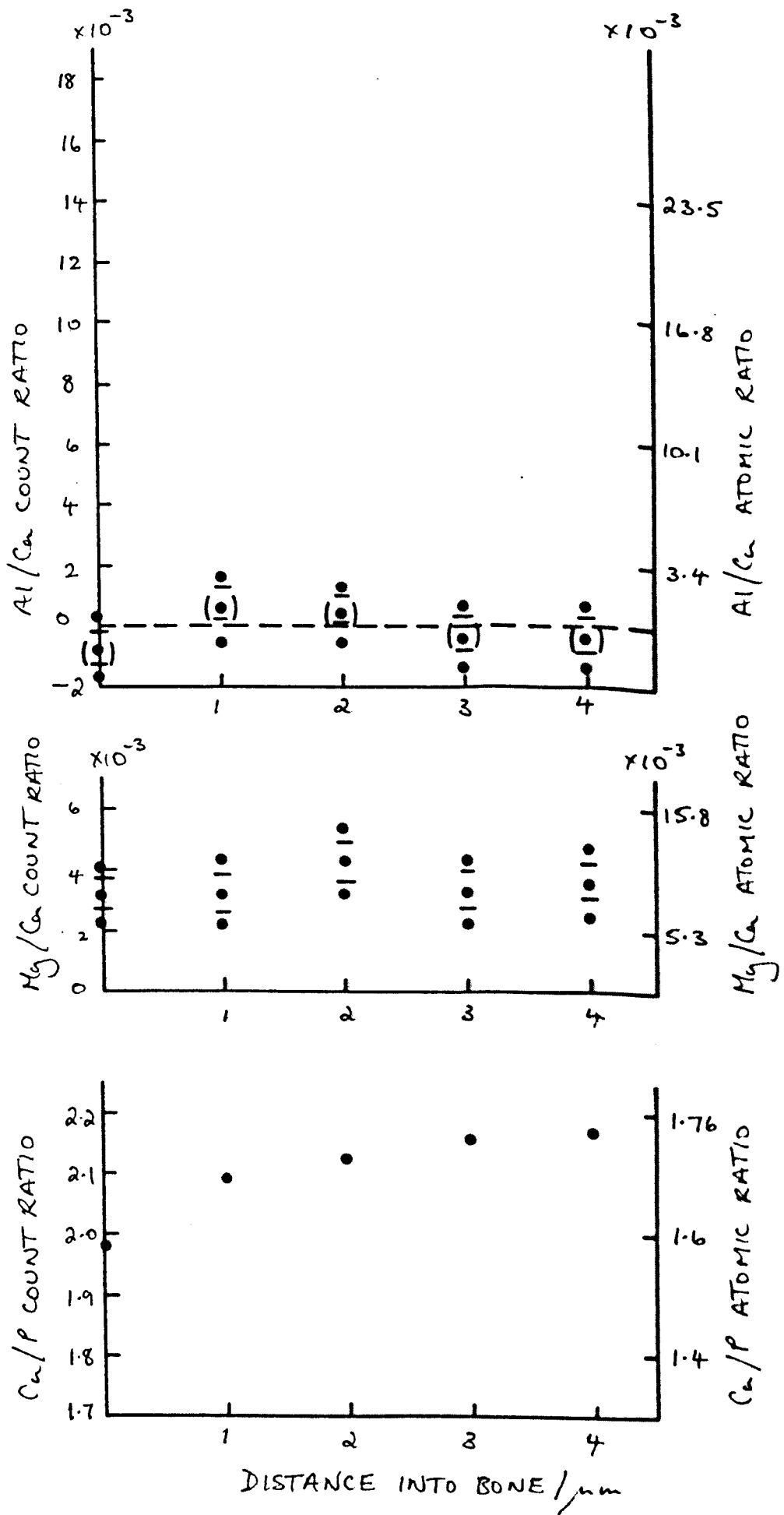
FIGURE A.8   CONTROL SAMPLE 3   (84/102)
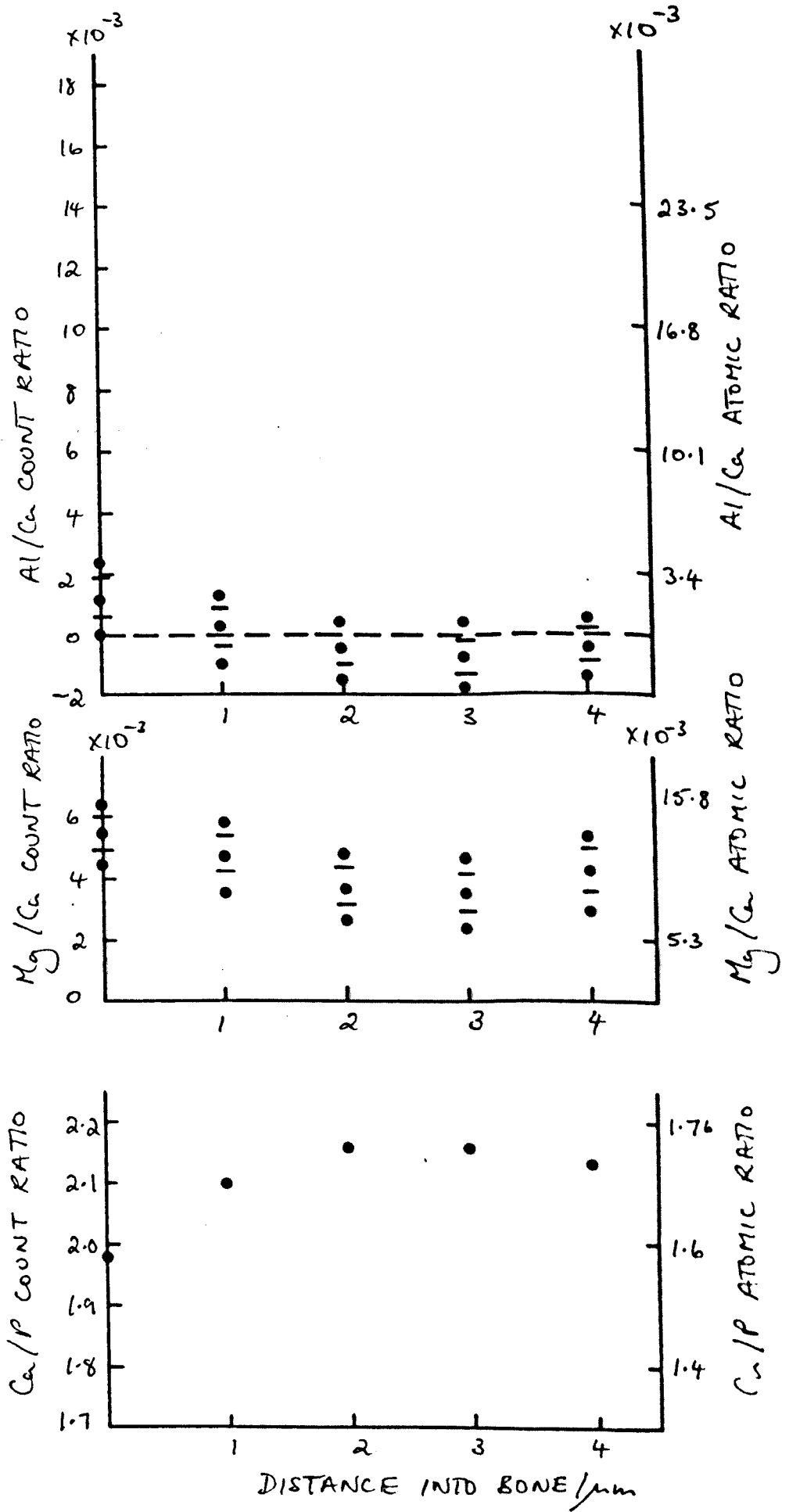
FIGURE A.9 CONTROL SAMPLE 4 (84/99)

3.1(a) The Ca/P ratios

The Ca/P ratios determined for both the experimental and control samples increase with increasing depth into the bone. The atomic (ie molar) Ca/P ratios obtained for the deep bone (>2μm from the surface) were 1.67 ± 0.02 for the control samples, and 1.66 ± 0.04 for the experimental samples. The difference between these ratios is clearly not significant, and these values lie within the range of values quoted in the literature for hydroxyapatite (1.62: Landis 1978) and fully mineralised bone (1.67: Nicholson et al, 1980).

The Ca/P ratio obtained from the surface bone region of the experimental samples was 1.46 ± 0.03, and the ratio determined from the surface region of the control samples was 1.58 ± 0.01. There is a significant difference between the ratios obtained from these two regions and the deep bone ratios.

The progressive shift to higher molar Ca/P ratios in extracellular matrices with increasing mineralisation and maturation accompanied by increasing crystallinity has been observed in non-Al poisoned bone by previous workers (eg Landis, 1978). The molar Ca/P ratios determined by Landis (1978) for a number of different calcium phosphates are summarised in table A.1. The value of the ratio obtained here for the experimental sample surface bone (1.46 ± 0.03) is very similar to the value determined by Landis (1978) for ACP/PCH (1.45) whilst the ratios obtained here for control sample surface bone (1.58 ± 0.01) lies between the values obtained by Landis (1978) for tri-calcium phosphate (1.50) and HA (1.62).

Ca PHOSPHATE	ATOMIC Ca/P RATIO
calcium metaphosphate	
$(Ca(PO_3)_2)$	0.50
moneite	
$(CaHPO_4)$	1.00
brushite	
$(CaHPO_4.2H_2O)$	1.03
octacalcium phosphate	
$(Ca_6H_2(PO_4)_6.5H_2O)$	1.34
ACP and PCH	1.45
tri-calcium phosphate	
$Ca_3(PO_4)_2$	1.50
well crystalised HA	1.62

Table A.1 The ratios have been taken from Landis (1978)

A.3.1(b) Interpretation

(a) Previous workers have shown that Al inhibits the bone mineralisation process. As discussed in section A.2, Termine et al (1967) have suggested that bone mineralisation takes place in essentially two stages; firistly most of the ACP,PCH is deposited in the bone matrix then secondly, most of the ACP,PCH etc. is converted to crystaline HA. Blumenthal et al (1984) found that Al inhibited in vitro crystal growth, only once it had begun. It might be predicted from this work that the regions of bone which contain Al in relatively high concentrations would have a higher ACP,PCH to HA ratio than the equivalent regions in non-Al poisoned bone. This is indeed suggested from the results described in this Appendix, since the Ca/P ratios are significently lower in experimental sample surface bone, compared to control sample surface bone. To test whether crystalline HA was present (significantly) the selected area diffraction technique (SAD) was used to investigate the crystalline structure of different regions of normal and pathological bone. This is described in section A.3.4.

(b) Regions of dormant bone surface in the control samples are not fully mineralised (ie to a Ca/P ratio of 1.62 to 1.67). This is probably due to the bone at this site having undergone less maturation than deep bone.

A.3.2(a) The Al/Ca ratios

Al was detected in the experimental samples and no Al was found in the control samples. The Al/Ca ratios determined for the experimental samples decrease with increasing depth into the bone. This trend has been suggested from previous studies (eg. Boyce et al, 1981). The Al/Ca

ratios typically fall below the level of detectability about 2μm from the bone surface, although in one sample (sample 3) Al was detected at about twice the level observed in most of the other samples, and was still easily detectable >4μm into the bone. It is interesting to note that 3 of the 5 experimental samples have very similar values of Al/Ca ratios (about 27×10^{-3}).

A.3.2(b) Interpretation

Al might be incorporated into the bone or onto the surface of the bone as multiples of a basic Al phosphate unit; ie since the (surface bone) ratio 27×10^{-3} occurs most often, 64×10^{-3} is about twice this ratio , and 6.4×10^{-3} is about one quarter of the 27×10^{-3} value. Clearly more data would be required to investigate this further.

A.3.3(a) The Mg/Ca ratios

The ratios for the control samples remain approximately constant with increasing depth into the bone. In contrast, the ratios from the experimental samples decrease with increasing bone depth.

A.3.3(b) Interpretation

Mg is thought to be associated with mineral nucleation (eg Quint et al 1980) with the Mg being subsequently "buried" in HA. Quint found that the Mg/Ca ratios were highest at the surface region of mineralising turkey tendon (which Quint regarded as a good model for studying bone mineralisation). The Ca/P and Al/Ca data presented in this thesis suggests that the mineralising process is stopped at an early stage if

sufficient Al is present. Consistent with this is the pronounced decrease in the experimental Mg/Ca ratios, compared to the control ratios, with increasing depth into the bone.

3.4 Investigation of bone structure using selected area diffraction

Figure A.10 shows a schematic diagram of a region of experimental bone which was investigated using EDX. A graph of atomic (ie molar) Ca/P ratios is shown underneath. The ratios correspond to the average of all the Ca/P ratios determined for all the experimental samples (excluding sample 3). The range of Ca/P ratios which correspond to ACP, PCH and the range which correspond to crystalline HA is indicated in Figure A.10. A selected area diffraction pattern obtained from predominately ACP, PCH will be diffuse; however, the pattern obtained from predominately HA will have a sharp ring structure. Figure A.10 shows that it is necessary to select an area of bone less than about $2\mu m$ from the surface bone in order to obtain a SAD pattern from the region of bone thought to be ACP, PCH.

3.4(a) Selected area diffraction: experimental technique

The JEOL JEM 100C TEM was used to obtain the SAD patterns. The smallest area that could be selected was determined using a calibration specimen and found to be $0.46\mu m$. The two main sources of uncertainty in the SAD technique are due firstly, to spherical aberration of the objective lens and secondly, to incorrect focusing of the objective lens. Both these effects cause a displacement of the image in the plane of the SAD aperture; ie the diffraction pattern is obtained from a slightly different region of specimen than that which is apparently

(a) ACP, PCH   CRYSTALLINE HA

SOFT TISSUE / OSTEOID

AREA SELECTED FOR SAD.

MINERALISED BONE SURFACE

(b)

CRYSTALLINE HA

Ca/P COUNT RATIO

2·2
2·1
2·0
1·9
1·8
1·7

1·76

1·60

1·40

ACP, PCH

1   2   3   4

DISTANCE INTO BONE / μm
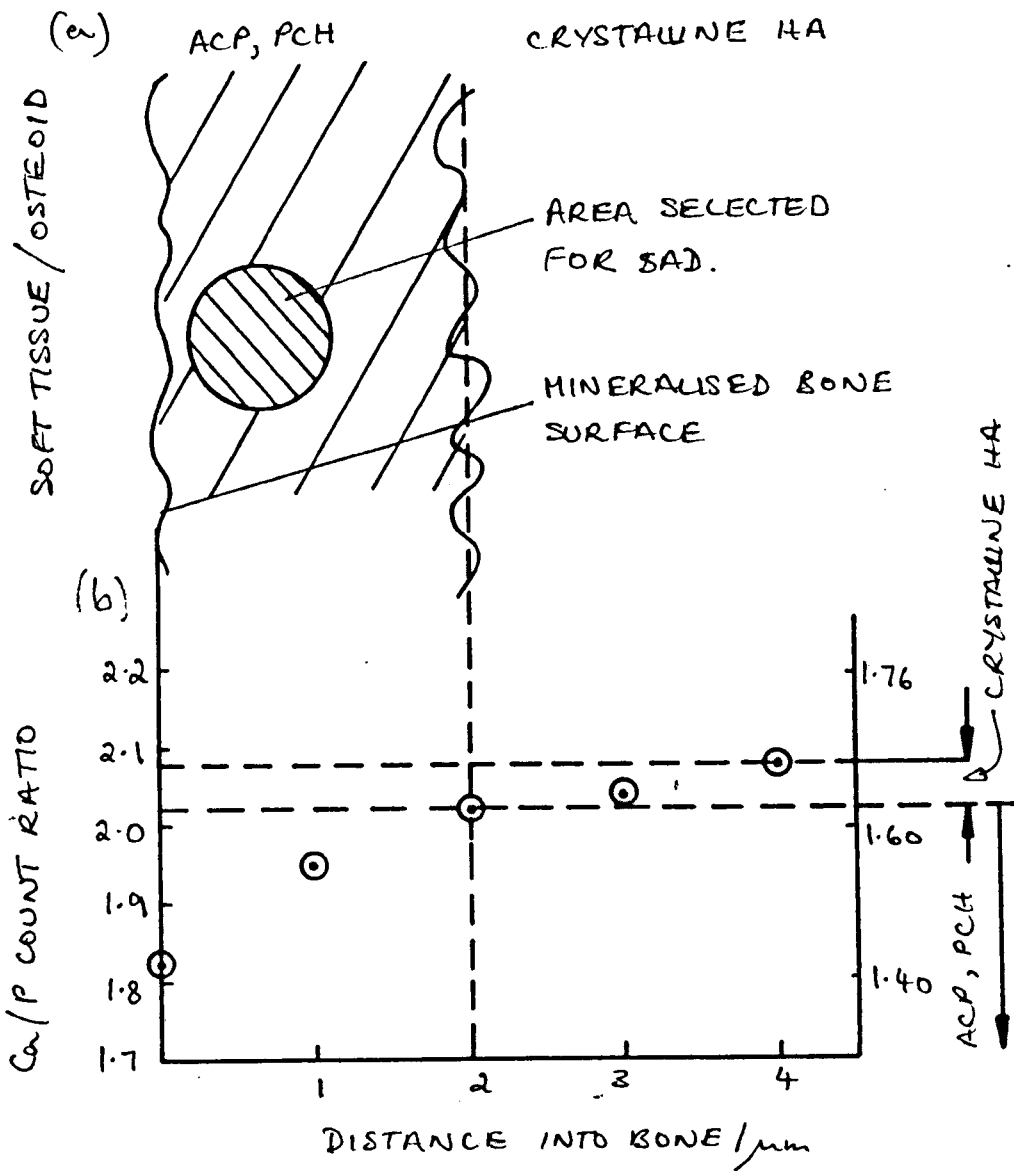
FIGURE A.10   (a) SCHEMATIC DIAGRAM OF A REGION OF MB, (b) AVERAGE Ca/P RATIOS VERSUS DISTANCE INTO BONE.

selected. The amount of displacement (d) between these areas is given by

$$d = C_s \alpha^3 + D\alpha$$

where C_s is the spherical aberration coefficient for the objective lens, α is the maximum scattering angle for the electrons forming the SAD pattern, and D is the distance between the plane of focus of the objective lens and the specimen. The value of C_s quoted by the manufacturers is 8.2×10^{-3}m, and D was assumed to be less than 1000Å. The angle α was determined from

$$\alpha = 2r/L$$

where r is the radius of the largest diffraction ring of interest, and L is the camera length. was found to be 1.5cm, and the camera length was calibrated using a polycrystaline Al specimen and calculated to be 112cm. The value of d was thus determined as 0.02μm, which is not significant compared with the 0.46μm diameter region selected. Therefore there is negligible uncertainty in selecting a region of bone.

3.4(b) Results

Figure A.11 shows a SAD pattern recorded from all the regions of bone where Al was not detected (ie from the deep bone of the experimental and control samples and the surface bone of the experimental samples). As expected, the rings are sharp and clearly defined indicating the presence of crystaline HA. In section A.3.4 it was suggested that the surface bone region of the experimental samples might give rise to a diffuse diffraction pattern indicating the presence of microcrystalline ACP, PCH. For most samples (samples 1, 2, 4 and 5) this was not the case, and patterns showing clear rings were observed

A1.8
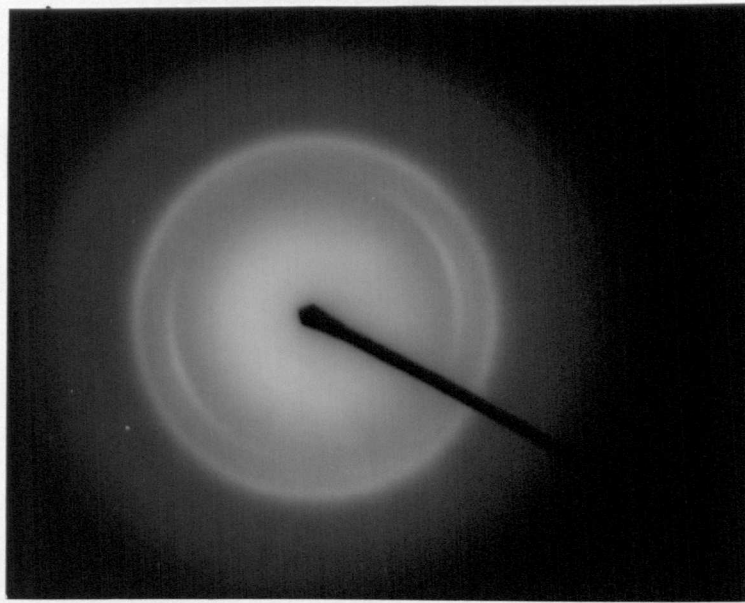
CRYSTALLINE HA

Figure A.11
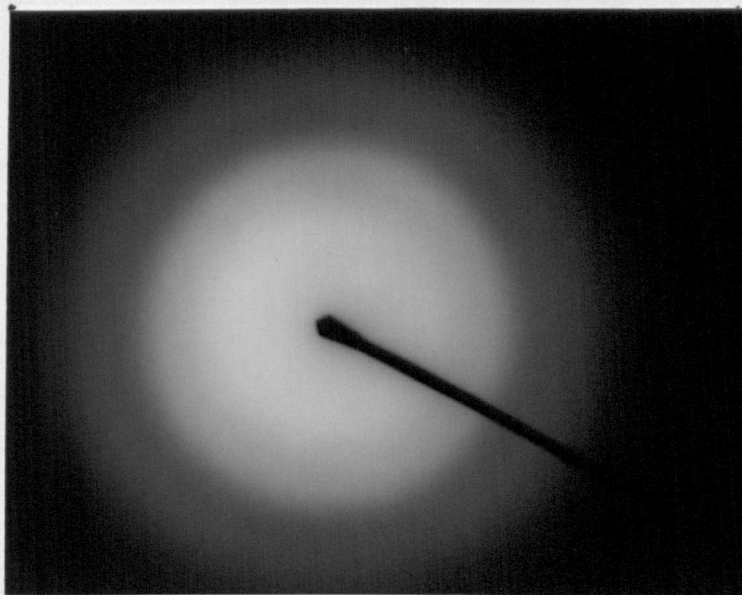
PCH, ACP

Figure A.12

(ie very similar to figure A11). However, a diffuse pattern was consistently obtained from the surface bone regions of sample 3 (see figure A.12).

3.4(c) Interpretation

The wet-cutting specimen preparation technique may have precipitated ACP, PCH to HA crystallisation since ACP is known to be unstable in aqueous media (eg Landis, 1978). Sample 3 contained about twice the level of Al observed in the other samples, and this may have been sufficient to inhibit the crystallisation process. The experiment is now being repeated using non-aqueous specimen fixation, dehydration, and staining techniques.

A.3.5 Conclusion

The results obtained from the MB study described here are consistent with the finding of previous workers; ie that when Al is present in sufficiently high concentrations it is incorporated into mineralising bone inhibiting the mineralisation process. The suggestion put forward in this thesis is that Al acts by inhibiting the ACP,PCH transformation that occurs during mineralisation.

REFERENCES

P.F. Adam (1986) Ph.D. Thesis, University of Glasgow

C.C. Ahn and P. Rez (1985) Ultramicroscopy 17 105.

A.C. Alfrey et al (1972) Trans. Am. Soc. Artif. Intern. Org. 18, 257.

A.C. Alfrey, G.R. LeGendre, W.D. Kachney (1976) N. Engl. J. Med. 294, 184.

H.C. Anderson, T.F. Johnson, A. Avramides (1981) Bone Histomorphometry (ed W.S. Jee and A.M. Parfitt), p79

D. Andress, A. Felsenfeld, A. Voigts, F. Uach (1983) Kidney Int. 23, 94.

A.L. Arsenault, F.P. Ottensmyer and A.B. Hodsman (1983a) in "Clinical Disorders of Bone and Mineral Metabolism "(eds. B. Frame and J.T. Potts) Excerpta Medica, Amsterdam-Oxford-Princeton p220

A.L. Arsenault and F.P. Ottensmyer (1983b) Proc. Natl. Acad. Sci. USA 80 1322

D. Berenyi, G. Hock (1978) Jap. J. Appl. Phys. supp 17-2 78

B. De Bernard (1982) Clin. Orthop. 162, 233.

H.A. Bethe (1930) Ann. der. Phys. 5, 325.

N.C. Blumenthal and A.S. Posner (1984) Calcif. Tissue Int. 36, 439.

E. Bonucci (1971) Clin. Orthop. 78, 108

B.F. Boyce, H.Y. Elder, G.S. Fell, W.A.P. Nicholson, G.D. Smith, D.W. Dempster, C.C. Gray, I.T. Boyle (1981) SEM 3, 329.

B.F. Boyce, H.Y. Elder, H.L. Elliot, I. Fogelman, G.S. Fell, B.J. Juniors, G. Beastal, I.T. Boyle (1982) The Lancet Nov.6, 1009.

A. Boyde, V.R. Switsurland and A.D.G. Stewart (1963) Arch. Oral. Biol. Spec., Suppl. 8 185.

E.F. Bres, J.C. Barry and J.L. Hutchison (1984) Ultramicroscopy 12 p367

J.N. Chapman, C.C. Gray, B.W. Robertson, W.A.P. Nicholson (1983) X-ray Spectrom 12 4 153.

J.N. Chapman, W.A.P. Nicholson and P.A. Crozier (1984) J. of Microscopy. 136, 179.

C.C. Colliex and P. Trebbia (1981) in "Microprobe analysis of Biological Systems" (eds. T.E. Hutchison and A.P. Somlyo) Academic Press p251

C. Colliex, T. Manoubi, M. Gasgnier and L.M. Brown (1984) published in "SEM 84" p324.

A.J. Craven, A.M. MacLeod, R.P. Ferrier (1980) in "Proc 7th European Congress on E.M." (P. Brederoo and G. Bloom ed.) 1, 170

A.J. Craven, T.W. Buggy (1981a) Ultramicroscopy 7, 27.

A.J. Craven, T.W. Buggy, R.P. Ferrier (1981b) in "Quantitative microanalysis with high spatial resolution" published by The Metals Society, p141.

A.J. Craven, P.F. Adam, W.A.P. Nicholson, J.N. Chapman, R.P. Ferrier (1984a) Journal de Physique 45, pc2-437.

A.J. Craven, T.W. Buggy (1984b) J. Microsc. 136 2 227

A.J. Craven, P.F. Adam and R. Howie (1985) in "EMAG/85" Inst. Phys. Conf. Ser. No 78 7, 189.

A.V. Crewe (1971) in "Electron Microscopy in Materials Science" (U. Valdre and A. Zichichi ed.) Acad. Press, N.Y., p162.

P. A. Crozier, J.N. Chapman, A.J. Craven and J.M. Titchmarsh (1983) Proc. EMAG, IOP) p107.

P. A. Crozier, J.N. Chapman, A.J. Craven and J.M. Titchmarsh (1984) Analytical Electron Microscopy (eds. D.B. Williams and D.C. Joy) San Francisco Press, p79

P.A. Crozier (1985) Ph.D. Thesis, University of Glasgow.

S. Csillag (1984) in proceedings of 8th European Congress on Electron Microscopy (A. Csanady, P. Rohlich and D. Szabo ed.) p419.

D.V. Dempster, W.A.P. Nicholson, H.Y. Elder D.A.S. Smith and R.P. Ferrier (1978) 9th Inter. Congr. Electron Microscopy, Toronto 3, 666.

D.V. Dempster, H.Y. Elder, W.A.P. Nicholson and D.A. Smith (1979) J. Physiol. 291 61p

D.W. Dempster, H.Y. Elder, W.A.P. Nicholson D.A. Smith,
V.A. Moss (1980a) Calcif. Tissue Inter. 30 p135.

D.W. Dempster, H.Y. Elder, W.A.P. Nicholson and D.A. Smith
(1980b) J. Physiol. 300 67p.

D.W. Dempster, C.C. Gray and I.T. Boyle (1981) Scanning
Electron Microscopy 3 329

R.M. Dolby (1963) J.Sci. Inst. 40 345.

T. Drueke (1980) Nephron 26, 207.

R.F. Egerton (1979) Ultramicroscopy. 4, 169.

R.F. Egerton (1982) Ultramicroscopy 9 387.

R.F. Egerton (1983) in "Quantitative Electron Microscopy"
(J.N. Chapman and A.J. Craven ed.) Published by Scottish
Universities Summer School.

R.F. Egerton (1984) Scanning Electron Microscopy 2, 505.

R. Eisberg and R. Resnick (1974) in "Quantium Physics of
Atoms, Molecules, Solids, Nuclei and Particles" (publ. by
J. Wiley and sons)

H.L. Elliot et al (1978) Br. Med. J. 1, 1101.

H.A. Ellis, J.A. McCarthy and J. Herrington (1979) 32,
832.

U. Fano (1954) Phys. Rev. 95, 1198.

R.P. Ferrier (1981) in "Microprobe Analysis of Biological
Systems" Academic Press. p231.

D.J. Fisher, D. Mc Connell (1969) Science 164, 551.

J. Friedel (1954) Adv. Phys. 3, 446.

C.V. Gay (1977) Calcif Tiss. Res. 23, 215.

I.J. Goldstein, J.L. Costley, G.W. Lorimer and S.J.B. Reed
(1977) Scanning Electron Microscopy. 1, 315.

C.C. Gray (1981) Ph.D. Thesis, Univesity of Glasgow.

C.C. Gray, J.N. Chapman, W.A.P. Nicholson, B.W. Robertson
and R.P. Ferrier (1983) X-ray Spectrom. 12, 4 163.

R.A. Harper, A.S. Posner (1966) Proc. Soc. Exp. Biol. Med.
122, 137.

B.L. Henke and R.L. Ebsu (1974) in "Advances in X-ray Analysis" Vol 17, Plenum Press, New York, p150

K.F.J. Heinrich C.E Fiori and R.L. Myklbust (1979) J.Appl. Phys. 50, 5589.

H.J. Höling, H. Schopfer, H. Holing et al (1970) Naturwiss 57 357.

H.J. Höling, V.A.P. Nicholson, J. Schreiber et al (1972) Naturwiss 59 423.

M. Inokuti (1966) Argonne National Lab. Report No. ANL-7220 p1 (unpublished).

M. Inokuti (1971) Rev. Mod. Phys. 43, 297.

M. Inokuti, Y. Itikawa and J.E. Turner (1978) Rev. Mod. Phys. 50, 23.

Md.R. Kahn, M Karimi (1980) X-ray Spectrom. 7, 32.

K. Kandiah (1966) in "Radiation measurements in Nuclear Power" J. O. P. and Phys. Soc. London p420.

H.V. Koch, J.V. Motz (1959) Rev. Mod. Phys. 31, 920.

V. Kossel (1920) 2. Phys. 1, 119.

J. Lacer, E.E. Haller, R.C. Cordi (1977) IEEE Trans. Nuc. Sci. 24, 53.

V.J. Landis, M.J. Glimcher (1978) published in 24th Annual ORS, Dallas, Texas Feb 21-23.

A. Langberg, J. van Eck (1979) J. Phys. B 12, 1331.

R.D. Leapman, P. Rez and D.F. Mayers (1980) J. Chem. Phys. 72 (2), 1232.

R.D. Leapman (1983) :- R.D. Leapmans comment in the discussion of the paper by F.P. Ottensmyer and A.L. Arsenault (1983) SEM 4, 1867.

T. Malis and J.M. Titchmarsh (1985) Inst. Phys. Conf. Ser. No. 78 78, 181.

D.M. Maher, D.C. Joy, M.B. Ellington, N.J. Zalnzec and P.E. Mochel (1981) in "Analytical Electron Microscopy" (R.H. Geiss ed.) San Francisco Press, p33.

H.S.V. Massey and C.B.O. Mohr (1931) Proc. Royal Soc. (London) A132 p605

J. Morrisey, M. Rothstein, G. Mayer, E. Slatopolsky (1983)
Kidney Int. 23, 699.

J. Morrisey, M. Rothstein, E. Slatopolsky (1982) Calif.
Tissue Int., 34 (suppl 1), 543

G.R. Morrison (1981) PhD Thesis, University of Glasgow.

N.F. Mott, H.S.W. Massey (1949) "The Theory of Atomic
Collisions", Oxford University, London.

J.A. Nelder and R. Mead (1965) Computer J., 7 308

W.A.P. Nicholson (1974) in "Microprobe Analysis as Applied
to Cells and Tissues" (T.A. Hall, P. Echlin, R. Kaufmann
eds.) Academic Press, London and New York, p239.

W.A.P. Nicholson, B.W. Robertson and J.N. Chapman (1977a)
Inst. Phys. Ser. No. 36 (ed. D. Missel) Institute of
Physics, p373.

W.A.P. Nicholson, B.A. Ashton, H.J. Hohling, P. Quint and
J. Schreiber (1977b) Cell Tiss. Res. 177 331.

W.A.P. Nicholson and D.V. Dempster (1980) in "Scanning
Elecron Microscopy/1980" (eds. O. Johari and R.P. Becker)
Published by S.E.M. Inc. Chicago, 2, 517.

W.A.P. Nicholson, P.F. Adam, A.J. Craven, J.D. Steele
(1984) in "Analytical Electron Microscopy" (ed. D.B.
Williams and D.C. Joy), San Francisco Press, San
Francisco, p257.

C. Nockolds, M.J. Nasir, G. Cliff, G.W. Lorimer (1979) in
"Electron Microscopy and Analysis" (T. Mulvey ed.), IOP,
London, p417.

I.S. Parkinson et al (1979) Lancet 1, 406.

G.M. Phillips and P.J. Taylor (1973) in "Theory and
Applications of Numerical Analysis" Academic Press

A.M. Pierides et al (1980) Kidney Int. 18, 115.

C.J.Powell (1976) Rev. Mod. Phys. 48, 33.

R.H. Pratt, H.K. Tseng, C.M. Lee and L. Kissel (1977) A.
Data Nuel. Data ,Tables. 20, 175.

P. Quint, J. Althoff, H.J. Hohling, A. Boyde and W.A.
Laabs (1980) Calcif. Tiss. Int. 32, 257.

H. Raether (1980) in "Excitation of Plasmons and Interband
Transitions by Electrons (Springer Verlag)

J. Rolteinbourge et al (1980) Ann. Med. Inter. 131, 71.

E. Rutherford (1911) Phil. Mag. 21, 669.

P. Rez (1984) X-ray Spectrom. 13, 2 55.

T.P. Schreiber, A.M. Wims (1981) Ultramicroscopy. 6, 323.

J. Schreiber (1977) Cell Tiss. Res. 177 331

J.H. Scofield (1974) Phys. Rev. A 9, 1041.

K. Shima, S. Nagai, T. Mikumo, S. Yasumi (1983) Nuc. Inst.
and Meths. 217, 515

N. Siegel, A. Haug (1983) Biochem. Biophys. Acta 744, 36.

G. Springer and B. Nolan (1976) Canadian J. Spectros. 21,
134.

P.J. Statham (1981) J. Microsc. 123, 1

E.A. Stern (1978) Contemp. Phys. 19, 289.

P.C. Sternweis, A.G. Gilman (1982) Biochemistry 79, 4888.

J.O. Terwine (1967) Clin. Orthop. 85, 207.

T.P. Thinh and J. Leroux (1979) X-ray Spectrom 8, 85.

J.A. Trant et al (1981) Kidney Int. 19, 130.

M.C. de Vernejoul et al (1985) Bone 6, 15.

E.M. Wadell (1982) Ph.D. Thesis, University of Glasgow.

M.D. Ward et al (1979) Lancet 1, 406.

N.J. Zaluzec (1979) in "Introduction to Analytical Elecron
Microscopy" eds. J.J. Hren, J.I. Goldstein and D.C. Joy.
Plenium Press p121

N.J. Zaluzec (1981) in "Microbeam Analysis 1981" (ed R.H.
Geiss) San Francisco Press, p329.

N.J. Zaluzec, (1984) AEM 279 Analytical Electron
Microscopy (D.B. Williams and D.C. Joy ed.) San Francisco
Press Inc. p276

TABLE OF FREQUENTLY USED SYMBOLS

m_0c^2 electron rest mass energy = 511.0 keV

E_0, E_n initial and final total energy of an electron in a collision in m_0c^2 units

k, k_n chapter 2: initial and final momentum of an electron in a collision in m_0c units

k chapter 5: X-ray variable defined by equation 5.4b

chapter 6: EEL variable defined by equation 6.3

section 5.6 only: peak shift factor

T_0 initial kinetic energy of an electron in a collision in mc units

β_0 ratio of v_0 to the velocity of light

σ_n total cross-section per atom for the ionisation of the nth shell of an element

I_n ionisation energy of nth shell in m_0c^2 units

I_i incident beam current

U_K overvoltage for the K-shell of an element

b_n, c_n Bethe parameters for the nth shell of an element

ω_x fluorescence yield of element x

s_x ratio of the Kα intensity to the total K-shell yield for element x

Z_x atomic number of element x

N_x chapter 2: number of atoms per unit area of element x

all other chapters: number of atoms of element x

α probe convergence semi-angle

β section 4.3 to 4.3.2 only: ratio of electron velocity to

velocity of light

otherwise: electron collection semi-angle

E   energy of emitted photon in $m_0 c^2$ units

$\epsilon(E)$ X-ray detector efficiency at photon energy E

P_x number of characteristic K X-rays of element x detected

$B_x(E)$ number of bremsstrahlung X-rays detected in a window dE, centred
at photon energy E, from a sample of element x

$\mu/\rho(E)$ mass-absorption coefficient at photon energy E

r   parameter defineing curvature in $A(\Delta E)^{-r}$ EEL background

A_r value of A determined from equation 6.12 for given r

A_1^r initial estimate to A_r calculated from equation 6.15

ΔA range of A values tried in equation 6.12

$(\chi_1^2)_r$ value of pre-edge chi-square determined from equation 6.13 for
given r and A_r

k_r value of k determined from equation 6.13 for given r and A_r

k_1^r initial estimate to k_r calculated from equation 6.17

Δk range of k values tried in equation 6.13

$(\chi_2^2)_r$ value of post-edge chi-square determined from equation 6.13 for
given r, A_r and k_r

t   section 4.1 and sections 7.3 to 7.3.9: spectrum acquisition time
sections 4.2(a) to 4.3.4 and sections 7.1 to 7.2.4: thickness

MBH   Modified Bethe Heitler (eg Koch and Motz 1959)

MB   chapter 2 only: modified Bethe (equation 4.20)

otherwise: mineralised bone

SAD   selected area diffraction

ACP   amorphous calcium phosphate